

**Biological synthesis of metallic
nanoparticles and their interactions with
various biomedical targets**

A thesis submitted in fulfilment of the requirements
for the degree of

DOCTOR OF PHILOSOPHY

of

RHODES UNIVERSITY

By

Afolake Temitope Sennuga

December 2011

Abstract

The synthesis of nanostructured materials, especially metallic nanoparticles, has accrued utmost interest over the past decade owing to their unique properties that make them applicable in different fields of science and technology. The limitation to the use of these nanoparticles is the paucity of an effective method of synthesis that will produce homogeneous size and shape nanoparticles as well as particles with limited or no toxicity to the human health and the environment. The biological method of nanoparticle synthesis is a relatively simple, cheap and environmentally friendly method than the conventional chemical method of synthesis and thus gains an upper hand. The biomineralization of nanoparticles in protein cages is one of such biological approaches used in the generation of nanoparticles. This method of synthesis apart from being a safer method in the production of nanoparticles is also able to control particle morphology.

In this study, a comparative biological synthesis, characterization and biomedical effects of metallic nanoparticles of platinum, gold and silver were investigated. Metallic nanoparticles were biologically synthesized using cage-like (apoferritin), barrel-like (GroEL) and non-caged (ribonuclease) proteins. Nanoparticles generated were characterized using common techniques such as UV-visible spectroscopy, scanning and transmission electron microscopy, inductively coupled optical emission spectroscopy, Fourier transform infra-red spectroscopy and energy dispersion analysis of X-rays (EDAX).

Nanoparticles synthesised biologically using apoferritin, GroEL and RNase with exhibited similar chemical and physical properties as those nanoparticles generated chemically. In addition, the metallic nanoparticles fabricated within the cage-like and barrel-like cavities of apoferritin and GroEL respectively, resulted in nanoparticles with relatively uniform morphology as opposed to those obtained with the non-caged ribonuclease. The enzymatic (ferroxidase) activity of apoferritin was found to be greatly enhanced with platinum (9-fold), gold (7-fold) and silver (54-fold) nanoparticles. The ATPase activity of GroEL was inhibited by silver nanoparticles (64 %), was moderately activated by gold nanoparticles (47 %) and considerably enhanced by platinum nanoparticles (85 %). The hydrolytic

activity of RNase was however, lowered by these metallic nanoparticles (90 % in Ag nanoparticles) and to a higher degree with platinum (95 %) and gold nanoparticles (~100 %). The effect of synthesized nanoparticles on the respective enzyme activities of these proteins was also investigated and the potential neurotoxic property of these particles was also determined by an in vitro interaction with acetylcholinesterase. Protein encapsulated nanoparticles with apoferritin and GroEL showed a decreased inhibition of acetylcholinesterase (< 50 %) compared with nanoparticles attached to ribonuclease (> 50 %).

Thus, it can be concluded that the cavities of apoferritin and GroEL acted as nanobiofactories for the synthesis and confinement of the size and shape of nanoparticles. Furthermore, the interior of these proteins provided a shielding effect for these nanoparticles and thus reduced/prevented their possible neurotoxic effect and confirmed safety in their method of production and application. The findings from this study would prove beneficial in the application of these nanoparticles as a potential drug/drug delivery vehicle for the prevention, treatment/management of diseases associated with these enzymes/proteins.

Keywords: *Metallic nanoparticles, Platinum, Gold, Silver, Apoferritin, GroEL, Ribonuclease (RNase), Ferroxidase, ATPase, Acetylcholinesterase (AChE)*

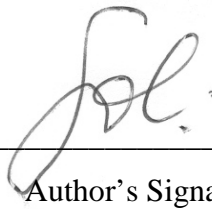
Publication(s) from this study

Sennuga A., van Marwijk J. and Whiteley C.G. (2012). Ferroxidase activity of apoferritin is increased in the presence of platinum nanoparticles. *Nanotechnology*, **23**:035102.

Sennuga A., van Marwijk J., Boshoff A. and Whiteley C.G. (2012). Enhanced activity of chaperonin GroEL in the presence of platinum nanoparticles. *Journal of Nanoparticle Research*, Article in Press.

Declaration

I declare that this thesis is my own, unaided work. It is being submitted for the degree of Doctor of Philosophy at Rhodes University. It has not been submitted before for any degree or examination in any other university.



Author's Signature

14/03/2012

Date

Table of Contents

Contents

Abstract	ii
Declaration	iv
Table of Contents.....	v
List of Figures	xii
List of Tables.....	xvii
List of Abbreviations	xviii
Dedication.....	xxi
Acknowledgements	xxii
Chapter 1: Literature review	1
1.1 Introduction: Nanoparticles and nanobiotechnology.....	1
1.2 Classification of nanoparticles and applications	2
1.2.1 Fullerenes: Buckyballs and carbon nanotubes	3
1.2.2 Liquid crystals	4
1.2.3 Liposomes.....	4
1.2.4 Quantum dots.....	5
1.2.5 Superparamagnetic nanoparticles	5
1.2.6 Dendrimer.....	6
1.3 Metal nanoparticles.....	7
1.3.1 Synthesis.....	8
1.3.1.1 Chemical approach	9
1.3.1.2 Biological approach.....	10
1.4 Characterization of nanoparticles	12

1.4.1	Characterization methods	14
1.4.1.1	Optical methods.....	15
1.4.1.2	Spectroscopic methods	15
1.4.1.3	Electron probe methods.....	17
1.4.1.3.1	Scanning electron microscopy (SEM).....	18
1.4.1.3.2	Transmission electron microscopy (TEM).....	20
1.4.1.4	Scanning probe microscopy (SPM) methods	22
1.4.1.5	Atom probe microscopy (APM) methods	23
1.4.1.6	Non-radioactive and non-electron characterization methods	24
1.4.1.6.1	Mass spectrometry (MS)	24
1.4.1.6.2	Thermodynamic methods	25
1.4.1.7	Other methods of characterization.....	26
1.4.1.7.1	Quartz crystal microbalance (QCM)	26
1.5	Safety of nanoparticles	26
1.6	Research Focus	27
1.6.1	Hypothesis	27
1.6.2	Objectives	27
Chapter 2: Biological synthesis of metallic nanoparticles in apoferritin		28
2.1	Introduction	28
2.2	Materials and Methods	31
2.2.1	Materials	31
2.2.2	Methods	31
2.2.2.1	Nanoparticle synthesis.....	31
2.2.2.2	Characterization.....	32
2.2.2.2.1	UV-Visible spectroscopy.....	32
2.2.2.2.2	Inductively coupled plasma optical emission spectroscopy (ICP OES)	
	32	
2.2.2.2.3	Fourier Transfer Infra Red (FTIR)	32
2.2.2.2.4	Transmission Electron Microscopy (TEM).....	33
2.2.2.2.5	Energy dispersive X-ray spectroscopy (EDX)	33

2.2.2.3	Assay of HSA ferroxidase activity	33
2.2.2.3.1	Effects of M-nps on the ferroxidase activity of HSA.....	33
2.2.2.4	Protein determination	34
2.2.2.5	Statistical Analysis	34
2.3	Results and Discussion	34
2.3.1	Synthesis of nanoparticles	34
2.3.2	Characterization.....	37
2.3.2.1	ICP OES analysis	37
2.3.2.2	UV-visible spectroscopy	40
2.3.2.3	FTIR analysis.....	41
2.3.2.4	TEM analysis.....	43
2.3.2.5	EDX analysis	48
2.3.2.6	The effect of M-nps on the ferroxidase activity of HSA.....	49
2.4	Conclusions	51
Chapter 3: Biosynthesis of metallic nanoparticles in GroEL.....		52
3.1	Introduction	52
3.2	Materials and Methods	54
3.2.1	Cloning, expression and purification of GroEL	54
3.2.1.1	Materials	54
3.2.1.2	Methods	54
3.2.1.2.1	Transformation	54
3.2.1.2.2	Induction/Induction studies	54
3.2.1.2.3	Purification	54
3.2.1.2.4	SDS-PAGE, western blot analysis and molecular mass determinations	
	55	
3.2.1.2.5	GroEL ATPase activity	56
3.2.1.2.6	Protein estimation.....	56
3.2.2	Nanoparticle synthesis.....	56
3.2.3	Characterization.....	57
3.2.4	Effect of nanoparticles on the ATPase activity of GroEL.....	57

3.2.5	Statistical analysis	57
3.3	Results and Discussion	57
3.3.1	Expression of GroEL	57
3.3.2	Purification	58
3.3.3	Synthesis and characterization of M-nps	61
3.3.3.1	Synthesis	61
3.3.3.2	Characterization	61
3.3.3.2.1	UV-visible spectroscopy	61
3.3.3.2.2	TEM, EDX, ICP and FTIR ananlysis	64
3.3.4	Effect of M- nps on the ATPase activity of GroEL	71
3.4	Conclusions	75
Chapter 4: Biosynthesis of metallic nanoparticles with ribonuclease		76
4.1	Introduction	76
4.2	Materials and Methods	78
4.2.1	Materials	78
4.2.2	Methods	78
4.2.2.1	Synthesis	78
4.2.2.2	Characterization	79
4.2.2.3	RNase assay	79
4.2.2.4	Effect of synthesized nanoparticles on RNase activity	79
4.2.2.5	Protein determination	80
4.3	Results and Discussion	80
4.3.1	Synthesis	80
4.3.2	Characterization	82
4.3.2.1	UV-Vis spectroscopy	82
4.3.2.2	Inductively coupled plasma optical emission spectroscopy (ICP OES) .	84
4.3.2.3	FTIR analysis	86
4.3.2.4	TEM & EDAX analysis	88
4.3.3	The effect of M-nps on the enzymatic activity of RNase	91
4.4	Conclusions	93

Chapter 5: Interaction of metallic nanoparticles with acetylcholinesterase	94
5.1 Introduction	94
5.2 Materials and Methods	96
5.2.1 Preparation of nanoparticle stock solutions.....	96
5.2.2 AChE assay	96
5.2.3 Interaction of M-nps with AChE.....	98
5.2.4 Statistical Analysis	98
5.3 Results	98
5.3.1 The effects of nanoparticles on AChE.....	98
5.3.1.1 M-nps-HSA	98
5.3.1.2 M-nps-GroEL	100
5.3.1.3 M-nps-RNase.....	100
5.4 Discussions and Conclusions	103
Chapter 6: General discussion and conclusions	104
6.1 Discussions	104
6.1.1 Biosynthesis of nanoparticles	104
6.1.2 Interaction of nanoparticles with AChE.....	108
6.2 Conclusions	109
6.3 Future work	109
References.....	110
Appendices	141
Appendix A – Method of preparation of buffers and solutions	141
<i>A1: Tris buffer saline (TBS), pH 8.0 (1L).....</i>	141
<i>A2: 1 M Tris-HCl, pH 8.0 (1 L).....</i>	141
<i>A3: 3 M NaCl.....</i>	141
<i>A4: 50 mM borate-cacodylate buffer, pH 5.5.....</i>	141

<i>A5: Phosphate buffer saline (PBS) – 500 ml</i>	141
<i>A6: Chloramphenicol (CAM, 35 mg/ml stock, 10 ml)</i>	142
<i>A7: L-arabinose (40 %, 10 ml)</i>	142
Appendix B – Preparation of metal standards for ICP OES and metal standard curves	142
<i>B1: Platinum</i>	142
<i>B2: Gold</i>	143
<i>B3: Silver</i>	144
Appendix C – Standard curve of ferritin	147
<i>C1: Ferritin stock preparation (1 ml)</i>	147
Appendix D- Protein standard curve for estimation of protein concentration by Bradford method	148
Appendix E- Recipe for 2x YT broth and Agar	149
<i>E1: 2 x YT broth (1 L)</i>	149
<i>E2: 2xYT Agar + CAM plates (300 ml)</i>	149
Appendix F: Polyacrylamide gel electrophoresis (PAGE) and western analysis procedures	149
<i>F1: Native PAGE protocols for Bio-Rad mini –protean II apparatus (modified method of Bollag et al., 1996)</i>	149
<i>F2: SDS PAGE for the molecular weight determination of proteins (modified method of Bollag et al., 1996)</i>	150
<i>F3: Staining and destaining solution for both native and SDS gels (Gálvez et al., 2008)</i>	152
<i>F4: Protein molecular weight determination</i>	153
<i>F5: Western blot analysis-preparation of buffers and solutions protocols</i>	153

Appendix G: Phosphate standard curve for estimation of phosphate release by the ATPase activity of GroEL.....	156
<i>G1: Ascorbate-molybdate reagent</i>	156
<i>G2: Phosphate standard curve protocol</i>	156
<i>G3: ATPase assay of GroEL</i>	158
Appendix H: RNase protein estimation by bicinchoninic acid(BCA) and activity determination	158
<i>H1: BCA working reagent.....</i>	158
<i>H2: Protein standard curve for protein estimation by BCA method (Smith, 1985).....</i>	159
<i>H3: Acetate-perchloric acid solution – 10 ml</i>	159
<i>H4: RNase activity preparation.....</i>	160
Appendix I: Activity calculations and percentage inhibition of AChE	160
<i>I.1: Calculation of AChE activity</i>	160
<i>I.2: Percentage inhibition calculation.....</i>	160

List of Figures

Figure 1.1: Versatility of nanoparticless conjugated to various biomolecules such as antibodies in antigen detection, fluorescent signalling probes and peptides etc. (Adapted from Salata, 2004).	2
Figure 1.2: TEM images of (A) SWNT (B) bundle of SWNTs and (C) MWNT. (Taken from GTIR Nanotechnology Lab.	4
Figure 1.3: Changes in optical properties of quantum dots as size increases (Taken from Aerospace concepts Pty Ltd).	6
Figure 1.4: A schematic representation of the structure of a dendrimer (Smith, 2008).	7
Figure 1.5: An illustration of the cage-shaped protein apoferritin without iron core and ferritin with iron core (Taken from Iwahori and Yamashita, 2007).	12
Figure 1.6: The scanning electron microscope (SEM). (a) SEM instrument. (b) Schematic representation of the SEM. (Taken from the University of Queensland center for microscopy and microanalysis; Bradbury <i>et al.</i> , 2011).	19
Figure 1.7: A conventional transmission electron microscope. (a) Instrument (b) Schematic representation. (Taken from Insight experts, 2008; Bradbury <i>et al.</i> , 2011).	22
Figure 2.1: A schematic representation of metallic nanoparticles synthesis in apoferritin (Gálvez <i>et al.</i> , 2008).	30
Figure 2.2: Metal nanoparticles synthesized with varying molar concentrations of metal salts to a fixed concentration of HSA (250-4000 M:HSA). HSA = Control. (a) Pt-nanoparticles, (b) Au-nanoparticles and (c) Ag-nanoparticles. Each sample presented was diluted 10-fold.	35
Figure 2.3: SEC elution profile (I) and native PAGE gels (II) of M-nps-HSA synthesized with different molar concentration of metal salt to a fixed concentration of HSA. (a) Pt-nps; (b) Au-nps and (c) Ag-nps. HSA = Control. (i) HSA only,(ii) 250:1, (iii) 500:1,(iv) 1000:1, (v) 2000:1 and (vi) 4000:1 (M:HSA) in all groups.	37
Figure 2.4: UV-visible absorbance spectra of M-nps-HSA showing typical SPR bands associated with each M-nps. (a) Pt-nps, (b) Au-nps and (c) Ag-nps. Peaks observed around 280 nm were due to the protein absorbance of HSA. Samples were diluted 10-fold.....	40
Figure 2.5: FTIR spectra of M-nps-HSA. (a) Pt-nps ;(b) Au-nps and (c) Ag-nps. Spectrum (i) HSA (i.e. control);(ii) 250:1;(iii) 500:1;(iv) 1000:1;(v) 2000:1 and (vi) 4000:1. Each spectrum presented was an average of 20 scans.....	42

Figure 2.6: TEM micrographs and size distribution of M-nps made from varying molar ratios of metal salts to HSA. (a) Pt-nps, (b) Au-nps and (c) Ag-nps. Scale bar = 100 nm. 200 particles were analyzed in each group. (i) 250:1;(ii) 500:1;(iii) 1000:1;(iv) 2000:1 and (v) 4000:1.	45
Figure 2.7: TEM micrographs of stained M-nps-HSA. (a) HSA only (control); (b) Pt-nps; (c) Au-nps and (d) Ag-nps. Samples were negatively stained with 1% uranyl acetate. Scale bar = 100nm. Green and red arrow represents a typical nanoparticle within the core of HSA and an empty HSA shell respectively.....	47
Figure 2.8: EDAX spectra of M-nps-HSA. (a)Pt-nanoparticles, (b) Au-nanoparticles and (c) Ag-nanoparticles.	48
Figure 2.9: The effect of M-nps on the ferroxidase activity of HSA. (a) Pt-nanoparticles; (b) Au-nanoparticles and (c) Ag-nanoparticles. Results presented are the mean of three independent assays done in triplicate. Error bars represents the standard error of the mean values. * = p <0.05; and *** = p<0.001 versus controls (i.e. HSA)	50
Figure 3.1: Schematic representation (top and side views) of GroEL (crystal structures, right). (Adapted from Ishii et al. 2003; Ortac and Severcan, 2007).....	53
Figure 3.2: SDS-PAGE (12%) analysis of the expression of GroEL and GroES as a function of time. Lane M, protein marker; lanes T ₀ –T ₅ , extract of cells induced for 0-5 h respectively.....	58
Figure 3.3: GroEL purification. (a) SDS-PAGE (12 %) analysis of the purification steps of GroEL. Lane 1= Crude lysate of cells induced after 5 h (100 µg); Lane 2 = Batch purification on DEAE anion exchanger (100 µg) and Lane 3 = FPLC size exclusion chromatography on Sephacryl HR-300 of GroEL after (NH ₄) ₂ SO ₄ precipitation (100 µg). Lane M = Protein markers. (b) Western blot analysis of purification steps of GroEL detected with GroEL antibody. Lanes i-iii represents 100 µg protein of samples obtained from the purification steps of protein in reverse order respectively. (c) TEM image of purified GroEL. Blue and red arrows indicate anterior and lateral respectively. Scale bar = 200 nm.	60
Figure 3.4: UV-visible spectra of M-nps at different molar ratios of metal salts to GroEL. Insets: Observed colour changes in M-nps solution. (a) Pt; (b) Au and (c) Ag.	63
Figure 3.5: Typical M-nps synthesized in the absence (a) and presence (b) of GroEL. Scale bar: a = 500 nm; b = 20 nm.	65
Figure 3.6: TEM micrographs and size distributions of M-nps synthesized by varying molar concentration of metal salts to a fixed concentration of GroEL. (a) Pt: (i) 1:125, (ii) 1:250, (iii) 1:500, (iv) 1:1000 and (v) 1:2000. Lesser molar ratios were not visible. (b) Au; (c) Ag. (i) - (vii) in b & c represents: 1:14, 1:25, 1:50, 1:100, 1:200, 1:500 and 1:1000	

respectively. 200 particles were analysed in each set of molar concentration ratios per group. Scale bar: a = 20 nm; b =10 nm and c = 100 nm.	66
Figure 3.7: TEM micrograph of stained M-nps-GroEL. (a) GroEL only (control); (b) Pt; (c) Au and (d) Ag. Scale bar = 100nm.....	67
Figure 3.8: HRTEM (a) and EDAX (b) analysis of M-nps crystals synthesized in the presence of GroEL (i) Pt; (ii) Au and (iii) Ag. Calculated crystal atomic spacing for Pt, Au and Ag was 0.224, 0.242 and 0.236 nm respectively.	68
Figure 3.9: FTIR spectra of M-nps-GroEL. (i) GroEL only (control); (ii) Pt (1:2000); (iii) Au (1:200) and (iv) Ag (1:200).	70
Figure 3.10: Effects of M-nps on the ATPase activity of GroEL. (a) Pt; (b) Au and (c) Ag. Significant ATPase activity ($p < 0.001$) increase of 5.20 and 2.60 $\mu\text{molPi.ml}^{-1}.\text{min}^{-1}$ was seen at molar ratios of 1:25 and 1:50 – 1:100 with Pt and Au-nps respectively. An inhibitory effect was seen with Ag-nps. *** = $p < 0.001$ versus the controls (i.e. GroEL). Error bars represents the standard error of means of three independent assays.....	72
Figure 4.1: Enzymatic (hydrolysis) reaction catalyzed by RNase (a). The transition state products of the hydrolysis reaction (b), (Adapted from Worthington, 2011).....	76
Figure 4.2: Ribbon diagram of the three dimensional structure of pancreatic RNase A from Bovine. (a) Unlabelled; (b) Labelled. The inscriptions (i.e. coloured in yellow) indicates the location of the eight cysteine residues that forms the four disulfide bonds, the three amino acids residues crucial for catalysis: His 12, His 119 and Lys 41, and residues that stabilizes the intermediate product during catalysis: Lys 7 and Lys 66 (Adapted from Wikipedia, 2011; Raines, 1998).	78
Figure 4.3: Metallic nanoparticles of (a) Pt, (b) Au and (c) Ag synthesized with different molar concentration of metal salts to a fixed molar concentration of RNase. 125-2000 in (a) represents molar concentration ratios of Pt salts to fixed molar concentration of RNase. 12.5-200 in (b) & (c) represents that of Au and Ag metal salts respectively.	81
Figure 4.4: UV-Visible characterization spectra of M-nps synthesized with RNase. (a) Pt; (b) Au and (c) Ag.....	83
Figure 4.5: FTIR spectra of M-nps-RNase. (a) Spectral scan from 1800-1000 cm^{-1} and (b) 3600-1800 cm^{-1} . (i) - (iv) in (a) and (b) represents FTIR spectra of control (RNase only), Pt, Au and Ag respectively. Each spectrum represented was an average of 20 scans.	87
Figure 4.6: TEM analysis of M-nps-RNase complexes (a) Pt; (b) Au and (c) Ag. <i>In</i> (a), (i) 1:125, (ii)1:250,(iii) 1:500, (iv) 1:1000 and (v) 1:2000 (RNase:Pt); in (b), (i) 1:12.5, (ii) 1:25, (iii) 1:50 and (iv) 1:100 (RNase:Au) and in (c), (i) 1:12.5, (ii) 1:25 and (iii) 1:50	

(RNase:Ag). TEM analysis was not possible at molar ratios of 1:200 in Au-nps-RNase and 1:100-1:200 in Ag-nps-RNase due to particle aggregation and precipitation.....	90
Figure 4.7: EDAX spectra of M-nps-RNase. (a) Pt; (b) Au and (c) Ag.....	91
Figure 4.8: The effect of M-nps synthesis on the hydrolytic activity of RNase. Secondary x and y axis represents the molar concentration ratios of a fixed concentration of RNase to varying concentration of precursor metal salts of platinum use in nps synthesis and RNase activities of Pt-nps-RNase respectively. 1 Unit = $1\mu\text{mol}\cdot\text{min}^{-1}$	92
Figure 5.1: Schematic representation of the enzymatic activity of AChE at the neuromuscular cholinergic synapse. (Taken from Proteopedia-life in 3D).....	95
Figure 5.2: The inhibitory effect of M-nps-HSA on AChE. (a) Pt-nps; (b) Au-nps and (c) Ag-nps. Legends represent the M-nps synthesized with a molar concentration ratio of HSA to varying molar concentrations of metal salts. * = $p < 0.05$; ** = $p < 0.01$ and *** = $p < 0.001$	99
Figure 5.3: The AChE inhibitory effect of M-nps-GroEL. (a) Pt-nps; (b) Au-nps and (c) Ag-nps. * = $p < 0.05$; ** = $p < 0.01$ and *** = $p < 0.001$	101
Figure 5.4: The effect M-nps-RNase on the activity of AChE. (a) Pt-nps; (b) Au-nps and (c) Ag-nps. * = $p < 0.05$; ** = $p < 0.01$ and *** = $p < 0.001$	102
<i>Figure B.1: Standard curves of platinum measured at different wavelengths. (a) 214.4 nm; (b) 224.5 nm and (c) 265.9 nm. Each point represents mean values with standard deviations <10 %.....</i>	143
<i>Figure B.2: Standard curves of gold measured at different wavelengths. (a) 197.8 nm; (b) 242.7 nm and (c) 267.5 nm. Each point represents mean values with standard deviations <10 %.....</i>	145
<i>Figure B.3: Standard curves of silver measured at different avelengths. (a) 243.7 nm; (b) 328.2 nm and (c) 338.3 nm. Each point represents mean values with standard deviations <10 %.....</i>	146
<i>Figure C.1: Ferritin standard curve.</i>	147
<i>Figure D.1: Protein standard curve using BSA by Bradford method.</i>	148
<i>Figure F.1: Molecular weight calibration curve using protein markers ranging from 10-170 kDa (Fermentas-Inqaba Biotech, South Africa).</i>	153

<i>Figure F.2: A schematic illustration for the arrangement of the gel-membrane sandwich for protein transfer.</i>	155
<i>Figure G.1: Phosphate standard curve</i>	157
<i>Figure G.2: A plot of ATPase of GroEL activity against time. (a) Activity absorbance at 850 nm versus time. (b) Calculated activity in $\mu\text{mol.ml}^{-1}$ versus time.</i>	158
<i>Figure H.1: BSA protein standard curve by BCA method.</i>	159

List of Tables

Table 1.1: Examples of metallic nanoparticles used in some biomedical applications.....	8
Table 1.2: Exterior and interior diameters of some protein cages used in nps synthesis (Klem et al., 2005).....	13
Table 1.3: Some techniques used in nanoparticle characterization (Adapted from Gabor et al., 2008).....	14
Table 2.1: Estimation of metal: protein stoichiometries of M-nps-HSA. M-nps and protein concentration were determined by ICP OES and Bradford's method respectively.	39
Table 3.1: Purification table of GroEL from 1 L cell culture.....	59
Table 3.2: ICP OES results of M-nps-GroEL.....	69
Table 4.1: Metal nanoparticles concentrations of synthesis and metal to protein stoichiometries.....	85
Table 5.1: Stock concentrations and particle sizes of metal nanoparticles synthesized with different proteins.....	97
<i>Table B.1: Protocol for preparation of platinum standard curve</i>	<i>142</i>
<i>Table B.2: Protocol for preparation of gold standard curve</i>	<i>144</i>
<i>Table B.3: Protocol for preparation of silver standard curve.</i>	<i>144</i>
<i>Table C.1: Protocol of ferritin standard curve.</i>	<i>147</i>
<i>Table D.1: BSA protein standard curve protocol by Bradford method.</i>	<i>148</i>
<i>Table F.1: Protocol for 5 % discontinuous native PAGE (2 x 0.75 mm gels)</i>	<i>151</i>
<i>Table F.2: Recipe for 12 % SDS resolving gels (2 X 0.75 mm gels).....</i>	<i>152</i>
<i>Table G.1: Phosphate standard curve protocol.</i>	<i>157</i>
<i>Table H.1: BSA protein standard curve protocol by BCA method.....</i>	<i>159</i>

List of Abbreviations

ACh	Acetylcholine
AChE	Acetylcholinesterase
Ag	Silver
Ag-nps	Silver nanoparticles
ATChI	Acetylcholine iodide
ATP	Adenosine triphosphate
ATR	Attenuated total reflectance
Au	Gold
Au-nps	Gold nanoparticles
BCA	Bicinchoninic acid
BSA	Bovine serum albumin
CAM	Chloramphenicol
CdSe	Cadmium selenium nanoparticles
CI	Cholinesterase inhibitor
DEAE	Diethylaminoethyl
Dps	DNA binding proteins from starved cells
DTNB	5, 5'-Dithio-bis (2-nitrobenzoic acid)
DTT	Dithiothreitol

EDTA	Ethylenediaminetetraacetic acid
EDX/EDAX	Energy dispersion and analysis of X-rays
FPLC	Fast protein liquid chromatography
FTIR	Fourier transform infrared
HRTEM	High resolution transmission electron microscopy
HSA	Horse spleen apoferritin
Hsp	Heatshock proteins
ICP OES	Inductively coupled plasma optical emission spectroscopy
KCl	Potassium chloride
M-nps	Metal/Metallic nanoparticles
M-nps-GroEL	Metal nanoparticles-GroEL complex
M-nps-HSA	Metal nanoparticles-HSA complex
M-nps-RNase	Metal-nanoparticles-RNase complex
Nps/nps	Nanoparticles
PMSF	Phenylmethylsulfonyl fluoride
Pt	Platinum
Pt-nps	Platinum nanoparticles
RNA	Ribonucleic acid
RNase	Ribonuclease

SDS	Sodium dodecyl sulphate
SDS-PAGE	Sodium dodecyl sulphate polyacrylamide gel electrophoresis
SEC	Size exclusion chromatography
SEM	Scanning electron microscopy
sHsp	Small heat shock proteins
SPR	Surface plasmon resonance
TEM	Transmission electron microscopy
UV-Vis	Ultraviolet-visible

Dedication

This thesis is dedicated to

The Lord God Almighty, the one who began this good work with me and enabled me to complete it (Philippians 1:6).

The three most important men in my life: my husband, Steve Arowolo, and two sons, Daniel and Emmanuel, Arowolo (I love you dearly).

Mum (Mrs. Funmilola Sennuga) and Dad (Mr. Alexander O. Sennuga).

Mentor (Dr. E.M. Obuotor)

Acknowledgements

- My supervisor and wife, Professor and Mrs Christopher and Susan Whiteley, for their academic and emotional contributions and support.
- Organization for women in science for the developing world (OWSDW) formerly known as Third world organization for women in science (TWOWS), who made this possible.
- National Research Foundation and Rhodes University, for financial assistance.
- Members of Lab 309/129C from 2009-2011, you are all appreciated.
- Members of my steering committee, Professors Greg Blatch and Brett Pletschke; Drs. Brendan Wilhelmi, Aileen Boshoff and Adrienne Edkins, it all came together at last.
- Members of the department of Biochemistry, Microbiology and Biotechnology of Rhodes University, especially to Mrs Margot Brooks (what could I have done without you?).
- All family and friends that I would have loved to mention, but for space, words cannot express my immense gratitude to you all for all your prayers and words of encouragement, God bless you all.

Chapter 1: Literature review

1.1 Introduction: Nanoparticles and nanobiotechnology

Nanoparticles are simply defined as particles in the 10^{-9} nm range. Comparing this size, a human hair is said to be approximately 70000 nm in diameter, a red blood cell about 5000 nm and some simple organic molecules fall within 0.5-5 nm range (Aitken *et al.*, 2004). Nanotechnology/nanobiotechnology, on the other hand, simply denotes the man-made use of these nano-sized particles, for industrial and medical purposes. Application depends on the unique properties of each type of nanoparticle. In the past this field was referred to as a science of fiction; i.e. impossible and unattainable, but has now become a hot and fast growing research area. In an article published by a European Institute of Occupational medicine (IOM, 2008), nanotechnology is anticipated to be the foundation of many technological innovations of the 21st century. Nanotechnology as a multi-disciplinary field bridges the whole spectrum of science, touching medicine, physics, engineering and chemistry, yet the common defining characteristic is that of size. It is well known that properties of materials are greatly enhanced when size is decreased. For example, materials like carbon or silicon at nanoscale, demonstrates novel properties such as increased strength, electrical conductivity, chemical reactivity, and other properties which are not observed under normal micro or macro-level conditions (Aitken *et al.*, 2004). A large number of versatile and highly stable materials such as nanowires, nanotubes, derivatives of fullerene (buckyballs) and other nano-materials have already been produced. Also, because of their small size, they are able to interact with biomolecules like proteins making it possible for them to pass through cellular machinery unnoticed by the immune system: as the larger protein acts as a protection or a vehicle to transport these nanoparticles may interact with the target site without eliciting any immune response (Riddin *et al.*, 2006). Moreover, the coupling of nanoparticles to biomolecules like antibodies, carbohydrates, peptides or proteins and DNA through a number of methods involving covalent and hydrogen bonding have been shown to extend their already exceptional versatility (Fig.1.1) and also greatly increase their stability (Vinogradov *et al.*, 2002; Ishii *et al.*, 2003).

1.2 Classification of nanoparticles and applications

A broad library of nanoparticles consisting of different physical and chemical properties has been constructed. Due to new discoveries made in nanotechnology, however, classifications of nanoparticles are constantly changing. Currently nanoparticles can be separated into several different classes.

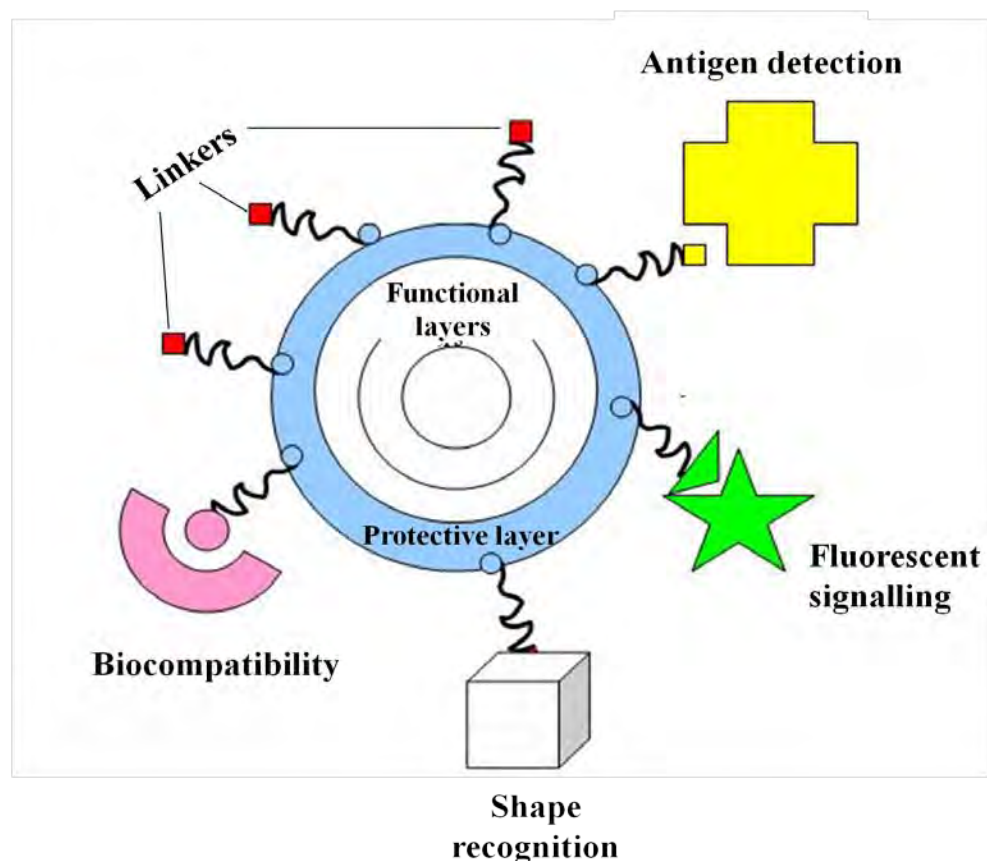


Figure 1.1: Versatility of nanoparticles conjugated to various biomolecules such as antibodies in antigen detection, fluorescent signalling probes and peptides etc. (Adapted from Salata, 2004).

First, there are the nanoclusters that are defined as semi crystalline nanostructures with dimensions within 1-10 nm and a narrow size distribution. Second there are the nanopowders that result from the aggregation of non-crystalline nanomaterials with dimensions between 10-100 nm. Third are the nanocrystals that are single crystalline nanomaterials with dimensions between 100 – 1000 nm. These examples are only the most basic classification of nanoparticles; others include nanorods, nanocups, nanospheres,

nanodiamonds, nanostars and the quantum dots (Philips, 2004). The specific names of each type of particle are used only in the most abstract of research articles. Listed below are some examples of general and multi-functional classes of nanoparticles used in biotechnology and particularly in the area of nanomedicine.

1.2.1 Fullerenes: Buckyballs and carbon nanotubes

Fullerenes are molecules made exclusively of carbon and they exist in different forms such as hollow spheres, ellipsoids or tubes. The spherical forms of fullerenes are referred to as buckyballs, and tubular forms as carbon nanotubes (CNTs) or buckytubes. Fullerenes possess a structure similar to that of graphite that is composed of stacked sheets of graphene and often linked by hexagonal, pentagonal or heptagonal (not very common) rings (Theodore and Kunz, 2005; Kroto and Walton, 2011). Discovery of fullerenes has increased the number of known allotropes of carbon, which was previously limited to graphite, diamond, and amorphous carbon.

Due to their novel characteristics, a great deal of research on buckyballs and CNTs has been carried out especially in the various technological fields of material sciences, nanotechnology and electronics. Bulky ball, also known as, Buckminsterfullerene or C_{60} is the smallest form of fullerenes and the most abundant in nature, as it is mostly found in soot, though a second type of buckyball composed of boron atoms (i.e. boron bulky ball or B_{80}) instead of carbon has been described (Gopakumar *et al.*, 2008) in which each boron atoms that makes up the B_{80} structure forms about 5-6 bonds and is believed to make the structure more stable than the C_{60} buckyball (Gonzalez Szwacki *et al.*, 2007; Prasad and Jemmis, 2008).

CNTs are also allotropes of carbon that, as mentioned earlier, are cylindrical in structure. Nanotubes with length-to-diameter ratio of 132 000 000:1 have been fabricated (Wang *et al.*, 2009) and this makes them much larger than any other material. CNT have unique properties that make them important to nanoscience/nanotechnology and other fields of science like material science, optics and even architecture. A possible use of them in the construction of body armour has been reported (Mintmire *et al.*, 1992). They display exceptional strength and peculiar electrical properties. In addition to this, CNTs have also been found to be excellent conductors of heat and are referred to as thermal conductors.

The major drawback, however, in their widespread application is their potential to possess some toxic properties.

CNTs are classified into various forms including single walled carbon nanotubes (SWCNT), double walled carbon nanotubes (DWCNT) and multi walled carbon nanotubes (MWCNT) (Fig.1.2). The uniqueness in the properties of each type of CNTs is what determines their applications in different scientific areas. For example, the SWNT which is the most studied of all the CNTs have particularly strong electric properties which is lacking in the other types (Martel *et al.*, 2001; Theodore and Kunz, 2005).

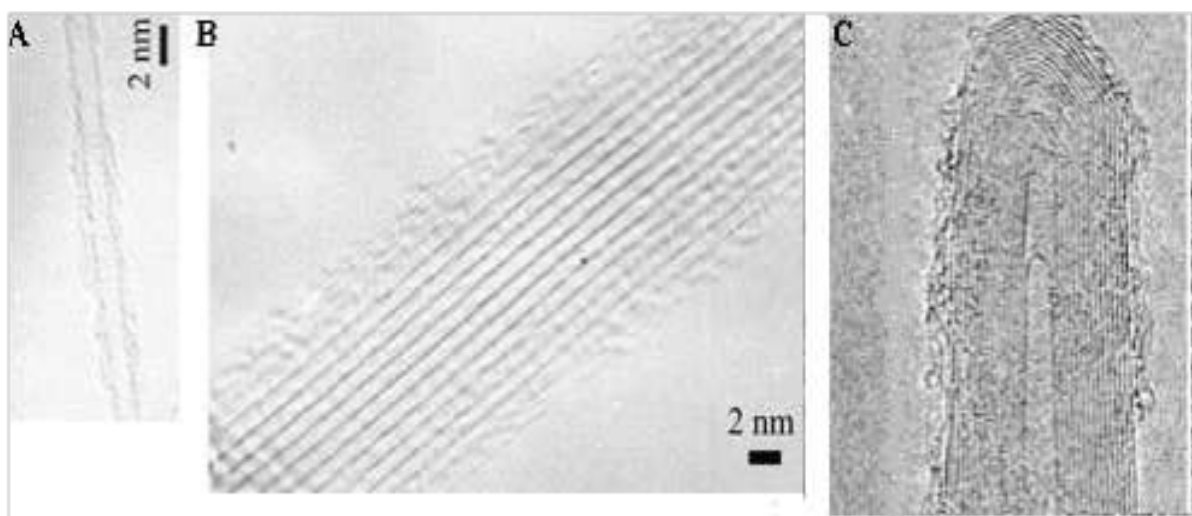


Figure 1.2: TEM images of (A) SWNT (B) bundle of SWNTs and (C) MWNT. (Taken from GTIR Nanotechnology Lab.)

1.2.2 Liquid crystals

These are pharmaceuticals made from liquid organic crystalline materials and are designed to mimic naturally-occurring biomolecules like proteins or lipids. They are regarded as a very safe and specific vehicle of drug delivery as they can target a particular area of the body where tissues are inflamed and are capable of detecting tumors (Philips, 2004).

1.2.3 Liposomes

An initial study on liposomes or lipid vesicles originated in the 1960's when there was a need to understand new types of polymer nanocontainers. Initially, liposomes were used as model systems to study biological membranes but by 1970 had been developed into a

medium for the transportation of drugs (Graff *et al.*, 2004). Liposomes, in general, had been reported to be highly useful in biophysics as a good model system in understanding the properties of cell membrane and channels. In chemistry, they served as an excellent illustration of catalysis, energy conversion and photosynthesis while in biochemistry they improved the understanding of the biological function of proteins and were a good representation of secretion, cell function, trafficking and signalling, gene delivery and function in cell biology (Graff *et al.*, 2004).

Liposomes have various extensive applications in the pharmaceutical industry as directed delivery agent for drugs such as anticancer, anti-fungals and vaccines. They are also useful in cosmetics in the manufacturing of shampoos and other skin care products. They are very important tools in diagnostics as they are able to degrade in the cells once delivery has been carried out (Philips, 2004; Graff *et al.*, 2004; Salata, 2004). Liposomes were said to be the first synthesized nanoparticles used for drug delivery but a major limitation was their tendency to fuse together in aqueous environments and release contents before getting to the target site. This has led to the search for either a replacement or a method of stabilization using newer substitute nanoparticles.

1.2.4 Quantum dots

Quantum dots (QDs) or nanocrystals are semiconductor nanoparticles that can emit light in all colours of the spectrum depending on their size (Fig.1.3). The size of QDs decrease as they get closer to the blue-end of the spectrum, and increase as they proceed to the red end. They have unique properties such that they can even be tuned beyond visible light, into the infra-red or into the ultra-violet spectrum and were able to confine conduction band electrons, valence band holes, or excitons in all three spatial directions (Murray *et al.*, 2000). QDs are valuable tools in biotechnology most especially in cellular imaging and labelling as they are believed to be an excellent alternative to conventional fluorescent dyes used in imaging.

1.2.5 Superparamagnetic nanoparticles

Superparamagnetic nanoparticles are a class of inorganic based particles having an iron oxide core [superparamagnetic iron oxide nanoparticles (SPION)] coated by either inorganic materials (silica, gold) or organic materials like phospholipids, fatty acids,

polysaccharides, peptides, surfactants, polymers (Gupta and Curtis, 2004; Schüth *et al.*, 2007). An important property of SPIONs that makes them unique compared to other nanoparticles is their induced magnetization, i.e. they are able to attract to a magnetic field without retaining residual magnetism after the removal of the field. This property makes them attractive for many applications, ranging from various selective bio separations and contrast enhancing agents for MRI to drug delivery systems, magnetic hyperthermia (local heat source in the case of tumor therapy) and magnetically assisted transfection of cells (Gupta and Gupta, 2005; Neuberger *et al.*, 2005; Hofmann-Amttenbrink *et al.*, 2009).

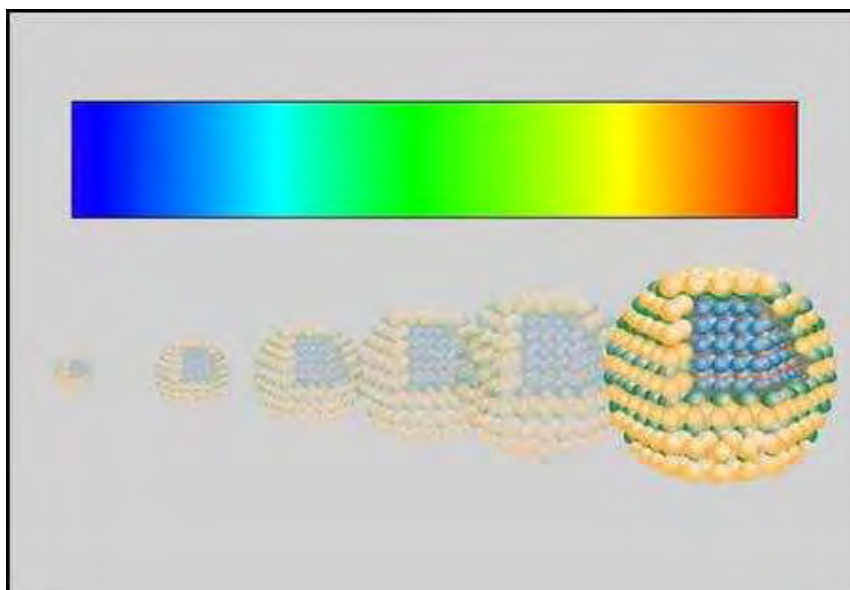


Figure 1.3: Changes in optical properties of quantum dots as size increases (Taken from Aerospace concepts Pty Ltd).

1.2.6 Dendrimer

Dendrimers are highly branched structures with uniform size, radial symmetry and assume a circular shape in solution (Graff *et al.*, 2004). Dendrimers are built layer-by-layer from core to periphery by repetitive covalent bond-forming reactions. The density of the dendrimers increased for every layer formed in each step as a result of the geometric growth at each branching point (Tomalia, 2005). By choosing the final reagent, it was possible to design dendritic molecules with different active surface groups (Fig. 1.4).

The first dendritic molecule was synthesized in about 1980, but interest in them only developed during the 2000's due to increased discovery of various applications especially

in the biotechnological areas (Phillips, 2004). In nanomedicine, dendrimers had been found to be an invaluable tool in attaching fluorescent dyes, enzymes cell identification tags and other molecules because of the many molecular “hooks” present on their surface. Production of these molecules, however, can be quite challenging and expensive and a drawback for their large scale application. Nevertheless, their high stability and the possibility of functionalizing them with biomolecules like antibodies and receptors, makes them a very important medium in target drug delivery (Smith and Diederich, 2000; Esfanda and Tomalia, 2001).

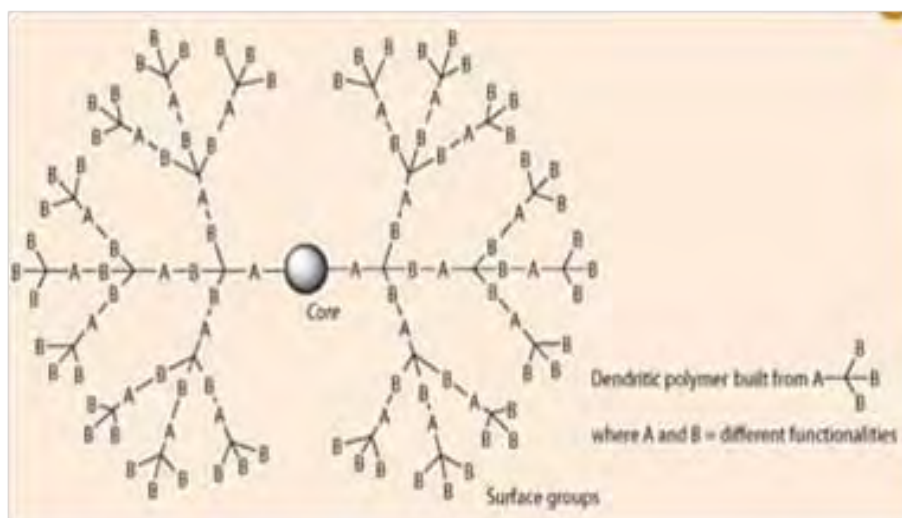


Figure 1.4: A schematic representation of the structure of a dendrimer (Smith, 2008).

1.3 Metal nanoparticles

Nanoparticles of metallic origin have been shown to exhibit unusual properties that they normally will not display in their bulk form (Elechiguerra *et al.*, 2005; Blackman, 2009). Due to their huge potential and benefits to nanotechnology, they have come under intense scrutiny as far as applications across various disciplines are concerned. In biochemistry, for example, they are considered to be better catalysts (Astruc, 2008) and good biological and chemical sensors (Nam *et al.*, 2003; Nie *et al.*, 2007); in information systems, their size and magnetic properties are being explored in the production of data storage devices where the issue of miniaturization is posing an overwhelming challenge (Mayes and Mann, 2004); in medicine their potential as drug delivery agents has being reported (Nie *et al.*, 2007). Other biological applications of some metal nanoparticles are summarized in Table 1.1.

1.3.1 Synthesis

Metallic nanoparticles are an important tool for actualizing nanotechnology within various areas since they are not only abundant in nature but all living organisms operate at a nanoscale. Since metal nanoparticles display unusual physical and chemical properties that depend on their size and shape, it then became expedient to synthesize uniform nanoparticles with controlled morphology. Nanoparticles are the product of different physical, chemical and biological processes, some of which have long been used in the past in conventional science and technology and some that are new and radically different (Aitken, 2004; Doyle, 2006; Johans, 2003).

The synthesis of nanoparticles can occur either as part of the top-down or bottom-up process. The former means the production of nanoparticles from its bulk material and involves the breakdown of the bulk material into smaller pieces by the use of chemical or mechanical means. The bottom-up approach, involves the synthesis of nanomaterials by the chemical reactions between atomic or molecular species. This approach allows for the gradual growth of the precursor particles (nucleation). Both methods can be carried out in liquid, gas or supercritical fluids, solids, or in vacuum (Luther, 2004).

Table 1.1: Examples of metallic nanoparticles used in some biomedical applications

Nanoparticle	Applications	References
Ag	Anti-microbial agents	Shrivastava <i>et al.</i> , 2007; Mishra <i>et al.</i> , 2008
Au	Drug/gene transport systems	Nie <i>et al.</i> , 2007; Jain, 2005
Au/Fe ₂ O ₃	Cancer therapeutics	Hirsch <i>et al.</i> , 2003; Pissuwan <i>et al.</i> , 2006; Nie <i>et al.</i> , 2007
Au/Ag/CdSe	Biomarkers/biosensors in Cellular imaging	Nie <i>et al.</i> , 2007; Nam <i>et al.</i> , 2003
Au/Ag/CdS	Biomolecular labelling	Elechiguerra <i>et al.</i> , 2005

1.3.1.1 Chemical approach

The major chemical approaches available for the synthesis of nanoparticles can be grouped into two main areas: sol-gel method and gas phase synthesis. Various types of nanoparticles of diameters in the range of 1 to 10 nm with uniform crystal structure, and a high level of monodispersity have been generated by these methods with about 20% variation in their size; however, for achieving a much better quantum confinement, this value must be reduced to about 5% or less (Murray *et al.* 1993; WTEC hyper-librarian, 1999). The chemical method of synthesis depends greatly on the availability of the right metal/metal-organic precursors (Theodore and Kunz, 2005). The main disadvantage of these approaches is the very high and harsh conditions, such as temperature and pressure and the use of highly flammable organic solvents that are required in the production of the nanoparticles. These processes may lack scalability and the control over crystalline dispersion is very limited (Mukherjee *et al.*, 2001).

Sol processing is a wet method of chemical synthesis and differs from other chemical methods as nanomaterials can be produced at low temperatures in direct contrast to the other high temperature methods (Luther, 2004; Theodore and Kunz, 2005). Precursors used for sol-gel processing can follow one of two main routes, namely the inorganic or metal-organic routes. The inorganic route uses metal salts in aqueous solutions as raw materials, while the metal-organic route occurs in organic solvents and uses metal alkoxides as starting material. The process consists of sol formation followed by gelling, shape forming, drying and densification. The size distribution of the nanoparticles produced by this method can be controlled by the introduction of a dopant (Kyprianidou-Leodidou *et al.* 1994) or by treatment with heat (Wang and Ying, 1999).

Gas phase synthesis for the production of metal nanopowders, first reported in 1930 (Luther, 2004) incorporates a vacuum chamber with a heating element, the precursor metal to be made into nanoparticles or nanopowder, equipment for the collection of powder and a vacuum hardware. An inert gas is also used at pressures high enough to boost the formation of nanoparticles while at the same time low enough to enable the generation of spherical nanoparticles. Then, the precursor metal is placed on the already heated element and melted quickly. The melted metal is rapidly adjusted to temperatures far above the

melting point of the metal, but less than its boiling point so as to allow enough vapour pressure to be easily attained. At this point, a continued supply of gas is introduced into the chamber with excess gas removed by pumps in such a way that the gas flow removes the evaporated metal from the heating element. Nanoparticles begin to form as the gas cools the metal vapour though the nanoparticles are still liquid as a result of the very high initial temperature involved. The particles still in the liquid phase collide and fuse together in a fixed environment such that the nanoparticles can grow in a specified manner and thus remain spherical with smooth surfaces. As these liquid nanomaterials continue to cool, growth stops and since they are very reactive they must be coated to prevent aggregation with each other or other materials (Horst, 1997; Robert and Wendelin, 2006; Wegner *et al.*, 2006).

Other chemical techniques used in the synthesis of nanoparticles are sonochemical processing (Suslick, 1997), cavitation processing (Sunstrom *et al.* 1996), microemulsion processing (Kishida *et al.* 1998), and high-energy ball milling (Leslie-Pelecky and Reike 1996; Ying and Sun 1997).

1.3.1.2 Biological approach

A biological method of synthesis of nanoparticles has several advantages over the previously described chemical approaches. For instance, the chemical methods involve the use of toxic solvents, high energy consumption and generation of hazardous by-products which constitute a high risk to the environment and human health (Kaushik *et al.*, 2009). Furthermore the high cost of production and the generation of limited shapes of nanoparticles (mostly spherical) greatly diminish their potential properties and applications (Riddin *et al.*, 2006; Kaushik *et al.*, 2009). Consequently, there is an urgent need to design and develop other synthetic methods that will eliminate all of the above listed factors as well as produce the desired results. The biological method seems to be the right approach in achieving this.

Various biosynthetic methods for the synthesis of metallic nanoparticles are currently being employed, for example the synthesis of highly stable gold, silver, platinum, palladium, selenium, titanium and other metals/metal alloys have been successfully synthesized by micro organisms such as actinomycetes, bacteria, fungi, viruses and yeasts

(Ahmad *et al.*, 2003; Sastry *et al.*, 2003; Riddin *et al.*, 2006; Narayana and Sakthivel, 2010). Previously, the use of micro organisms in bioremediation technologies have been reported (Riddin *et al.*, 2006 and Philips, 2009) due to their ability to detoxify an environment usually by reduction of the metal, but recently they are considered useful as eco-friendly nanofactories (Whiteley *et al.*, 2009). Many single-celled organisms have also been reported to produce mineral structures from inorganic materials either intracellularly or extracellularly (Riddin *et al.*, 2006). Although nanoparticles synthesized by micro organisms are very stable, studies have shown that these particles are not monodispersed and the rates at which they are synthesized are quite slow (Phillips, 2009). One of the ways by which this challenge may be overcome is to optimize some factors involved in synthesis such as the cultivation method of the micro organism and the technique of harvesting or the use of a combination approach such as photo-biological method (Vaidyanathan *et al.*, 2010; Narayana and Sakthivel, 2010). Understanding the mechanism by which the nanoparticles are synthesized by these microbes at cellular, biochemical and molecular level may provide information on how to improve the rate of synthesis, quality and intrinsic properties of the nanoparticles produced (Narayana and Sakthivel, 2010). Biomass or extracts obtained from plants (Narayana and Sakthivel, 2010) have been shown to be another biological tool in metal nanoparticle synthesis. Rapid synthesis of silver, gold and other noble metallic nanoparticle using plant leaf and fruit extracts have been reported (Gardea-Torresdey *et al.*, 2008; Parsons *et al.*, 2007; Jae and Beom, 2009; Dubey *et al.*, 2010). These routes, however, do not adequately address the issue of particle monodispersity and uniformity which is very crucial in the applications of these nanoparticles.

Biom mineralization involving the use of cage-like proteins as a biotemplate/limiting growth field in the synthesis of nanostructured materials may be the key to a potential method for obtaining particles with a homogenous distribution in size (Xu, 2005) Table 1.2. The protein shell serves as a guide to control particle growth and to prevent aggregation between the nanoparticles by coating each one as it is produced. Examples of proteins such as ferritin, ferritin-like-protein (FLP), chaperonin and viruses such as cowpea chlorotic mottle virus (CCMV) which have cavities in the center have been used to synthesize various types of nanoparticles most especially that of metals (Ueno *et al.*, 2004; Gálvez *et*

al., 2008; Ishii *et al.*, 2003; de la Escosura *et al.*, 2009). The most commonly used being ferritin and apoferritin. These two protein templates have exactly the same structure except that ferritins possess an iron core while apoferritin does not (Fig. 1.5).

Recently, protein encapsulated nanoparticles have proven to be an efficient carrier of food and drugs to specific targets in biological system (Jahanshahi *et al.*, 2008; Rahimnejad *et al.*, 2009). One of the properties that make them useful in this vein is their biodegradability after delivery. The orientation and size/diameter of the interior cavity of these proteins often determine the morphology of the nanoparticles produced within them (Table 1.2).

Other properties that make nanoparticles synthesized in protein cages important in delivery includes their non-toxicity, non-antigenicity, high stability (provided by the protein of encapsulation) and a longer shelf life.

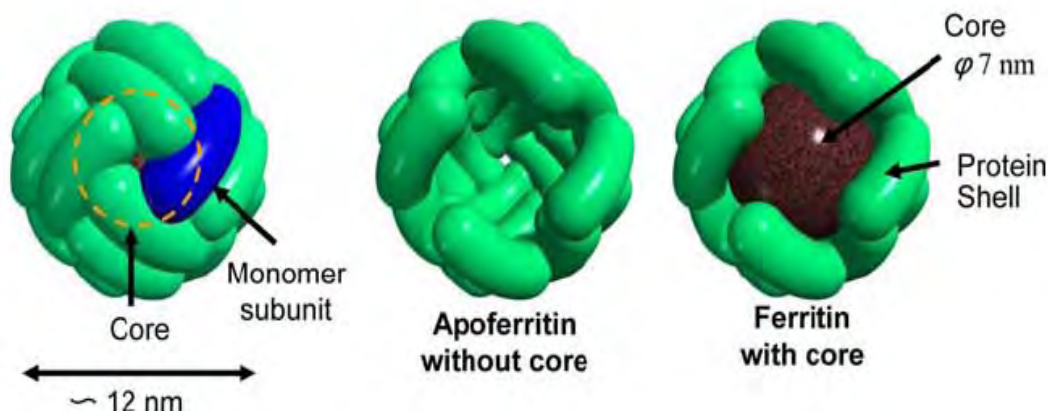


Figure 1.5: An illustration of the cage-shaped protein apoferritin without iron core and ferritin with iron core (Taken from Iwahori and Yamashita, 2007).

1.4 Characterization of nanoparticles

In nanotechnology, nanoparticles synthesized either biologically or chemically must be characterized in order to understand their intrinsic properties such as size, monodispersity, aqueous stability, the net charge, adsorption to biomolecules, aggregation and flocculation in various media. This provides vital information in terms of application of these nanoparticles (McNeil, 2011). For instance, it provides answers to know whether a

particular nanoparticle can be used in a biological application, or else to improve their synthetic processes, and/or chemical functionalization.

Table 1.2: Exterior and interior diameters of some protein cages used in nps synthesis (Klem *et al.*, 2005).

Protein Cage	Interior diameter (nm)	Exterior diameter (nm)
Horse spleen ferritin	8	12
[†] Dps from <i>Listeria innocua</i>	6	9
Cowpea chlorotic mottle virus (CCMV)	24	28
subE CCMVmutant	24	28
[‡] sHsp from <i>Methanococcus jannaschii</i>	8	12
Lumazine synthase from <i>Bacillus subtilis</i>	8	15
Tobacco mosaic virus	4	18

[†] Dps = DNA binding proteins from starved cells. [‡] sHsp = small heat shock proteins

A variety of characterization techniques are currently available some which precede the advent of nanoscience and technology and mostly drawn from material science. The development of new and integrated methods suited to probe nanomaterials is, however, a continuous process (Poole and Owens, 2003). The common techniques used in the characterization of nanoparticles are ultraviolet-visible (UV) spectroscopy, Fourier transform infrared spectroscopy (FTIR), inductively coupled atomic/optical emission spectroscopy (ICP AES/OES), fluorescence spectroscopy (FS), X-ray photoelectron spectroscopy (XPS), scanning/transmission electron microscopy (SEM/TEM), dynamic light scattering (DLS), atomic force microscopy (AFM) and energy dispersion and analysis of x-rays (EDAX) (Table 1.3).

1.4.1 Characterization methods

Nanotechnology, being an interdisciplinary field of science, will have many characterization and analytical techniques available in the elucidation of nanomaterials (Gabor *et al.*, 2008). Techniques of characterization can be classified into single-signal and/or multi-signal and over 700 and 100 respectively of these methods have been documented (Kelsall *et al.*, 2005). These characterization methods are based on two physical processes: the first being primary (1°) analytical probes such as photons, neutrons, ions and electrons, which may be combined with input stresses like magnetic and electric fields and mechanical stress.

Table 1.3: Some techniques used in nanoparticle characterization (Adapted from Gabor et al., 2008).

Characterization technique	Properties analyzed
UV-visible spectroscopy	Surface plasmon of nanoparticles especially of metal origin
ICP AES/OES/FS	Identification and quantification of chemical elements in nanoparticles
Zeta potential	Surface charge of nanoparticles
TEM, SEM and EDAX	Particles size, morphology, monodispersity and composition
XPS	Analysis of surface/depth atoms of Nps
FTIR	Characterization of functional groups on Nps surface
DLS	Size distribution of nanoparticles in solution
AFM	Topology/imaging/surface structure of nanoparticles

Second, the measurable secondary (2°) effect obtained e.g. the release or absorption of electrons, electromagnetic radiation, volume change, mechanical distortion and third, the choice of the investigating medium, energy, temperature, time, intensity, phase or angle. During characterization, the 1° probe, which may be either a beam of electron or a photon of light, interacts with the analyte or matter causing a change in its equilibrium and responds in order to gain its previous state of equilibrium thus modifying the 1° probe. Examples of alteration produced as a result of interaction of 1° probe with matter are excitation of electrons, phonons, excitons or plasmons. Modification of the 1° probe as a result of this produces a 2° effect which is the measured signal (Kelsall *et al.*, 2005).

1.4.1.1 Optical methods

This method, based on the principle of light absorption by a sample, as a technique of characterization is very effective in the analysis of nanoparticles, particularly in probing their size by their characteristic optical spectra (Roy and Fendler, 2004; Zhang and Noguez, 2008). In this case The primary (1°) is usually a photon of visible light with wavelength between 400-800 nm and in most cases the secondary (2°) signal that is often generated is another photon that results from a series of physical phenomena such as elastic and inelastic scattering, absorption or emission (fluorescence) of light (Gabor *et al.*, 2008; Herrera and Sakulchaicharoen, 2009).

Dynamic light scattering (DLS) and Brewster angle microscopy (BAM) are examples of optical methods used in the characterization of nano-structured materials. DLS is used in particle size determination of small particles in suspension or polymer in solution (Urban and Schurtenberger, 1998). BAM on the other hand, is used for analyzing particle phase behavior at air-water interface (Hoenig and Moebiu, 1991). Although most optical methods are used for imaging, they can also be used in chemical analysis (Gabor *et al.*, 2008).

1.4.1.2 Spectroscopic methods

Like the optical methods of characterization, the 1° probe is a photon and the 2° signal generated is another photon (i.e. 1° photon in and 2° photon out). UV/Vis spectroscopy is based on the absorbance of photons in the visible, near-UV and near-infrared regions of the electromagnetic spectrum. UV-Vis spectroscopy, as a technique of characterization, also

involves the transition of electrons, and it complements fluorescence spectroscopy which deals with transitions of electrons from excited state to ground state. (Skoog *et al.*, 2007).

Generally, spectroscopy is used to identify elements and compounds for structural elucidation of matter at the atomic and molecular levels, the most common form being ultraviolet-visible (UV/Vis) spectroscopy (Chu *et al.*, 2011; Gabor *et al.*, 2008). Nanoparticles of gold and silver have been extensively characterized by this technique due to their plasmonic nature and optical properties which are sensitive to size, shape, concentration and aggregation state (Ormonde *et al.*, 2004; Lu *et al.*, 2006). Although the wavelength for UV/Vis spectroscopy is within the nanoscale (i.e. $<1\mu\text{m}$), some nanomaterials have much smaller dimensions and may require other spectroscopic techniques for characterization (Gabor *et al.*, 2008).

Raman and Fourier transform infrared spectroscopy (FTIR) are other forms of spectroscopy that deal with the measurement of molecular and photon vibrations of materials. In both methods, waves carrying the 2° photons are analyzed and information about the vibrational states is obtained. Symmetrical vibrations (polarization) are measured by Raman spectroscopy while asymmetrical vibrations are quantified by infrared spectroscopy. These techniques are very important in the characterization of nanomaterials as they provide information on the organization of chemical bonds between attached surface atoms or functional groups found on nanoparticle surfaces which may give an insight into their application (Morais *et al.*, 2006; Alexandrova *et al.*, 2008; Talley *et al.*, 2005; Dieringer *et al.*, 2006). Surface plasmon spectroscopy (SPS) is mostly used in the characterization of metallic nanoparticles. This process forms the basis on which other standard instruments are used for the measurement of adsorption of materials onto planar metal surfaces (mostly silver and gold) and also the surface of metal nanoparticles. It is also the basic principle behind the applications of many colour-based biosensors (González-Díaz *et al.*, 2008). In SPS, the absorption of the 1° photon causes the electrons on the surface of metals or metal nanoparticles to oscillate. The wavelength of maximum absorption observed indicates the surface state of the metal/metal nanoparticles e.g. molecular adsorption of biopolymers such as DNA or proteins (Hiep *et al.*, 2007; Gabor *et al.*, 2008).

X-ray spectroscopy forms another important 1° photon excitation tool for analysis at the nanoscale. Wavelength of X-rays on the electromagnetic spectrum is between 0.01-10 nm which corresponds to the size of most nanoparticles. The major nano-related X-ray methods are X-ray diffraction (XRD), energy-dispersive analysis of x-ray (EDAX) and X-ray photoelectron spectroscopy which provides structural, chemical composition and surface chemistry of nanomaterials respectively (Moretti, 2003; Joshi *et al.*, 2008). Other spectroscopic methods of characterization are based on 1° photon absorption or excitation atomic absorption spectroscopy (AAS), Atomic emission spectroscopy (AES), fluorescence spectroscopy (mostly used in the characterization of semi-conductor nanoparticles) and inductively coupled plasma spectroscopy (ICP), all of which are generally used for elemental analysis (Gabor *et al.*, 2008).

1.4.1.3 Electron probe methods

In this method of characterization, the 1° probe is usually a high-energy beam of electrons and the 2° signal generated is in the form of electrons (2° electrons), radiation (photons or X-rays) and heat. These secondary signals often interact with matter or a sample to be analyzed to produce images (electrons) or spectra (radiation) (Egerton, 2005; Gabor *et al.*, 2008). Characterization methods involving the electron probe approach is very important in nanotechnology because of their ability to analyze the structure of very small particles. The most common forms of electron probe characterization techniques are scanning electron microscopy (SEM) and transmission electron microscopy (TEM) which are sometimes coupled with other characterization tools such as energy dispersive analysis of X-ray (EDAX or EDS).

When an electron beam interacts with matter, a variety of measurable 2° signals are generated as a result of electron-matter interaction. Primary (1°) are electrons either transmitted, backscattered or diffracted (Goldstein *et al.*, 2003; Herrera and Sakulchaicharoen, 2009). TEM makes use of the transmitted electrons to produce sample image while SEM on the other hand, utilizes backscattered electrons and secondary electrons emitted from the sample to generate images. Transmitted electrons pass through the sample without significant loss of energy of the incident electrons depending on the thickness of the sample (attenuation of the electrons depends mostly on the density and thickness of the sample), and form a 2-dimensional projection of the sample. This is the

principle behind TEM imaging. Furthermore, as mentioned earlier, electrons can be diffracted by particles of the sample if they are favorably positioned toward the electron beam. These diffracted electrons are used to obtain information on the crystal structure and orientation of the sample. This is the basis of electron diffraction in electron microscopy. Finally, 1° electrons can collide with atoms in the sample and become back scattered and may as a result; remove electrons from the discrete orbitals of atoms that makes up the sample (2° electrons). The process of back scattering of electrons and production of secondary ones increases and become more efficient with an increase in the atomic number of atoms that make up the specimen. A 3-dimensional image of the sample is thus possible when the 1° electron beam is focused on the sample surface and the production of secondary or backscattered electrons are plotted as a function of the position of the 1° electron beam. This technique forms the basis for SEM (Egerton, 2005; Herrera and Sakulchaicharoen, 2009). Other electron probe methods of characterization are Auger electron spectroscopy (AES), a technique used in material science for chemical analysis of particle or material surfaces (MacDonald and Waldrop, 1971). Low-energy electron diffraction spectroscopy (LEED), a tool of characterization used in investigating the structure of material surfaces (Calbick, 1963) and electron energy loss spectroscopy (EELS), a complementary method to EDX that works well for low atomic number elements (Keast *et al.*, 2003).

1.4.1.3.1 Scanning electron microscopy (SEM)

In SEM, high resolution images are generated by focusing a high-energy beam of electrons on the surface of the specimen in a raster scanning fashion. These electrons interact with the specimen to produce signals that provides information about the sample such as the surface morphology, elemental or chemical composition, crystal structure and positions of atoms or materials that makes up the sample (Swapp, 2011). A high-energy beam of electrons are thermoionically emitted from an electron gun (Figure 1.6b) fitted with a tungsten or lathanum hexaboride (LaB_6) cathode filament towards an anode; another source of electrons can be through field emission (FE). The most common filament is tungsten because of its affordability and high melting temperature compared to other metals (Jeffrey and Read 1991; Raffi, 2007).

A typical electron beam with energy within the range of 0-50 keV is focused by two consecutive condenser lenses into a very fine spot of approximately 5 nm. As the 1° electron beam strikes and interacts with the sample surface, the energy of the electron is dissipated due to continuous random scattering and absorption and effectively spreads into a teardrop-shaped volume of the sample (interaction volume) extending about 1-5 μm into the surface. Several 2° signals are thus generated which are picked up by specialized detectors depending on the type of instrumentation (e.g. X-rays are detected with SEM fitted with EDAX). Signals include 2° electrons, backscattered or diffracted backscattered electrons, visible light, photons (X-rays) and heat.

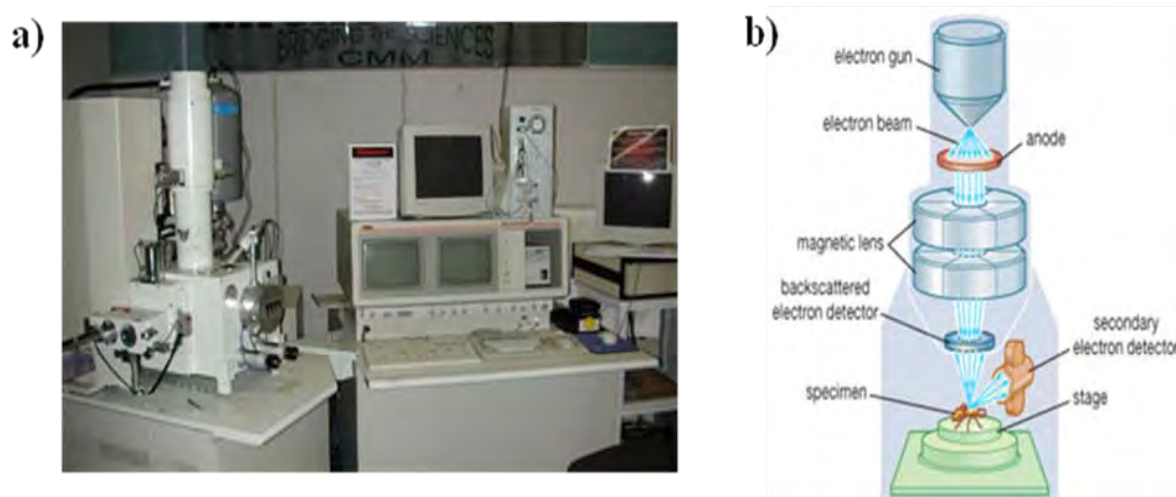


Figure 1.6: The scanning electron microscope (SEM). (a) SEM instrument. (b) Schematic representation of the SEM. (Taken from the University of Queensland center for microscopy and microanalysis; Bradbury et al., 2011).

Secondary and backscattered electrons which result from elastic scattering of incident electrons are used for generating sample image: 2° electrons are important for determining the topography and morphology of samples while backscattered electrons are important for the determination of the crystal structure and orientation of samples. X-rays, which are produced by inelastic scattering of 1° electrons by discrete atoms in the sample, are used to determine the elemental composition of the sample. As the excited electrons return to lower energy states, X-rays of fixed wavelength are generated (which is a function of the difference in energy levels of electrons in different orbitals of a particular element). Thus, specific X-rays are produced for each element. SEM is, to a certain extent, a limited tool to

characterize nanoparticles. The resolution of SEM depends on the size of the electron spot which in turn depends on the magnetic electro-optical system generating the electron beam. Furthermore, its resolution also depends on the size of the interaction volume and level of sample interaction with the electron beam. However, the major drawback of this method of characterization is the inability to resolve images of samples down to the atomic nanoscale. This is due to the fact that the size of the electron spot and interaction volume are very large compared to the distance between atoms that make up the sample, thus limiting SEM resolution at this level. Another problem encountered with the use of SEM in nanoparticle characterization is the difficulty in separation of nanoparticles from that of substrate thus the possibility of differentiating one from the other becomes impossible. This becomes more aggravated when nanoparticles being analyzed is adhesive in nature and consequently becomes aggregated.

Nevertheless, SEM is an important tool in the determination of the purity of nanoparticles and also provides information about the extent of agglomeration. Furthermore, SEM becomes a valuable tool in the determination of the level of dispersion and uniformity of metallic nanoparticles. Finally, X-ray beams are non-destructive to samples (especially of organic origin) and make it very useful in the characterization of certain particles (such as those generated using soft/organic polymers/biomolecules). Thus, this makes it possible for repeated sample analysis (Jeffrey and Read 1991; Liu 2006; Raffi 2007; Herrera and Sakulchaicharoen, 2009).

1.4.1.3.2 Transmission electron microscopy (TEM)

Nano-sized particles are often present in different types of materials and TEM, as a characterization tool, makes it possible to obtain information about particle size, shape, and surface properties (Henry, 2005). More recently, structural changes in nanoparticle, as a result of interactions with solid-, liquid-, or gas- phase substrates, can now be monitored by this technique (Bentley *et al.*, 2006).

TEM operate by the same principles as SEM with the only difference being that the detector in TEM is a phosphor plate that has the ability to capture images made by transmitted electrons. Another key difference is that unlike SEM, where the accelerating voltage is between 0-50 keV, TEM uses a much higher voltage of about 300 keV. The

wavelength of the accelerated electron beam is usually in the μm range. The thermoionic gun consists of a filament, made of tungsten or lithium hexaboride, which is heated under applied potential until electrons are produced. Another difference from SEM is that TEM has a projector lens system at the base of the column. The image observed by TEM operator on the phosphor screen is the projected image of the sample (Joshi *et al.*, 2008).

In a conventional TEM (Figure 1.7), a thermoionic or field gun is used to generate accelerated electrons of 100-400 keV. These electron beams are further accelerated by the anode plate and are collimated via an aperture. Electrons are scattered as they pass through the sample and are focused by a double condenser lens system (transparency of sample is very important for effective transmission, ideal thickness of sample should be between a few nanometres to $1\ \mu\text{m}$), channelled through another aperture. This is further amplified by a magnifying (projector) which in turn projects the desired image onto the phosphor fluorescent screen for viewing purposes and finally, images are captured by a camera (Poole and Owens, 2003; Gabor *et al.*, 2008).

The resolution of a good TEM should be at least 0.2 nm which is similar to the distance between two atoms and atomic radii of some heavy metals. A recent achievement in TEM resolution of 0.08 nm has been reported by Carl Zeiss with an experimental ultrahigh-resolution 200 keV field emission gun transmission electron microscope (FEG-UHRTEM), a resolution very close to the theoretical limit of TEM analysis (Thesen *et al.*, 2005).

Limitations of TEM include time consumption in sample preparation, thus limiting the number of samples to be imaged and analyzed. In addition, only smaller sections of samples can be viewed which may not represent the overall sample. The morphology of the sample has also been known to drastically change as a result of exposure to highly energetic electron beam of the TEM, causing damage to samples (e.g. biological samples). This factor has made it almost impossible to carry out electron diffraction analysis on beam susceptible nanoparticles. The use of a low electron beam current makes it possible to obtain lattice fringe images and electron diffraction patterns of these particles (Bentley *et al.*, 2006; Herrera and Sakulchaichaoen, 2009). Finally, TEM, being a high-vacuum instrument, is very expensive to operate and manage and certainly stands as a major challenge in conducting research in nanotechnology. TEM remains a valuable tool of

characterization, however, because it allows for any type of sample to be imaged. More so, the astonishing resolution ability of TEM makes it possible to carry out studies on materials at the atomic level (Howe *et al.*, 2008; Joshi *et al.*, 2008; Herrera and Sakulchaicharoen, 2009).

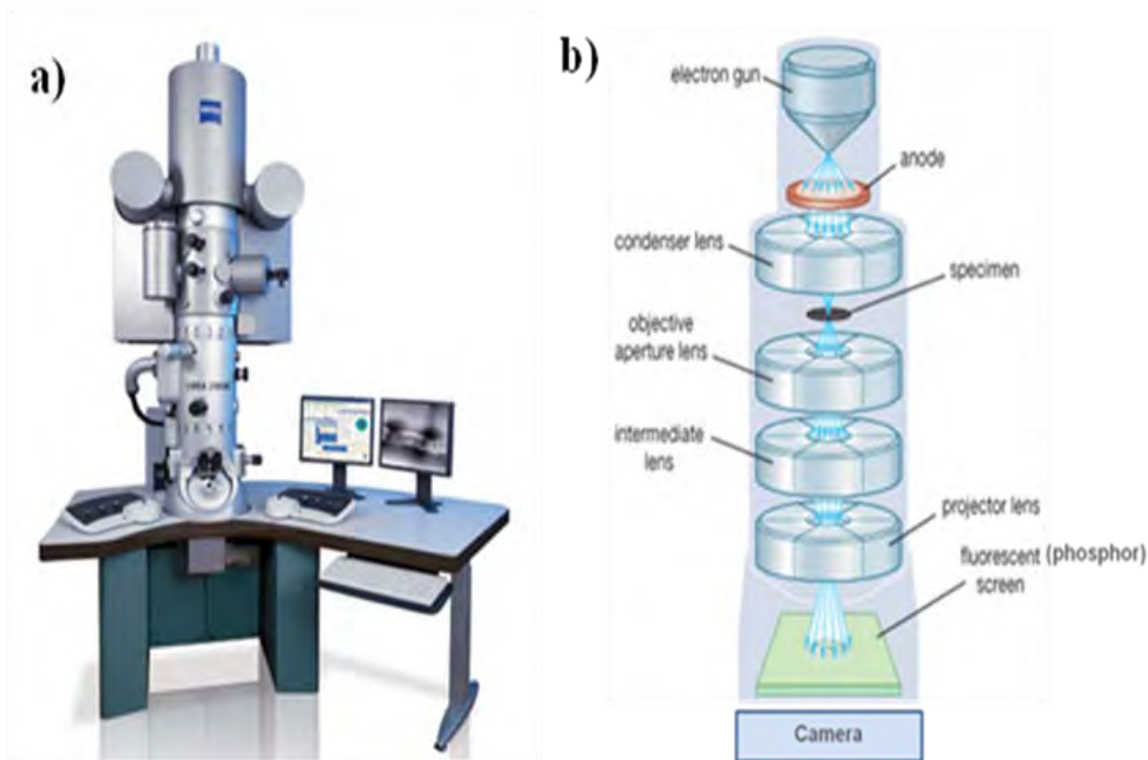


Figure 1.7: A conventional transmission electron microscope. (a) Instrument (b) Schematic representation. (Taken from Insight experts, 2008; Bradbury *et al.*, 2011).

1.4.1.4 Scanning probe microscopy (SPM) methods

SPM is a technique of mechanical probe microscopy that involves the use of a physical probe in forming images of sample surfaces by the movement of the probe tip on the surface of the sample in a raster format. The probe-surface interaction as a function of position of the probe is recorded. SPM is important especially in the field of nanoscience and technology because it enables researchers to image surfaces of nanomaterials at atomic scale and also provides a detailed 3-dimensional image. Moreover, instead of the use of a beam of light or electrons like other forms of microscopic characterization, a probe is used thus removing the limitation encountered by researchers of wavelength of light or electrons (Bhushan, 2004).

SPM is a general terminology used in describing this constantly developing technique due to the fact that various microscopes are available to image samples based on the different interactions between scanning probe and the particle surfaces. There are two main types of scanning probe microscopy relevant to nanoscience/nanotechnology, a) scanning tunnelling microscopy (STM) and b) atomic force microscopy (AFM).

The STM technique, involves the measurement of the magnitude of tunnelling current between the tip of the probe and surface of the specimen. STM samples must accordingly be electrically conducting limiting the analysis of non-conducting materials surfaces. AFM was established to remove this factor and thus allow for the characterization of insulated samples. AFM measures the force of probe-sample interaction to the order 1 μN or less and this determines the resolution of this technique (Binnig *et al.*, 1982; Binnig and Quate, 1986; Wiesendanger, 1994). Also, the sharpness of the probe tip determines the resolving power of both scanning tunnelling and atomic force microscopes. The probe which is usually made of silicon or Si_3N_4 for AFM and tungsten for STM is sharpened to a very fine tip. Ideally, a probe tip sharpened to 1 nm should give the best resolution (Gabor *et al.*, 2008).

Other important SPM methods in nanotechnology, developed as a result of the offshoot of AFM, are lateral force microscopy, force modulation microscopy (FMM), electrostatic force microscopy (EFM), magnetic force microscopy (MFM), scanning capacitance microscopy (SCM), scanning thermal microscopy (S_{Th}M) and chemical force (CFM) (Gabor *et al.*, 2008).

1.4.1.5 Atom probe microscopy (APM) methods

This technique was invented in 1967 by Erwin W. Müller, John A. Panitz, and S. Brooks McLane with the combination of the principles of field ion microscopy (FIM) and time-of-flight mass spectroscopy (Müller *et al.*, 1968). APM is similar to FIM (the first microscopic approach used in achieving atomic resolution). A major drawback of this technique is its inability to analyze the chemical properties of individually imaged surface atom. APM is able to achieve this and so possesses a high level of individual particle sensitivity (Müller *et al.*, 1968; Tsong, 1990). APM like FIM is made up of a movable fine probe tip that usually operates at cryogenic temperatures and very high vacuum. As the tip

moves on the particle surface, ionization is induced and ions generated are repelled by the probe tip towards a detector where their time of arrival can be determined. The time taken for an ion to reach the detector is a function of the mass of the surface atom generating it. A chemical profile of the surface is achieved this way with a resolution of 1 nm spacing.

In 1974, a new form of APM known as imaging atomic probe (IAP) was invented by John A. Panitz. IAP unlike the previously described atom probe method does not require the movement of the probe tip. Emitted ions from the surface are analyzed by a detector placed about 12 cm from the probe tip in order to afford a large area of observation (Panitz 1974 and 1978). Atom probe tomography (APT) uses a detector that is position sensitive to a chosen area. This method has also led to the development of other position –sensitive probe (PoSAP) invented in 1988 (Bunton *et al.*, 2006).

Recent atomic probes are able to provide 3-dimensional atomic resolution, chemical analysis and compositional imaging of surface atoms at the atomic scale (Peet *et al.*, 2004). Also this technique allows for individual atoms of a sample to be removed and analyzed. Atoms are isolated by a combination of high electric field generated by a voltage pulse or laser. The removal of ions/atoms from a sample surface in order to view and identify them makes this method technically destructive. Recent advances in scanning probe microscopy, however, involving the use of cold-atom scanning microscope with ultra-soft probing tips has made it possible to non-destructively analyze atoms of nanomaterials (Gierling *et al.*, 2011).

1.4.1.6 Non-radioactive and non-electron characterization methods

1.4.1.6.1 Mass spectrometry (MS)

Mass spectrometry, as a method of characterization, measures the mass-to-charge (m/e) ratio of fragmented or molecular clusters. MS is used in determining sample composition by analysing resultant mass spectrum of the fragmented components of the sample. Analysis by MS is also capable of providing information about isotopic ratio, structural and qualitative analysis (Sergeev, 2006). The most common type of MS used in the characterization of nanoparticles is Matrix-assisted laser desorption/ionization (MALDI) and Time-of-flight (TOF) spectrometry. Various types of nanoparticles especially of

metallic origin have been characterized using these approaches (or a combination of the two) to elucidate structure-property relationships of nanomaterials (Thierry de Ville d'Avray *et al.*, 1998; Jason *et al.*, 2009; Harkness *et al.*, 2010).

1.4.1.6.2 Thermodynamic methods

Thermodynamic method, as a technique of characterization in material science or nanotechnology, analyzes materials/nanomaterials as a function of temperature. In other words, the 1° probe is solely temperature. Several thermodynamic methods are currently available in the characterization of nanomaterials and are classified based on the property (2° effect) they measure (Gabor *et al.*, 2008; Scott, 2011).

Thermogravimetric analysis (TGA) as a thermodynamic technique measures the change of mass as a function of temperature in a preselected environment. Data obtained from this technique are usually expressed in percentage weight loss versus temperature, and this is quite useful in evaluating the thermal stability and reaction rates at various atmospheric conditions. It is also a good method for establishing purity of materials. This approach is often used to determine the purity of carbon (both single and multi-walled) and metallic nanotubes (Pang *et al.*, 1993; Kijima *et al.*, 2003). Differential scanning calorimetry (DSC) analysis is another thermodynamic approach where the isothermal differential power of a sample and a reference is measured with change in temperature. In DSC, temperatures of both sample and reference are kept almost equal throughout analysis and it is expected that the reference sample has a distinct heat capacity over the temperature range at which scanning is to be carried out. DSC is commonly used in determining the heat of reaction (endothermic or exothermic) and heat capacity of materials (Skoog *et al.*, 1998). Differential thermal analysis (DTA), like DSC, monitors the temperature difference between a sample and a reference material as a function of temperature. Differential temperature is then plotted against temperature or time (often referred to as thermo gram or DTA curve). Thermo gram reveals information about the phase transition, heat of reaction and reaction kinetics of the sample (Bhadeshia, 2002).

Recent advancement in nanoscale thermal analysis was achieved by the discovery of thermal nanoproboscopes as a novel means of characterising, imaging and differentiating

amorphous from crystalline nanomaterials (Harding *et al.*, 2007). Thermal nanoprobe coupled with a heated AFM tip was used to perform localized thermomechanical analysis of samples thus generating images as a function of temperature.

1.4.1.7 Other methods of characterization

1.4.1.7.1 Quartz crystal microbalance (QCM)

QCM is a mass sensing device used in measuring changes on the surface of a quartz crystal resonator. QCM is able to detect mass changes within the nanogram range making it a very sensitive method for detecting monolayers of deposited materials. QCM can also be used in monitoring the thickness of metals deposited on material surfaces in different deposition techniques such as vacuum or liquid deposition and etching (Viitala, 2007). The working principle of QCM is derived from the resonance behaviour of piezoelectric materials when an electric field is applied across them. The high sensitivity of this device makes QCM an attractive technique in designing of sensors and drug/drug delivery research (Marx 2003; Gabor *et al.*, 2008).

1.5 Safety of nanoparticles

Nanotechnology, as a new tool in science and technology, is extremely important beyond any doubt. Nonetheless, the same novel and unique physicochemical properties possessed by these nanomaterials that make them promising compared to their bulk materials may pose a serious health risk to humans and the environment. Accordingly (Oberdörster *et al.*, 2005; Mironava *et al.*, 2010 and Liu *et al.*, 2010), the toxicity of current and emerging nanomaterials are yet to be understood by biomedical and health professionals with respect to the environment and workplace. There is therefore an increased concern about safety of these nano-sized materials and a call from the public, government and academia for more research to be done in order to bridge the knowledge gap arising from this multidisciplinary field (Kagan *et al.*, 2005; Zhao and Nalwa, 2006). Nanotoxicology as a branch of bionanoscience/bionanotechnology has evolved as a result of this in order to study the interactions of these ultrafine particles with biological system and the environment and also to evaluate their potential risk at the molecular level (Oberdörster *et al.*, 2005; Kagan *et al.*, 2005; Zhao and Nalwa, 2006). Various studies on the effects of nanoparticles on biological cells, tissues, systems and the environment has since increased,

to an extent, with the continuous emergence of new nanomaterials (Inoue *et al.*, 2006; Saxena *et al.*, 2007; Nowack and Bucheli, 2007; Wang *et al.*, 2008).

1.6 Research Focus

1.6.1 Hypothesis

- The biological synthesis of metal nanoparticles in protein cages will produce particles with uniform morphology.
- The synthesis of metallic nanoparticles with both caged and non-caged proteins/enzymes would enhance the enzymatic activity/function of these proteins/enzymes.
- The synthesis of metal nanoparticles in protein cages will be less toxic when compared to those generated with a non-caged protein due to the shielding effect of protein cages.

1.6.2 Objectives

- To synthesis and characterize metallic nanoparticles (Pt, Au and Ag) in cages/non-cage protein/enzymes (GroEL, Apoferritin and RNase).
- To study the effect of nanoparticles synthesis on the enzymatic activities of these enzymes/protein cages.
- To investigate effect of these nanoparticles on a biomedical target (AChE activity).

Chapter 2: Biological synthesis of metallic nanoparticles in apoferritin

2.1 Introduction

Noble metallic nanoparticles have been shown to exhibit novel and significant mechanical, electronic, magnetic, optical and catalytic properties which are highly influenced by their size, shape and composition (Elechiguerra *et al.*, 2005; Liu, 2006). Thus, these properties require the development of specific synthetic routes that allow a better control of morphology and size (Yu *et al.*, 1997). Research has already led to many significant breakthroughs and several products have been made commercially available. For example in the life science, applications of metal nanoparticles include biosensors (Nam *et al.*, 2003), labels for cell and biomolecules (Elechiguerra *et al.*, 2005), drug and gene transport systems as well as cancer therapeutics (Hirsch *et al.*, 2003). Silver nanoparticles have recently been shown to be a promising antimicrobial agent (Shrivastava *et al.*, 2007). In addition, it has been demonstrated that silver nanoparticles undergo a size-dependent (1-10 nm) attachment to the HIV-1 virus and prevent it from binding to host cells (Elechiguerra *et al.*, 2005).

Metallic nanoparticles have been synthesized using various chemical and biological approaches with the former reported to be environmentally hazardous with limited appeal (Riddin *et al.*, 2006; Vigneshwaran *et al.*, 2006). The biological route offers great advantages over the chemical methods as it is cost effective, simple to produce and eco-friendly. Biosynthesis of metal nanoparticles through bio-reduction of metal salts by various prokaryotic and eukaryotic microorganisms has been reported (Sastry *et al.*, 2003; Ahmad *et al.*, 2003; Riddin *et al.*, 2006; Whiteley *et al.*, 2009, 2011). A limitation to this method is the ability to control the mechanism that determines size and shape, an important factor in the application of nanoparticles. The use of a protein cavity (cage) as a limited growth field for nanoparticles is not novel (Yoshimura, 2006) but serves as an ideal template to confine particle growth in a homogenous distribution as well as a stabilizer to prevent particle aggregation; one such protein is apoferritin. More so, it is anticipated that

biomolecules-incorporated nanomaterials would display properties and function that they would not normally have exhibited in their native form.

Apoferritin is a globular protein capable of binding and storing several atoms of iron (about 4500 Fe atoms). It combines with ferric hydroxide phosphate to form ferritin, the form in which iron is stored in the spleen, liver and other tissues. Apoferritin has a molecular weight of approximately 440 kilodaltons (kDa) and consists of 24 identical subunits each with a molecular weight of ~18 500 Daltons (Bryce and Crichton, 1973; Gálvez *et al.*, 2006). These subunits form a spherical protein shell surrounding an aqueous cavity with an inner diameter of about 8 nm and an outer diameter of 12 nm (Fig. 2.1, Gálvez *et al.*, 2006; Iwahori and Yamashita, 2007). Apoferritin has been reported to bind metal ions in its cavity at specific sites, with stoichiometric binding not higher than 60 atoms per apoferritin at pH 7.4 (Pead *et al.*, 1995). However, some studies have shown that the number of metal atoms strongly increases when working at higher pH. For instance, Gálvez *et al.*, 2008 have shown that when horse spleen apoferritin is treated with Cu (II), Co (II), Ni (II) or Ag (I) and the pH dynamically adjusted to 8, the number of metal ions per apoferritin reaches values of about 300. Theoretical computations show that the potential of the outer surface of apoferritin is net positive while the inner surface has a negative net charge (Douglas and Ripoll, 1998; Gálvez *et al.*, 2006). The inner and outer surfaces are connected by channels, generated by the multi-subunit construction of the apoferritin shell. Four positively charged and eight negatively charged (also called hydrophilic channels) of about 4 Å, provide a pathway for cations and molecules of sufficiently small size into the cavity of apoferritin (Chaspeen, 1998; Gálvez *et al.*, 2006). Encapsulated cations (mostly metal (II)-apoferritin) are susceptible to reaction with an appropriate reducing agent to give rise to the nucleation and growth of a new metal (0)-apoferritin nanoparticle of uniform size since particles are confined to the diameter of the apoferritin core (Fig. 2.1).

Several zero-valent, apoferritin-encapsulated metallic nanoparticles formed by the reduction of charged metal salts within the apoferritin cavity have been reported. These include palladium (Ueno, *et al.*, 2004), copper (Gálvez *et al.*, 2005), cobalt and nickel (Gálvez *et al.*, 2006), cadmium (Iwahori and Yamashita, 2007), gold (Zhang *et al.*, 2007) and platinum (Deng *et al.*, 2009; Liu *et al.*, 2011; Sennuga *et al.*, 2011). Encapsulated

nanoparticles may have possible biomedical applications as a reactive oxygen scavenger (ROS), in bio-imaging and as a vehicle for drug delivery (Galv ez *et al.*, 2008; Liu *et al.*, 2011).

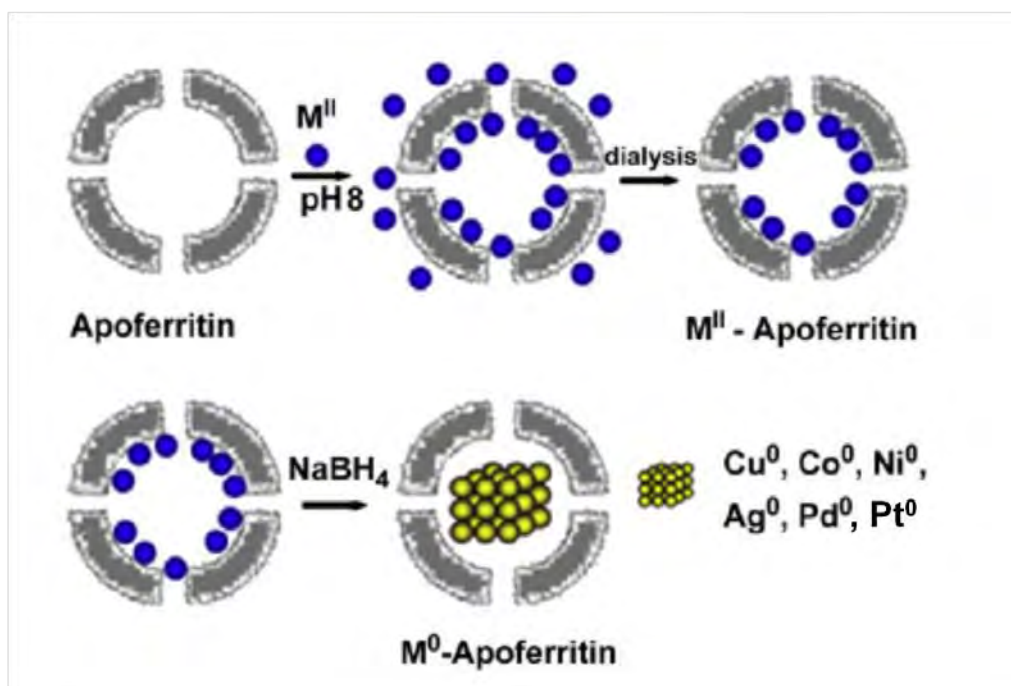


Figure 2.1: A schematic representation of metallic nanoparticles synthesis in apoferritin (G alvez *et al.*, 2008).

The binding of proteins to nanoparticles surfaces have also been reported to induce conformational changes in the structure of some proteins and consequently their biological function (Fei and Perrett, 2009). At the exponential growth of nanotechnology with respect to protein-nanoparticle fabrication, it is important to understand the effect of nanoparticle synthesis on the natural biological function of these proteins, especially those fabricated for potential use in the biological system. Nothing is known about the effect that nanoparticle within the cavity of apoferritin may have on its natural biological function, which as mentioned earlier, function naturally to sequester and mineralize Fe (O) OH into its cavity. This prevents the toxic build up of cytosol and serum iron that may lead to oxidative stress and eventual death of cells of tissues. Earlier studies have mimicked this function by an *in vitro* demonstration of the oxidation of Fe²⁺ by apoferritin under conditions not complicated by auto oxidation (Macara *et al.*, 1973; Bryce and Crichton, 1973; Bakker and

Boyer, 1986; Hanna *et al.*, 1991). These studies were able to establish the mechanism by which the uptake of iron was achieved by apoferritin. Further, these studies pointed to the fact that apoferritin possessed catalytic properties and was regarded as a ferroxidase enzyme with products that remained associated.

The objective of this chapter is to:

- i. Biologically synthesize metallic nanoparticles of platinum, gold and silver within the core of apoferritin.
- ii. Characterise the nanoparticles using various techniques.
- iii. Investigate the effect of nanoparticles on the ferroxidase activity of apoferritin.

2.2 Materials and Methods

2.2.1 Materials

Horse spleen apoferritin (HSA, 48 mg/ml), potassium chloroplatinate (II) (K_2PtCl_4), gold (III) chloride ($AuCl_3$), silver nitrate ($AgNO_3$) and ferrous ammonium sulphate ($(NH_4)_2 Fe(SO_4)_2 \cdot 6H_2O$), were obtained from Sigma-Aldrich (South Africa). Sodium borohydride ($NaBH_4$) was purchased from Merck (South Africa). HSA was used without further purification. All other reagents were of analytical grade. All reagents and buffers were prepared using deionized water obtained from a Milli-Q system.

2.2.2 Methods

2.2.2.1 Nanoparticle synthesis

Metal nanoparticles (M-nps) of Pt, Ag and Au nanoparticle were synthesized in the presence of HSA as described by Gálvez *et al.*, 2008 with some modifications. HSA (10 μ M) in Tris buffered saline (TBS) pH 8.0 (Appendix A) was incubated with varying concentrations of K_2PtCl_4 to give a theoretical loading of 250 - 4000 metal atoms per HSA (M:HSA). The pH was maintained at pH 8 with a few drops NaOH (0.1 M) and the mixture was allowed to react by stirring (1 h, 4 °C) after which $NaBH_4$ (20-fold of metal salt concentration) was added. The solution was stirred further for 1 h (3 h in the case of Pt) until full reduction was achieved as determined by visual change in color. This was followed by exhaustive dialysis against TBS buffer for 24 h using slide-A-lyzer dialysis cassette (G2 1000 MWCO Pierce) with a change in dialysate every 6 h. Dialyzed solutions

were centrifuged (2 min, 5000 rpm) using an Eppendorf bench top centrifuge and filtered through a 0.22 μm filter. The protein content of HSA was then estimated after nanoparticle synthesis by Bradford (Bradford, 1976). The sample (250 μl) of each was purified by size exclusion chromatography (SEC) on a Sephadex G-50 (1.8 x 15 cm) column. The M-HSA containing fraction was monitored by UV-Vis spectroscopy at 280 nm. The presence, purity and stability of the M-nps-HSA samples were assessed by native polyacrylamide gel electrophoresis (native PAGE, 5%, Appendix F).

2.2.2.2 Characterization

2.2.2.2.1 UV-Visible spectroscopy

Samples were diluted 10-fold in each set of M-nps synthesized in the presence of HSA. A spectral scan between 230–850 nm was carried out using a UV-visible spectrophotometer (Spectroquant Pharo300 Merck) to evaluate plasmon resonance bands associated with each metal particle formation.

2.2.2.2.2 Inductively coupled plasma optical emission spectroscopy (ICP OES)

Metal nanoparticles-HSA complexes (M-nps-HSA, 250 μl) were dissolved in aqua regia (1:3 nitric and hydrochloric acid respectively, 350 μl). A 500 μl sample was used in the case of Ag-nps-HSA. Samples were digested with hydrogen peroxide (1.0 ml, 60 $^{\circ}\text{C}$, 1 h) to remove all organic substances present in the solution of nanoparticles. All sample solutions were then made up to 25 ml with deionized water. Metal quantification was determined using an inductively coupled optical emission spectrophotometer (iCAP 6000 series, Thermoelectron Corporation) after an appropriate standard curve was generated with varying concentrations of metal standards (Sigma, Appendix B).

2.2.2.2.3 Fourier Transfer Infra Red (FTIR)

The infra-red spectrum (650 – 4000 cm^{-1}) of each sample of M-nps-HSA (about 2 mg) was recorded on a FTIR spectrometer (Perkin Elmer 100 equipped with a universal attenuated total reflectance (ATR) sampling accessory). 20 scans were performed per sample with a scan resolution of 4 cm^{-1} . Equipment was blanked with TBS buffer pH 8.0 and an equal concentration of HSA only was used as the control.

2.2.2.2.4 Transmission Electron Microscopy (TEM)

Samples were diluted with deionized water and a drop was applied on a carbon coated Cu grids, excess sample was removed after a minute using blotting paper and air-dried at room temperature. Samples were negatively stained with uranyl acetate to view the protein shell and also to establish the position of particles around the protein shell. This was done by adding a drop of 1 % solution of uranyl acetate to an already blotted grid loaded sample of M-nps-HSA. Mean particle size and standard deviations were determined by the analysis of 200 particles from 5 - 10 micrographs of each sample using the computer software called "Scandium". The electron micrographs of nanoparticles were taken using JEOL JEM-1210 TEM operating at 80 keV.

2.2.2.2.5 Energy dispersive X-ray spectroscopy (EDX)

Elemental analysis was performed with a TESCAN scanning electron microscope (SEM) with an EDX scanner (INCA Pental FeTx3, Oxford Instruments) operating at 20 keV. Freeze dried samples were placed on a carbon tape which was in turn placed on a brass SEM support stub. EDX instrument was standardized by quant-optimization with a copper grid under standard conditions of operation.

2.2.2.3 Assay of HSA ferroxidase activity

The ferroxidase activity of HSA was determined spectrophotometrically at 420 nm by the method described by Bryce and Crichton, 1973 with slight modifications. HSA (1 μ M) in borate-cacodylate buffer (50 mM, pH 5.5, Appendix A) was incubated at 22°C with $(\text{NH}_4)_2\text{Fe}(\text{SO}_4)_2 \cdot 6\text{H}_2\text{O}$ (50 mM i.e. Fe^{2+}) dissolved in the same buffer at 22°C. The reacting mixture was rapidly shaken and the change in absorbance monitored over 4 min at 420 nm. A control containing $(\text{NH}_4)_2\text{Fe}(\text{SO}_4)_2 \cdot 6\text{H}_2\text{O}$ only was used as the blank. Specific activity was expressed in $\text{pmolferritin} \cdot \text{min}^{-1} \cdot \text{mg}^{-1}$. The amount of ferritin (i.e. Fe^{3+}) produced was estimated from a ferritin standard curve (Appendix C). Absorbance was read on a Power wave X microplate spectrophotometer (Biotek Instruments Inc., USA).

2.2.2.3.1 Effects of M-nps on the ferroxidase activity of HSA

The assay was performed exactly as described in 2.2.2.3. M-nps-HSA (1 μ M, based on protein estimation in borate-cacodylate buffer (50 mM, pH 5.5) was incubated with

$(\text{NH}_4)_2\text{Fe}(\text{SO}_4)_2 \cdot 6\text{H}_2\text{O}$ salts (50 mM). HSA containing no M-nanoparticles was used as the control.

2.2.2.4 Protein determination

The protein content of HSA in all experiments was estimated in triplicate by Bradford method (Bradford, 1976). In a 96-well microtiter plate was placed protein samples (5 μl) followed by Bradford reagent (245 μl). The mixture was incubated (22 $^\circ\text{C}$, 15 min), the absorbance of the solution was measured at 595 nm and the concentration of the unknown samples was determined using a BSA standard curve (Appendix D).

2.2.2.5 Statistical Analysis

All assays were carried out in triplicate and values reported as the means with standard error. Where necessary analysis of variance was conducted using Graph Pad InStat for Windows, version 3 (Graphpad Software Inc.) demo version and Microsoft Excel 2007. The level of significance of means was determined at $p < 0.05$; $p < 0.01$ and $p < 0.001$ versus controls (i.e. HSA only).

2.3 Results and Discussion

2.3.1 Synthesis of nanoparticles

Metallic nanoparticles of Pt, Au and Ag were synthesized in the presence of HSA by the incubation of metal salts of these metals with an aqueous solution of HSA at pH 8 followed by reduction with NaBH_4 . Synthesis was carried out at pH 8 in order to increase the electro negativity of the interior of HSA thereby improving electrostatic attraction between positive metal cations and the core of HSA. Promoting electrostatic attraction, leads to increase in the uptake of metal atoms by HSA. Excess metal salts were removed by dialysis and any aggregated metal particles that were not stabilized by HSA removed by centrifugation and filtration.

Different molar concentrations of metal salts were incubated with a fixed concentration of HSA in the hope of varying particle size (Domínguez-Vera *et al.*, 2007; San *et al.*, 2011). The change in nanoparticles size was determined by TEM analysis. Variation in molar ratios of M:HSA was also performed in order to determine the saturation point of HSA in terms of the amount of metal atoms HSA was capable of encapsulating.

Nanoparticle formation was initially visibly monitored by colour change from light orange to dark brown (Pt), yellow to reddish brown (Au) and colourless to yellow in the case of Ag (Fig. 2.2a-c). These colour changes were consistent with other studies for Pt, Au and Ag nanoparticle synthesis or stabilized by enzymes/proteins or any other stabilizer (Gálvez *et al.*, 2008; Govender 2009; Deng *et al.*, 2009; Zhang *et al.*, 2007). Despite the fact that colour change has been reported to be the initial evidence of nanoparticle formation (Liu *et al.*, 2004), other qualitative and quantitative characterization methods were employed in this study to confirm nanoparticle formation. Furthermore, it was observed that the intensity of colour increased with an increased amount of metal salts added to an aqueous solution of HSA. A control containing only an equal amount of HSA was used and no colour change was observed after addition of NaBH_4 to this control solution (Fig. 2.2a-c).

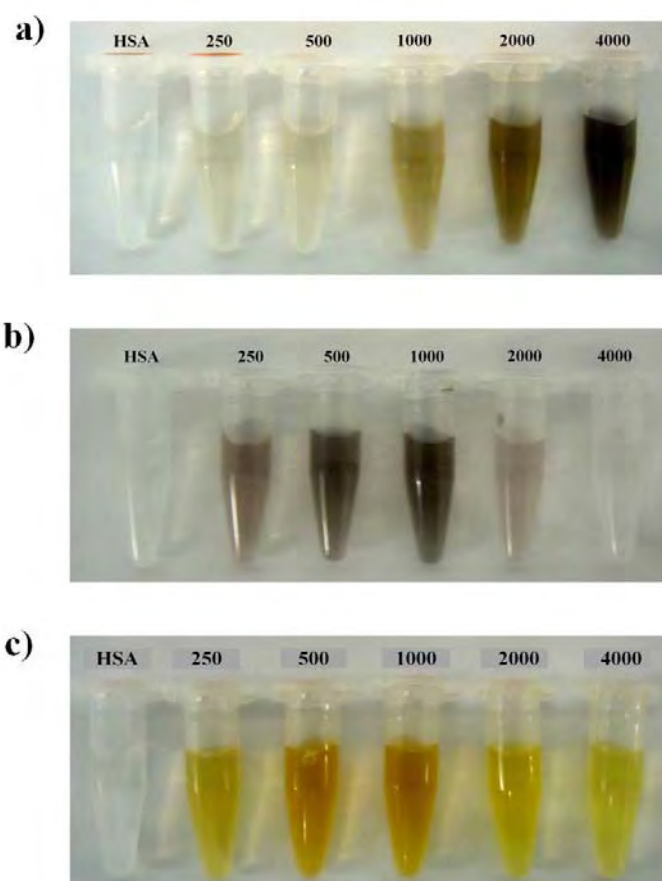


Figure 2.2: Metal nanoparticles synthesized with varying molar concentrations of metal salts to a fixed concentration of HSA (250-4000 M:HSA). HSA = Control. (a) Pt-nanoparticles, (b) Au-nanoparticles and (c) Ag-nanoparticles. Each sample presented was diluted 10-fold.

The solutions of M-nps-HSA were exhaustively dialyzed to remove excess metal salts that may not have been reduced by NaBH_4 . Samples were also centrifuged and filtered to remove aggregated particles that were not stabilized by HSA. It was also seen that more particles were stabilized as the precursor metal salts to HSA increased from 250:1 to 4000:1. This suggested an increase in the encapsulation of metal atoms with increasing metal atoms available in solution. This was not the case with Au and Ag, as a copious amount of nanoparticles was precipitated after synthesis at metal to HSA greater than 1000:1. This left the solution with lighter colour intensity and consequently a drop in nanoparticle concentration after centrifugation and filtration (Fig. 2.2 b & c) which implied that the saturation point of HSA had been reached with these metals beyond a molar concentration ratio of metal salt to HSA of 1000:1.

The purification by SEC showed an elution of M-nps-HSA around the same elution volume as that of the control (i.e. HSA) except with higher UV absorption peaks suggesting a co-elution of M-nps with HSA (Fig. 2.3a_I-c_I). Further analysis with native PAGE (5%) showed a co-migration of HSA and M-nps-HSA (Fig. 2.3a_{II}-c_{II}). The bands suspected to contain nanoparticles were excised and digested as described in 2.2.2.2.2 (pg. 32) and elemental analysis by ICP-OES confirmed the presence of corresponding metals. All these results implied that M-nps was, without a doubt attached to HSA.

The protein content of HSA was determined in each M-nps-HSA, before and after nanoparticle synthesis, with the concentration of HSA being 10 μM in both control and experimental samples and it was seen that a certain degree of stability was retained by HSA. In some instances, however, a significant amount was unaccounted for (Table 2.1[‡]). For example at a higher Pt:HSA ratio of 4000:1, a significant drop of about 44 % was observed in the protein content of HSA. A more significant percentage loss was observed in Au:HSA ratio from 2000:1-4000:1 (87-93 %, respectively). A similar trend was observed with Ag-nps stabilized by HSA with a loss of 92 % at Ag:HSA ratio of 4000:1. Unaccounted protein loss at higher molar concentration to HSA may be as a result of masking of protein by nanoparticles against the Bradford reagent. Previous studies have reported Pt incubation with HSA of up to a theoretical load of 15000 Pt atoms/ HSA and have found HSA to be intact by circular dichroism (Zhang *et al.*, 2010).

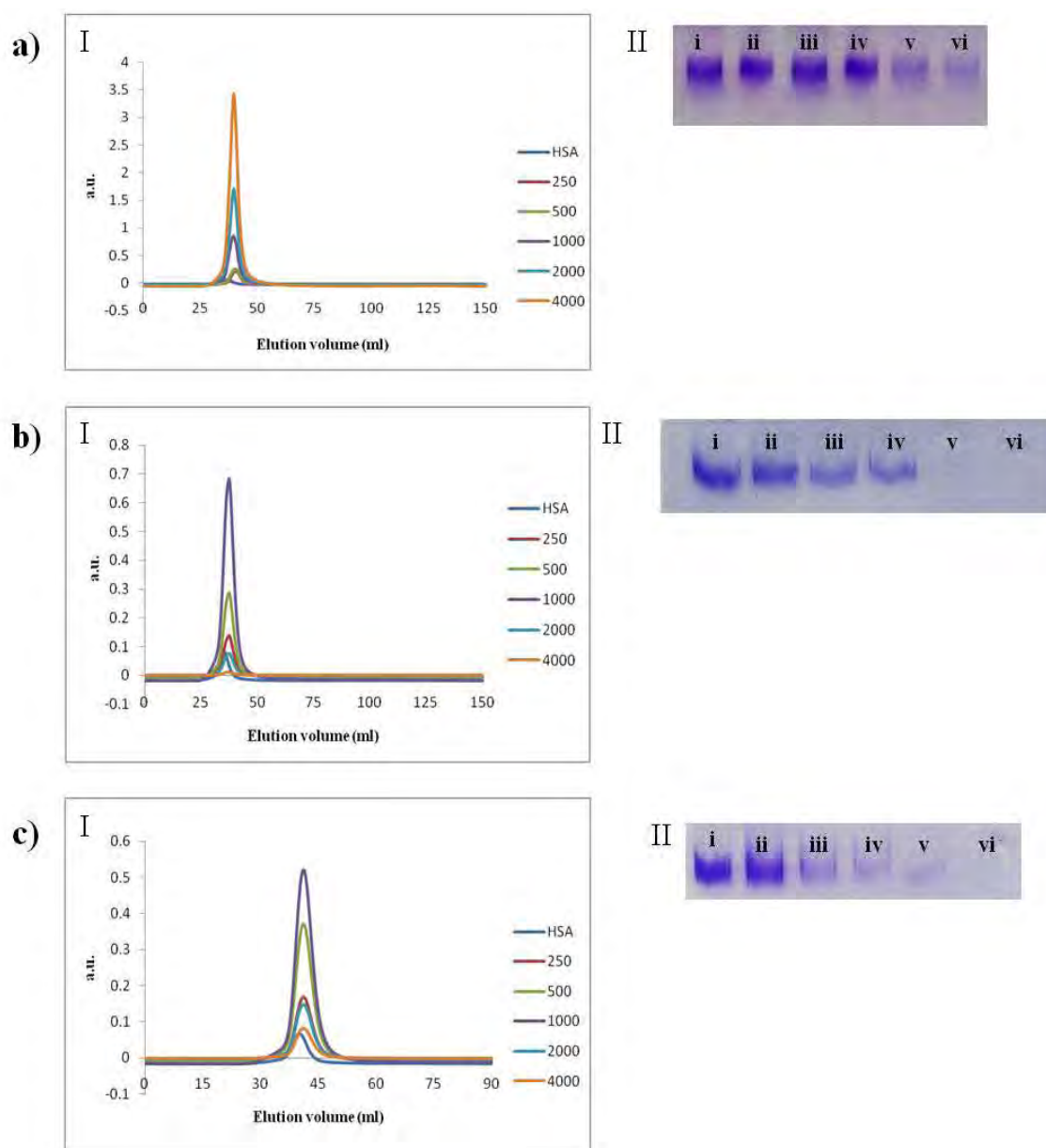


Figure 2.3: SEC elution profile (I) and native PAGE gels (II) of M-nps-HSA synthesized with different molar concentration of metal salt to a fixed concentration of HSA. (a) Pt-nps; (b) Au-nps and (c) Ag-nps. HSA = Control. (i) HSA only, (ii) 250:1, (iii) 500:1, (iv) 1000:1, (v) 2000:1 and (vi) 4000:1 (M:HSA) in all groups.

2.3.2 Characterization

2.3.2.1 ICP OES analysis

ICP OES was used to estimate the number of M-nps stabilized by HSA in each molar ratio sample, in order to determine the metal stoichiometry of M-HSA samples in solution and to establish the saturation point of HSA in terms of encapsulated metal atoms.

Results showed a general increase in metal nanoparticle concentration with increased molar ratio of precursor metal salts to a fixed concentration HSA as expected (Table 2.1^{††}). No metal was detected in the controls (HSA only). In Au-nps-HSA and Ag-nps-HSA, however, a decrease in metal concentration was observed from M:HSA ratio of 2000:1-4000:1. This was due to the increased nanoparticle aggregation and precipitation observed after nanoparticles synthesis (Fig. 2.2 b-c; Table 2.1^{†††}), which again, might be explained by the saturation point of HSA being reached at M:HSA of 1000:1.

The results obtained were used further to calculate the actual molar ratio of M atoms to HSA after nanoparticle synthesis. It also provided insight into the starting metal to protein required to generate nanoparticles of a particular size. Table 2.1 shows the calculated M:HSA ratio based on protein content of HSA before and after synthesis. The highest amount of metal atoms stabilized overall was seen in Pt-nps-HSA (404 and 920, based on the concentration of HSA before and after synthesis respectively) while the least stabilized was Ag, 77 and 202 (Table 2.1). An amount of 357 and 661 was observed with Au, making it the second highest stabilized metal atom. A study by Gálvez *et al.*, 2008 on metal nanoparticles stabilized by HSA, have suggested divalent precursor metal salts are preferably accommodated within the core of HSA. An explanation for this might be due to the fact that apoferritin, in its normal biological function, takes up iron in its Fe²⁺ state which is later converted to Fe³⁺ within its core. This may explain why Pt had the highest stabilization by HSA since the platinum salts used in the synthesis of Pt nanoparticles was a Pt (II) salt, that formed divalent metal ions in solution. Thus results obtained may imply that HSA had a greater affinity for divalent metal ions within its cavity. An earlier synthesis of Pt nanoparticle with a tetravalent metal salt of Pt (i.e. K₂PtCl₆) reported stabilization of 500 Pt atoms after nanoparticle synthesis (Deng *et al.*, 2009). This result was similar to what was obtained in the present experiment (404 Pt atoms) based on the starting HSA concentration of HSA and almost 2-fold (920 Pt atoms) based on the final concentration of HSA after synthesis. The low metal stabilization with Ag might also be explained by the little affinity of HSA for single valence metal salts contrary to what was reported by Gálvez *et al.*, 2008. The values obtained with Au were much lower than 1500 reported based on starting concentration of HSA (Zhang *et al.*, 2007). This might be as the result of large amount of precipitation observed in this study.

Table 2.1: Estimation of metal: protein stoichiometries of M-nps-HSA. M-nps and protein concentration were determined by ICP OES and Bradford's method respectively.

\dagger M : HSA	$\dagger\dagger$ [HSA] (μ M)	\ddagger [HSA] (μ M)	$\ddagger\dagger$ [M] (μ M)	\wedge M : HSA *	$\wedge\wedge$ M : HSA *
Pt					
Control	10	7.1	-	-	-
250	10	7.6	410.8	41	54
500	10	7.3	646.2	65	89
1000	10	7.2	1449.3	145	201
2000	10	7.4	2699.0	270	365
4000	10	4.4	4041.7	404	920
Au					
Control	10	7.6	-	-	-
250	10	7.6	1082.2	108	142
500	10	6.2	2369.8	237	382
1000	10	5.4	3571.7	357	661
2000	10	1.3	209	21	160
4000	10	0.7	94	9	13
Ag					
Control	10	9.5	-	-	-
250	10	9.6	497.7	50	52
500	10	10.1	642.5	64	64
1000	10	9.6	1251.5	125	130
2000	10	3.8	767.2	77	202
4000	10	0.8	63.6	6	80

\dagger = theoretical ratio of metal atoms to HSA; $\dagger\dagger$ = starting concentration of HSA based on estimation by Bradford method; \ddagger = Protein concentration of HSA after nanoparticles synthesis; $\ddagger\dagger$ = molar concentration of M-nanoparticles based on metal atom concentration as estimated by ICP OES; \wedge = calculated M-atoms: HSA ratio based on the starting concentration of HSA (i.e. 10 μ M) and $\wedge\wedge$ = estimated M atoms: HSA ratio based on HSA concentration after synthesis. * = values represents mean of triplicate samples with standard deviation <10%.

2.3.2.2 UV-visible spectroscopy

Synthesized nanoparticles were characterized by UV-visible spectroscopy and absorption maximum of solutions of M-nps-HSA was analyzed by a spectral scan between 230-800 nm. The control sample was HSA only. Results showed all M-nps-HSA showed typical surface plasmon resonance (SPR) bands consistent with metal nanoparticles encapsulated by protein shells as reported in the literature (Fig. 2.4 a-c).

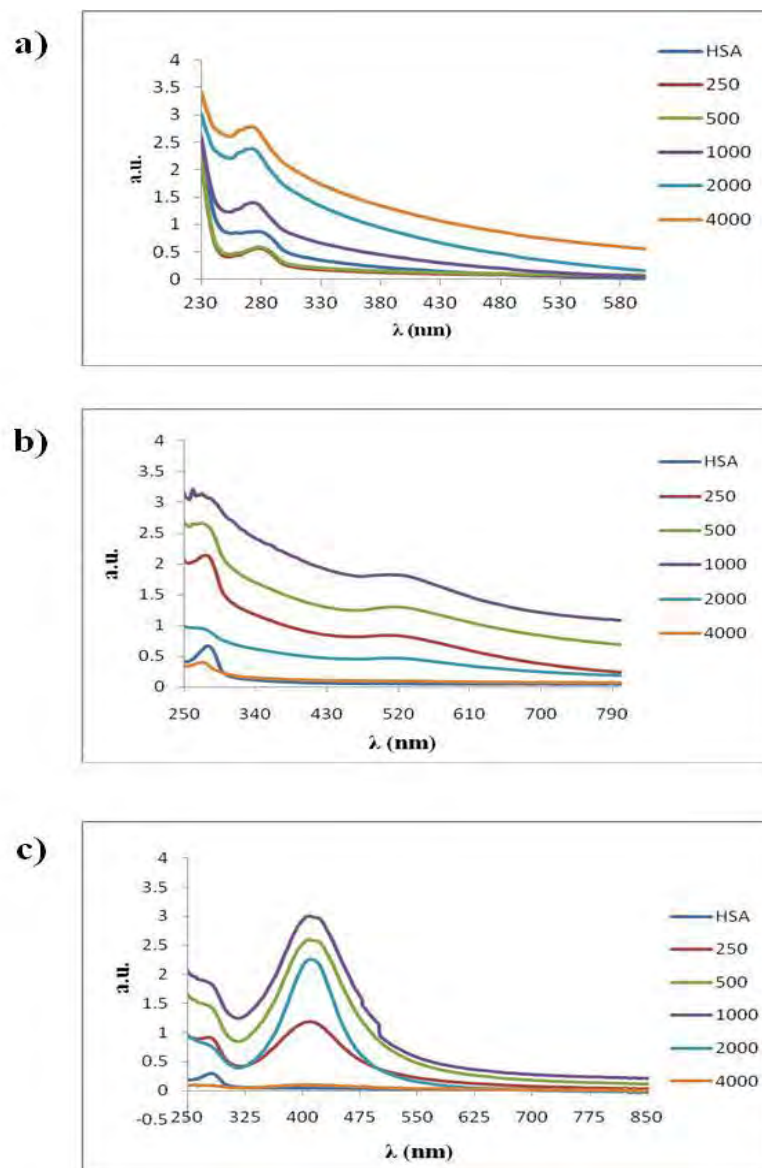


Figure 2.4: UV-visible absorbance spectra of M-nps-HSA showing typical SPR bands associated with each M-nps. (a) Pt-nps, (b) Au-nps and (c) Ag-nps. Peaks observed around 280 nm were due to the protein absorbance of HSA. Samples were diluted 10-fold.

Similar absorbance spectra were seen in HSA and Pt-nps-HSA at all Pt:HSA ratios used in this study. The only difference being that Pt-nps-HSA showed increasing absorbance maxima with increasing concentration of Pt-nps attached to HSA around 230-280 nm (Fig. 2.4 a). Previous studies have reported similar observations in protein stabilized/encapsulated Pt-nps (Liu *et al.*, 2011; San *et al.*, 2011). This was not the case with Au and Ag nanoparticles, however. In the UV-visible spectra of Au-nps-HSA, two absorbance peaks were observed at 280 and 520 nm with the former being attributed to HSA, being a protein, while the latter absorbance at 520 nm represented a characteristic SPR peak of spherical Au-nps < 20 nm in diameter (Zhang *et al.*, 2007; Fan *et al.*, 2010).

Absorbance maxima of Au-nps-HSA increased with increasing Au-nps concentration up to 1000:1, after which a sharp drop in SPR peaks was observed. This was due to large precipitation of Au-nps at Au:HSA ratio of 2000:1-4000:1 (Fig. 2.4 b). Characterization of Ag-nps-HSA gave similar results as that of Au-nanoparticles-HSA, except that the second absorbance peak was observed around 400 nm (Fig. 2.4 c) similar to values reported of ~4-nm sized Ag particles surrounded by a shell with high refractive index (Galvez *et al.*, 2008).

The intensity of the SPR band increased with increasing M: HSA. A drop in intensity of the SPR band was, however, seen in Au-nps-HSA and Ag-nps at M:HSA >1000:1. A decrease in the intensity of SPR bands at these concentrations was also due to a large nanoparticle precipitation during synthesis.

2.3.2.3 FTIR analysis

The biologically synthesized M-nps-HSA complexes were analyzed by FTIR spectroscopy in order to investigate the structural integrity of HSA after nanoparticle synthesis as well as to predict the binding sites of the nanoparticles by identifying functional groups responsible for their stabilization and/or coordination. Although samples were scanned from 650 - 4000 cm^{-1} , noticeable results were observed from 1300 - 1700 cm^{-1} . Thus, results presented are an expanded view of FTIR spectra from 1200-1800 cm^{-1} . Overall, results showed that the structure of HSA remained intact judging from the similarity in the spectrum of the control (i.e. HSA only, Fig. 2.5a-c, spectrum i) to the spectra profiles with increasing metal:HSA from 250:1 to 4000:1 (spectra ii-vi).

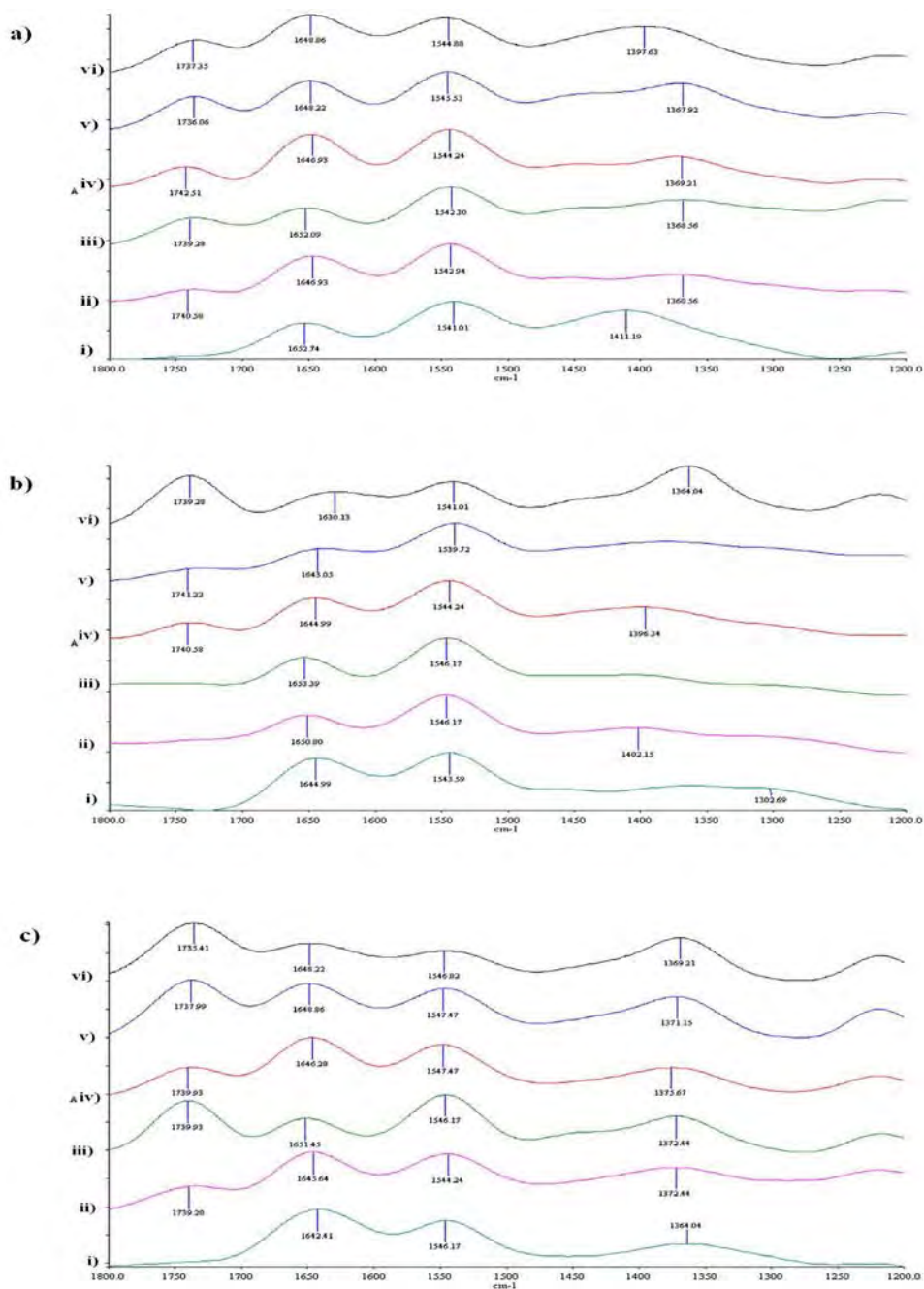


Figure 2.5: FTIR spectra of M-nps-HSA. (a) Pt-nps ; (b) Au-nps and (c) Ag-nps. Spectrum (i) HSA (i.e. control);(ii) 250:1;(iii) 500:1;(iv) 1000:1;(v) 2000:1 and (vi) 4000:1. Each spectrum presented was an average of 20 scans.

The presence of amide I ($1600\text{-}1700\text{ cm}^{-1}$) and amide II ($1500\text{--}1560\text{ cm}^{-1}$) bands that are characteristic bands found in infra red spectra of proteins and peptides (Gallagher, 1997) observed in both spectra of HSA and M-nps-HSA indicated protein stability. Furthermore, the presence of amide I ($1630\text{-}1653\text{ cm}^{-1}$) and amide II ($1540\text{-}1550\text{ cm}^{-1}$) peaks, often

ascribed to predominantly α - helical structured proteins (like HSA) in aqueous solutions, all pointed to the fact that the synthesis of M-nps in the presence of HSA did not compromise, in anyway, the overall structure of HSA (Haris and Severcan, 1999). These observations are similar to results obtained with native PAGE analysis in 2.3.1(pg. 36) as discussed.

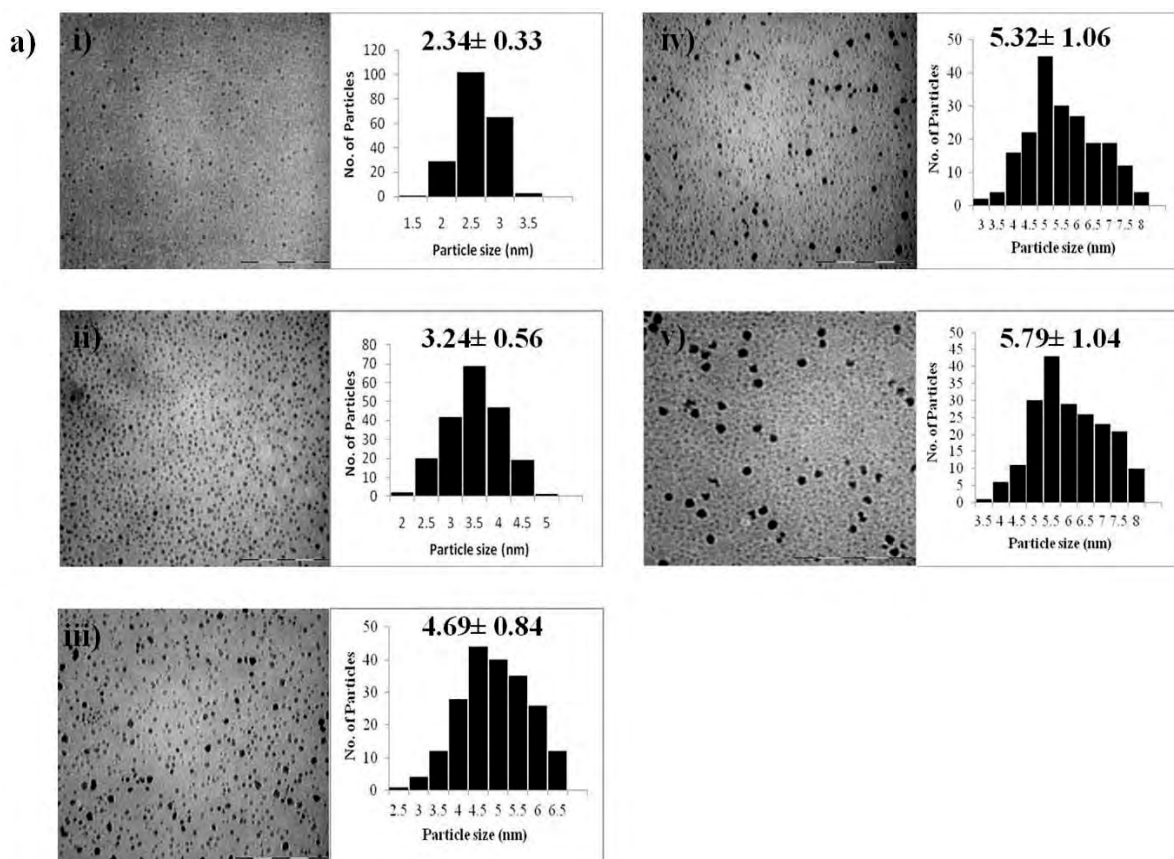
With a more detailed analysis of the FTIR spectra of Pt-nps-HSA, additional bands were observed in the amide I maxima of Pt-nps-HSA in the region $1736\text{-}1740\text{ cm}^{-1}$ (Fig. 2.5 a, spectra ii-vi) . This was not seen in the spectrum of HSA (Fig. 2.5 a, spectrum i). This may suggests the binding of Pt^{2+} (before its reduction to Pt^0 i.e. Pt-nps) to the carboxylate ion of the carboxylic acid containing side chains of acidic amino acids inducing a new stretching vibration in the carboxylic acid residue. The presence of acidic amino acids within the core of HSA is what gives the interior of HSA its net negative charge at physiological pH (Douglas and Ripoll, 1998; Gálvez *et al.*, 2006) which reflected the possibility of Pt-nps synthesis within the cavity of HSA. Similar results were obtained in Ag-nps-HSA. In Au-nps-HSA spectra, however, additional bands in the amide I band were only seen at $1739\text{ - }1742\text{ cm}^{-1}$ from Au:HSA ratio of 1000:1-4000:1 (Fig. 2.5 b, spectra ii-vi) and the reason for this may be due to increased stretching of the carbonyl group of the carboxylic residue of acidic amino acids at higher molar concentration ratios of Au:HSA.

2.3.2.4 TEM analysis

M-nps-HSA complexes were characterized by TEM in order to determine particle size distribution, position of nanoparticles around HSA and to confirm the synthesis of metallic nanoparticles of Pt, Au and Ag in the presence of HSA. From the results, the shapes of nanoparticles was predominantly spherical (Fig. 2.6) that agreed, obviously, with the spherical shape of HSA interior. Analysis of 200 particles in each set of experimental sample revealed a general increase in the size of nanoparticles with an increase in molar concentration of precursor metal salt to a fixed molar concentration of HSA. This was due to increased nucleation of nanoparticles during synthesis as a result of increased amount of metal salt in solution.

With respect to Pt-nps-HSA, size of nanoparticles increased with an increase in Pt:HSA ratio at all ratios used in nanoparticle synthesis with HSA (Fig. 2.6a). It was noticed,

however, that there was no significant increase in the size of Pt-nps at Pt:HSA ratio 2000-4000 implying that the maximum nucleation within the cavity of HSA has been reached. This shows further that the cavity of HSA restricted platinum nanoparticle nucleation and growth within its core. The average size of Pt nanoparticles obtained with different molar concentration of Pt salt was between 2-6 nm (Fig.2.6 a) which was in good agreement to that reported in the literature. Incubation of HSA with 100-24000 molar equivalent of platinum afforded a nanoparticle size of between 2 – 5 nm (Zhang *et al.*, 2010; Liu *et al.*, 2011; Fan *et al.*, 2011). More so, since the size of nanoparticles obtained was below that of the interior of HSA (8 nm, Galvez *et al.*, 2008), it gives further evidence that Pt-nps formed within the core of HSA. The TEM micrograph of negatively stained Pt-nps (Fig. 2.7 b), shows light protein rings surrounding the black dotted Pt-nps-crystals (green arrows) thus confirming the synthesis of Pt-nps within the cavity of HSA. This was similar with what has been reported (Liu *et al.*, 2011). In addition, the presence of empty HSA shells in the back ground (red arrow) suggested that HSA may still take up more Pt atoms without necessarily affecting the particle size from molar ratio of >2000 Pt atoms/HSA.



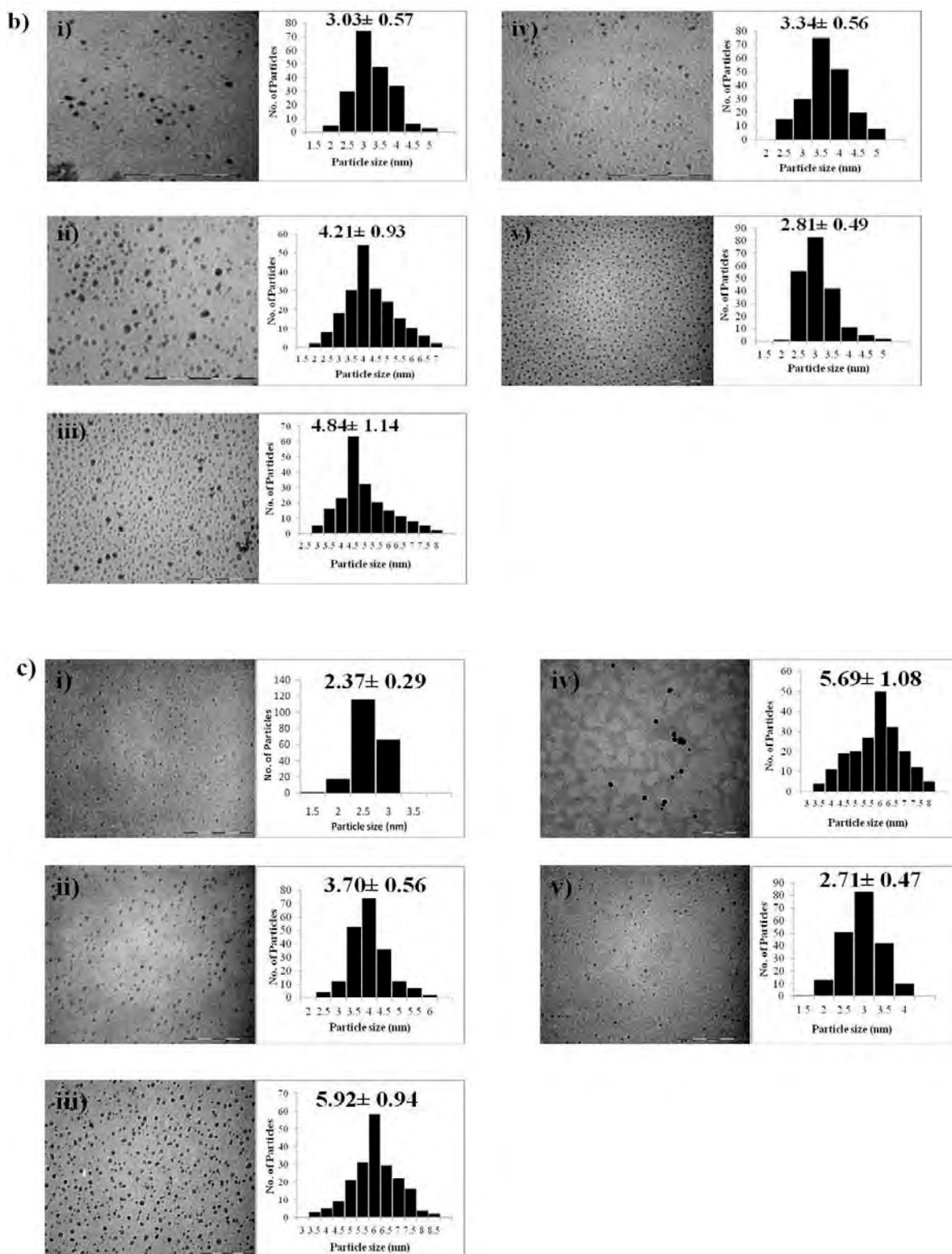


Figure 2.6: TEM micrographs and size distribution of M-nps made from varying molar ratios of metal salts to HSA. (a) Pt-nps, (b) Au-nps and (c) Ag-nps. Scale bar = 100 nm. 200 particles were analyzed in each group. (i) 250:1;(ii) 500:1;(iii) 1000:1;(iv) 2000:1 and (v) 4000:1.

Similar results were obtained with Au-nps-HSA except that a reduction in nanoparticle size was seen after a metal to HSA molar ratio of 1000:1 (Fig. 2.6b). This was due to the increased precipitation of Au nanoparticles observed at these concentrations (Fig. 2.2 b, pg. 35). Average nanoparticle size was between 3 - 5 nm; smaller than what has previously been reported for Au nanoparticles stabilized by HSA (Zhang *et al.*, 2007). Au-nps twice the size of HSA cavity was observed in that study when MOPS was used as the reducing agent though smaller size nanoparticles was obtained using NaBH₄ in that same study. Although the size obtained with Au-nps-HSA was below the core size of HSA, it was difficult to tell if nanoparticles were formed within the core of HSA. This was because TEM results obtained from negative stained micrograph of Au-nps-HSA did not conclusively indicate the position of Au-nps around HSA (Fig. 2.7 c). Notwithstanding, however, a few particles were seen within the cavity of HSA (Fig.2.7 c_{ii}). An earlier study had reported challenges with trivalent cationic, mono anionic and neutral forms of Au salts (HAuCl₄, AuCl₄⁻ and AuCl₃ respectively), as the synthesis of Au-nps with these salts and HSA resulted in the nucleation of Au-nps outside the protein cage (Zhang, *et al.*, 2007).

Reasons attributed to these observations were, firstly due to the anionic nature of HSA cavity in the case of mono anionic forms of Au (i.e. AuCl₄⁻); secondly, the preference of the cavity of HSA for monovalent and divalent metal salts as opposed to the trivalent salts of Au (HAuCl₄) as reported by Gálvez *et al.*, 2008; Thirdly, the natural affinity of some metal ions for the HSA exterior, or the simple non preference of some metal ions for either the interior or exterior of HSA like AuCl₃ (Fan *et al.*, 2010) . These three features provide explanations to the results obtained with Au-nps-HSA synthesis. Recent studies have, however, claimed success with Au-nps synthesis in HSA cavity by genetic modification of amino acid residues of HSA interior (Butt *et al.*, 2008) and the dual use of a strong and mild reducing reagent with an unmodified form of HSA in a two step biosynthetic approach (Fan *et al.*, 2010).

The results obtained with Ag-nps-HSA showed average particle size of 3 - 6 nm (Fig. 2.6 c). The size of the nanoparticles also increased with increased molar concentrations of Ag salt used in nanoparticle synthesis up to 1000:1 (Ag:HSA), after which no change in nanoparticle size made any significant difference. Reduction in particle size of Ag-nps was however observed at a molar ratio of 4000:1 (Ag:HSA). Again, this might be explained by

the increase of nanoparticle precipitation observed at this ratio after nanoparticle synthesis. Negative staining confirmed the formation Ag nanoparticles within the core of HSA (Fig. 2.7 d). Very few empty cages were observed after a molar concentration ratio of 500:1 (Ag:HSA) indicating complete saturation and nucleation of Ag-nps within the HSA interior. These results agree with a reported study of Ag nanoparticles in HSA (Domínguez-Vera *et al.*, 2007). The nucleation of some Ag nanoparticles on the HSA exterior was, however, noticed at molar concentration ratios $>500:1$ contrary to what was reported with molar ratio of 5000 Ag atoms/HSA (Domínguez-Vera *et al.*, 2007 (Fig.2.7 d_{ii})). This observation of an exterior nucleation may be due to over-saturation of the HSA core.

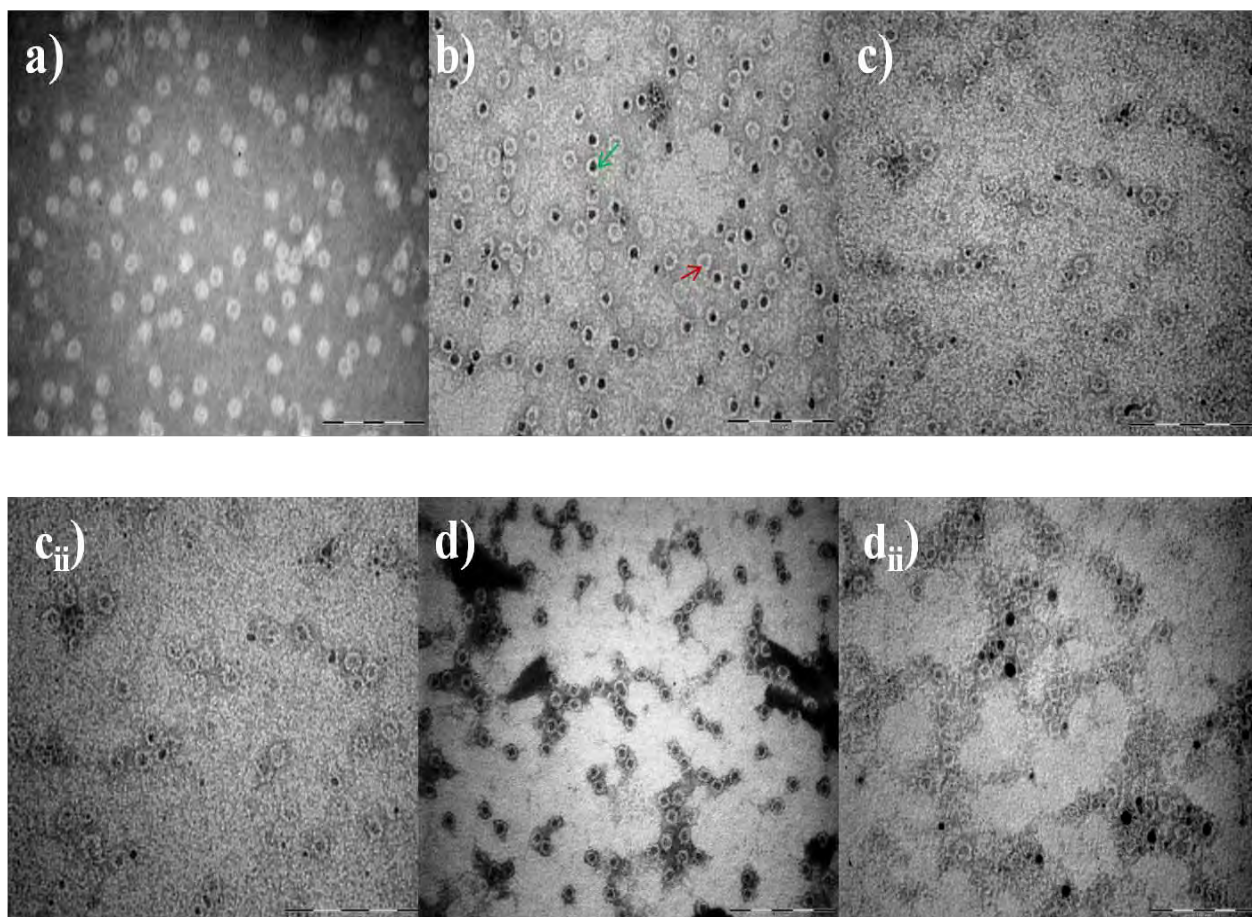


Figure 2.7: TEM micrographs of stained M-nps-HSA. (a) HSA only (control); (b) Pt-nps; (c) Au-nps and (d) Ag-nps. Samples were negatively stained with 1% uranyl acetate. Scale bar = 100nm. Green and red arrow represents a typical nanoparticle within the core of HSA and an empty HSA shell respectively.

2.3.2.5 EDX analysis

EDX analysis of M-nps-HSA confirmed the presence of Pt, Au and Ag in their respective samples of M-nanoparticles-HSA solution (Fig. 2.8 a-c). This further confirmed the synthesis and stabilization of M-nanoparticles by HSA.

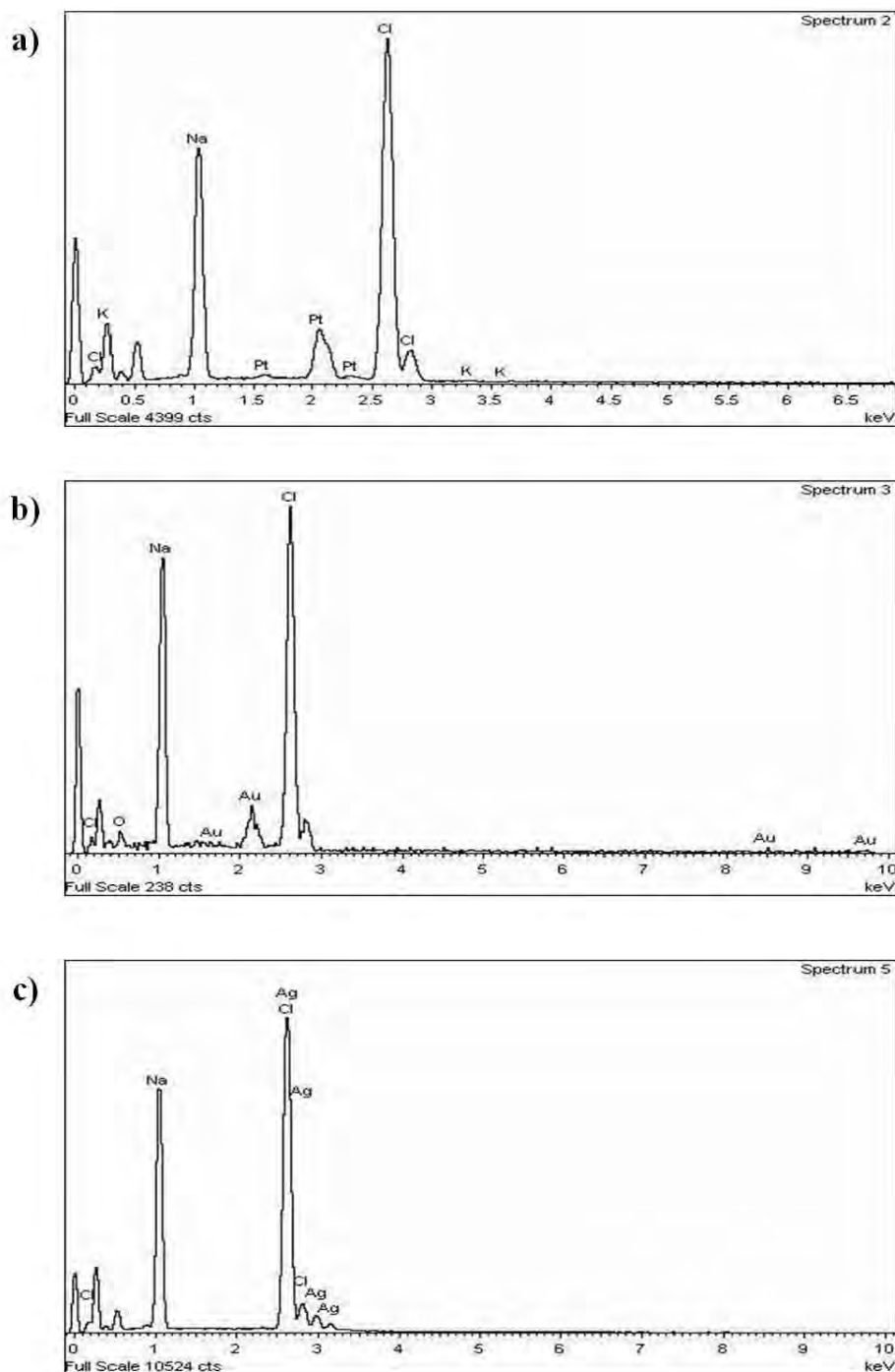


Figure 2.8: EDAX spectra of M-nps-HSA. (a) Pt-nanoparticles, (b) Au-nanoparticles and (c) Ag-nanoparticles.

2.3.2.6 The effect of M-nps on the ferroxidase activity of HSA

This experiment was done in order to determine the effect of the different sized particles synthesized in the presence of HSA on its ferroxidase activity (Fig. 2.9 a-c). It was noticed that apart from a general increase in the ferroxidase activity with all M-nps stabilized by HSA, increase was also noted with increasing M:HSA used in this study. This increasing trend with M:HSA was not seen at a ratio of >1000M:HSA in Au and Ag-nps. This may be explained by a large amount of nanoparticles precipitation observed at these molar concentration ratios.

The ferroxidase activity was seen to increase with specific activities of about 72 – 360 $\mu\text{mol}\cdot\text{min}^{-1}\cdot\text{mg}^{-1}$ (i.e. a 3 to 9 fold increase over the control, Fig. 2.9 a) with increasing Pt:HSA ratios (250:1-1000:1) with Pt-nps. A 2 to 7-fold (i.e. 28 – 100 $\mu\text{mol}\cdot\text{min}^{-1}\cdot\text{mg}^{-1}$, Fig. 2.9 b) with Au-nps between molar ratios of 250:1-2000:1 (Au:HSA) and a profound increase of about 800 – 2700 $\mu\text{mol}\cdot\text{min}^{-1}\cdot\text{mg}^{-1}$ (16 to 54-fold, Fig. 2.9 c) was noticed with Ag-nps at ratios of 250:1-2000:1 (Ag:HSA). The investigation on the effect of Pt-nanoparticles synthesis on the ferroxidase activity of HSA could not proceed beyond molar concentration of 1000:1. This was due to very high absorbance of >2.0 at 420 nm brought about by Pt-nps attached to an estimated 1 μM of protein used in this experiment as absorbance change determined ferroxidase activity. An important characteristic of noble metallic nanoparticles is their catalytic property (Euis and El-Sayed, 2006; Sau *et al.*, 2010; Mohanty *et al.*, 2010; Fratoddi *et al.*, 2011) especially that of Pt, Au and Ag which may explain the increase in the enzymatic activity observed in this study.

Certain mechanisms of Fe^{2+} uptake and oxidation by apoferritin have been proposed (Niederer, 1970; Macara *et al.*, 1972). Some of which have suggested that the basic and nitrogen containing amino acids residues within the core of apoferritin to be responsible for its ferroxidase activity. This site was thus different from the site containing acidic amino residues reported to be implicated in the uptake and nucleation of other metal ions and subsequent stabilization of its reduced form within the apoferritin core.

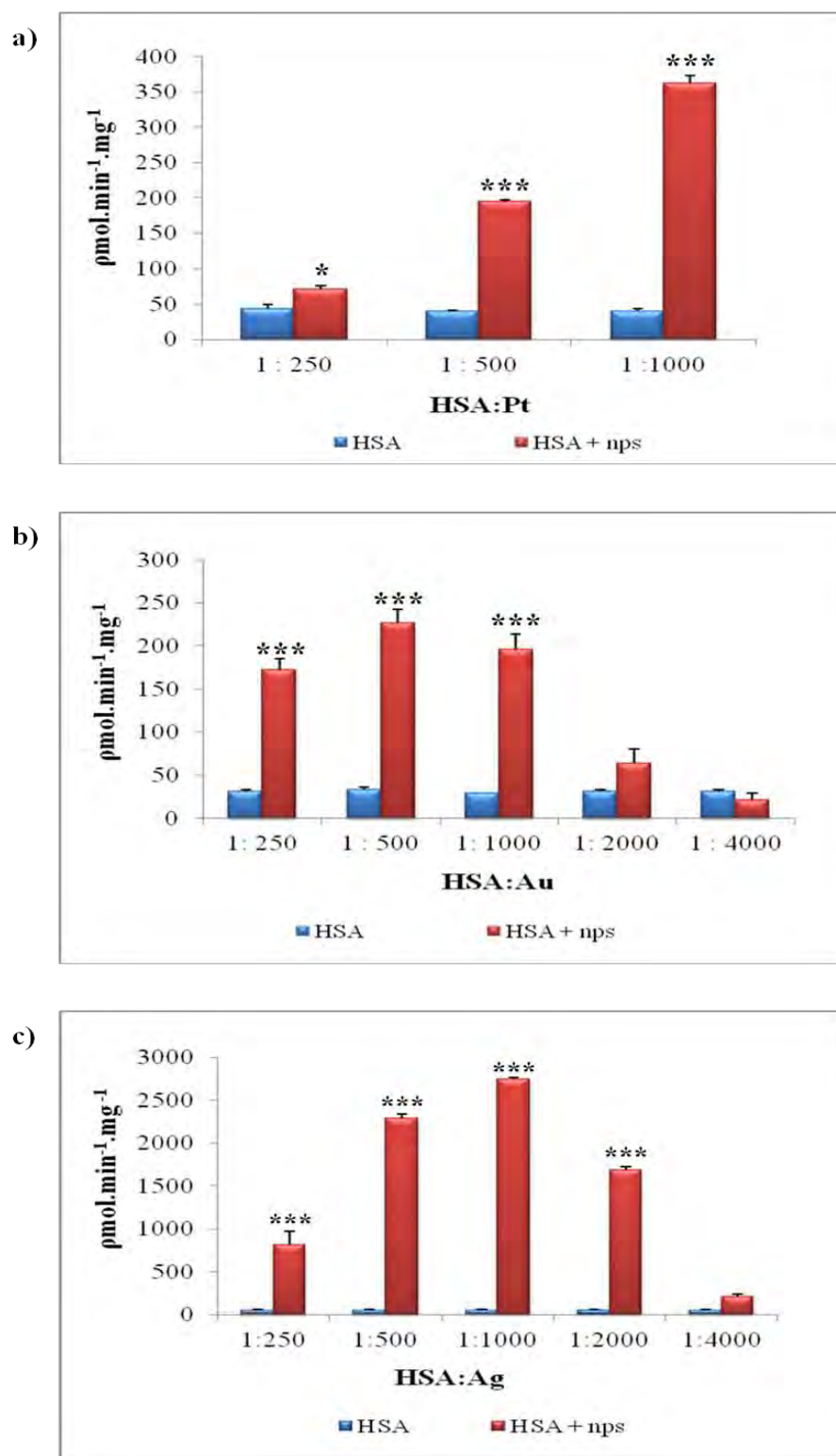


Figure 2.9: The effect of M-nps on the ferroxidase activity of HSA. (a) Pt-nanoparticles; (b) Au-nanoparticles and (c) Ag-nanoparticles. Results presented are the mean of three independent assays done in triplicate. Error bars represents the standard error of the mean values. * = $p < 0.05$; and *** = $p < 0.001$ versus controls (i.e. HSA)

2.4 Conclusions

A comparison of this biological process for the synthesis of metallic nanoparticles of Pt, Au and Ag over conventional chemical method of synthesis, concluded that the methods employed in this study were generally mild and ecofriendly, in terms of pH and temperature.

Relatively uniform sized and shaped metal nanoparticles obtained from this study confirmed that HSA was able to control particle growth within its interior. Furthermore, the generated particles possessed similar physical (excluding particle morphology) and chemical properties to the chemically synthesized nanoparticles and thus made them applicable.

Finally, the encapsulation of metallic nanoparticles within the cavity of HSA did not affect its overall protein structure but would improve an *in vivo* iron uptake as reflected by an enhanced ferroxidase activity seen in this study. This can have possible clinical applications in the treatment of diseases associated with poor iron absorption and possible reduction of oxidative stress associated with the toxic levels of iron in the biological system.

Chapter 3: Biosynthesis of metallic nanoparticles in GroEL

3.1 Introduction

Molecular chaperones promote the proper folding of nascent or denatured proteins into their active native forms. The process of refolding and release of native proteins requires a co-chaperone, ATP and other co-factors such as K^+ and Mg^{2+} or Mn^{2+} . Chaperones are used in biotechnology for obtaining active recombinant proteins (Hoffmann and Rinas, 2004) and have been reported to prevent *in vivo* aggregation of proteins at elevated temperatures associated with diseased conditions in the biological system (Melkani *et al.*, 2003; Fei and Perret, 2009).

One of the best characterized chaperonin is GroEL from *E.coli* (an Hsp60 homologue). A symmetric tetradecamer made up of two supramolecular rings with each ring consisting of seven subunits (each subunit has a molecular mass of 60 kDa). These rings stack on each other in a double-decker architectural fashion forming a three-dimensional barrel structure with a hydrophilic interior of about 4.5 nm in diameter and a wall thickness of 4.6 nm (Fig. 3.1, Ortac and Severcan, 2007). The structure of GroEL is hybridized by its co-chaperone, GroES (Hsp10) forming a capping assembly on either side of its barrel-like cavity. Misfolded or denatured proteins are encapsulated within the barrel-like cavity of GroEL through hydrophobic or electrostatic interactions and are refolded into their native forms. After refolding, the substrate proteins, still in their inactive forms when bound to GroEL, are released into their active states by the addition of ATP and sometimes GroES (Mendoza *et al.*, 1996; Melkani *et al.*, 2003; Fan and Mark, 2006).

A previous study has mimicked the chaperonin function of GroEL, from *Escherichia coli* and *Thermus thermophilus* HB8, by using its cavity for the encapsulation, folding and ATP- assisted release of CdS semiconductor nanoparticles (Ishii *et al.*, 2003). Another study used a modified cavity of GroEL-like proteins to size-selectively bind and arrange metallic and semiconductor nanoparticles into ordered nanoparticle arrays (McMillan *et al.*, 2002). Both studies proved beneficial particularly in the field of material science and may be employed in the generation of new bio-responsive, electronic and photonic devices.

Furthermore, since the release of many GroEL-bound proteins is dependent on the hydrolysis of ATP, it may be expected that a faster rate of ATP hydrolysis of GroEL might improve its chaperonin function.

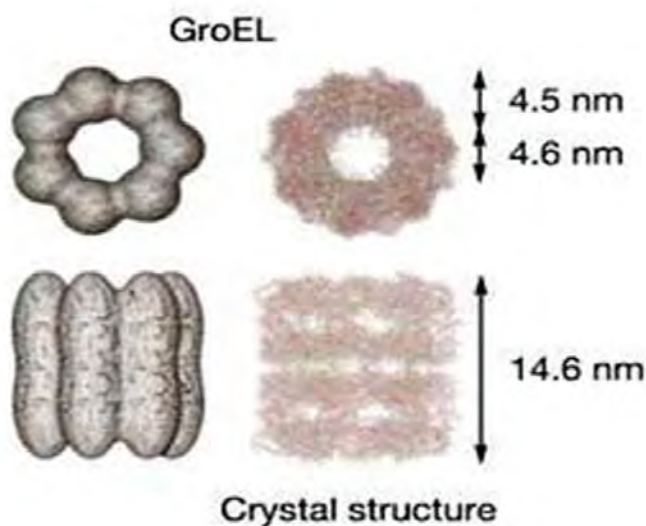


Figure 3.1: Schematic representation (top and side views) of GroEL (crystal structures, right). (Adapted from Ishii *et al.* 2003; Ortac and Severcan, 2007).

Two reports on the role of nanoparticles as assistants to help protein refolding (Fei and Perret, 2009) have appeared in the literature. One a nanogel formed by the self-aggregation of pullulan bearing a cholesterol group (Akiyoshi, *et al.*, 1999; Nomura *et al.*, 2003; Ikeda *et al.*, 2006) and the second gold nanoparticles functionalized with 2-(10-mercaptodecyl) malonic acid (De and Rotello, 2008). It would be of interest to investigate if nanoparticles, either acting alone, or in conjunction with chaperones themselves, would improve the efficiency of protein folding by increasing the ATPase activity of GroEL.

Thus, the objectives of this chapter are to:

- i. Biologically synthesize metallic nanoparticles of Pt, Au and Ag within the barrel-like cavity of GroEL.
- ii. Characterize these nanoparticles using various techniques.
- iii. Study the biological effect of synthesized nanoparticles on ATPase activity of GroEL.

3.2 Materials and Methods

3.2.1 Cloning, expression and purification of GroEL

3.2.1.1 Materials

PGRO7 plasmid coding for both GroEL/GroES gene was obtained from Takara Bio Inc. *Escherichia coli* (*E. Coli*) strain XL1-Blue competent cells were obtained from Stratagene Cedar Creek Texas, USA. Adenosine triphosphate (ATP), chloramphenicol (CAM), arabinose and lysozyme were obtained from Sigma-Aldrich (South Africa). All other reagents were of analytical grade and all solutions were prepared with deionised water.

3.2.1.2 Methods

3.2.1.2.1 Transformation

Cells of *E. coli* strain XL1 Blue was transformed with the plasmid pGRO7. Selective pressure was maintained by CAM. Cell aliquots (100 μ l) was thawed on ice and 2 μ l of plasmid DNA (PGRO7) was added, gently mixed and incubated on ice for 20 mins. Cells were heat shocked for 2 min at 42 °C followed by incubation on ice for another 2 min. A 900 μ l of 2xYT broth (Appendix E) was each added to the 100 μ l aliquots of transformed cells and incubated at 37°C for 1 h. After incubation, the cells were centrifuged and supernatant removed and re-suspended in the residual broth. This was spread on 2xYT broth Agar plates containing CAM (20 μ g/ml) and incubated overnight at 37 °C.

3.2.1.2.2 Induction/Induction studies

A single colony of transformed *E.coli* cells was inoculated into 25 ml 2xYT broth with CAM (20 μ g.ml⁻¹) and grown overnight. This was diluted 10-fold with 2xYT broth and grown to mid-log phase (i.e. an OD_{600nm} = 0.4 to 0.6). Once mid-log phase was achieved, induction was initiated with 0.2 % L-arabinose. Samples (1.0 ml) were collected immediately and subsequently at 1 h interval for the next 5 h. These were centrifuged (13 000 rpm) and lysed with phosphate buffer saline (PBS, pH 7.4, Appendix A). Protein expression levels of GroEL were determined by sodium dodecyl sulfate polyacrylamide gel electrophoresis (SDS-PAGE, Fairbanks *et al.*, 1971).

3.2.1.2.3 Purification

Purification of GroEL was carried out as described (Kamireddi *et al.*, 1997) with some modifications. Cells were harvested by centrifugation (10000 x g; 15 min; 4 °C) and

washed with Tris-HCl (25 mM, pH 8.0). About 2.5 g cell paste obtained from 1 L induced cell culture was re-suspended in TEDP (50 mM Tris -HCl, pH 8.0, 1 mM EDTA, 1 mM DTT and 0.1 mM PMSF) buffer. Lysozyme (1 mg.ml⁻¹) was added to the re-suspended cells, frozen overnight at - 80 °C and ruptured by sonication (Vibra cell sonics & materials inc. Danbury Conetticut, USA, 60 s burst, and 5 cycles, with 60 s pulse on ice between cycles). Cell lysate was centrifuged (120 000 x g; 1 h; 4°C) and supernatant was treated with 25 ml packed volume of DE-52 previously equilibrated to pH 8.0 with TEDP buffer. The slurry was stirred slowly for 1 h on a magnetic stirrer and resin was removed by centrifugation (4000 rpm; 20 min; 4°C). GroEL in the supernatant was precipitated with ammonium sulphate at 50 % saturation at 4°C and allowed to equilibrate for 1 h. The precipitate was collected by centrifugation (12 000 g, 4°C), redissolved in TEDP buffer (pH 8.0, 5 ml) and further purified by gel exclusion chromatography (AKTA FPLC, GE Health). The sample was loaded onto the Sephacryl S300HR Hi Prep 16/60 column (Sigma-Aldrich) after the addition of ~5 % glycerol at a flow rate of 0.5 ml.min⁻¹. The active proteins were eluted with the same buffer and the fractions containing pure GroEL, as evaluated by SDS-PAGE, were pooled and concentrated by ultra filtration (Macrosep® centrifugal device 10k MWCO, Pall Corporation). The concentrated GroEL was dialyzed against buffer (50 mM Tris-HCl, pH 7.5 and 1 mM DTT) for 6 h. Glycerol was added to the sample to 10 % , aliquoted (1 ml), rapidly frozen in liquid nitrogen and stored at -80 °C for further use.

3.2.1.2.4 SDS-PAGE, western blot analysis and molecular mass determinations

The effectiveness of the purification process was determined by SDS-PAGE on samples exhibiting GroEL ATPase activity. Samples from each purification step (100 µg, 10 µl) and a standard molecular weight marker (10-170 kDa), were electrophoresed on 12 % SDS-PAGE at 150 V. The gels were stained with Coomassie Brilliant Blue R-250, then destained in methanol:acetic acid: water (4:1:5 v/v/v). The molecular weight of the purified GroEL was determined using a standard curve of log molecular weight versus log of relative mobility (R_f) of protein markers (Appendix F). Western analysis was also performed to further confirm that protein of interest was GroEL. GroEL antibody raised in rabbit (Sigma-Aldrich) was used to detect the presence of GroEL at each purification step (Appendix F).

3.2.1.2.5 GroEL ATPase activity

The ATPase activity of GroEL, expressed in $\mu\text{molPi}\cdot\text{ml}^{-1}\cdot\text{min}^{-1}$, was determined colorimetrically, at 850 nm as described (Modisakeng *et al*, 2009). GroEL (2 μM) was incubated with adenosine triphosphate (ATP, 800 μM , 37 °C, 1 h) in TDMK (50 mM Tris-HCl, pH 8.0, 1 mM DTT, 10 mM MgCl_2 and 20 mM KCl) buffer in a total volume of 500 μl . Samples (50 μl) were collected at 0, 15, 30, 45 and 60 min with the reaction stopped by addition of sodium dodecylsulphate (10 %, 50 μl). The amount of phosphate released was estimated colorimetrically at 850 nm with ascorbic acid (6 %) and ammonium molybdate (6 %), both dissolved, separately in acetic acid (5 %) and mixed in a 1:2.5 ratio respectively. The values obtained were normalized for ATP hydrolysis from a previously constructed phosphate standard curve made using KH_2PO_4 (Appendix G). An equal amount of boiled solution of GroEL (100 °C, 1 h) was used as the control (Appendix G).

3.2.1.2.6 Protein estimation

All protein estimation in this study was performed by the Bradford method (Bradford, 1976) as described in 2.2.2.4.

3.2.2 Nanoparticle synthesis

GroEL (10 μM , 400 μl) in TK (Tris-HCl, pH 8.0 containing 150 mM KCl) buffer was incubated with various concentrations of metal salts to give a GroEL: metal ratio between 1:5 - 1:1000 for Pt and 1:14 - 1:1000 for Au and Ag. These mixtures were allowed to incubate with stirring at 4°C followed by the addition of NaBH_4 (20-fold of metal concentration for Pt and 5-fold with Au and Ag). Formation of nanoparticles was allowed to proceed for 5 h in the case of Pt and 1 h for Au and Ag. Solutions obtained were dialyzed exhaustively (Slide-A-lyzer dialysis cassette G2 1000 MWCO from, Thermo Scientific) against TK buffer for 12 h with buffer change every 4 h. This was followed by centrifugation (5000 rpm, 1 min) and filtered through a 0.22 μm filter. Samples were stored at 4°C for further analysis. Two controls used were K_2PtCl_4 with no GroEL and GroEL. The protein concentration of GroEL used as the second control was the same as the starting concentration of GroEL used in the synthesis of nanoparticles.

3.2.3 Characterization

Nanoparticles obtained were analyzed using techniques such as UV/Vis spectroscopy, inductively coupled plasma optical emission spectroscopy (ICP OES), Fourier transform Infrared spectra (FTIR), transmission electron microscopy and energy dispersive analysis of X-rays (EDAX). Details of methods of sample preparation for all characterizations used in this study are outlined in 2.2.2.2 (pg. 32). Higher resolution transmission electron microscopy (HRTEM) analysis was performed in this study with the aid of a JEOL JEM-1210 TEM operating at 200 keV. HRTEM was attached to an EDAX scanner, thus EDAX spectrum obtained in this study was obtained from the same sample used for HRTEM analysis. Samples were prepared on lacy carbon grids (Agar Scientific, USA) as described in 2.2.2.2.4 (pg. 33).

3.2.4 Effect of nanoparticles on the ATPase activity of GroEL

Metal nanoparticles-GroEL complexes (M-nps-GroEL, 2 μ M, based on protein estimation by Bradford) were incubated with ATP (0.8 mM, 37°C, 1 h). ATPase activity of M-nps-GroEL was determined as described in 3.2.1.2.5 (pg. 56). GroEL without M-nps attached was used as the control experiment. An equal protein concentration of M-nps-GroEL and GroEL without ATP both in TMDK buffer was used as the absorbance blank in the reaction assay involving nanoparticles and the control respectively.

3.2.5 Statistical analysis

All enzyme assays were carried out in triplicate and values reported as the means with standard error of means. Where necessary analysis of variance was conducted using Graph Pad InStat for Windows, version 3 (Graphpad Software Inc.) demo version and Microsoft Excel 2007. The level of significance of means was determined at $p < 0.05$; $p < 0.01$ and $p < 0.001$ versus controls (i.e. GroEL only).

3.3 Results and Discussion

3.3.1 Expression of GroEL

The expression of GroEL was induced by 0.2 % L-arabinose at 37 °C and was monitored over a period of 5 h with samples taken at 1 h intervals. The levels of expression were determined by SDS-PAGE (Fig. 3.2), GroEL in 2xYT medium continued to increase till the 5th hour (T_5) after which degradation was observed. Thus, in subsequent expressions,

induced cells were harvested after 4 h (T_4) of induction. Previous expressions of GroEL/GroES proteins using a different cloning vector (pRE1) and inducible systems have reported the improvement of GroEL up to 6 h (Kamireddi *et al.*, 1997) before degradation started and so prolonged and stable protein expression may be considered in this case. In terms of time taken to reach optimal expression, however, this method may be the most appropriate.

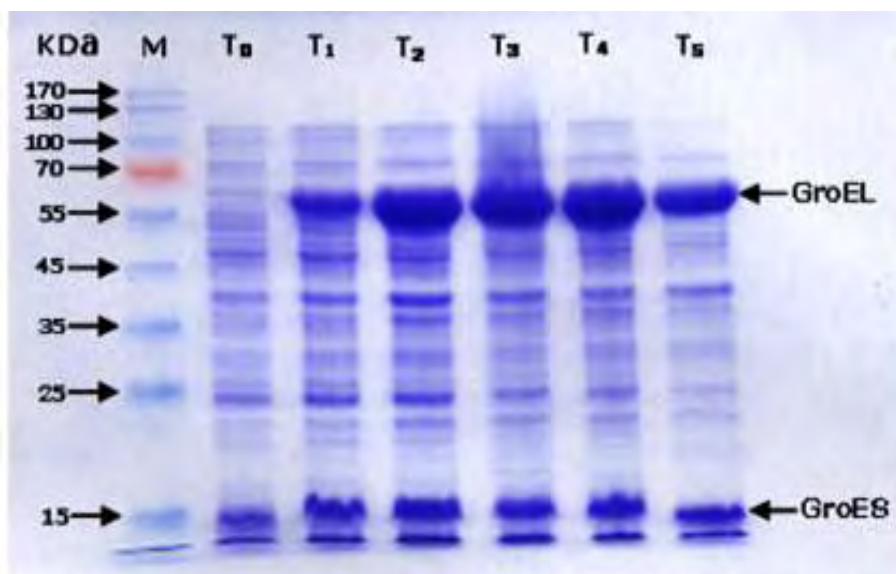


Figure 3.2: SDS-PAGE (12%) analysis of the expression of GroEL and GroES as a function of time. Lane M, protein marker; lanes T_0 – T_5 , extract of cells induced for 0–5 h respectively.

3.3.2 Purification

GroEL was extracted and purified from a 2.5 g cell paste obtained from a 1 L cell culture as described in 3.2.1.2.3 (pg.54). In the purification step involving ion exchange batch purification on DEAE-cellulose anion exchanger (DE52), GroEL did not bind to this matrix suggesting that GroEL may possess an overall negative charge. Consequently a batch adsorption of the crude cell lysate to DE52 removed most of the GroES and a substantial amount of other proteins with a very high concentration of GroEL remaining in solution (i.e. the supernatant, Fig. 3.3 a, lane 2). GroEL in solution was precipitated by ammonium sulphate (50 % saturation) and then further purified by FPLC on a Sephacryl HR 300 column. GroEL was eluted in the void volume, fractions obtained were analyzed by SDS-PAGE and pure fractions as judged by this analysis were pooled. Western blot

analysis using GroEL antibody confirmed the presence of GroEL protein at all purification steps (Fig. 3.3 b). Estimated molecular weight of GroEL from Fig. 3.3 a was 59.17 kDa (Appendix F) which was similar to that reported (Ortac and Severcan, 2007).

The purification table constructed to determine the effectiveness of each purification steps of GroEL from a 1 L cell culture is shown (Table 3.1). About 45 mg of pure GroEL per litre cell culture was obtained after gel filtration on Sephacryl HR 300. This is quite low compared to a 100 mg protein (Kamireddi *et al.*, 1997) reported in an earlier study although a different cloning vector and inducer was used with a prolonged time of protein expression. The TEM micrograph of the anterior (blue arrows) and lateral (red arrows) view of purified GroEL are shown (Fig. 3.3 c). A double-layer ring spherical protein structure with a measured inner cavity diameter of 4.32 ± 0.36 nm was observed which was consistent with that described (Ishii *et al.* 2003; Ortac and Severcan, 2007).

Table 3.1: Purification table of GroEL from 1 L cell culture.

	Volume (ml)	[Protein] (mg/ml)	[Total protein] (mg)	Activity U/ml	Total Activity (U)	Specific activity (U/mg)	Yield (%)	P.F*
Crude	20	16.83	336.64	1.90	38.06	0.11	100	1
DEAE (DE 52)	15	4.43	66.38	2.24	33.59	0.51	88	4.6
Gel filtration	11	4.07	44.72	2.69	29.54	0.66	78	6.0

* P.F = purification fold.

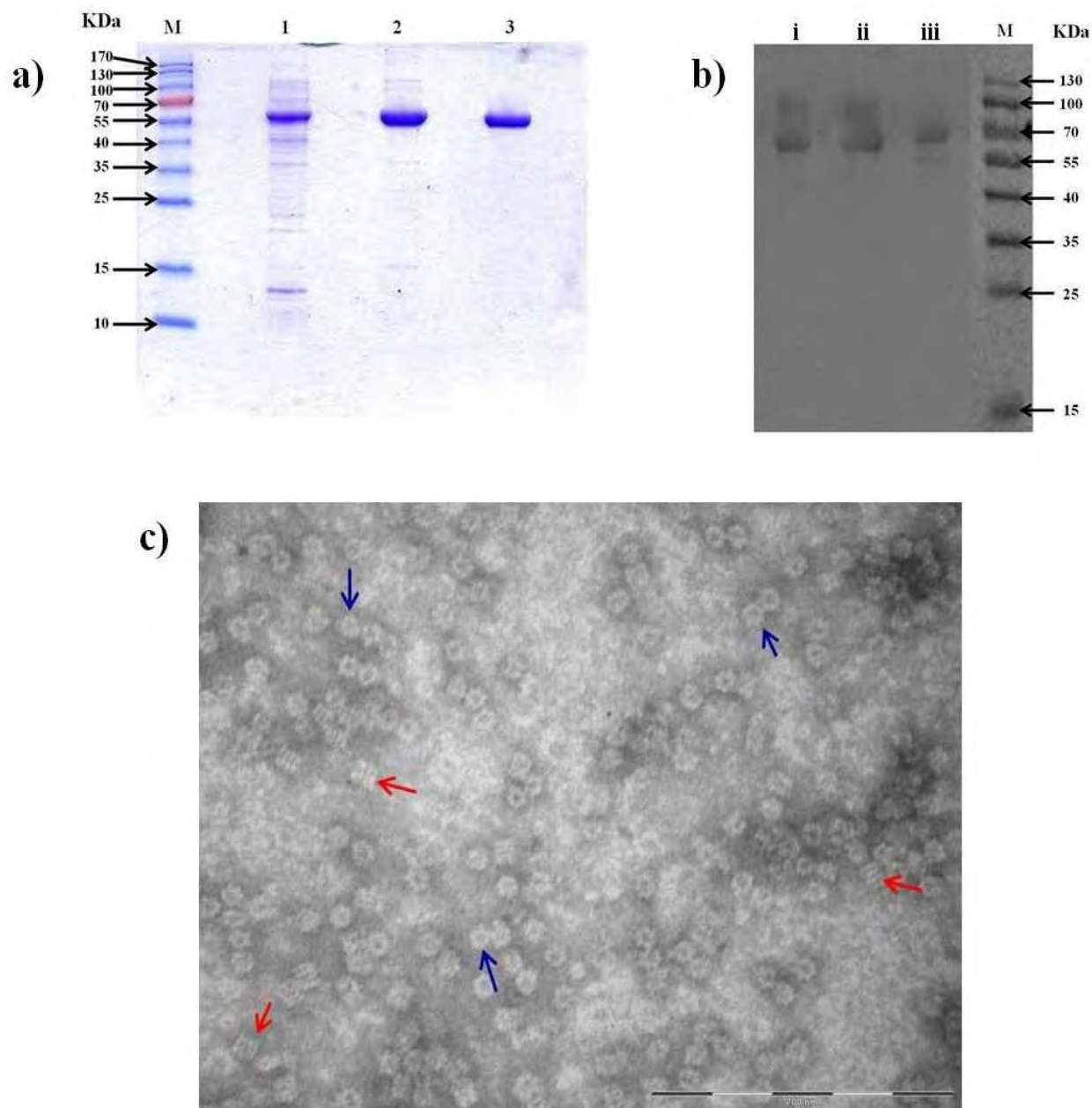


Figure 3.3: GroEL purification. (a) SDS-PAGE (12 %) analysis of the purification steps of GroEL. Lane 1= Crude lysate of cells induced after 5 h (100 μ g); Lane 2 = Batch purification on DEAE anion exchanger (100 μ g) and Lane 3 = FPLC size exclusion chromatography on Sephacryl HR-300 of GroEL after $(\text{NH}_4)_2 \text{SO}_4$ precipitation (100 μ g). Lane M = Protein markers. (b) Western blot analysis of purification steps of GroEL detected with GroEL antibody. Lanes i-iii represents 100 μ g protein of samples obtained from the purification steps of protein in reverse order respectively. (c) TEM image of purified GroEL. Blue and red arrows indicate anterior and lateral respectively. Scale bar = 200 nm.

3.3.3 Synthesis and characterization of M-nps

3.3.3.1 Synthesis

A fixed concentration of GroEL was incubated with varying concentration of metal salts to give a theoretical GroEL: metal atom ratios of 1:5-1:2000 in Pt and 1:14- 1:1000 in Au and Ag followed by the reduction of metal ions with NaBH₄. A slow colour change was observed with Pt from colourless/pale orange solution (depending on the concentration of Pt salts in solution) to a brownish solution with increasing colour intensity depending on the amount of Pt metals present in an aqueous solution of GroEL (Fig.3.4 a, inset). On the other hand, the colour change observed in Au and Ag was rather rapid with colour change from yellow to reddish black with Au and colourless to yellow/ orange with Ag (Fig. 3.4 b & c, insets). The colour intensity of M-nps solution also increased with increasing concentration of precursor metal salts in solution in all cases. Aggregation and precipitation, however, was noticed from molar concentration ratio of GroEL: metal above 1:500 in Au and Ag leading to a decrease in colour intensity to a virtually colourless solution of some nanoparticles at these ratios. This was not the case with Pt nanoparticles, however, since during an initial trial synthesis with GroEL: Pt atom ratios of 1:4000 there was a significant loss of Pt nanoparticles (results not shown). Consequently any subsequent synthesis did not exceed a molar ratio of 1:2000. All of these observations implied that GroEL may have reached full saturation at GroEL: metal ratio of 1:2000 (Pt) and 1:200 (Au and Ag). As mentioned in the previous chapter, the colour change was the first indication of nanoparticle formation. Furthermore, the colour observed for nanoparticle synthesis was consistent with that of synthesized M-nps reported in the literature (Gálvez *et al.*, 2008; Fan *et al.*, 2011; Zhang *et al.*, 2007). A different colour was observed with the controls (black) indicating the formation of nanoparticles with a different physical/chemical property. Nanoparticles rapidly aggregated and precipitated, however, suggesting that GroEL may have stabilization properties like most proteins/organic materials used as stabilizers in nanoparticle synthesis.

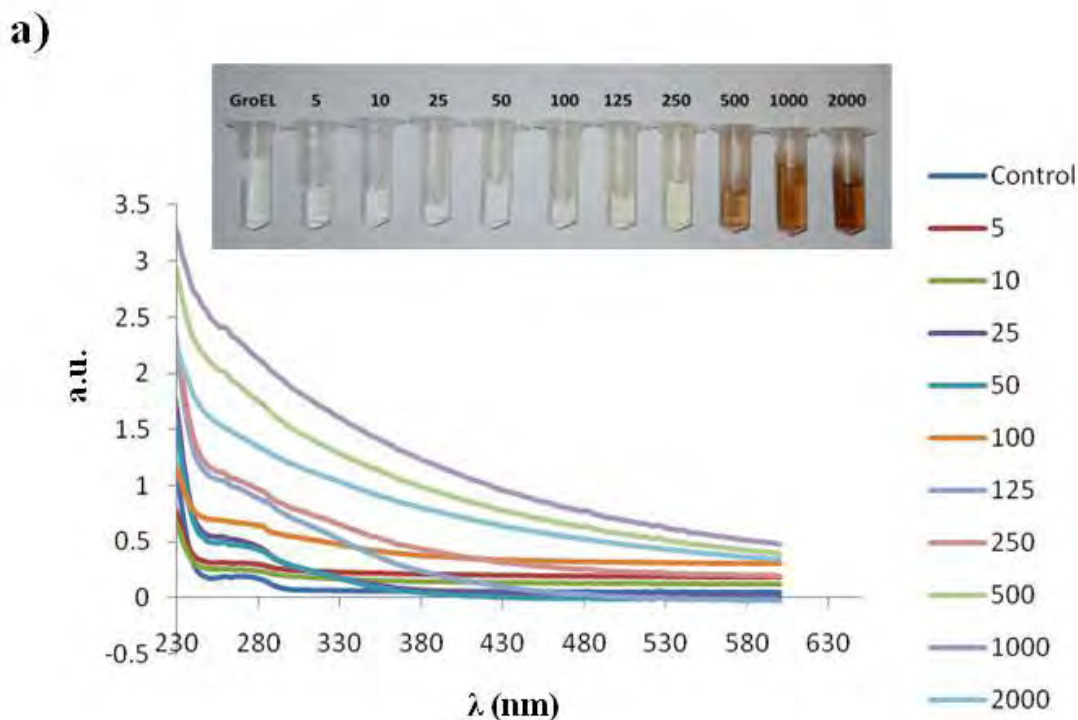
3.3.3.2 Characterization

3.3.3.2.1 UV-visible spectroscopy

The M-nps-GroEL complexes were analyzed by UV-visible spectroscopy with a spectral scan between 200-800 nm; a control sample contained only GroEL. All solutions of M-

nps-GroEL complex showed absorbance peaks identifiable for each M-nps. An additional peak was generally observed at 280 nm in the spectra of all characterized M-nps-HSA (Fig. 3.4) attributed to the protein peak of GroEL (as seen in the spectrum of the control i.e. GroEL). This further proved the attachment of M-nps to GroEL. The broad absorbance spectrum of between 250-350nm in Pt-nps- GroEL was typical of reduced Pt colloids (Fig. 3.4 a, Xie *et al.*, 2005; Fan *et al.*, 2011). The intensity of the absorbance peak increased with an increase in GroEL: Pt molar ratio. This implied an increase in Pt-nps concentration with increasing molar concentration ratios of Pt atoms to GroEL.

Characteristic SPR bands of Au and Ag nps were also noticed at 520 and 400 nm respectively (Zhang *et al.*, 2007; Domínguez-Vera *et al.*, 2007) and there was a shift towards the red region with Ag-nps at molar ratios 1:100 and 1:200 (GroEL:Ag). Any shift in the absorbance spectrum of a nanomaterial to the blue or red region of the electromagnetic spectrum could provide information on the physical property of that particles such as the size, shape, aggregation state and dielectric constant of the surrounding medium (Prathna *et al.*, 2011). A red shift may also denote increased particle size and a possible chance of particle aggregation (Alvarez *et al.*, 1997; Safavi and Zeinali, 2010). This may explain the rapid aggregation seen at molar ratios of above 1:200.



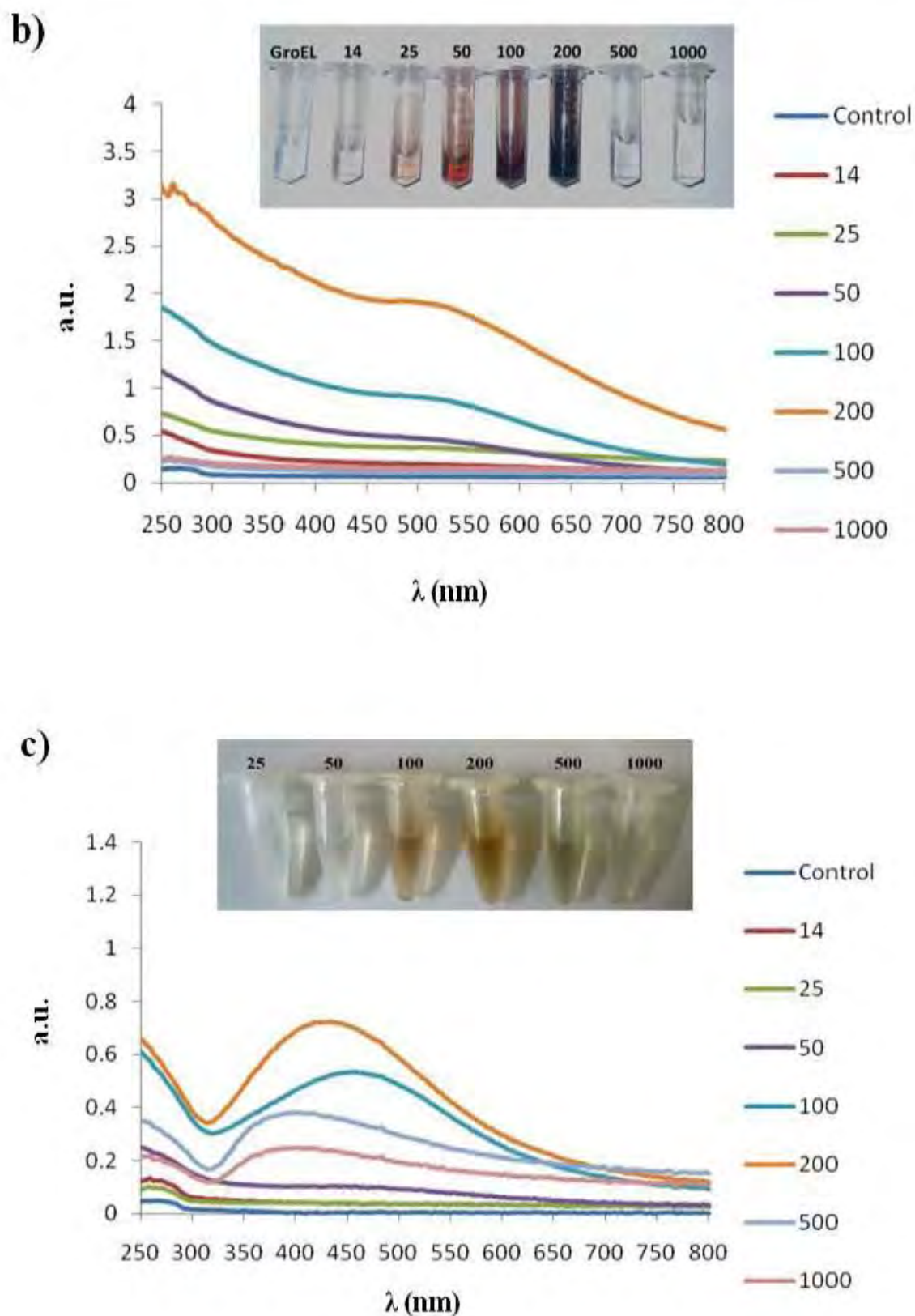


Figure 3.4: UV-visible spectra of M-nps at different molar ratios of metal salts to GroEL. Insets: Observed colour changes in M-nps solution. (a) Pt; (b) Au and (c) Ag.

3.3.3.2.2 TEM, EDX, ICP and FTIR analysis

TEM analysis of M-nps synthesized in the presence or absence of GroEL was carried out in order to determine the morphology and position of nanoparticles around GroEL (Fig. 3.5). Similar studies have reported aggregation of M-nps synthesized without a protein or stabilizer (Deng *et al.*, 2009; Fan *et al.*, 2011). Although in the present study, aggregation had occurred in the absence of GroEL but then, after the subjection of the control to the same purification process as nanoparticles synthesized in the presence of GroEL (as described in 3.2.2, pg. 56), free nanoparticles were seen as revealed by TEM. A study on the synthesis of silver nanoparticles reported that NaBH_4 was able to stabilize nanoparticles, to some degree, at low temperature (Solomon *et al.*, 2007); this may provide an explanation with regards to the presence of nanoparticles in the control that lacked protein. The properties of these nanoparticles, however, were different from those synthesized in GroEL in terms of size and shape as these particles were much larger than those synthesized by GroEL and their shape was far from uniform when compared to the almost spherical nanoparticles observed in Fig.3.5. TEM analysis also further revealed that the size of nanoparticles increased significantly with an increase in the molar concentration of metal salts to GroEL with Pt and Ag nps (although it was very difficult to view Pt:GroEL molar ratios below 1:125). Particle size variation observed with Au-nps was not significant compared to Pt and Ag. Particles with increasing GroEL: Pt and GroEL: Ag molar ratios of 1:125- 1:2000 and 1:14-1:1000 had average particle size diameter of 1.72 - 3.5 nm (Fig. 3.6 a) and 2.45 – 5.50 nm (Fig. 3.6 c) respectively. GroEL:Au, on the hand, with molar ratios of 1:14-1000 only had an average size of 2.80 - 3.26 nm (Fig. 3.6 b). An increase in particle size may have resulted from increased nucleation of M-nps within the cavity of GroEL with increased availability of precursor metal salts in solution. Negative staining with 1 % uranyl acetate revealed that nanoparticles of Pt and Ag were synthesized within the cavity of GroEL (Fig 3.7 a & d). It was difficult, however, to tell the exact position of Au nps (Fig. 3.7 c) due to the inability to view protein cavity of GroEL as can be seen in other metals. Nonetheless, the fact that the average particle size obtained was less than the diameter of the internal cavity of GroEL (4.5 nm) may support the synthesis of M-nps within the cavity of GroEL.

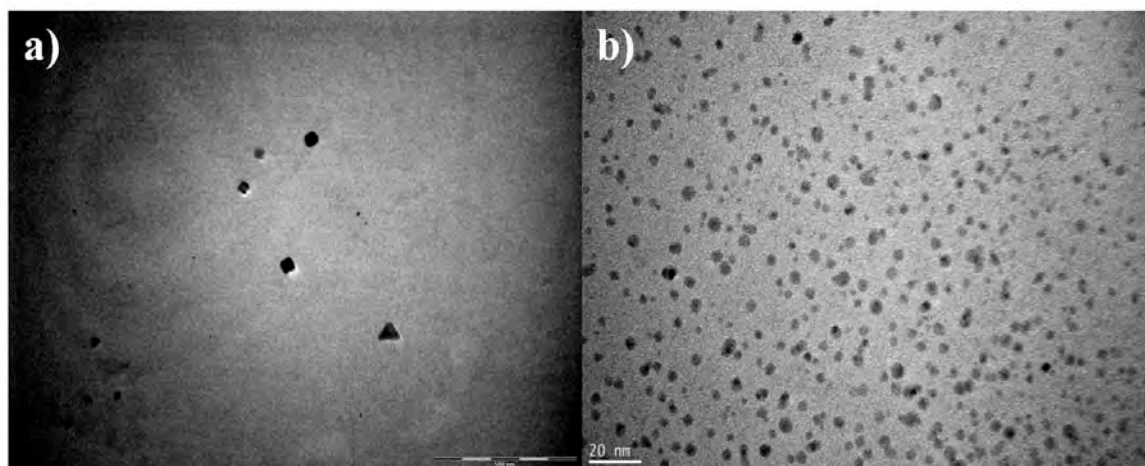
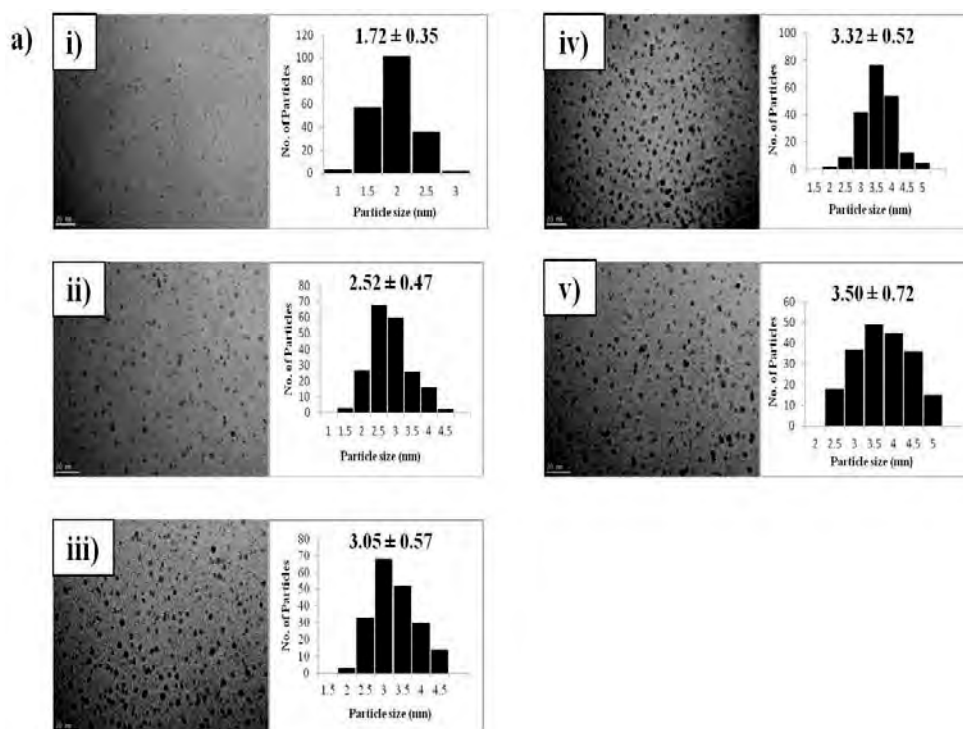


Figure 3.5: Typical M-nps synthesized in the absence (a) and presence (b) of GroEL. Scale bar: a = 500 nm; b = 20 nm.

High resolution TEM (HRTEM) and EDAX confirmed that each sample of metal nanoparticle was indeed crystalline particles of Pt, Au and Ag (Fig. 3.8). The particle atomic spacing measured in each metal (Pt, Au and Ag) was 0.224, 0.242 and 0.236 nm respectively. These values were similar to reported crystal lattice fringes of 0.225, 0.245 and 0.235 nm (Pt, Au and Ag respectively) of these metals (Liu *et al.*, 2011; Zhang *et al.*, 2007; Domínguez-Vera *et al.*, 2007).



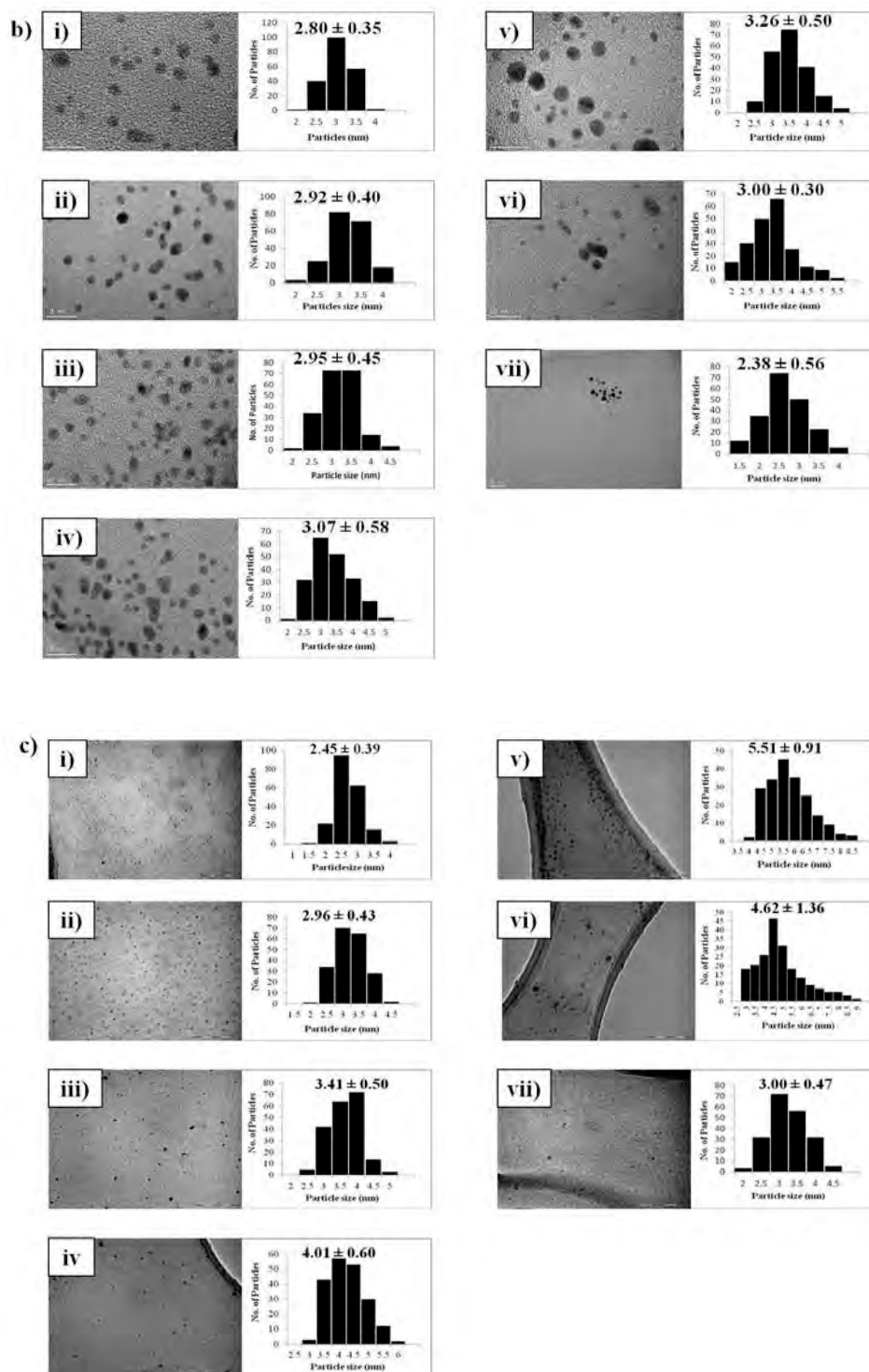


Figure 3.6: TEM micrographs and size distributions of M-nps synthesized by varying molar concentration of metal salts to a fixed concentration of GroEL. (a) Pt: (i) 1:125, (ii) 1:250, (iii) 1:500, (iv) 1:1000 and (v) 1:2000. Lesser molar ratios were not visible. (b) Au; (c) Ag. (i) - (vii) in b & c represents: 1:14, 1:25, 1:50, 1:100, 1:200, 1:500 and 1:1000 respectively. 200 particles were analysed in each set of molar concentration ratios per group. Scale bar: a = 20 nm; b = 10 nm and c = 100 nm.

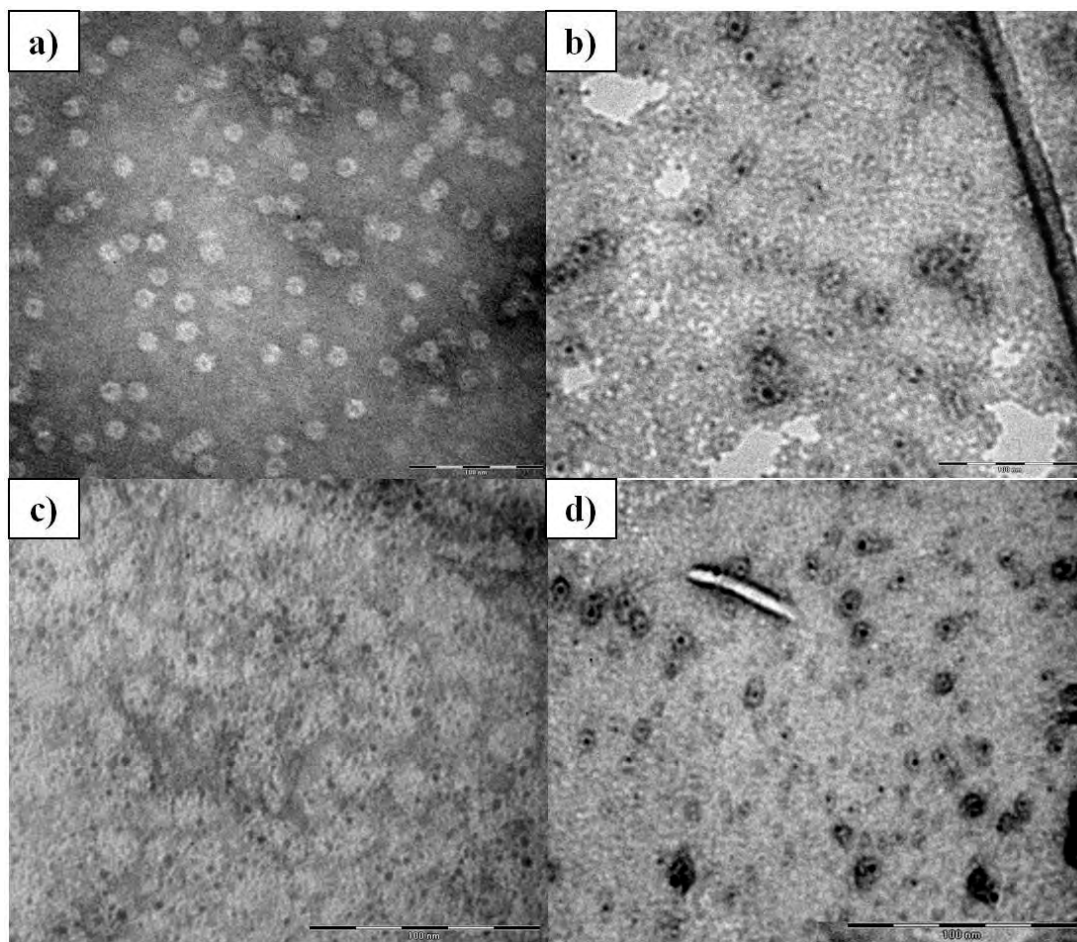


Figure 3.7: TEM micrograph of stained M-nps-GroEL. (a) GroEL only (control); (b) Pt; (c) Au and (d) Ag. Scale bar = 100nm.

Elemental analysis by ICP OES confirmed the presence of these metal atoms in solution. Quantification of metal atoms in each group revealed an increase in the concentration of M-nps with increased molar concentration of precursor metal salts to a fixed concentration of 10 μM of GroEL (Table 3.2). A change in this trend was observed, however, with Au and Ag at molar ratio $> 1:200$ where a decrease in metal atom concentration was noticed, which was due to increased nanoparticle aggregation and precipitation. Results suggested that GroEL may have reached its full saturation at molar ratio of 1:200 (GroEL: Au/Ag). No metal was detected in the control (i.e. GroEL only).

ICP OES analysis also showed that the maximum concentration of metal atoms stabilized by 10 μM of GroEL in Pt, Au and Ag nps solutions was 800, 1372 and 96 μM respectively (Table 3.2, bolded values) after nanoparticle synthesis.

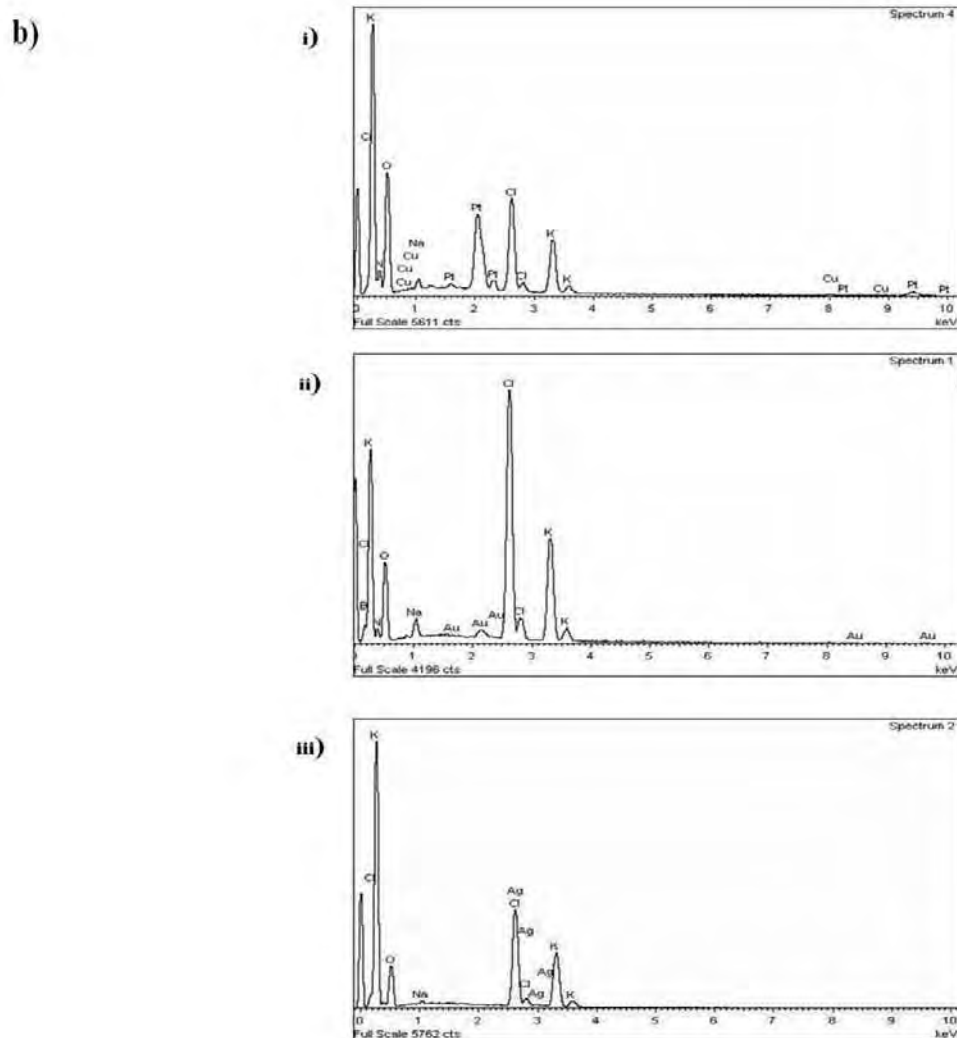
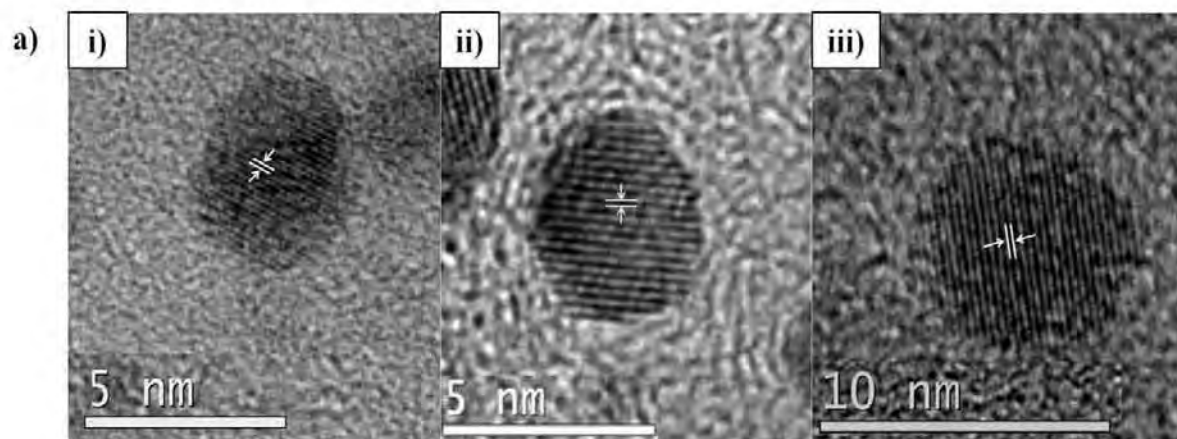


Figure 3.8: HRTEM (a) and EDAX (b) analysis of M-nps crystals synthesized in the presence of GroEL (i) Pt; (ii) Au and (iii) Ag. Calculated crystal atomic spacing for Pt, Au and Ag was 0.224, 0.242 and 0.236 nm respectively.

Table 3.2: ICP OES results of M-nps-GroEL.

\ddagger M:GroEL	[GroEL] (μ M)	\wedge [M]* (μ M)	\ddagger M:GroEL*
<i>Pt</i>			
Control	10	-	-
5	10	38.9	3.9
10	10	61.5	6.2
25	10	74.2	7.4
50	10	124.1	12.4
100	10	145.9	14.6
125	10	209.5	21.0
250	10	202.2	20.2
500	10	487.0	48.7
1000	10	672.0	67.2
2000	10	800.3	80.0
<i>Au</i>			
Control	10	-	-
14	10	94.5	9.4
25	10	160.2	16.0
50	10	399.3	39.9
100	10	723.4	72.3
200	10	1372.4	137.2
500	10	100.5	10.1
1000	10	48.2	4.8
<i>Ag</i>			
Control	10	-	-
14	10	10.0	1.0
25	10	16.0	1.6
50	10	12.7	1.3
100	10	19.3	1.9
200	10	96.2	9.6
500	10	28.8	2.9
1000	10	8.0	0.8

\ddagger = theoretical molar ratio of metal atoms to GroEL; \wedge = Estimated metal atom concentration by ICP OES after synthesis; \ddagger = Calculated molar ratio of metal atoms to GroEL. Bolded values in each group are the highest concentration of metal nps stabilized by 10 μ M of GroEL. Values in red represent the highest number of metal atoms stabilized per GroEL. * Values represents the mean of three separate reading with standard deviations <10%.

Calculating the observed stoichiometry of metal atoms per GroEL after synthesis showed Au atoms to be the highest metal atom stabilized by GroEL with 137 Au atoms. Platinum nanoparticles had the next highest value of 80 Pt atoms; the least was Ag with only ~ 10 Ag atoms. Stoichiometry was determined based on the starting protein concentration of GroEL (10 μ M, as estimated by the method of Bradford).

FTIR analysis on GroEL and M-nps-GroEL having the highest concentration of nanoparticles in each group, revealed no significant effect on the structure of GroEL as can be seen from the similarity in the FTIR absorbance spectra of all three M-nps attached to GroEL compared with the control (i.e. GroEL alone, Fig. 3.9). Characteristic amide I (1640-1655 cm^{-1}), amide II (1550 cm^{-1}) of proteins and peptides was evident in the spectra of GroEL and M-nps-GroEL (Haris and Severcan, 1999). Furthermore, the appearance of peaks in regions 1722-1734 cm^{-1} of the FTIR spectra of both control and all M-nps-GroEL suggested stretching vibration of terminal carboxylic acid groups of GroEL protein in aqueous solution (Jabs, 2005).

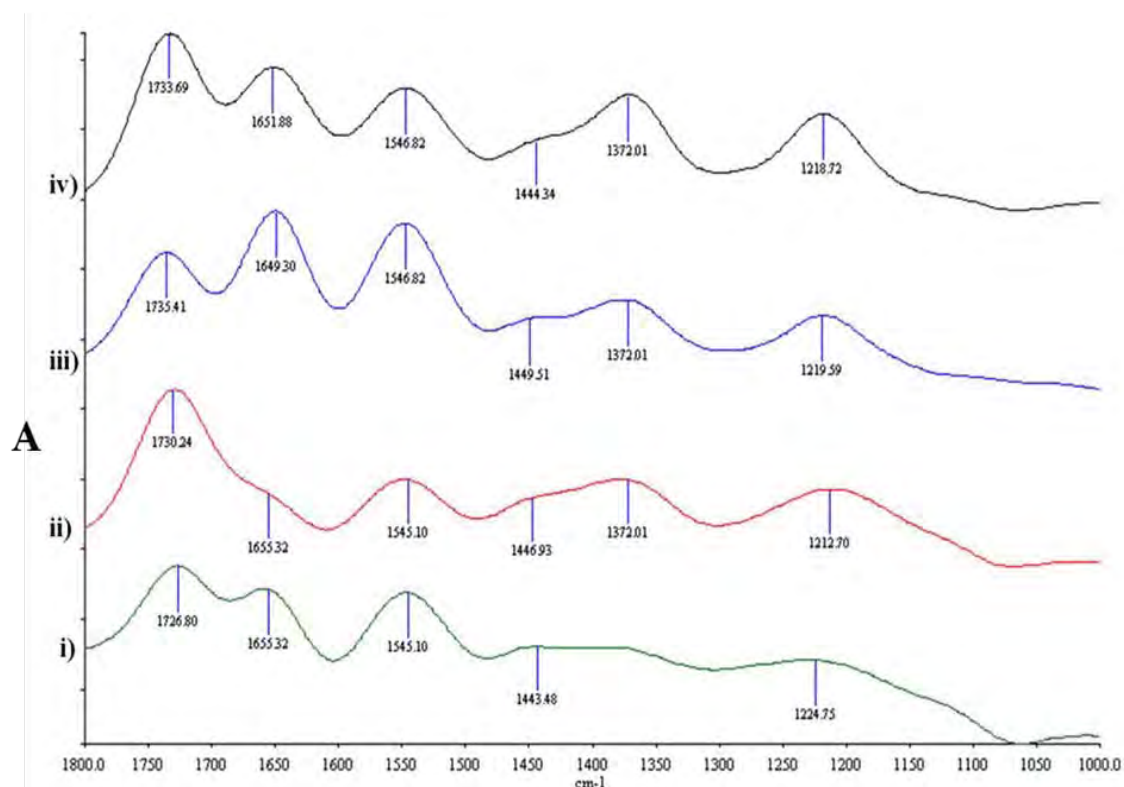


Figure 3.9: FTIR spectra of M-nps-GroEL. (i) GroEL only (control); (ii) Pt (1:2000); (iii) Au (1:200) and (iv) Ag (1:200).

In the FTIR spectrum of Pt-nps-GroEL, a flattened peak was noticed at region 1655 cm^{-1} which was not seen in the spectra of others. This type of peak in infra-red spectra of proteins implied an overlap of structural components of protein such as increased vibrational motion of α -helices (that predominately defined the structure of GroEL) at this region (Arrondo and Goni, 1993; Haris and Severcan, 1999). In addition, the observed broadening in Pt-nps-GroEL, which was not observed in other M-nps-GroEL, may be due to a variation in the strength of hydrogen bonds of these metals to the hydrogen of protein amide bonds which is suspected to be responsible for the coordination of nanoparticles. This hydrogen-bonding may have been more pronounced with Pt due to the ability that it would have in forming oxides and hydroxides.

3.3.4 Effect of M- nps on the ATPase activity of GroEL

The effect of M-nps on the ATPase activity of GroEL was investigated by the method described in 3.2.4 (pg. 57) with ATP as the substrate. Activity of the control (i.e. GroEL only) was assayed together with the experimental samples (M-nps-GroEL). Activity was expressed as $\mu\text{molPi released.ml}^{-1}.\text{min}^{-1}$.

Results showed an increase in ATPase activity with reduced molar concentration of GroEL: metal salts with Pt and Au-nps-GroEL (Fig.3.10 a & b). No significant increase was observed, however, with the ATPase activity involving Ag-nps (Fig. 3.10 c). The highest activity increase of about 85 % was seen at molar ratio of 1:25 (GroEL: Pt, Fig. 3.10 a). A lesser influence was noted either side of this ratio with 1:50 ratio offering a 50 % increase in activity, both the 1:10 and 1:250 ratio indicating a 37 % increase and only about 8 % increase being realised at a ratio of 1:500. A 47 % increase was observed as the highest ATPase activity increase with Au at molar ratios of 1:50 and 1:100 (GroEL: Au); this was followed by only 15 % at ratio 1:200. There was no observed activity increase in Ag-nps-GroEL at all molar concentrations used in this study. Rather, a decrease in activity was observed at higher molar ratios of GroEL:Ag (i.e. $> 1:50$, Fig. 3.10 c), suggesting an inhibition of the ATPase activity of GroEL at these ratios.

Noble metal nanoparticles especially those of platinum are increasingly reported in the literature for their outstanding catalytic properties (Wang *et al.*, 2009; San *et al.*, 2011). More so, platinum as a metal is a widely used catalyst and since they exhibit increased

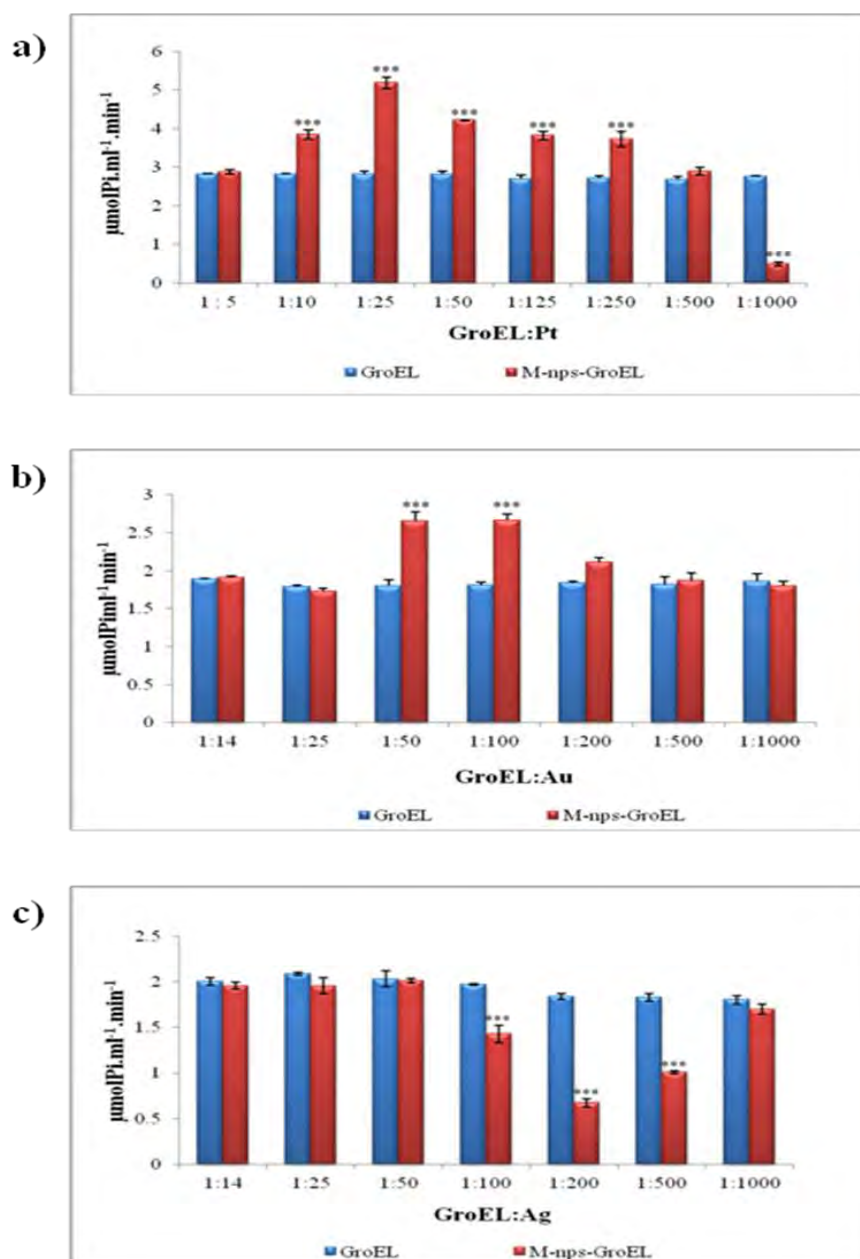


Figure 3.10: Effects of M-nps on the ATPase activity of GroEL. (a) Pt; (b) Au and (c) Ag. Significant ATPase activity ($p < 0.001$) increase of 5.20 and 2.60 $\mu\text{molPi.ml}^{-1}.\text{min}^{-1}$ was seen at molar ratios of 1:25 and 1:50 – 1:100 with Pt and Au-nps respectively. An inhibitory effect was seen with Ag-nps. *** = $p < 0.001$ versus the controls (i.e. GroEL). Error bars represents the standard error of means of three independent assays.

catalysis with increased surface area; it was not surprising that Pt at the nanoscale level showed enhanced activity of the ATPase activity of GroEL. An increased ATPase activity

observed at certain GroEL: Pt molar ratios (particularly the smaller ratios), however, may be as a result of particle size, as seen in TEM analysis (Fig. 3.6 a). The size of platinum nanoparticles was increased with increasing concentration of Pt ions in solution which supported the observations at these ratios.

.Similarly, as observed in this experiment platinum nanoparticless acted as an inhibitor of ATPase activity of GroEL at high molar ratios (>1:1000, GroEL:Pt), in fact no activity was observed at ratios above the molar ratios of 1:1000. This suggested that the effects of platinum on ATPase activity of GroEL may be size and concentration dependent judging by the fact that at lower concentrations, platinum nanoparticles acted as an activator while at higher concentrations, they were inhibitory. Furthermore, since larger nanoparticles were formed with an increase in the platinum nanoparticle precursor, the increase in nucleation during synthesis may have interfered with vital amino acid residues important for ATPase activity, since we suspected, based on the data presented, that nanoparticles were synthesized within the cavity of GroEL. In addition, an earlier study had reported an increased ATPase activity of GroEL at high temperatures by divalent cations that stabilized its structure (Melkani *et al.*, 2003). This may explain, further, why a greater enhancement of ATPase activity of GroEL of almost 2-fold (85 %), was observed with Pt compared to that observed with Au since a divalent metal salt of Pt was used in this study to generate Pt nanoparticles. Although GroEL incubation with Pt metal salts alone did not give a conclusive result in this present study (results not shown). More so, all ATPase assay experiments conducted in this present study were at physiological temperature (37° C) compared to 49° C reported (Melkani *et al.*, 2003).

On the other hand, gold metals in their bulk state do not possess any catalytic properties whatsoever. Thus, the activity increase in the ATPase activity of Au-nps-GroEL further corroborates the increased focus on the mechanism of action of gold nanoparticles as both homogenous and heterogeneous catalysts (Cortie and van der Lingen, 2002; Hashim, 2005; Thompson, 2007; Campbell *et al.*, 2011). Activity increase was observed to the same degree at molar ratios of 1:50 and 1:100. This may be explained by the insignificant change in the sizes of nanoparticles at these ratios and all ratios used in this study with the exception of molar ratio of 1:1000 (Fig. 3.6 b and Fig. 3.9 b). A decrease in catalysis, however, was observed at molar ratios > 1:200 which may imply that enhanced activity of

ATPase activity was more concentration related than size. The highest concentration of Au-nps was at molar ratio of 1:200 and the least concentrations at 1:14, 1:25, 1:500 and 1:1000 based on quantification by ICP OES (Table 3.2). A high concentration of Au-nps at ratio of 1:200 (GroEL: Au) may have caused a decrease due to an excess of what was required for the enhancement of ATPase activity of GroEL and hence a decrease in catalytic activity was observed at a molar ratio of 1:200. Further, there was no meaningful effect on the ATPase activity of GroEL at molar ratios of 1:14, 1:25, 1:500 and 1:1000 (Fig. 3.10 b). This may be as a result of a low concentration of Au-nps in solution to bring an increase in the ATPase activity of GroEL.

Finally, the ATPase activity of GroEL was not enhanced by Ag-nps but was rather inhibited. The highest inhibition of 64 % was at molar concentration ratio of 1:200 (GroEL to Ag), followed by a 45 % inhibition at ratio 1:500 and 28 % at ratio 1:100 (Fig. 3.9 c). Nanoparticles of silver are well known for their optical and antimicrobial properties (Liz-Marzán, 2004; Jain and Pradeep, 2005) and it was only recently that their catalytic properties had been reported (Zhou *et al.*, 2008; Li, 2011). It was quite unexpected that Ag-nps did not increase the ATPase activity of GroEL. Most catalytic properties of silver nanoparticles reported in the literature are usually of particle sizes between 20-80 nm. More so, the catalytic properties were established based on a non-biochemical reaction. Another study had reported an inhibitory effect of silver nanoparticles of 1 – 10 nm with proteins/enzymes in viruses and bacteria; this forms the basis for their antimicrobial properties (Elechiguerra *et al.*, 2005). In our opinion this may explain the inhibition pattern in this study since the average of size Ag-nps synthesized in this study was between 2 - 6 nm and the reaction tested were biochemically related.

In addition, the inhibition may be size and concentration dependent owing to the fact that the highest inhibition was at a molar ratio of 1:200 (GroEL: Ag) which had the highest concentration of silver nanoparticles (as judged by ICP OES, Table 3.2) and also the largest particle size as analyzed by TEM/HRTEM (5.50 nm, Fig. 3.6 c, pg. 66). Lesser inhibitions were observed at molar ratio 1:500, having the second highest and largest particle concentration and size respectively. This was followed by molar ratio of 1:100 (Fig. 3.6 c, Table 3.2). No significant effect was observed on the ATPase activity of GroEL

at lower molar concentration ratios < 1:100 and at 1:1000 at which smaller sized nanoparticles and lower particle concentration was observed.

3.4 Conclusions

In this study, a simple, cheap and eco-friendly biological method of metallic nanoparticles was described. Nanoparticles of Pt, Au and Ag were synthesized within the cavity of GroEL, a barrel-like shaped protein unlike the cage-like protein used in the previous chapter.

Synthesis of nanoparticles did not affect the structural integrity of the GroEL and the size of nanoparticles varied considerably with changes in molar concentration ratios of metal salt precursor to a fixed molar concentration of GroEL to Pt and Ag nanoparticles.

Biological synthesis of Pt and Au nanoparticles exhibited a catalytic effect on the ATPase activity of GroEL at physiological temperature. Catalytic enhancement was found to be size and concentration dependent with Pt and only concentration dependent in the case of Au. An opposite effect was observed with Ag-nps.

The enhancement of the ATPase activity of GroEL by nanoparticles of Pt and Au might boost the efficiency of GroEL as a molecular chaperone in mediating the proper folding and release of polypeptides or active proteins, since the hydrolysis of ATP is very critical in the release of properly folded proteins. Similar studies have shown an increased ATPase activity of GroEL at elevated temperatures (Mendoza *et al.*, 1996; Melkani *et al.*, 2003); this present study presents a comparable ATPase enhancement at physiological temperature.

Finally, the catalytic effect of nanoparticles of Pt and Au on the ATPase activity of GroEL may have futuristic application in the treatment or management of diseases associated with poor protein folding in the biological system.

Chapter 4: Biosynthesis of metallic nanoparticles with ribonuclease

4.1 Introduction

Ribonucleases (RNases) catalyses the hydrolytic cleavage of ribonucleic acid (RNA) molecules and are implicated in many biological functions like angiogenic, antitumor or antibiotic activities (Cho and Zhang, 2007; Benito *et al.*, 2005; Monti *et al.*, 2009). The cleavage of RNA by RNase usually occurs at the phosphodiester bond between the 5'-ribose of a ribonucleotide and the phosphate group attached to the 3'-ribose of an adjacent pyrimidine nucleotide (Fig. 4.1 a). This cleavage forms a 2'-3'-cyclic phosphate (Fig. 4.1 b), which is then hydrolyzed to the corresponding 3'-nucleotide (Worthington, 2011).

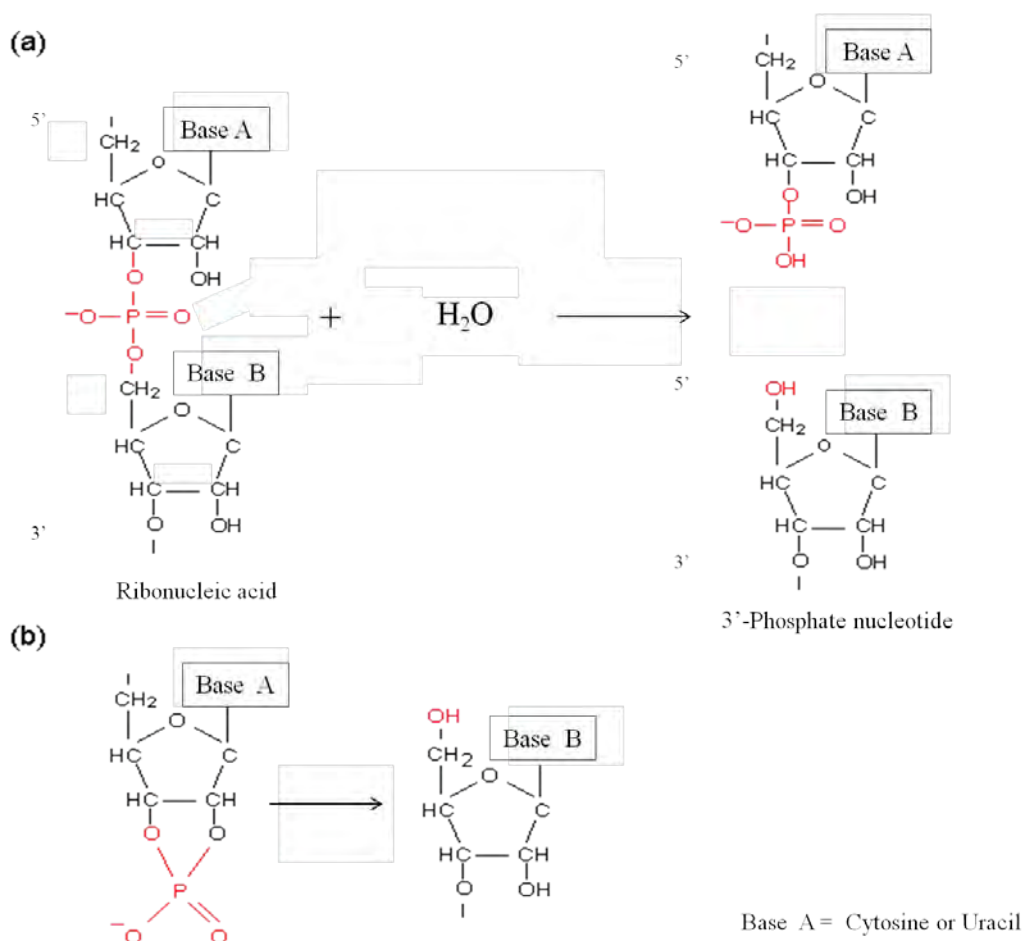


Figure 4.1: Enzymatic (hydrolysis) reaction catalyzed by RNase (a). The transition state products of the hydrolysis reaction (b), (Adapted from Worthington, 2011).

RNase is found in abundance in the pancreas of ruminant animals, where its endoribonucleolytic activity is notably high, perhaps, as a result of large amount of RNA produced by stomach microorganisms and also for the processing of nutrients from cellulose (Barnard, 1969; Raines, 1998). This high level of activity has made pancreatic Ribonuclease A (RNase A, EC 3.1.27.5) from bovine, the most studied enzyme of the 20th century. The “A” refers to the predominant form of the enzyme in the pancreas of *Bos taurus* while RNase B is the glycosylated form of RNase A that contains a single polysaccharide moiety attached through *N*-acetylgalactosamine to the nitrogen of asparagine 34 of the amino acid sequence of RNase (Arnold and Ulbrich-Hofmann, 1997; Raines, 1998). This added sugar chain is believed, not to only act as an aid in the proper folding of RNase B, but also for cellular signalling. Other than the polysaccharide attachment, RNase B is structurally the same as RNase A, however, this attachment allows for additional catalytic activity and kinetic stability. RNase C and RNase D forms are the least abundant in the bovine pancreas and are more heterogeneous in their glycosylation.

RNase A/B are relatively small (molecular weight = 13.7/15.5 KDa; 124 amino acids), kidney-shaped enzymes with their active sites in a cleft (Joao and Dwek, 1993; Raines, 1998), having all 20 natural amino acids residues except tryptophan (Raines, 1998). The secondary structure is made up of four-stranded anti-parallel beta-sheets flanked by two short alpha-helices (Fig. 4.2). The active site is defined by a third N-terminal alpha-helix and one-edge of the beta-sheet. The structure of RNase is stabilized by four disulfide bonds, two of which contribute to its thermal stability (Klink *et al.*, 2000).

Current research on RNase has focused on the synthesis and maturation of this enzyme in the endoplasmic reticulum of cells (Geiger *et al.*, 2011). Further, studies into the folding and aggregation of RNase and their role in gene regulation and cancer development are also been studied with promising chemotherapeutic agents being developed (Shlyakhovenko, 2009; Benito *et al.*, 2005; Arai *et al.*, 2010 and Scheraga, 2011).

The objectives of this chapter are to:

- i. Biologically synthesize metallic nanoparticles of Pt, Au and Ag with RNase (a non-caged protein).

- ii. Characterise these nanoparticles using various techniques.
- iii. Determine the biological effect of these nanoparticles on the enzymatic function (hydrolytic activity) of RNase.

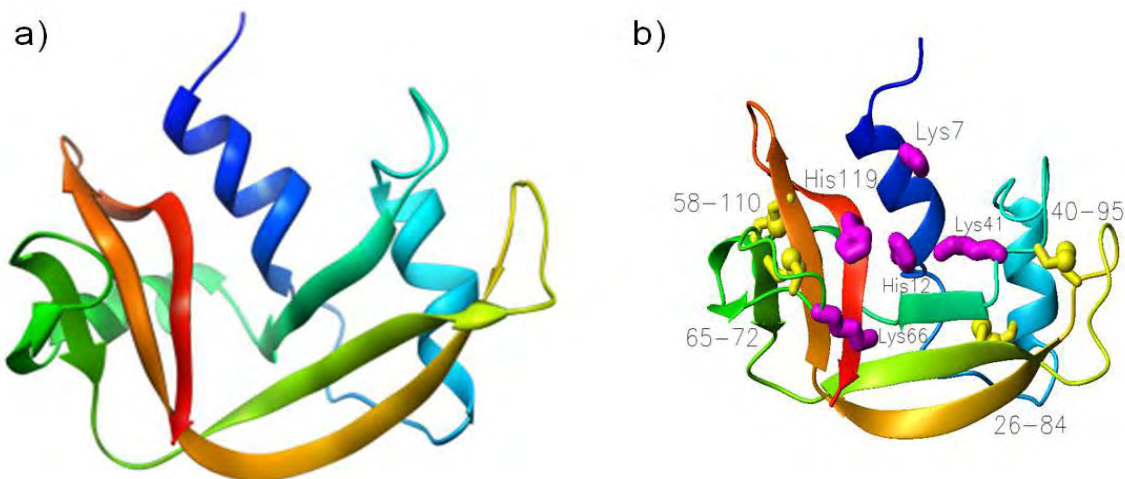


Figure 4.2: Ribbon diagram of the three dimensional structure of pancreatic RNase A from Bovine. (a) Unlabelled; (b) Labelled. The inscriptions (i.e. coloured in yellow) indicates the location of the eight cysteine residues that forms the four disulfide bonds, the three amino acids residues crucial for catalysis: His 12, His 119 and Lys 41, and residues that stabilizes the intermediate product during catalysis: Lys 7 and Lys 66 (Adapted from Wikipedia, 2011; Raines, 1998).

4.2 Materials and Methods

4.2.1 Materials

RNase B (bovine pancreas), yeast RNA, potassium chloroplatinate (II) (K_2PtCl_4), gold (III) chloride ($AuCl_3$) and silver nitrate ($AgNO_3$) were obtained from Sigma-Aldrich (South Africa). Sodium borohydride ($NaBH_4$) was purchased from Merck (South Africa). RNase B was used without further purification. All other reagents were of analytical grade. All reagents and buffers were prepared using RNase-free (i.e. autoclaved water).

4.2.2 Methods

4.2.2.1 Synthesis

RNase B (10 μ M, 450 μ l) was incubated (1h, 4 $^{\circ}$ C) with metal salts of Pt, Au and Ag in phosphate buffer (pH 7.5, 0.2 M) to give a theoretical RNase to metal molar ratio of 1:125-1:2000 in Pt and 1:12.5-1:2000 in Au and Ag. The metal salts in the solution were reduced

with NaBH₄ (5-fold metal salt concentration for Pt and 2-fold in the case of Au and Ag). The synthesis of Pt-nps in the presence of RNase was allowed to proceed for 5 h at 4 °C while that of Au and Ag was kept for 1 h at the same temperature under constant stirring. Solutions of the nanoparticles were then dialyzed against deionised water at 4°C using snake skin dialysis tubing 10K MWCO (Thermo scientific). Dialysis was carried out for 12 h with a change in dialysate every 4 h. This was followed by centrifugation (5000 rpm, 2 min) and then filtered through a 0.22 µm filter. Samples were stored at 4 °C for future characterization. A control solution with an equal concentration of RNase without metal salts was treated in the same manner as the experimental samples.

4.2.2.2 Characterization

Characterization of M-nps-RNase was carried out as described in 2.2.2.2 (pg. 32).

4.2.2.3 RNase assay

The hydrolytic activity of RNase B was determined by a modified method of Kalnitsky *et al.*, 1959. The rate of hydrolysis of yeast RNA at pH 5.0 was determined by measuring the amount of acid soluble oligonucleotide released. One unit of RNase at 37 °C causes an absorbance increase of 1.0 at 260 nm and pH 5.0.

Briefly, RNase (4 µg of protein, 100 µl) in sodium acetate buffer (0.1 M, pH 5.0) was incubated (5 min, 37 °C) for and the reaction started with 1 % RNA (100 µl). The reaction was allowed to proceed for exactly 4 min and was stopped by the addition of acetate-perchloric acid solution (0.75% and 25 % respectively, 100 ml, Appendix H). This was cooled on ice (5 min) and the resulting suspension was clarified by centrifugation (10 000 rpm, 1 min). The clear supernatant (10 µl) was diluted with 290 µl of RNase-free water and absorbance was read at 260 nm. A control with no RNase was used as the blank. Activity of RNase was expressed as Units.mg of protein⁻¹ (Appendix H).

4.2.2.4 Effect of synthesized nanoparticles on RNase activity

M-nps-RNase (4 µg of protein, based on quantification by BCA) sodium acetate buffer (pH 5.0, 0.1 M) was incubated with 1 % RNA (100 µl) and an assay was carried out as described in 4.2.2.3. An equal concentration of RNase without nanoparticles was used as the control.

4.2.2.5 Protein determination

The protein content of RNase, before and after synthesis, was estimated in triplicate using the bicinchoninic acid (BCA) method (Smith, 1985). Protein samples (25 μ l) were each placed in a 96-well microtiter plate followed by the addition of 200 μ l of BCA working reagent (Sigma-Aldrich, Appendix H). The mixture was incubated (37 °C, 30 min), the absorbance of the solution measured at 562 nm and the concentration of the unknown samples was determined using a BSA standard curve (Appendix H).

4.3 Results and Discussion

4.3.1 Synthesis

RNase was incubated with metal salts of Pt, Au and Ag, and subsequent reduction of metals salts in the incubated mixtures resulted in the production of Pt, Au and Ag nanoparticles respectively. This was evident by the colour change as observed in previous experiments (Figs. 2.2, pg. 35 and 3.4, pg. 63). Furthermore, a fixed concentration of RNase incubated with different metal salt concentrations of Pt, Au and Ag as described in 4.2.2.1 yielded nanoparticle solutions with varying colour intensities. Observed colours were consistent with what was obtained from previous experiments (chapters 2 and 3) and in the literature in Pt (brownish black), Au (reddish brown) and Ag (yellow/orange) nanoparticles solutions (Fig. 4.3 a-c, Gálvez *et al.*, 2008; Fan *et al.*, 2011; Zhang *et al.*, 2007). Colour intensity also increased with an increase in concentration of precursor metal salts at varying molar concentration ratios of metal salts to RNase, except with Au and Ag at molar ratios $> 50:1$ (metal:RNase), where a less intense colour was noticed (Fig. 4.3 b & c). This was due to poor stabilization of Au and Ag nanoparticles at those concentrations. In addition, an overall observation in the colour intensity of nanoparticle across all metal groups showed that Ag- nps were least stabilized by RNase, followed by Au-nps particles with Pt being the greatest stabilized (Fig. 4.3 a-c).

Furthermore, a different molar concentration range of RNase to metal (1:12.5 -1:200) was used in the synthesis of Au and Ag nanoparticles when compared to that of Pt (1:125-1:2000) due to very little or no stabilization of nanoparticles at a molar concentration range used in synthesizing platinum nanoparticles.

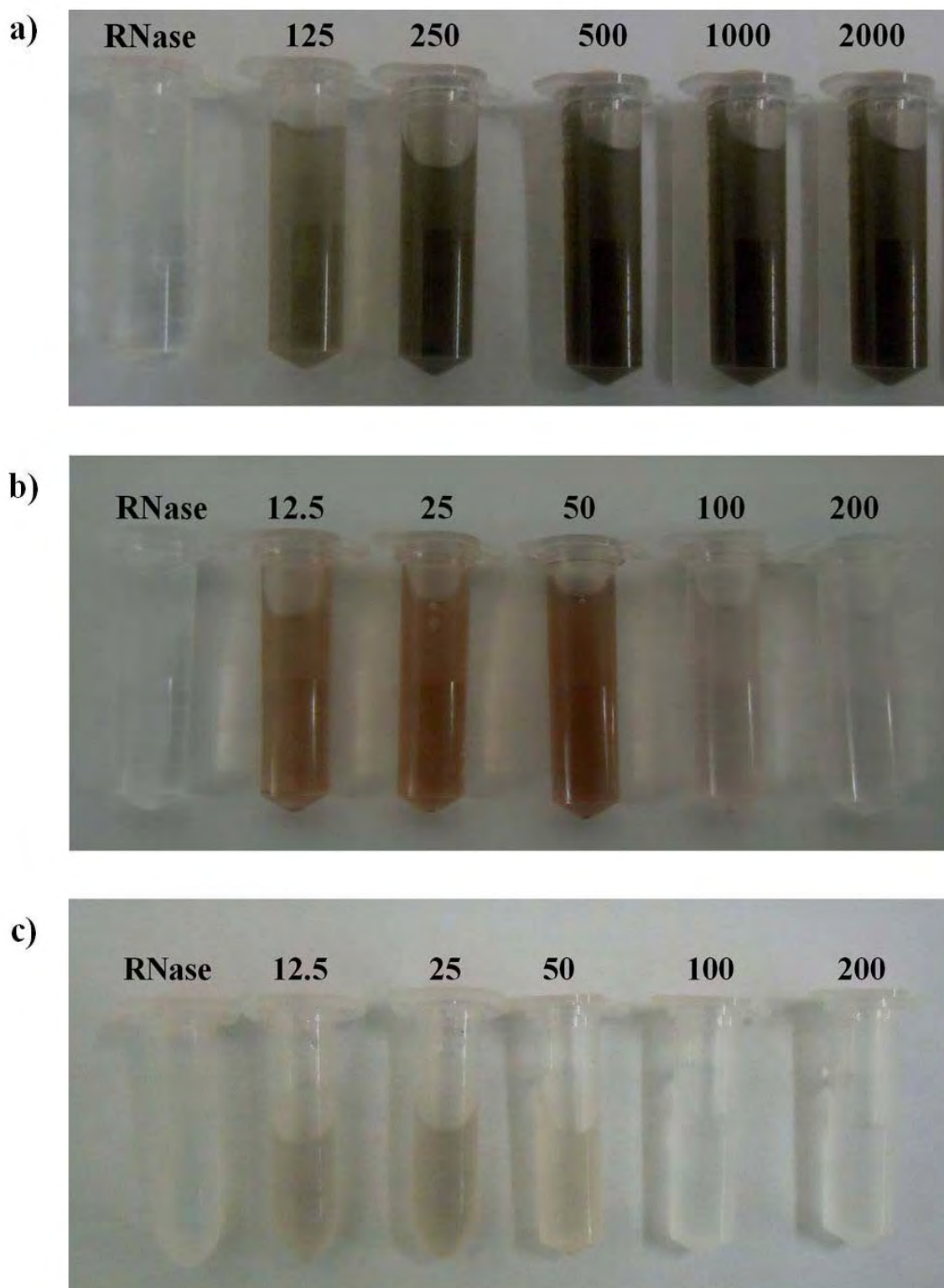


Figure 4.3: Metallic nanoparticles of (a) Pt, (b) Au and (c) Ag synthesized with different molar concentration of metal salts to a fixed molar concentration of RNase. 125-2000 in (a) represents molar concentration ratios of Pt salts to fixed molar concentration of RNase. 12.5-200 in (b) & (c) represents that of Au and Ag metal salts respectively.

4.3.2 Characterization

4.3.2.1 UV-Vis spectroscopy

Optical characterization of nanoparticles by UV-Visible spectroscopy revealed surface plasmon resonance (SPR) bands related to Pt, Au and Ag nanoparticles. In Pt nps, a slightly broad peak was observed between 250 - 300 nm which is indicative of spherical Pt colloids (Fig 4.4 a, Fan *et al.*, 2011). The broadening of SPR peaks also increased with increasing molar concentration of Pt:RNase except at molar ratio of 1:500 where a decrease in the SPR band appeared beneath that of 1:250 (Fig.4.4). This may be indicative of the formation of nanoparticles with a slightly smaller size than what was seen in the 1:250 ratio. Absorbance peaks around 280 nm were due to the presence of the protein RNase in Pt-nps solution.

Au-nps showed typical SPR peaks of nanoparticles, less than 20 nm in size, at 528 nm (Zhang *et al.*, 2007; Fan *et al.*, 2010). Protein peaks at 280 nm were due to RNase attachment to Au-nps, however, absorbance peaks at molar ratios of 100 and 200 appeared broad and the SPR peak of Au-nps observed at lower molar ratios had disappeared. This may indicate very little or no protein and Au-nps in solution at these lower ratios. Lower protein or nanoparticles concentration was due to precipitation of a large amount of Au-nps at these molar ratios. In addition, studies have shown that as colloids of Au-nps become larger and aggregate, the frequency of the SPR band decreases and shifts to a longer wavelength (i.e. a red shift). This was because the extinction of light by larger particles (> 10 nm) of Au was primarily due to light scattering instead of absorbance as observed with smaller particles of < 10 nm (El-Sayed and Link, 2000). Precipitation of nanoparticles may also have lead to the precipitation/degradation of protein out of solution which, after the subsequent purification steps carried out after synthesis, must have been removed.

With respect to the SPR peaks of Ag-nps synthesized by RNase (Fig. 4.4 c), a very broad and low absorbance peak that stretched from 380-530 nm was noticed with an upper limit of the peaks to be around 480 nm. This wavelength was much higher when compared to an expected wavelength of 400 nm due to aggregations of colloidal metal particles of Ag that had been reported to lower plasmon frequencies and shift absorbance to longer wavelengths (Moore and Goettmann, 2006; Solomon *et al.*, 2007; Li *et al.*, 2011) This may explain the lower SPR band and the shift towards the red region seen in Ag-nps

synthesized with RNase. Moreover, from the results obtained in Fig. 4.3 c and explained in 4.3.1, it was quite visible that very little Ag-nps was stabilized at all molar concentration ratios used in this study.

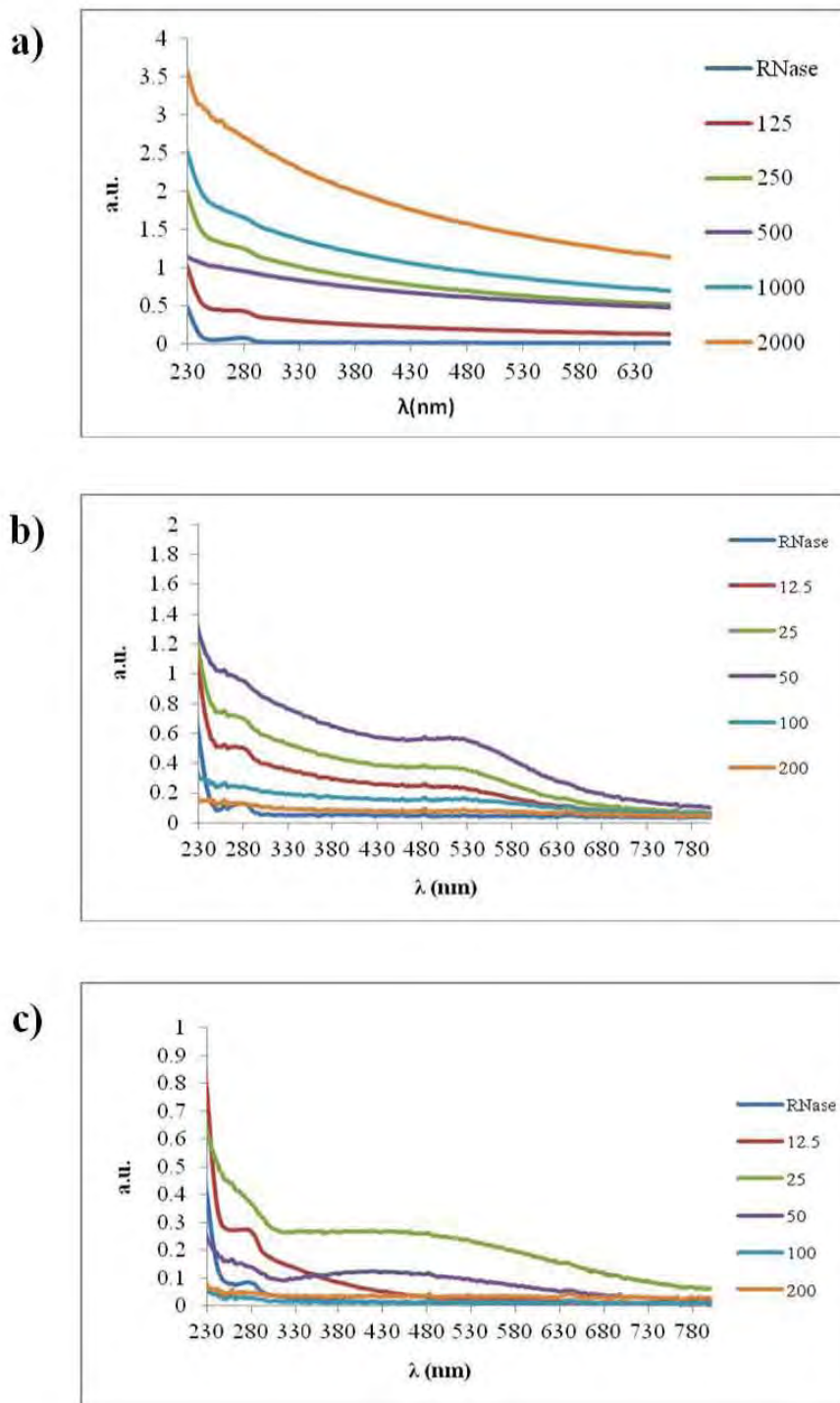


Figure 4.4: UV-Visible characterization spectra of M-nps synthesized with RNase. (a) Pt; (b) Au and (c) Ag.

4.3.2.2 Inductively coupled plasma optical emission spectroscopy (ICP OES)

Metal atom quantification by ICP OES of M-nps synthesized by RNase confirmed the presence of Pt, Au and Ag nps in the respective samples. No metals or nanoparticles were detected in their respective controls. Similar to what was observed previously (chapter 2&3), the results showed a general increase in the concentrations of nanoparticles in each sample with increasing concentration of starting metal salts. At a ratio of > 50:1 (metal:RNase) in Au and Ag nanoparticles, however, a decrease in concentration was observed as a result of rapid particle aggregation. This was consistent with what was observed in 4.3.1 (Fig.4.3 b & c). Results revealed further that the metal atom stabilized the most by RNase was Pt, followed by Au then Ag (Table 4.1).

Analysis by ICP OES and protein quantification of RNase before and after nanoparticle synthesis showed Pt-nps to have the highest metal atom to protein stability after synthesis. Platinum to RNase ratio (i.e. Pt:RNase) of 72 and 127 based on protein concentration before and after synthesis respectively was recorded as the highest ratio (Table 4.1). This was achieved at a theoretical molar ratio of Pt:RNase of 2000:1. With Au-nps, the highest ratio, based on protein quantification before and after synthesis, was 23 and 30 respectively at Au:RNase of 50:1 while with Ag, the highest ratio was 7 and 11 at 25:1.

Protein quantification in this present study was by the BCA method (Table 4.1) due to poor detection and lack of reproducibility of results by the Bradford method. An earlier study had reported variable response of Bradford reagent in the detection of some proteins and RNase was one of them (Marshall and Williams, 1986). Although that study had suggested the inclusion of 0.5 % phenol with the Bradford's reagent to improve sensitivity, this still failed to produce favourable results.

Protein quantification of RNase after synthesis at certain molar concentration ratios of metal atoms to RNase showed more protein content relative to the control (Table 4.1[‡]). This was unexpected, though literature revealed that metal ions (especially divalent cations) were able to structurally enhance and stabilize, and in some cases, improve catalysis of most RNases (Goedken and Marqusee, 1999; Hsieh *et al.*, 2010). This may explain the higher protein concentration observed in M-nps-RNase at certain molar ratios compared to their controls. Conversely, lower protein concentration of RNase observed at

molar ratios 1:2000 and 1:100 -1:200 (RNase:metals) in Pt and Au/Ag respectively, may be due to the formation of larger sized particles or aggregated particles in an aqueous solution of RNase (Shang *et al.*, 2007; Fei and Perret, 2009) and hence a reverse effect on RNase stability.

Table 4.1: Metal nanoparticles concentrations of synthesis and metal to protein stoichiometries.

\dagger M : RNase	$\dagger\dagger$ [RNase] (μ M)	\ddagger [RNase] (μ M)	$\ddagger\dagger$ [M] (μ M)	\wedge M : RNase*	$\wedge\wedge$ M : RNase*
Pt					
Control	10	6.9	-	-	-
125	10	8.0	77.6	8	10
250	10	7.9	252.2	25	32
500	10	7.4	386.7	39	52
1000	10	6.9	509.8	51	74
2000	10	5.7	723.6	72	127
Au					
Control	10	6.7	-	-	-
12.5	10	9.1	95.3	10	10
25	10	7.9	155.9	16	20
50	10	7.7	227.4	23	30
100	10	5.3	44.3	4	8
200	10	4.6	13.2	1	3
Ag					
Control	10	6.4	-	-	-
12.5	10	6.1	48.8	5	8
25	10	6.3	69.8	7	11
50	10	7.3	38.2	4	5
100	10	5.5	15.6	2	3
200	10	5.0	10.1	1	2

\dagger = theoretical ratio of metal atoms to RNase; $\dagger\dagger$ = starting concentration of RNase based on estimation by BCA; \ddagger = Protein concentration of RNase after nps synthesis; $\ddagger\dagger$ = molar concentration of M-nps based on metal atom concentration as estimated by ICP OES; \wedge = M-atoms: RNase ratio based on the starting concentration of RNase (i.e. 10 μ M) and $\wedge\wedge$ = M atoms: RNase ratio based on concentration of RNase after synthesis. * = values represents mean of triplicate samples with standard deviation <10%.

4.3.2.3 FTIR analysis

The FTIR analysis of M-nps-RNase (Fig. 4.5) showed RNase stabilizing the highest amount of nanoparticles from each metal used in this study relative to the control (i.e. RNase only). The presence of amide I, amide II and amide III bands (Haris and Severcan, 1999; Kong and Yu, 2007) in protein FTIR spectra of both control and experimental samples from 1800 – 1000 cm^{-1} showed no significant change in the overall secondary structure of both RNase and M-nps-RNase (Fig. 4.5 a). In other words, there was stabilization of metal nanoparticles within the protein structural conformation of RNase. In addition, observable peaks at 1206-1215 cm^{-1} , ascribed to β -sheets (van de Weert *et al.*, 2001) in both spectra of RNase and M-nps-RNase further confirmed protein integrity remained after nanoparticle synthesis.

Broad peaks observed in the amide II band of Au and Pt-nps-RNase spectra at 1544 and 1551 cm^{-1} respectively suggested C-N stretching or N-H bending vibrations in this region due to increased strength of hydrogen bonding of, perhaps, the metal salt/nanoparticle to the amide hydrogen in this region (Fig. 4.5 a). This was also observed with Ag-nps but to a lesser degree. Likewise, the appearance of a peak in the FTIR spectra of Pt –nps-RNase in the amide II region of RNase at 1450 cm^{-1} may also result from N-H bending vibration from the binding of Pt metal salt to the amide nitrogen. Furthermore, the frequency in the amide I region at 1646 cm^{-1} in the spectra of Au-nps-RNase, which was not present in other spectra, may result from an increased vibration of the β -sheets structure of RNase brought about by stabilization of Au nanoparticles in this region (Haris and Severcan, 1999; Grdadolnik, 2002). The presence of this band may also be HOH-bending vibration as a result of some interference from water, often referred to as anomalous dispersion effect observed in ATR characterization techniques (van de Weert, 2001).

Similarly, the presence of an amide B peak (Jabs, 2005; Kong and Yu, 2007) at 3257 cm^{-1} in the control spectrum of M-nps-RNase (Fig. 4.5 b) that was absent in the spectra of Pt and Ag-nps-RNase, implied hydrogen bond interactions of these metals with a nitrogen containing side chain or basic amino acid (Grdadolnik, 2002; IR-wizard, 2011). In the Ag-nps-RNase, additional peaks at 3090 and 3375 cm^{-1} in the amide B region may further confirm N-H bending vibrational energies resulting from hydrogen bonding of the amide hydrogen to silver (Jabs, 2005; IR wizard, 2011).

All these observations suggested that the stabilization by RNase might be through a nitrogen containing or basic amino acid residues.

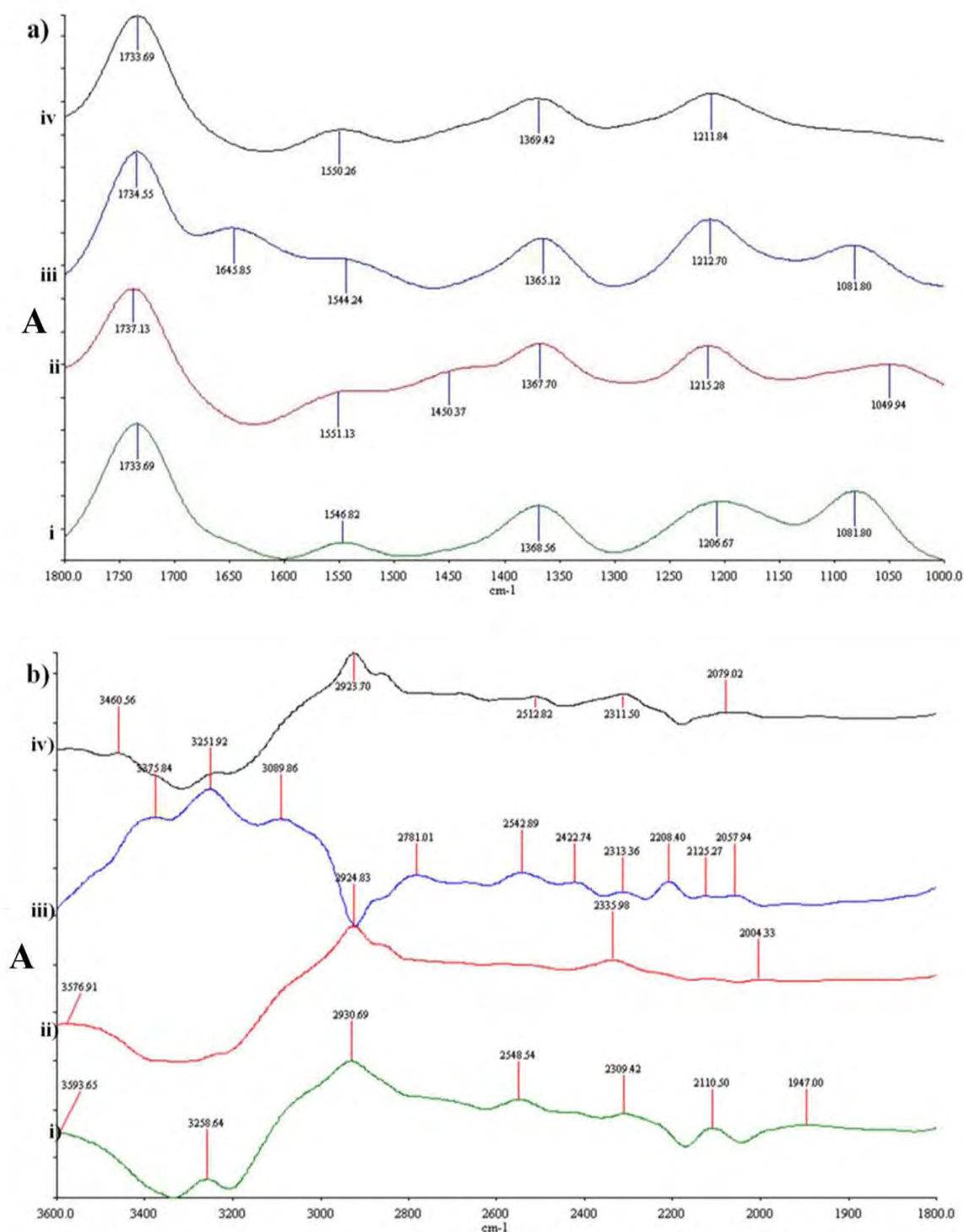


Figure 4.5: FTIR spectra of M-nps-RNase. (a) Spectral scan from 1800-1000 cm^{-1} and (b) 3600-1800 cm^{-1} . (i) - (iv) in (a) and (b) represents FTIR spectra of control (RNase only), Pt, Au and Ag respectively. Each spectrum represented was an average of 20 scans.

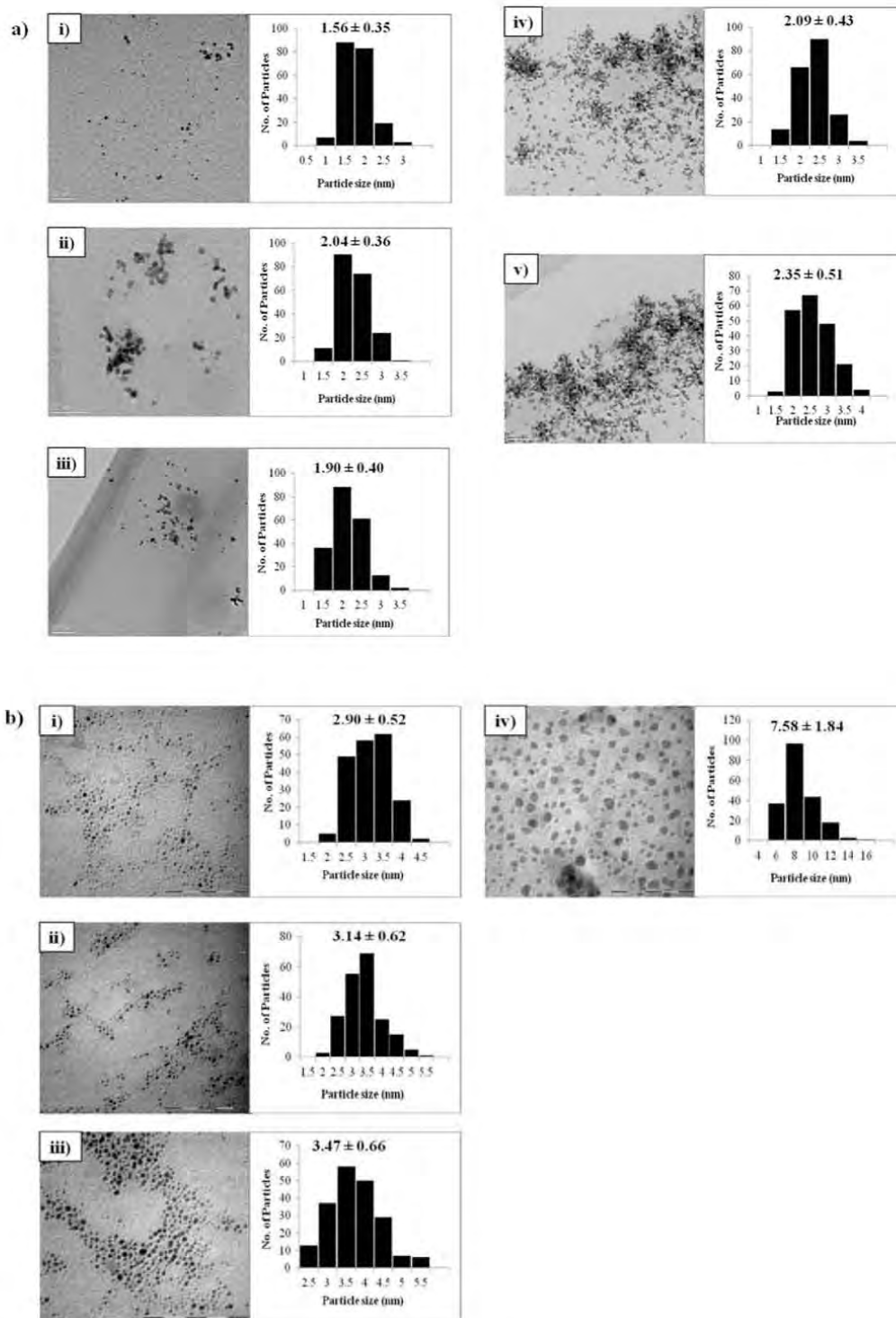
4.3.2.4 TEM & EDAX analysis

The TEM results of M-nps synthesized by RNase (Fig. 4.6) with respect to Pt-nps-RNase revealed particles with undefined morphology. Although Pt colloids were without doubt, present, they existed in a cluster with an average particle size of ~2 nm with every Pt:RNase ratio. In other words, no significant change was observed in the size of Pt nanoparticles with changes in the molar ratios of precursor platinum salts to a fixed molar concentration of RNase. These observations implied that the stabilization of Pt-nps by RNase did not necessarily affect the nucleation and growth of Pt-nps and hence the size of the particles. As with protein cages/barrel (chapters 2 & 3), the size of the particles increased with increasing Pt salt concentration within the cavity of the proteins until a saturation point was reached defined by the size of the protein cavity of these proteins. The sizes of the particles obtained in this study were similar to those that were obtained using non-caged polymers (Xie *et al.*, 2005; Cuenya *et al.*, 2010).

A similar trend was observed with Au-nps-RNase at an initial molar concentration ratios of 1:12.5 – 1:50 (RNase:Au), where an increase in particle size was not very significant (Fig. 4.6 b). The particle size, however, was almost doubled (7.58 ± 1.84 nm) at a RNase:Au ratio of 1:100 to that at 1:50 (3.47 ± 0.66 nm, Fig. 4.6 b). An increase in particle size of that magnitude must have resulted from an increased particle aggregation at that molar concentration. This may explain why no particles were observed in the TEM samples of RNase:Au ratios of 1:200 as most of the aggregated samples had precipitated from solution and were filtered off during subsequent purification steps after synthesis. Au nanoparticles obtained in the presence of RNase were more dispersed in solution than what was observed with Pt nanoparticles. On the other hand, TEM results of Ag-nps-RNase revealed an increasing average particle size with increasing molar concentration ratios (4.55-8.94 nm, 1:12.5-1:50 respectively, Fig. 4.6 c). Although particles appeared dispersed in solution, TEM results revealed further that the size of the particles were far from uniform as can be seen from the wide particle size distributions in each group of Ag-nps-RNase (Fig. 4.6 c_{i-iii}). Further, like with Au-nps, fewer to no particles were observed at molar concentrations >1:50 (RNase:Ag) due to increased observable particle aggregation and precipitation. These results were similar to those from ICP OES where metal concentration of Au and Ag

in RNase solution was very low at molar ratio $> 50:1$ (Table 4.1). Thus, the synthesis of M-nps with RNase did not control particle morphology.

Analysis of M-nps-RNase identified Pt, Au and Ag in the EDAX spectra/samples of respective aqueous solution of nanoparticles (Fig. 4.7).



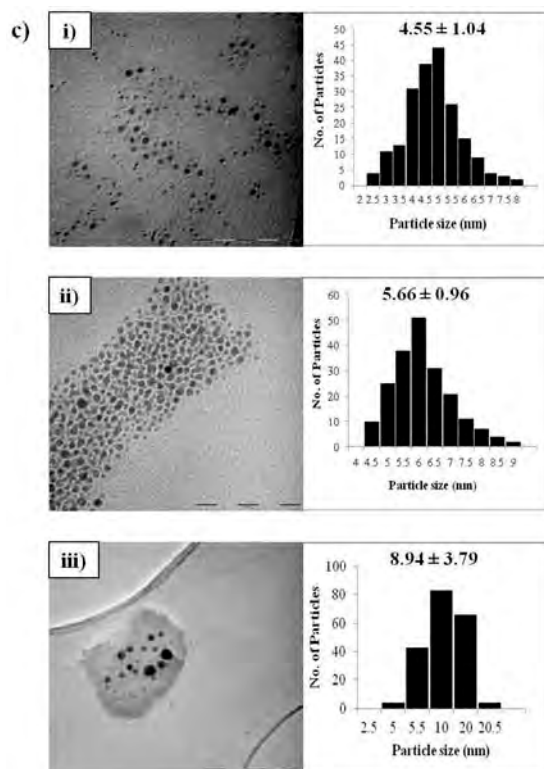
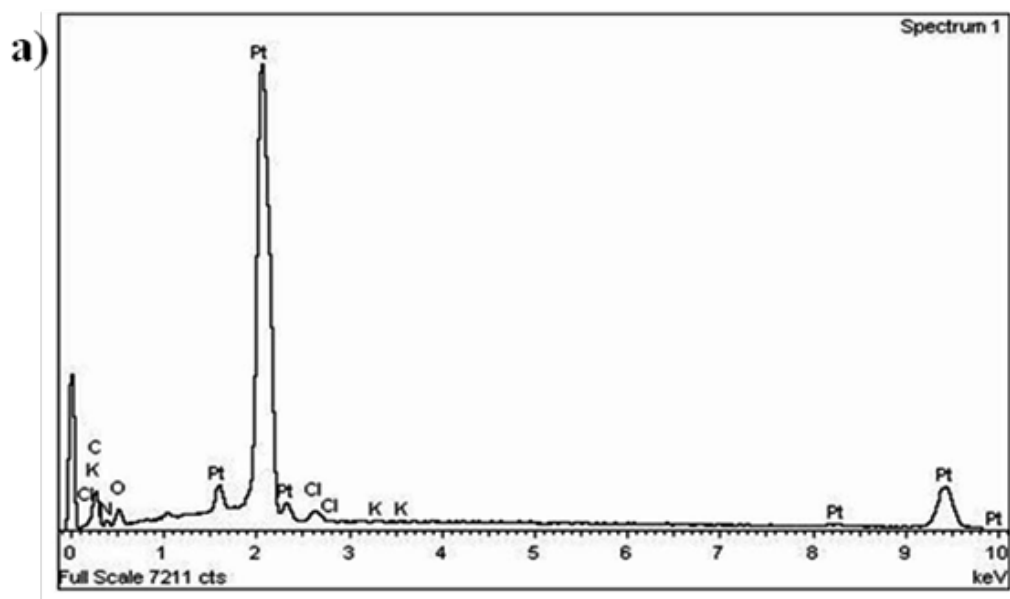


Figure 4.6: TEM analysis of M-nps-RNase complexes (a) Pt, (b) Au and (c) Ag. In (a), (i) 1:125, (ii) 1:250, (iii) 1:500, (iv) 1:1000 and (v) 1:2000 (RNase:Pt); in (b), (i) 1:12.5, (ii) 1:25, (iii) 1:50 and (iv) 1:100 (RNase:Ag) and in (c), (i) 1:12.5, (ii) 1:25 and (iii) 1:50 (RNase:Ag). TEM analysis was not possible at molar ratios of 1:200 in Au-nps-RNase and 1:100-1:200 in Ag-nps-RNase due to particle aggregation and precipitation.



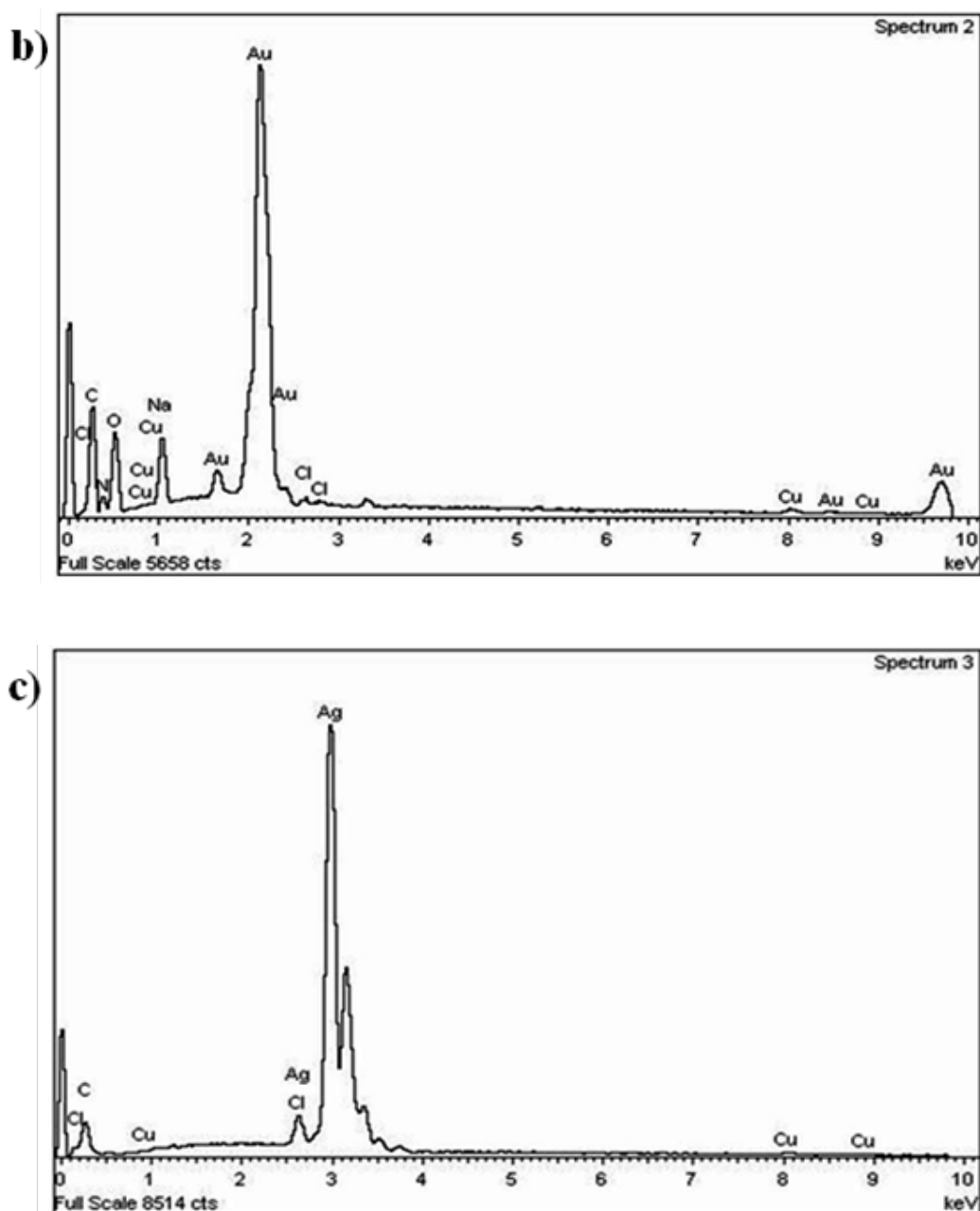


Figure 4.7: EDAX spectra of M-nps-RNase. (a) Pt; (b) Au and (c) Ag.

4.3.3 The effect of M-nps on the enzymatic activity of RNase

The effect of nanoparticle synthesis on the hydrolytic activity of RNase was investigated as described 4.2.2.4. Results revealed a general decrease in the RNA hydrolysis activity by RNase in M-nps-RNase compared to the control (Fig. 4.8). This decrease in RNase activity was also found to be concentration dependent with respect to the molar concentration ratio of metal to RNase. Au-nps had the highest inhibitory effect of 48 % to almost a 100 %, this was followed by Pt-nps-RNase with 20-95 % inhibition and about 18-90 % with Ag-nps.

Heavy metal ions are known to be one of the most potent inhibitors of RNases (Genelink, 2011; Worthington, 2011) which might be the reason why the activity of RNase was strongly inhibited particularly at higher molar concentrations of metals to RNase.

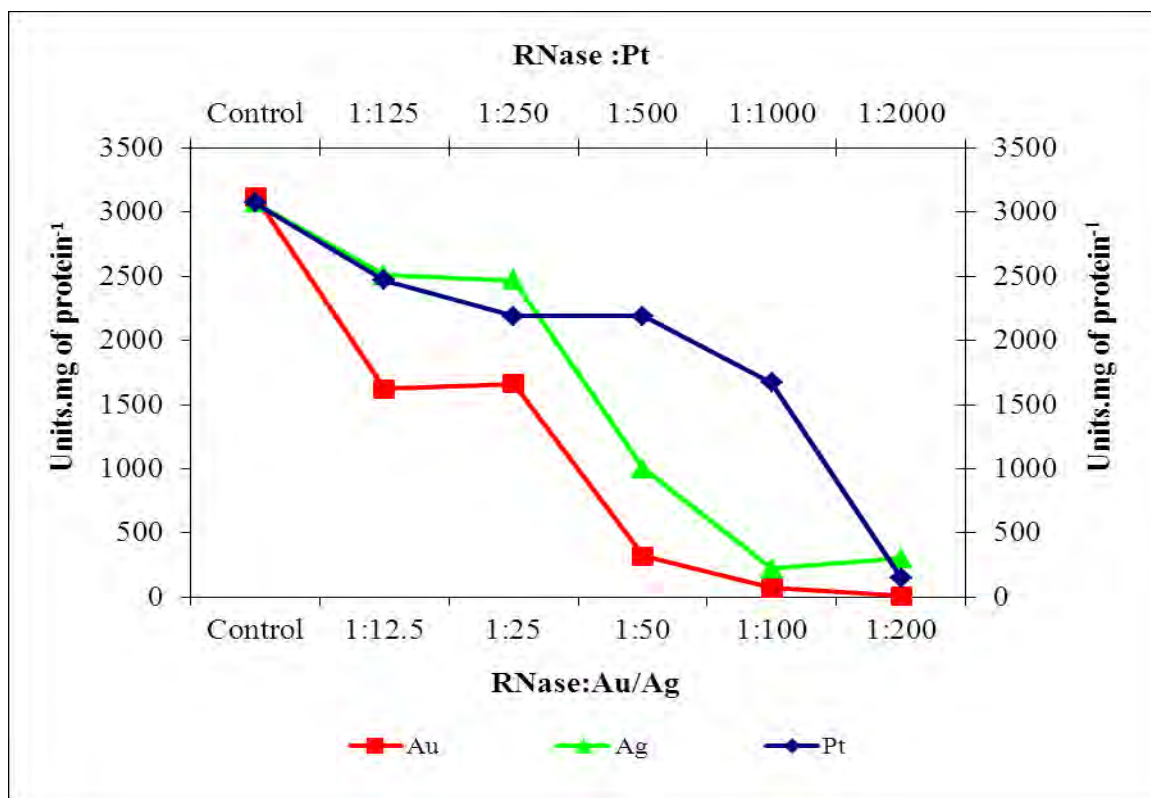


Figure 4.8: The effect of M-nps synthesis on the hydrolytic activity of RNase. Secondary x and y axis represents the molar concentration ratios of a fixed concentration of RNase to varying concentration of precursor metal salts of platinum use in nps synthesis and RNase activities of Pt-nps-RNase respectively. 1 Unit = $1\mu\text{mol}\cdot\text{min}^{-1}$.

Furthermore, an explanation for the inhibition of RNase activity by metallic nanoparticles might be due to interaction/stabilization of nanoparticles by vital amino acids responsible for its enzymatic function. As can be seen from results obtained from the FTIR analysis, it can be concluded that nitrogen containing or basic amino acids residues (e.g. histidine, lysine and arginine) are responsible for nanoparticle stabilization. These are the same reported amino acids presents in the active sites of RNase and are vital for effective catalysis of RNase (Raines, 1998), hence, the observed inhibitory effect of metal nanoparticles on RNase activity.

4.4 Conclusions

The biological synthesis of metallic nanoparticles using a non-caged protein/enzyme is described and has shown the biosynthesis of metallic nanoparticles with similar chemical and physical properties as chemically synthesized particles. Controlled particle morphology, however, was not achieved with the use of this RNase in the biological synthesis of metallic nanoparticles. Moreover, there was poor stabilization of metal nanoparticles by RNase in comparison to what was obtained using cage/barrel-like protein reported previously (chapters 2&3).

Furthermore, the synthesis of metallic nanoparticles did not affect the overall structural conformation of RNase; its enzymatic activity however, was greatly compromised (decreased) by these nanoparticles. RNase A and related variants have been implicated in the growth and development of tumors in cancer research (Matoušek, 2001; Benito *et al.*, 2005) and many studies have reported the anti-tumor and chemotherapeutic properties of RNases (Leland and Raines, 2001; Arnold and Ulbrich-Hofmann, 2006; Ardel *et al.*, 2009) and as such are been considered as a potential cancer therapeutic. Thus, the inhibition of RNase by nanoparticles as a potential biomedical target in the treatment of cancers may not be applicable.

Recent advances and studies, however, implicated the role of RNases in tumor growth, as the malignancy of some tumors in pancreatic cancer and chronic myeloid leukaemia has been associated with a high level of RNases activity (Shlyakhovenko, 2009). As such, the inhibition of RNases by nanoparticles may prove beneficial as the possible inhibitors of tumor growth and/or the treatment of cancers. In addition, the strong inhibition of RNase by Au-nps compared to what was obtained with Pt and Ag may further explain the chemotherapeutic use of gold nanoparticles in tumor removal and cancer treatment (Huang *et al.*, 2007; Cai *et al.*, 2008). Likewise, the inhibition of RNase by Pt-nps may also provide a rationale behind the use of some platinum based drugs (Kelland, 2007; Todd and Lippard, 2009; Bonander, 2011) in the management/treatment of tumors/cancers.

Chapter 5: Interaction of metallic nanoparticles with acetylcholinesterase

5.1 Introduction

Metallic nanoparticles (especially of noble metals) possess unique physical and chemical properties which are constantly been explored in the different field of science and technology. In other words, nanotechnology employs the unique properties of these nanoparticles and many commercial nano-based products are increasingly been made available and have become part of our daily life (Adili *et al.*, 2008; Bello *et al.*, 2009; Prabhu *et al.*, 2010).

Despite the importance of nanotechnology, there has been a great concern about the safety of these engineered nanomaterials to both human health and the environment as most fabricated nanoparticles are geared towards different applications in biomedicine (Oberdörster *et al.* 2007; Mironava *et al.*, 2010; Liu *et al.*, 2010). Although many studies are beginning to emerge and have reported different effects/health risks that some of these nanoparticles may possess at molecular, cellular and systemic levels (Unfried *et al.*, 2007; Grieger *et al.*, 2009; Pfaller *et al.*, 2010). Research in these areas is still limiting and nothing when compared to research based on the synthesis and production of nanoparticles and their respective products (Bello *et al.*, 2009). In addition, most studies available have focused only on the chemically synthesized nanoparticles and just a few have looked at the potential toxicity of bio-engineered nanomaterials. Two recent studies have reported the cellular uptake of apoferritin encapsulated platinum through receptor-mediated endocytocysis (Zhang *et al.*, 2010; Liu *et al.*, 2011). These studies have reported very minute cytotoxic effects and reduction of oxidative stress in various cell lines compared to naked chemically synthesized Pt nanoparticles. Furthermore, due to the small size of nanoparticles that enables them to cross through the blood-brain barrier unnoticed by the immune systems, particularly when attached to larger proteins (Liu *et al.*, 2011), it would be of utmost importance to ascertain the potential neurotoxic effects of biologically synthesized nanoparticles on the central nervous system. An important mammalian enzyme

that nanoparticles were capable of binding to in the nervous system is acetylcholinesterase (AChE).

This enzyme, important for the proper coordination and functioning of the nervous system is found mainly on the membranes of excitable tissue such as the cholinergic and neuromuscular junctions of the nervous system. It catalyses the rapid hydrolysis of acylcholinesters with a high specificity for acetylcholine (ACh), a neurotransmitter, to form an acetate group and choline (Fig. 5.1), consequently terminating the synaptic transmission and allowing for the next impulse to be transmitted.

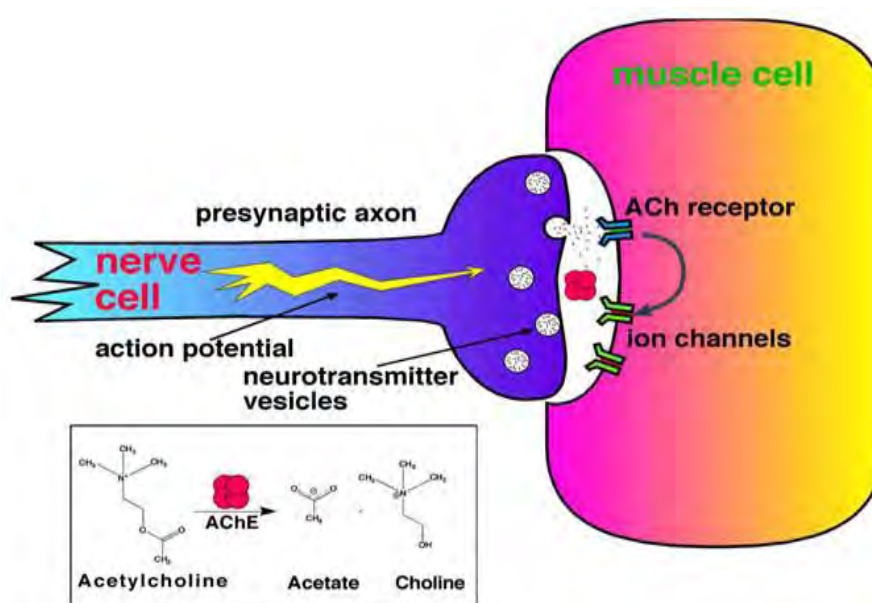


Figure 5.1: Schematic representation of the enzymatic activity of AChE at the neuromuscular cholinergic synapse. (Taken from Proteopedia-life in 3D).

AChE is a biomedical target for many compounds (particularly organophosphates), cognitive enhancing drugs and pesticides (e.g. Carbamates). These agents are often referred to as cholinesterase inhibitors (CIs) or anti-cholinesterase (anti-AChE) compounds (Arufe *et al.*, 2007; Bucur *et al.*, 2005). Inhibition of AChE leads to the accumulation of ACh in the synapse resulting in various symptoms and life threatening conditions such as neuromuscular paralysis and respiratory failure (Worek *et al.*, 2002). Conversely, the use of some reversible cholinesterase inhibitors has been employed in the management of cognitive diseases such as dementia and Alzheimer's (Loewenstein *et al.*, 2004; Press and Alexander, 2011). Since the use of nanoparticles as drugs and other biomedical agents is

beginning to escalate, it is very important to look at the potential neurotoxicity properties of these particles. One of the ways of achieving this was by looking at the effect of nanoparticles on AChE. A limited amount of research work has been done to show this effect and not until recently did Wang *et al.*, 2009 study the effect of chemically synthesized nanoparticles on AChE in terms of adsorption and inhibition of this enzyme. It is therefore equally important to look at the potential neurotoxicity of biologically synthesized nanoparticles on AChE. Since the biological approach of nanoparticle synthesis was believed to be a safer and eco-friendly, this may further support the biological route over the chemical method of nanoparticle synthesis.

The objective of this chapter is to:

- i. Interact biologically synthesized metal nanoparticles of platinum, gold and silver in/with Apoferritin (HSA), GroEL and RNase with AChE.
- ii. Determine the anti-cholinesterase properties of these nanoparticles.

5.2 Materials and Methods

Electric eel acetylcholinesterase (AChE), acetylthiocholine iodide (ATChI) and 5, 5' dithio-bis-2-nitrobenzoic acid (DTNB) were purchased from Sigma-Aldrich (South Africa). All solutions and buffers were prepared with deionized water obtained from a Milli-Q system.

5.2.1 Preparation of nanoparticle stock solutions

Selected stock solutions of metallic nanoparticles (Table 5.1) were prepared using nanoparticles synthesized with HSA, GroEL and RNase. This was done by diluting a solution of nanoparticles in phosphate buffer (0.1 M, pH 8.0) to give the desired final concentrations, as determined by metal quantification using ICP OES (Table 5.1) and mixture was rapidly shaken using a vortex mixer (Bio-Rad).

5.2.2 AChE assay

The *in vitro* activity assay of AChE was performed by the method of Ellman *et al.*, 1961 with modifications to microtiter plate assay. AChE (0.125 U, 20 μ l) in phosphate buffer (0.1 M, pH 8.0) was incubated (37 $^{\circ}$ C, 10 min) after which DTNB (a chromogen, 10 μ l) was added and the reaction was started with ATChI (50 μ M, 10 μ l), the final volume of

reaction mixture was 200 μl . The activity of AChE was determined colorimetrically by measuring the rate of change of absorbance at 412 nm over 3 min. Activity of AChE was calculated and activity expressed in $\mu\text{mol}\cdot\text{ml}^{-1}\cdot\text{min}^{-1}$ (Appendix D).

Table 5.1: Stock concentrations and particle sizes of metal nanoparticles synthesized with different proteins

M:HSA	[M] (μM)	Average particle size (nm)	M:GroEL	[M] (μM)	Average particle size (nm)	M:RNase	[M] (μM)	Average particle size (nm)
<i>Pt</i>			<i>Pt</i>			<i>Pt</i>		
250	410.8	2.34 ± 0.33	125	159.5	1.72 ± 0.35	125	77.6	1.56 ± 0.35
500	646.2	3.24 ± 0.56	250	202.2	2.52 ± 0.47	250	252.2	2.04 ± 0.36
1000	1449.3	4.69 ± 0.84	500	487.4	3.05 ± 0.57	500	386.7	1.90 ± 0.40
2000	2699	5.32 ± 1.06	1000	672.1	3.32 ± 0.52	1000	509.8	2.09 ± 0.43
4000	4041.7	5.79 ± 1.04	2000	800.3	3.50 ± 0.72	2000	723.6	2.35 ± 0.51
<i>Au</i>			<i>Au</i>			<i>Au</i>		
250	1082.2	3.03 ± 0.57	14	94.5	2.80 ± 0.35	12.5	95.3	2.90 ± 0.52
500	2369.8	4.21 ± 0.93	25	160.2	2.92 ± 0.40	25	155.9	3.14 ± 0.62
1000	3571.7	4.84 ± 1.14	50	399.3	2.95 ± 0.45	50	227.4	3.47 ± 0.66
2000	209	3.34 ± 0.56	100	723.4	3.07 ± 0.58	100	44.3	7.58 ± 1.84
4000	94	2.81 ± 0.49	200	1372.4	3.26 ± 0.50	200	13.2	-
			500	100.5	3.00 ± 0.30			
			1000	48.2	2.38 ± 0.56			
<i>Ag</i>			<i>Ag</i>			<i>Ag</i>		
250	497.7	2.37 ± 0.29	14	10	2.45 ± 0.39	12.5	48.8	4.55 ± 1.04
500	642.5	3.70 ± 0.56	25	16	2.96 ± 0.43	25	49.8	5.66 ± 0.96
1000	1251.5	5.92 ± 0.94	50	12.7	3.41 ± 0.50	50	38.2	8.94 ± 3.79
2000	767.2	5.69 ± 1.08	100	19.3	4.01 ± 0.60	100	15.6	-
4000	63.6	2.71 ± 0.47	200	96.2	5.51 ± 0.91	200	10.1	-
			500	28.8	4.62 ± 1.36			
			1000	8	3.00 ± 0.47			

5.2.3 Interaction of M-nps with AChE

Different concentrations of M-nps prepared as described in 5.2.1, were incubated with AChE (0.125 U, 37 °C, 10 min). Assay was done as described in 5.2.2. AChE without any nanoparticle was used as the control. The effect of nanoparticles on the activity of AChE was calculated and expressed as % inhibition of AChE (Appendix D).

5.2.4 Statistical Analysis

AChE activity assays were done in triplicate and values reported as the means with standard deviation. A one-way analysis of variance (ANOVA) was conducted using Graph Pad InStat for Windows, version 3 (Graphpad Software Inc.) demo version and Microsoft Excel 2007. The level of significance of means was determined at $p < 0.05$; $p < 0.01$ and $p < 0.001$ assuming percentage mean of the control was zero.

5.3 Results

The effect of nanoparticles from the three various biomacromolecules - HSA, GroEL and RNase on the AChE activity was investigated; Table 5.1 shows the different particle size obtained from varying concentration of metal salts to a fixed concentration of protein and corresponding nanoparticle concentration as determined by TEM and ICP OES respectively. Selected nanoparticle concentrations were varied in order to determine the dose-related effect of nanoparticles on AChE.

5.3.1 The effects of nanoparticles on AChE

5.3.1.1 M-nps-HSA

AChE was incubated with different concentrations of M-nps from different molar ratios of M:HSA (based on metal quantification by ICP OES). The metal concentration used was 50 - 500 μM in Pt and Au-nps while 5-50 μM was used in Ag-nps (Fig. 5.2 a-c). Results revealed an inhibition of AChE activity of less than 50 % for all metals at all concentrations. In Pt-nps significant inhibition of 12 - 35 % was seen at concentrations of 100 - 500 μM in all HSA:metal nanoparticles groups (i.e. 1:250-1:4000 HSA to Pt) used in this study (Fig. 5.2 a). A similar result was obtained with Au-nps, although noticeable inhibition was observed with Au-nps concentration of 50 - 500 μM with percentage inhibitions ranging from 17-30 % (Fig. 5.2 b). Inhibition of AChE by Ag-nps was observed at a lower nanoparticle concentration of 5-50 μM with about 9-30 % inhibition of AChE

(Fig. 5.2 c). Inhibition of AChE with Pt, Au and Ag nanoparticles appeared to be dose and relatively size dependent in all groups of nanoparticles tested as percentage inhibition of AChE increased with increasing concentration of nanoparticles.

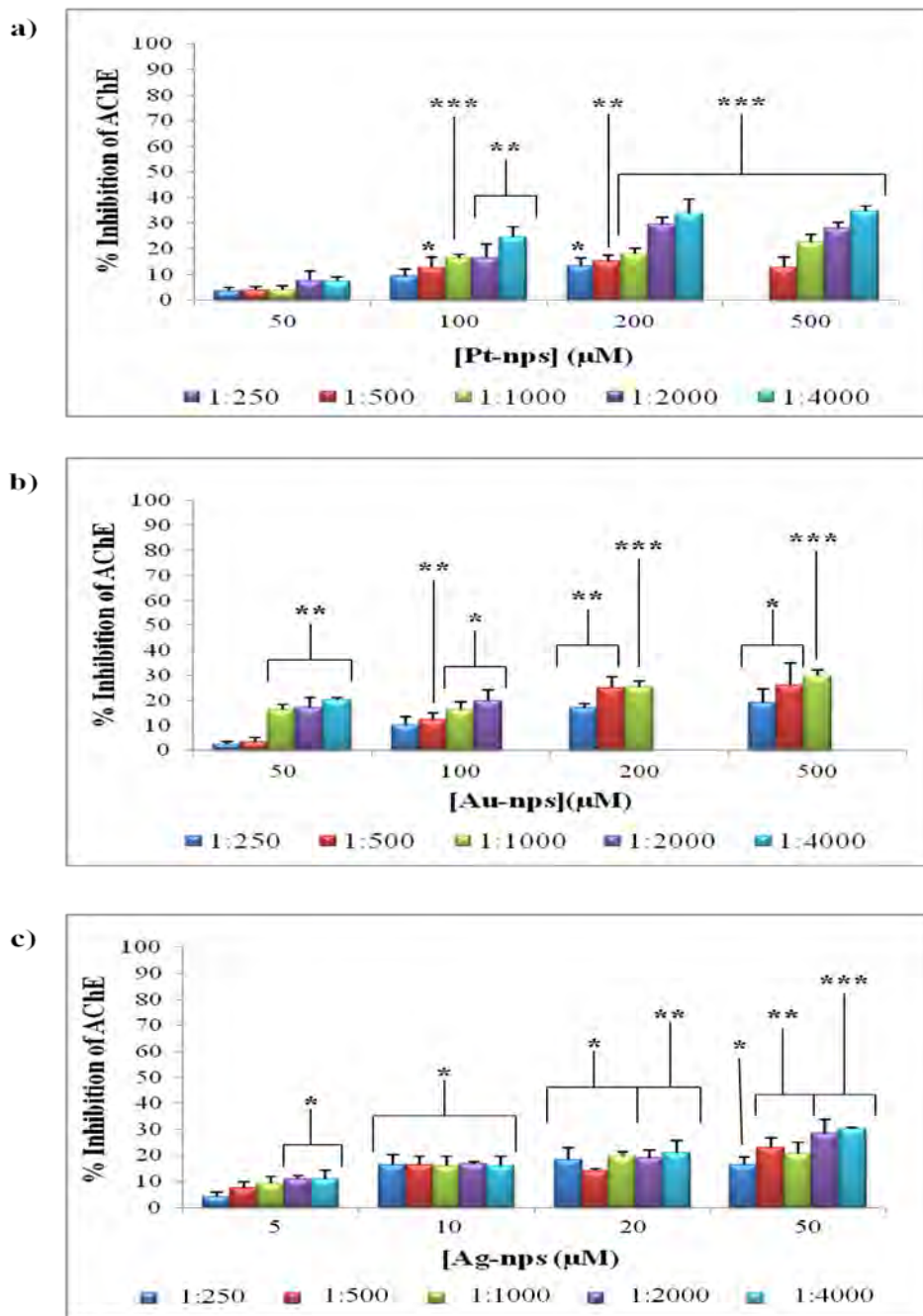


Figure 5.2: The inhibitory effect of M-nps-HSA on AChE. (a) Pt-nps; (b) Au-nps and (c) Ag-nps. Legends represent the M-nps synthesized with a molar concentration ratio of HSA to varying molar concentrations of metal salts. * = $p < 0.05$; ** = $p < 0.01$ and *** = $p < 0.001$.

Likewise, significant inhibition ($p < 0.001$) was observed at higher concentrations of nanoparticles except with Pt at 100 μM of a 1:1000 (HSA:Pt) Pt-nps (Fig. 5.2 a). The inhibitory effect of M-nps could not be tested beyond a concentration of 500 μM in Pt and Au and 50 μM in Ag, due to sample absorbance being > 2 at these concentrations. This made it difficult to calculate the true effect of M-nps on the AChE activity. In addition, the effect of M-nps-HSA at 1:250 with Pt could not be determined at Pt-nps concentration of 500 μM because the stock concentration of Pt-nps at this molar ratio was less than 500 μM (Table 5.1). This also explained the reason why the effect of Au-nps on AChE at molar ratios 1:2000 and 1:4000 could not be studied at Au-nps concentration of $> 100 \mu\text{M}$.

5.3.1.2 M-nps-GroEL

The inhibitory effect of metal nanoparticles synthesized with GroEL is shown in Fig. 5.3 a-c. Inhibitions of 11-33 % was observed in Pt-nps at nanoparticles concentrations of 5-50 μM (Fig. 5.3 a), similar to that which was obtained with Pt-nps-HSA except this inhibition in this case was achieved at lower Pt-nps concentrations. Significant inhibitions of 19 – 43 % were achieved with Au at Au-nps concentrations from 10 -50 μM (Fig. 5.3 b), while an 8 – 29 % inhibition of AChE was seen with Ag from Ag-nps concentrations of 5 – 25 μM (Fig. 5.3 c).

The inhibition of AChE activity by M-nps in this study was also found, to a certain degree, to be dose and size related judging by the increasing level of significance of inhibitions with increasing M-nps concentrations and particle size.

5.3.1.3 M-nps-RNase

The effect of M-nps-RNase on the activity of AChE is shown (Fig. 5.4 a-c). The activity of AChE was significantly inhibited by 10 - 42 % with Pt from Pt-nps concentration of 10 - 200 μM , which was slightly higher than that obtained with Pt-nps-HSA and Pt-nps-GroEL. A similar trend was noticed with Au-nps but with marked inhibition of 57 %, as the highest level of inhibition, at Au-nps concentration of 50 μM . A reverse effect, however, was seen with Ag-nps as the activation of AChE activity was observed at all concentrations tested in this assay. AChE activation of about 20-49 % was noticed from Ag-nps concentration of 5 – 25 μM (Fig. 5.4 c).

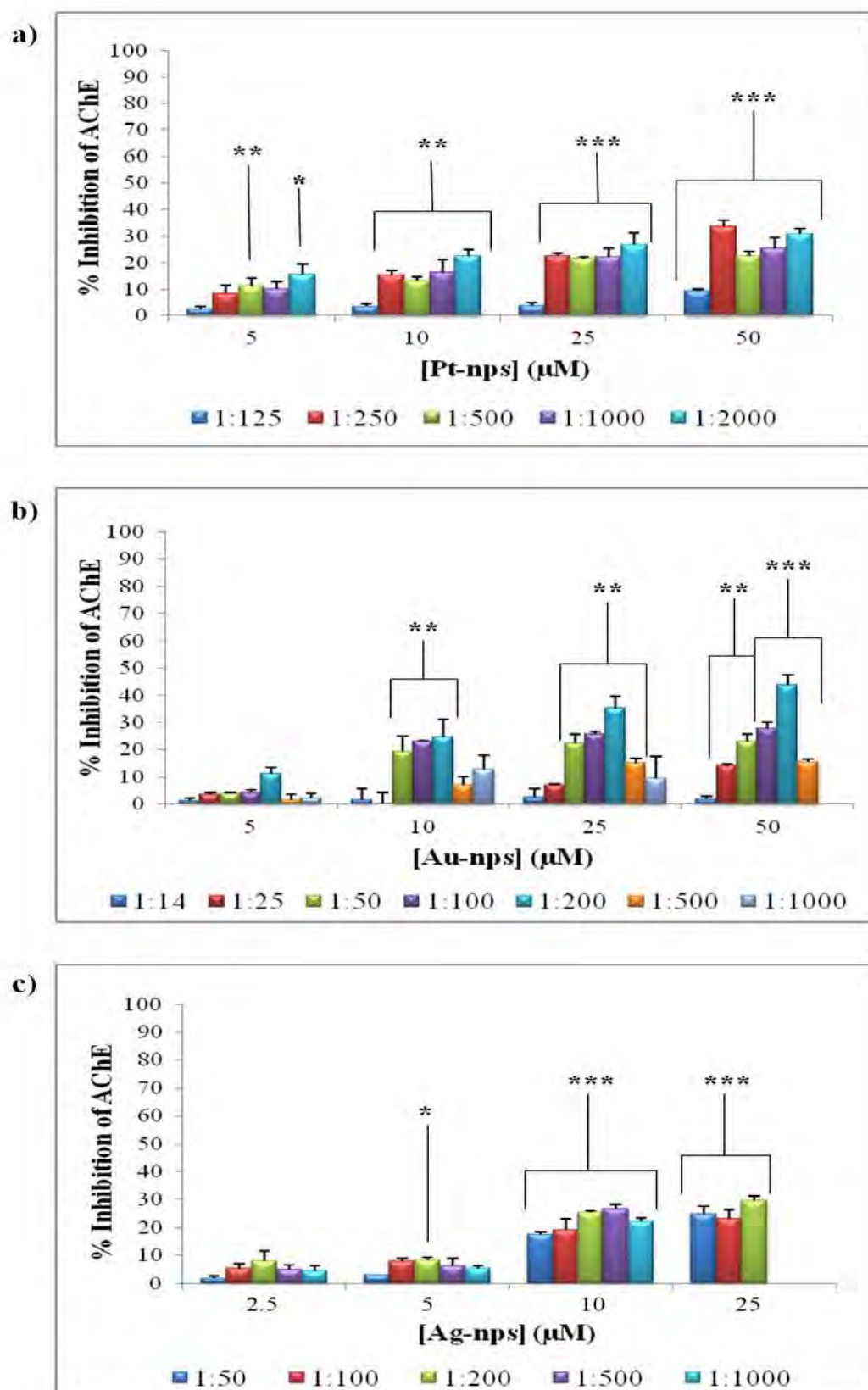


Figure 5.3: The AChE inhibitory effect of M-nps-GroEL. (a) Pt-nps; (b) Au-nps and (c) Ag-nps. * = $p < 0.05$; ** = $p < 0.01$ and *** = $p < 0.001$.

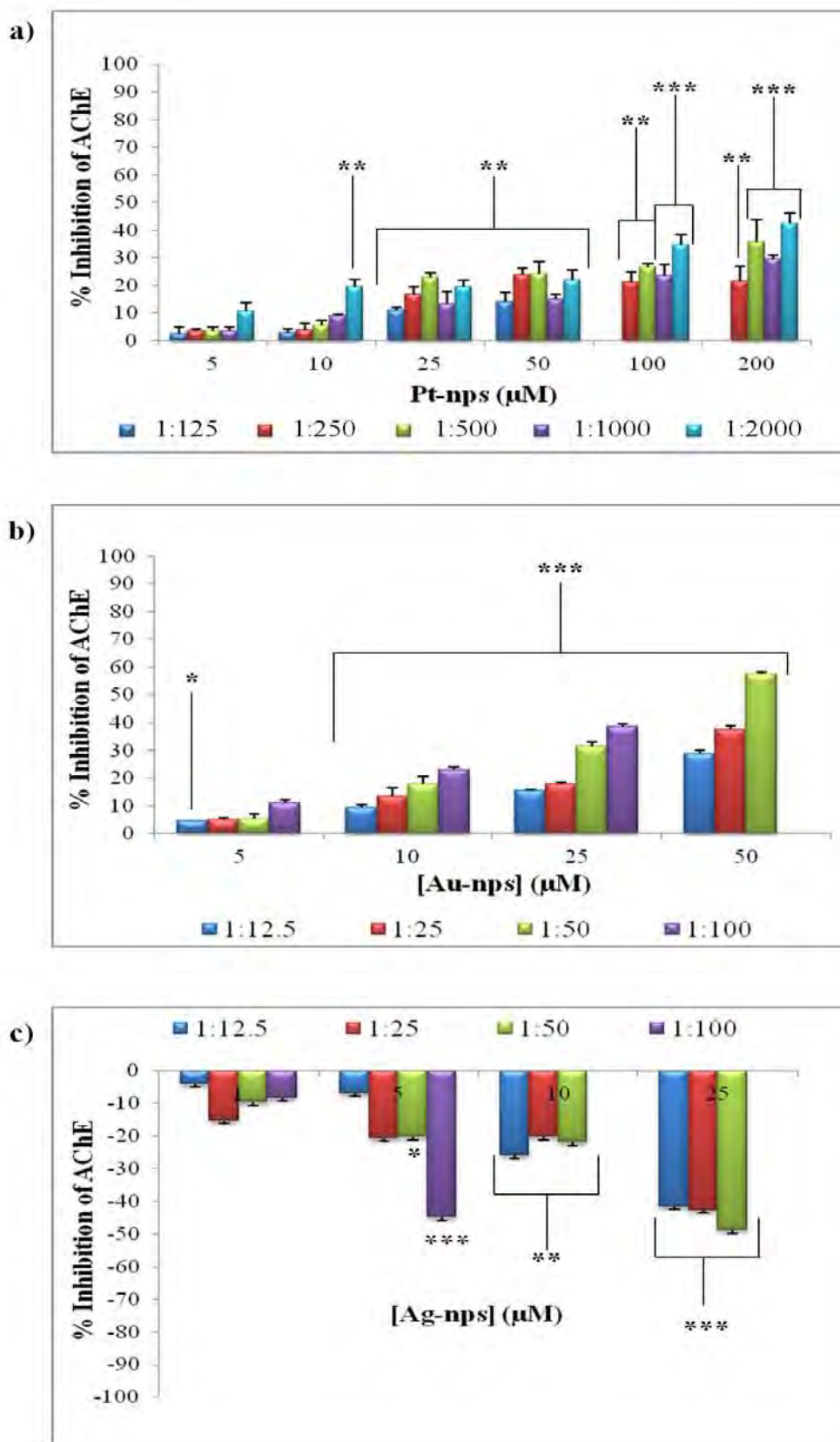


Figure 5.4: The effect M-nps-RNase on the activity of AChE. (a) Pt-nps; (b) Au-nps and (c) Ag-nps. * = $p < 0.05$; ** = $p < 0.01$ and *** = $p < 0.001$.

5.4 Discussions and Conclusions

The anti-cholinesterase effect of metallic nanoparticles made with different proteins was investigated in this study. All metallic nanoparticles showed some significant reduction in the hydrolysis activity of AChE at certain concentrations with the highest inhibition in HSA and GroEL generated nanoparticles was less than 50 % (30 and 35 % respectively) compared to that obtained with M-nps-RNase of 57 %. The least inhibition was observed in nanoparticles synthesized with HSA (30 %), this was followed by M-nps-GroEL (35 %) with the highest being M-nps-RNase (57 %). This suggested that the encapsulation of nanoparticles by the cage-like structure of HSA and the barrel-like structure of GroEL had lowered the inhibitory effect of these metal nanoparticles as opposed to the 'naked' nanoparticles obtained with non-caged RNase. Furthermore, the possible effect of proteins without nanoparticles on the activity of AChE was tested and no significant effect on the activity of AChE was noticed (results not shown). These results were comparable to those which were reported on cytotoxic properties of protein encapsulated versus chemically synthesized Pt nanoparticles using polyvinylpyrrolidone (PVP) as a stabilizer (Zhang *et al.*, 2010; Liu *et al.*, 2011).

The degree of inhibition of AChE by biologically synthesized nanoparticles was much lower than that reported by Wang *et al.*, 2009 using chemically synthesized nanoparticles. This supported a biological approach involving encapsulation of nanoparticles by proteins or other biomolecules may prove less neurotoxic than chemically produced nanoparticles in various environmental and biomedical applications.

Chapter 6: General discussion and conclusions

6.1 Discussions

6.1.1 Biosynthesis of nanoparticles

Noble metallic nanoparticles are becoming more attractive and fast gaining ground as tools and potential tools in various fields of science and technology due to their high surface-to-charge ratios, high surface energy and high volume to surface area ratio which forms part of the numerous properties that make them applicable. The uniformity in dispersion of these particles is also foreseen to be of tremendous advantage in biological systems and in biomedicine. Nevertheless, the safety of synthesis and application of these nanoparticles especially in biomedical applications, needed to be examined. The use of proteins and peptides are currently in high demand for the fabrication of nanosized materials due to their large structural and functional diversity, availability and utilization in the manipulation of material properties (Fan *et al.*, 2010). It was now known that particle size, shape and morphology are well contained by cage-structured proteins. More so, biotemplate-directed synthesis of inorganic nanoparticles using protein-cages offered a “greener” approach than the conventional methods available as the conditions of reaction and production were generally mild. This method further allowed for hard inorganic materials (like metals) to be interfaced with soft biological materials (such as proteins) to create novel biocomposite functionalities which was considered a major advantage (Varpness *et al.*, 2005).

Protein cages, like apoferritin, is a well known bio-template for the biological synthesis of metallic nanoparticles because of their exceptional stability and have been reported to endure a wide variety of conditions such as extremes of pH (2.8-10.6) and temperature (71 °C) (Liu *et al.*, 2011) and was chosen as one of the proteins used in the biosynthesis of nanoparticles in this study. GroEL, a chaperonin protein, represents another medium of confinement of particle growth and morphology. The use of genetically modified and unmodified cavity of this barrel-like protein together with other heat shock proteins have been explored in the synthesis of various types of nanoparticles with applications of these particles as catalysts, biosensors, storage devices and vehicles in drug delivery (McMillan

et al., 2002; Ishii *et al.*, 2003; Varpness *et al.*, 2005). Very little is known, however, about the synthesis of metallic nanoparticles with GroEL, hence, its use in this study. Although the use of enzymes in the synthesis and stabilization of nanoparticles is not uncommon in nanotechnology, RNase, as a non-caged protein/enzyme, was used as the third choice in the biological synthesis of nanoparticles in order to compare the physical properties of nanoparticles generated with protein cages as opposed to that obtained with a non-caged protein. It was hypothesized that nanoparticles generated within HSA and GroEL would be more uniformly dispersed than with RNase. In addition, the ‘protection’ of the nanoparticles inside the protein cage/barrel (i.e. HSA and GroEL) would not have much influence on toxicity.

Metallic nanoparticles of platinum, gold and silver were selected for biological synthesis and used in this study due to the fascinating properties each metal possess both in their bulk forms and at nanoscale. For example platinum is widely known for its catalytic properties and have been used in catalytic converters of automobile exhausts systems; catalytic production of hydrogen fuels and also in the production of medical implants (Helmers, 1997; Krebs, 2006; Brook, 2006). Platinum also forms part of some chemotherapy drugs used in the treatment/management of certain cancers (Einhorn, 1990; Todd and Lippard, 2009; Bonander, 2011). Platinum nanoparticles are more efficient catalysts than its bulk forms, as it is an acceptable fact that the properties of bulk materials are greatly enhanced at the nanoscale. Protein encapsulated platinum nanoparticles have been utilized as artificial hydrogenases in the production of hydrogen gas in hydrogen fuel cells and have been found to be 20-fold more efficient than free Pt nanoparticles and are not sensitive to oxygen like hydrogenase enzymes (Varpness *et al.*, 2005). Recently, the antioxidant properties of platinum nanoparticles have been reported (Zhang *et al.*, 2010) and have been shown to lower cellular oxidative stress by reduction of reactive oxygen species (ROS) like hydrogen peroxide and superoxide similar to catalase and superoxide dismutase (Fan *et al.*, 2010).

Gold nanoparticles have been proven to be an excellent tool in bioimaging, biosensing and gene/molecular engineering due to their unique optical, electronic and molecular recognition properties (Chen *et al.*, 2005; Zhang *et al.*, 2007; Cui *et al.*, 2011). In addition, they are used in photothermal therapy considering the strong heat absorption from gold

SPR band, thus making them sensitive to the environment in which they are localized. This property forms part of the basis of using gold nanoparticles in tumor removal and treatment of cancers (Visaria *et al.*, 2006; Cai *et al.*, 2008). The catalytic properties of Au nanoparticles have been well documented (Cortie and van der Lingen, 2002; Hashim, 2005; Thompson, 2007; Campbell *et al.*, 2011) and have recently been reported to improve the efficiency of organic solar cells (Coxworth, 2011).

Silver nanoparticles have been one of the most researched among noble metallic nanoparticles because they possess exceptional properties that make them useful. For instance, over the past decade, due to their uncommon size-dependent electronic, optical and magnetic properties, they have found use in the area of electronics, optics, catalysis (Elechiguerra *et al.*, 2005; Domínguez-Vera *et al.*, 2007; Sureshkumar *et al.*, 2010) and other areas of science and technology. At the moment, the studies and applications of silver nanoparticles in biotechnology and bioengineering include their use in the treatment of water (Kaegi *et al.*, 2011), textile engineering (Durán *et al.*, 2007) and in cosmetics (Kokura *et al.*, 2010). In addition, due to antimicrobial properties of Ag nanoparticles, their inclusion in a wide range of medical devices is being considered. The impregnations of surgical instruments with silver nanoparticles and also in wound dressing have also been reported (Eby *et al.*, 2009; Buu *et al.*, 2011).

The synthesis of metallic nanoparticles of Pt, Au and Ag within the proteins/enzymes described above, generated nanoparticles with similar physical and chemical properties to those synthesized chemically such as the size of particles being <100 nm and their optical properties. Moreso, this made the biological route of synthesis more ideal, as the conditions of synthesis were generally mild and more bio- and ecofriendly than what was seen with the conventional chemical methods. The morphologies of these particles (in terms of size) appeared, however, to be more controlled in nanoparticles produced with apoferritin and GroEL than with RNase, as was seen by the narrowness in the size distribution. In other words, the cage-like interior of apoferritin and the barrel-like cavity of GroEL were able to confine the growth of these particles contrary to what was obtained with non-caged RNase. Furthermore, in terms of particle stabilization by these proteins; apoferritin was seen to stabilize the highest number of nanoparticles in all groups of metals used in this study; this was followed by GroEL, with RNase stabilizing the least number of

particles. This may explain the recent focus and many reported studies involving the use of apoferritin in various synthesis and fabrications of different nanoparticles/nanomaterials (Ueno *et al.*, 2004; Clemente-León *et al.*, 2006; Domínguez-Vera *et al.*, 2007; Gálvez *et al.*, 2008; Fan *et al.*, 2010; Zhang *et al.*, , 2010; Fan *et al.*, 2011; Sennuga *et al.*, 2011). In addition, the mechanism of synthesis and stabilization of nanoparticles may be charge-related and involved the electrostatic attractions between proteins and metals salts used in this study as suggested by some earlier studies involving the synthesis of nanoparticles with protein/enzymes (Gálvez *et al.*, 2005&2006; San *et al.*, 2011). Moreover, the biosynthetic approach used in this study involved initial incubation of metal salts (i.e. cations) with aqueous solutions of proteins at pH conditions that promote attraction of metal ions to the protein followed by subsequent reduction of metal salts to nanoparticles. As reported elsewhere and in this study, the interior cavity of apoferritin and the overall charge of GroEL are negative at physiological pH (Gálvez *et al.*, 2008; Section 3.3.2, pg. 58). This also explained why more stabilization of metallic nanoparticles was seen in these proteins than with RNase being a basic protein (i.e. positively charged, Raines, 1998). Incubation of a positively charged RNase with metal salts may have repelled metal ions in solution and subsequent reduction of metal salts lead to the aggregation and precipitation of nanoparticles. In addition, the synthesis of nanoparticles in this study was carried out at pH 8.0 which was close to the isoelectric point (pI) of RNase (9.63, Raines, 1998) which supported the fact of poor stabilization of nanoparticles by RNase. Nevertheless, a certain degree of stabilization of metal nanoparticles by RNase observed in this study may result from the binding and stabilization of nanoparticles by sulphur, nitrogen and oxygen atoms of amino acids residues. These atoms have been found/established to also stabilize nanoparticles in proteins (Zhang *et al.*, 2007; Leon *et al.*, 2009).

It was also worth noting that the synthesized nanoparticles generated with these proteins did not affect the overall structural conformation of these proteins as determined by FTIR spectroscopy and other biochemical techniques. Rather, an enhancement of the enzymatic activity of this protein was seen in the presence of some group of metal nanoparticles, which further buttress the reported findings of enhanced efficiency of some protein/enzyme –inorganic nano-biocomposites than their native forms (Varpness *et al.*, 2005; Fei and Perrett, 2009). On the other hand, a decrease in the enzymatic activities observed in some

cases in this study may also prove to be beneficial as potential biomedical targets in the prevention, treatment and management of some diseases. However, in depth studies will have to be done to differentiate between the benefits and demerits of these observed responses.

6.1.2 Interaction of nanoparticles with AChE

The potential neurotoxicity of metallic nanoparticles was determined by an *in vitro* study of their effects on the enzymatic activity of AChE; a very important enzyme in neurotransmission. From the results obtained in this study, it was noticed that nanoparticles synthesized within the interior of HSA and GroEL exhibited the least anti-AChE activity than RNase. This suggested that the cage-like or barrel-like structure of HSA and GroEL may have decreased the neurotoxic effect of nanoparticles when compared with “naked” nanoparticles produced with RNase. The shielding effect of protein cages and thus reduction of toxicity of nanoparticles observed in this study was consistent with what was reported in a similar study (Liu *et al.*, 2011). Furthermore, the encapsulation of nanoparticles may prove beneficial in the area of drug delivery. For instance it has been shown that apoferritin encapsulated platinum nanoparticles can be transported in cells through the receptors in the cells that recognizes apoferritin without much deleterious effect on the cells (Liu *et al.*, 2011). Thus encapsulation of nanoparticles within proteins in this sense can be explored. Notwithstanding, the inhibition of AChE by M-nps-RNase was much lower than what is reported in the literature with chemically synthesized nanoparticles (Wang *et al.*, 2009 and 2010), which confirmed further the benefits of a biological rather than a chemical method.

Conversely, the inhibition of AChE as a biomedical target may still be beneficial as a therapy for cognitive diseases. The use of reversible inhibitors is currently one of the methods used in the treatment and management of memory dysfunctions associated with neuronal loss at the cholinergic system of the brain (Loewenstein *et al.*, 2004; Friedman, 2004; Press and Alexander, 2011). Since nanoparticles were smaller in size than the conventional drugs used and coupled with the fact that they can be attached to biomolecules might allow them entry through the blood brain barrier without causing any major immune response.

6.2 Conclusions

In conclusion, the importance of nanoparticles especially of metallic origin is immensely beneficial and new applications for these nanomaterials is constantly being discovered and reported. The homogeneity of size and shape together with the safety of these nanoparticles is crucial to their applications. A safe and effective method of synthesis is thus required to generate these particles which will be, not only beneficial, but also not constitute a threat to human health and the environment. The biosynthesis and functionalization of nanoparticles using proteins/protein cages might be one of the ways this can be achieved. On the other hand, it is equally important to look at challenges that may be encountered in scaling-up this method of synthesis and its potential application particularly in biomedicine and thus better refined if such problems arise.

6.3 Future work

This research can be considered the beginning of many future studies to come. The findings in this study have led to other research questions which if answered may increase the knowledge and understanding of the importance of protein-inorganic interface in nanotechnology/nanobiotechnology. From this study, it would be important for the relevant applications of biosynthesized particles to:

- 1) Optimize the condition responsible for synthesis of homogeneous sized and shaped nanoparticles in protein/enzyme cages.
- 2) Understand the mechanism that leads to the activation/inhibition of enzymes and proteins attached to or interacted with these particles.
- 3) Determine the mode of inhibition/activation of AChE by these nanoparticles to establish them as a neurotoxin or therapeutic agent.
- 4) Confirm further the non-toxic effects of biologically generated particles by performing further toxicity studies.
- 5) Perform a detailed analysis of the by-products that arises from this method of nanoparticle generation in the event of its adoption in large-scale production.

References

Adili A., Crowe S., Beaux II M.F., Cantrell T., Shapiro P. J., McIlroy D.N. and Gustin K.E. (2008). Differential cytotoxicity exhibited by silica nanowires and nanoparticles. *Nanotoxicology*, **2(1)**:1-8.

Aerospace concepts Pty Ltd – complex systems, engineering specialists.
<http://www.concepts.aero/concepts> , accessed 02/02/2011.

Ahmad A., Senapati S., Khan M.I., Kumar R., Ramani R., Srinivas V. and Sastry M. (2003). Intracellular synthesis of gold nanoparticles by a novel alkalotolerant actinomycete, *Rhodococcus* species. *Nanotechnology*, **14**:824-828.

Aitken R.J., Creely K.S. and Tran C.L. (2004). Nanoparticles: An occupational hygiene review. www.hse.gov.uk/research/rrpdf/rr274.pdf, accessed on 03/03/2011.

Akiyoshi K., Sasaki Y. and Sunamoto J. (1999). Molecular chaperone-like activity of hydrogel nanoparticles of hydrophobized pullulan: Thermal stabilization with refolding of carbonic anhydrase B. *Bioconjugate Chemistry*, **10**:321-324.

Alexandrova K., Markova – Deneva I., Gigova A. and Dragieva I. (2008). TEM/SEM and FT-IR characterization of biocompatible magnetic nanoparticles. *Multi-Material Micro Manufacture S. Dimov and W. Menz (Eds.). Published by Whittles Publishing Ltd.* Pg. 1-4.

Alvarez M.M., Khoury J.T., Schaaff T.G., Shafigullin M.N., Vezmar I. and Whetten R.L. (1997). Optical absorption spectra of nanocrystal gold molecules. *Journal of Physical Chemistry B*, **101**:3706–3712.

Ardelt W., Ardel B. and Darzynkiewicz Z. (2009). Ribonucleases as potential modalities in anticancer therapy. *European Journal of Pharmacology*, **625**:181-189.

Arnold U. and Ulbrich-Hofmann R. (1997). Kinetic and thermodynamic thermal stabilities of ribonuclease A and ribonuclease B. *Biochemistry*, **36**:2166-2172.

-
- Arnold U. and Ulbrich-Hofmann R. (2006). Natural and engineered ribonucleases as potential cancer therapeutics. *Biotechnology Letters*, **28**:1615-1622.
- Arrondo J.L.R. and Goni F.M. (1993). Infrared spectroscopic studies of lipid-protein interactions in membranes. In: Watts A. *Protein-Lipid Interactions*. Amsterdam: Elsevier Science. 321-349.
- Arufe M.I., Arellano J.M., García L., Albendín G. and Sarasquete C. (2007). Cholinesterase activity in gilthead seabream (*Sparus aurata*) larvae: characterization and sensitivity to the organophosphate azinphosmethyl. *Aquatic Toxicology*, **84**:328-336.
- Astruc D.D. (2008). Transition metal nanoparticles in catalysis: From historical background to the state of the art. . In: Astruc D.D *Nanoparticles and Catalysis*. Weinheim: Verlag GmbH & Co. KGaA. 1-48.
- Bakker G.R. and Boyer R.F. (1986). Iron incorporation into Apoferritin: The role of Apoferritin as a ferroxidase. *Journal of Biological Chemistry*, **261(28)**:13182-13185.
- Barnard E. (1969). Biological function of pancreatic ribonuclease. *Nature*, **221**:340-344.
- Bello D., Hsieh S-F., Schmidt D. and Rogers E. (2009). Nanomaterials properties vs. biological oxidative damage: Implications for toxicity screening and exposure assessment. *Nanotoxicology*, **3(3)**:249-261.
- Benito A., Ribó M. and Vilanova M. (2005). On the track of antitumour ribonucleases. *Molecular BioSystems*, **1**:294-302.
- Bentley J., Gilliss S.R., Carter C.B., Al-Sharab J. F., Cosandey F., Anderson I. M. and Kotula P. J. (2006). Nanoscale EELS analysis of oxides: composition mapping, valence determination and beam damage. *Journal of Physics: Conference Series*, **26**:69–72.

-
- Bhadeshia H.K.D.H. (2002). Differential thermal, *Thermal analysis techniques*, University of Cambridge, Material Science & Metallurgy.
<http://www.msm.cam.ac.uk/phase-trans/2002/Thermal1.pdf>, accessed 26/06/2011.
- Bhushan B. (2004). Scanning probe microscopy- Principle of operation, instrumentation and probes. In: Bhushan B. *Handbook of Nanotechnology*. New York: Springer-Verlag Berlin Heidelberg. 325-369
- Binnig G. and Quate C.F. (1986). Atomic force microscope. *Physical Review letters*, **56**:930-933.
- Binning G. Rohrer H., Gerber C. and Weibel E. (1982). Surface studies by scanning tunneling microscopy. *Physical Review letters*, **49**:57-61.
- Blackman J.A. (2009). Metallic nanoparticles. In: Misra P. and Black J.A. *Handbook of metal physics*. Amsterdam: Elsevier B.V. 4-6.
- Bollag D.M., Rozycki M.D. and Edelstein S.J. (1996). Protein methods. 2nd ed. New York: Wiley-Liss Inc.. 107-172.
- Bonander R. (2011). Platinum-based cancer treatment.
<http://platinum.cancertreatment.net/>, accessed on 17/11/2011.
- Bradbury S., Ford B.J. and Joy D.C. (2011). Scanning electron microscope.
<http://www.britannica.com/EBchecked/topic/526571/scanning-electron-microscope-SEM>, accessed on 16/05/2011.
- Bradford M.M. (1976). A rapid and sensitive method for quantitation of microgram quantities of protein utilizing the principle of protein-dye binding. *Analytical Biochemistry*, **72(1-2)**:248-254.
- Brook M.A. (2006). Platinum in silicone breast implants. *Biomaterials*, **27(17)**:3274-3286.
-

-
- Bryce, C.F.A. and Crichton, R.R. (1973). The catalytic activity of Horse spleen apoferritin. *Biochemical Journal*, **133**: 301-309.
- Bucur B., Dondoï M., Danet A. and Marty J. L. (2005). Insecticide identification using flow injection analysis system with biosensors based on various cholinesterases. *Analytica Chimica Acta*, **539(1-2)**:195-201.
- Bunton J., Lenz D., Olson J., Thompson K., Ulfig R., Larson D. and Kelly T (2006). Advances in instrumentation and techniques-atom probe field ion microscopy: Instrumentation developments in atom probe tomography: Applications in semiconductor Research. *Microscopy and Microanalysis*, **12 (2)**:1730–1731.
- Butt C.A., Swift J., Kang S., Costanzo L.D., Christianson D.W., Saven J.G. and Dmochowski I.J. (2008). Direct noble metal ion chemistry within a designed ferritin protein. *Biochemistry*, **47(48)**:12729-12739.
- Buu N.Q., Chau N.H., Dung N.T.T. and Tien N.G. (2011). Studies on manufacturing of topical wound dressings based on nanosilver produced by aqueous molecular solution method. *Journal of Experimental Nanoscience*, **6(4)**: 409-421.
- Cai W., Gao T., Hong H., and Sun J. (2008). Applications of gold nanoparticles in cancer nanotechnology. *Nanotechnology: Science and Applications*, **1**:17-32.
- Calbick C. J. (1963). The discovery of electron diffraction. *The Physics Teacher*, **1(2)**:63-69.
- Campbell C.T., Sharp J.C., Yao Y.X., Karp E.M. and Silbaugh T.L. (2011). Insights into catalysis by gold nanoparticles and their support effects through surface science studies of model catalysts. *Faraday Discussions*, **152**:227-239.
- Chaspeen N. D. (1998). Ferritin: Uptake, storage and release of iron. In: Sigel A. and Sigel H. *Iron transport and storage in microorganisms, plants and animals*. New York: Marcel Dekker, Inc. 479-514.

Chen J., Saeki F., Wiley B.J., Cang H., Cobb M.J. Li Z.Y., Au L., Zhang H., Kimmey M.B., Li X. D. and Xia Y. (2005). Gold nanocages: bioconjugation and their potential use as optical imaging contrast agents. *Nano Letters*, **5**:473-477.

Cho S. and Zhang J. (2007). Zebrafish ribonucleases are bactericidal: implications for the origin of vertebrate RNase A superfamily. *Molecular Biology and Evolution*, **24**(5):1259-1268.

Chu S., Graybeal J. D., Hurst G. S. and Stoner J. O. Jr.(2011). Spectroscopy. www.britannica.com/EBchecked/topic/558901/spectroscopy, accessed on 03/06/2011.

Cortie M.B. and van der Lingen E. (2002). Catalytic gold nanoparticles. *Materials Forum*, **26**:1-14.

Coxworth B. (2011). Gold nanoparticles boost organic solar cell efficiency. <http://www.gizmag.com/gold-nanoparticles-boost-solar-cell-efficiency/19565/>, accessed on 24/11/11.

Cuenya B.R., Croy J.R., Mostafa S., Behafarid F., Li L., Zhang Z., Yang J.C., Wang Q. and Frenkel A.I. (2010). Solving the structure of size-selected Pt nanocatalysts synthesized by inverse micelle encapsulation. *Journal of the American Chemical Society*, **132**:8747-8756.

Cui D., Zhang H., Wang K., Gao F., Zhang X., Asahi T., He R. and Osaka T. (2011). Gold nanoparticles enhance efficiency of *in vitro* gene transcription-translation system. *Nano Biomedicine and Engineering*, **3**(1):120-125.

de la Escosura A., Nolte R. J. M. and Cornelissen J. J. L. M. (2009). Viruses and protein cages as nanocontainers and nanoreactor. *Journal of Materials Chemistry*, **19**(16):2274-2278.

De M. and Rotello V.M. (2008). Synthetic "chaperones": Nanoparticle-mediated refolding of thermally denatured proteins. *Chemical Communications*, **14**(30):3504-3506.

-
- Deng Q.Y., Yang B., Wang J.F., Whiteley C.G. and Wang X. N. (2009). Biological synthesis of platinum nanoparticles with apoferritin. *Biotechnology Letters*, **31**:1505-1509.
- Dieringer J.A., McFarland A. D., Shah N.C., Stuart D. A., Whitney A. V., Yonzon C. R., Young M.A., Zhang X. and Van Duyne R. P. (2006). Surface enhanced Raman spectroscopy: New materials, concepts, characterization tools, and applications. *Faraday Discussions*, **132**:9–26.
- Dolye M.E (2006). *Nanotechnology: A brief literature review*. Madison: [Food Research Institute, UW-Madison, 33-37.
http://www.wisc.edu/fri/briefs/FRIBrief_Nanotech_Lit_Rev.pdf , accessed on 10/02/2011.
- Domínguez-Vera J.M., Gálvez, Sánchez P., Mota A.J., Trasobares S., Hernández J.C. and Calvino J.J. (2007). Size-controlled water-soluble Ag nanoparticles. *European Journal of Inorganic Chemistry*, 4823-4826.
- Douglas, T. and Ripoll, D.R. (1998). Calculated electrostatic gradients in recombinant H-chain ferritin. *Protein Science*, 7:1083-1091.
- Dubey S. P., Lahtinen M. and Sillanpää M. (2010). Tansy fruit mediated greener synthesis of silver and gold nanoparticles. *Process Biochemistry*, **45(7)**:1065-1071.
- Durán N., Marcato P. D., De Souza G. I. H., Alves O. L. and Esposito E. (2007). Antibacterial effect of silver nanoparticles produced by fungal process on textile fabrics and their effluent treatment. *Journal of Biomedical Nanotechnology*, **3**:203-208.
- Eby D. M., Luckarift H. R. and Johnson G. R. (2009). Hybrid antimicrobial enzyme and silver nanoparticle coatings for medical instruments. *Applied Materials and Interfaces*, **1(7)**:1553-1560.
- Egerton R.F. (2005). Imaging with electrons. In: Egerton R.F. *Physical principles of electron microscopy: an introduction to TEM, SEM, and AEM*. New York: Springer Science+Business Media, Inc. 34-155
-

-
- Einhorn L.H. (1990). Treatment of testicular cancer: a new and improved model. *Journal of Clinical Oncology*, **1**:1777-1781.
- Elechiguerra J.L., Burt J.L., Morones J.R., Camacho-Bragado A., Gao, X., Lara, H.H. and Yacaman M.J. (2005). Interaction of silver nanoparticles with HIV-1. *Journal of Nanobiotechnology*, **3(6)**:1-10.
- El-Sayed M. and Link S. (2000). Shape and size dependence of radiative, nonradiative and photothermal properties of gold nanocrystals. *International Reviews in Physical Chemistry*, **19 (3)**: 409-453.
- Esfanda R. and Tomalia D. A. (2001). Poly(amidoamine) (PAMAM) dendrimers: from biomimicry to drug delivery and biomedical applications. *Drug Discovery Today*, **6**:427-436.
- Eustis S. and El-Sayed M. A. (2005). Why gold nanoparticles are more precious than pretty gold: Noble metal plasmon resonance and its enhancement of radiative and nonradiative properties of nanocrystals of different shapes. *Chemical Society Reviews*, **36**:209-217.
- Fairbanks G., Steck T.L. and Wallach D.F.H (1971). Electrophoretic analysis of the major polypeptides of the human erythrocyte membrane. *Biochemistry*, **10**:2606-2617.
- Fan H. and Mark A.E. (2006). Mimicking the action of GroEL in molecular dynamics simulations: Application to the refinement of protein structures. *Protein Science*, **15**:441-448.
- Fan J. Yin J.-J., Ning B., Wu X., Hu Y., Ferrari M., Anderson G. J., Wei J., Zhao Y. and Nie G. (2011). Direct evidence for catalase and peroxidase activities of ferritin-platinum nanoparticles. *Biomaterials*, **32**:1611-1618.
- Fan R., Chew S.W., Cheong V.V. and Orner B.P. (2010). Fabrication of gold nanoparticles inside unmodified apoferritin. *Small*, **14**:1483-1487.

-
- Fei L. and Perrett S. (2009). Effect of nanoparticles on protein folding and fibrillogenesis. *International Journal of Molecular Sciences*, **10**:646-655.
- Fratoddi I., Venditti I., Battocchio C., Polzonetti G., Cametti C. and Russo M.V. (2011). Core shell hybrids based on noble metal nanoparticles and conjugated polymers: Synthesis and characterization. *Nanoscale Research Letters*, **6**:98.
- Friedman J.I. (2004). Cholinergic targets for cognitive enhancement in schizophrenia focus on cholinesterase inhibitors and muscarinic agonists. *Psychopharmacology*, **174**:45-53.
- Gabor L.H., Joydeep D., Harry F.T. and Anil K.R. (2008). Characterization methods. In: Gabor L.H., Joydeep D., Harry F.T. and Anil K.R. *Introduction to nanoscience*. Boca Raton: CRC press Taylor & Francis group. 108-175.
- Gallagher W. (2005). FTIR Analysis of Protein Structure. http://www.chem.uwec.edu/Chem455_S05/Pages/Manuals/FTIR_of_proteins.pdf , accessed on 19/09/2011.
- Gálvez N., Fernandez B., Valero E., Sánchez P., Cuesta R. and Domínguez-Vera J. (2008). Apoferritin as a nanoreactor for preparing metallic nanoparticles. *C.R. Chimie*, **11**:1207-1212.
- Gálvez, N., Sanchez, P. and. Domínguez -Vera, J. M. (2005). Preparation of Cu and CuFe prussian blue derivative nanoparticles using apoferritin cavity as nanoreactor. *Dalton Trans.*, 2492-2494.
- Gálvez, N., Sánchez, P., Domínguez-Vera, J.M., Soriano-Portillo, A., Clemente-León, M. and Coronado, E. (2006). Apoferritin-encapsulated Ni and Co superparamagnetic nanoparticles. *Journal of Material Chemistry*, **16**: 2757-2761.
- Gardea-Torresdey J. L., Peralta-Videa J. R., Parsons J.G., Mokgalaka N. S. and Guadalupe}pade la Rosa. (2008). Production of metal nanoparticles by plants and plant-derived materials. In: Corain B., Schmid G. and Toshima N. *Metal Nanoclusters*
-

in *Catalysis and Materials Science: The issue of size control*. New York, Boston: Elsevier. 401-411.

Geiger R., Gautschi M., Thor F., Hayer A. and Helenius A. (2011). Folding, quality control and secretion of pancreatic ribonuclease in live cells. *Journal of Biological Chemistry*, **286**(7):5813-5822.

Genelink (2011). RNase A. http://www.genelink.com/Literature/ps/PS40-5101_RNase%20A%20Ver%201.3.pdf , accessed on 18/11/2011.

Gierling M., Schneeweiss P., Visanescu G., Federsel P., Häffner M., Kern D.P., Judd T.E., Günther A. and Fortágh J. (2011). Cold-atom scanning probe microscopy. *Nature Nanotechnology*, **6**:446-451.

Goedken E.R. and Marqusee S. (1999). Metal binding and activation of the ribonuclease H domain from Moloney murine leukemia virus. *Protein Engineering*, **12**(11):975-980.

Goldstein J., Newbury D., Joy D., Lyman C., Echlin P., Lifshin E., Sawyer L. and Michael J. (2003). *Scanning electron microscopy and x-ray microanalysis*. 3rd ed. New York: Kluwer Academic/Plenum Publishers. 3-50

González-Díaz J.B., García-Martín A., García-Martín J.M., Cebollada A., Armelles G., Sepúlveda B., Alaverdyan Y. and Käll M. (2008). Plasmonic Au/Co/Au nanosandwiches with enhanced magneto-optical activity. *Small*, **4**(2): 202–205.

González-Szwacki N., Sadrzadeh A. and Yakobson B. (2007). B₈₀ Fullerene: an *ab initio* prediction of geometry, stability, and electronic structure. *Physical Review Letters*, **98**:166804-166808.

Gopakumar G., Nguyen M.T. and Ceulemans A. (2008). The boron buckyball has an unexpected T_h symmetry. *Chemical Physics Letters*, **450**:475-477.

-
- Govender Y., Riddin T., Gericke M. and Whiteley C.G. (2009). Bioreduction of platinum salt into nanoparticles: A mechanistic perspective. *Biotechnology Letters*, **31**:95- 100.
- Graff A., Benito S.M., Verbert C. and Meier W. (2004). Polymer nanocontainers nanobiotechnology. In: Niemeyer C.M. and Mirkin C.A. *Concepts, Applications and Perspectives*. Weinheim: WILEY-VCH Verlag GmbH & Co. KGaA. 168-170
- Grdadolnik J. (2002). A FTIR investigation of protein conformation. *Bulletin of the Chemists and Technologists of Macedonia*, **21**(1):23-34.
- Grieger K. D., Hansen S.F. and Baun A. (2009). The known unknowns of nanomaterials: Describing and characterizing uncertainty within environmental, health and safety risks. *Nanotoxicology*, **3**(3):222-233.
- GTIR Nanotechnology Lab. (2011). Carbon nanotubes. <http://eosl.gtri.gatech.edu/Home/Homep2/Homep3/Homep4/tabid/666/Default.aspx> , accessed on 03/02/2011.
- Gupta A.K. and Curtis A.S.G. (2004). Lactoferrin and ceruloplasmin derivatized superparamagnetic iron oxide nanoparticles for targeting cell surface receptors. *Biomaterials*, **25**(15):3039-3040.
- Gupta A.K. and Gupta M. (2005). Synthesis and surface engineering of iron oxide nanoparticles for biomedical applications. *Biomaterials*, **26**(18):3995-4021.
- Hanna P.M., Chen Y. and Chasteen. (1991). Initial iron oxidation in horse spleen apoferritin: Characterization of mixed-valence iron (II)-iron (III) complex. *Journal of Biological Chemistry*, **266**(2): 886-893.
- Harding L., King W. P., Dai X., Craig D. Q. M. and Reading M. (2007). Nanoscale characterization and imaging of partially amorphous materials using local thermomechanical analysis and heated tip AFM. *Pharmaceutical Research*, **24**(11):2048-2054.
-

-
- Haris P. I. and Severcan F. (1999). FTIR spectroscopic characterization of protein structure in aqueous and non-aqueous media. *Journal of Molecular Catalysis B: Enzymatic*, **7**:207-221.
- Harkness K. M., Cliffler D. E. and McLean J. A. (2010). Characterization of thiolate-protected gold nanoparticles by mass spectrometry. *Analyst*, **135**:868-874.
- Hashim A.S.K. (2005). The catalysis gold rush: New claims. *Angewandte Chemie International Edition*, **44**:6990 – 6993
- Helmers E. (1997). Platinum emission rate of automobiles with catalytic converters: Comparison and assessment of results from various approaches. *Environmental Science and Pollution Research*, **4**(2):99-103.
- Henry C.R. (2005). Morphology of supported nanoparticles. *Progress in Surface Science*, **80**:92–116.
- Herrera J.E. and Sakulchaicharoen N. (2009). Microscopic and spectroscopic characterization of nanoparticles, pg.238-249.
<http://www.eng.uwo.ca/people/jherrera/bookchapter1.pdf>, accessed on 18/06/2011.
- Hiep H.M., Endo T., Kerman K., Chikae M., Kim D., Yamamura S., Takamura Y. and Tamiya E. (2007). A localized surface plasmon resonance based immunosensor for the detection of casein in milk. *Science and Technology of Advanced Materials*, **8**(4):331-338.
- Hirsch L.R., Stafford R.J., Bankson J.A., Sershen S.R., Rivera B., Price R.E., Hazle J.D., Halas N.J. and West J.L. (2003). Nanoshell-mediated near-infrared thermal therapy of tumors under magnetic resonance guidance. *Proceeding of the National academy of Science*, **100**:13549-13554.
- Hoenig D. and Moebiu D. (1991). Direct visualization of monolayers at the air-water interface by Brewster angle microscopy. *Journal of Physical Chemistry*, **95** (12):4590–4592.
-

-
- Hoffmann F. and Rinas U. (2004). Roles of heat-shock chaperones in the production of recombinant proteins in *Escherichia coli*. *Advances in Biochemical Engineering/Biotechnology*, **89**:143-161.
- Hofmann-Antenbrink M., von Rechenberg B. and Hofmann H. (2009). Superparamagnetic nanoparticles for biomedical applications. In: Tan M. C., Chow M.G. and Ren L. *Nanostructured Materials for Biomedical Applications*. Kerala: Transworld Research Network. 119-121.
- Horst H. (1997). Gas phase synthesis of nanocrystalline materials. *Nanostructured Materials*, **9**:3-12.
- Howe J. M., Mori H. and Wang Z. L. (2008). In situ high-resolution transmission electron microscopy in the study of nanomaterials and properties. *Materials Research Society Bulletin*, **33**(2):115–121.
- Hsieh J., Koutmou K.S., Rueda D., Koutmos M., Walter N. G. and Fierke (2010). A divalent cation stabilizes the active conformation of the B.subtilis RNase P.Pre-tRNA complex: A role for an inner-sphere metal ion in RNase P. *Journal of Molecular Biology*, **400**:36-51.
- Huang X., Jain P. K., El-Sayed H.I. and El-Sayed M. A. (2007). Gold nanoparticles: Interesting optical properties and recent applications in cancer diagnostics and therapy. *Nanomedicine*, **2**(5): 681-693.
- Ikeda K., Okada T., Sawada S., Akiyoshi K. and Matsuzaki K. (2006). Inhibition of the formation of amyloid beta-protein fibrils using biocompatible nanogels as artificial chaperones. *FEBS Letters*, **580**:6587-6595.
- Inoue K., Takano H., Yanagisawa R., Hirano S., Sakurai M., Shimada A. and Yoshikawa T. (2006). Effect of airway exposure to nanoparticles on lung inflammation induced by bacteria endotoxin in mice. *Environmental Health perspectives*, **114**(9):1325-1330.
-

-
- Insight experts (2008). Transmission electron microscopy (TEM). <http://www.e-microscopy.com/info?id=5>, accessed on 17/05/2011.
- IOM, (2008). Risk assessment of nanoparticles. www.iom-world.org/research/nps.php, accessed on 29/11/2010.
- IR wizard (2011). <http://infrared.als.lbl.gov/content/web-links/60-ir-band-positions>, accessed on 09/11/2011.
- Ishii D., Kinbara K., Ishida Y., Ishii N., Okochi M., Yohda M. and Aida T. (2003). Chaperonin-mediated stabilization and ATP-triggered release of semiconductor nanoparticles. *Nature*, **423**:628-632.
- Iwahori, K. and Yamashita, I. (2007). Biotemplates synthesis of nanoparticle by cage-shaped protein supramolecule, apoferritin. *Journal of Cluster Science*, **18(2)**:358-370.
- Jabs A. (2005). Determination of secondary structure in proteins by Fourier transform spectroscopy (FTIR). *Jena Library of Biological Macromolecules*. http://www.imb-jena.de/ImgLibDoc/ftir/IMAGE_FTIR.html, accessed on 1/11/2011.
- Jae S. and Beom K. (2009). Rapid biological synthesis of silver nanoparticles using plant leaf extracts. *Bioprocess and Biosystems Engineering*, **32(1)**:79-84.
- Jahanshahi M., Najafpour G.D., Rahimnejad M. (2008). Applying the Taguchi method for optimized fabrication of bovine serum albumin (BSA) nanoparticles as drug delivery vehicles. *African Journal of Biotechnology*, **7(4)**:362-367.
- Jain K.K. (2005). The role of nanobiotechnology in drug discovery. *Drug Discovery Today*, **10**:1435-1442.
- Jain P. and Pradeep T. (2005). Potential of silver nanoparticle-coated polyurethane foam as an antibacterial water filter. *Biotechnology and Bioengineering*, **90(1)**:59-63.

Jason K.N., Grass M. E., Somorjai G. and Marsh A. L. (2009). Characterization of colloidal platinum nanoparticles by MALDI-TOF mass spectroscopy, *Analytical Chemistry*, **81(15)**:6295-6299.

Jeffrey, C. E.; Read, N. D. (1991). Ambient- and low-temperature scanning electron microscopy. In: Hall J. L. and Hawes C.R. *Electron microscopy of plant cells*. London: Academic Press. 313–413.

Joao H. and Dwek R. A. (1993). Effects of glycosylation on protein structure and dynamics in ribonuclease B and some of its individual glycoforms, *European Journal of Biochemistry*, **218**:239-244.

Johans C. (2003). Novel routes to metal nanoparticles: Electrodeposition and reactions at liquid/liquid interfaces. *Dissertation for the degree of Doctor of Science in Technology*, Helsinki University of Technology. ISBN 951-22-6467-6.

Joshi M., Bhattacharyya A. and Ali S.W. (2008). Characterization techniques for nanotechnology applications in textiles. *Indian Journal of Fibre & Textile Research*, **33**:304-317.

Kaegi R., Voegelin A., Sinnet B., Zuleeg S., Hagendorfer H., Burkhardt M. and Siegrist H. (2011). Behavior of metallic silver nanoparticles in a pilot wastewater treatment plant. *Environmental Science and Technology*, **45**:3902-3908.

Kagan V. E., Bayir A. and Shvedova A.A. (2005). Nanomedicine and nanotoxicology: two sides of the same coin. *Nanomedicine*, **1**:313-316.

Kamireddi M., Eisenstein E. and Reddy P. (1997). Stable expression and rapid purification of *Escherichia coli* GroEL and GroES chaperonins. *Protein Expression and Purification*, **11**:47-52.

Kaushik N.T., Snehit S.M. and Rasesh Y.P. (2009). Biological synthesis of metallic nanoparticles.

http://www.researchgate.net/publication/26679976_Biological_synthesis_of_metallic_nanoparticles, accessed on 14/02/2011.

-
- Keast V. J., Kappers M. J. and Humphreys C. J. (2003). Electron energy-loss near edge structure (ELNES) of InGaN quantum wells. *Journal of Microscopy*, **210(1)**:89–93.
- Kelland L. (2007). The resurgence of platinum-based cancer chemotherapy. *Nature Reviews Cancer*, **7**:573-584.
- Kelsall R.W., Hamley I.W. and Geoghegan M. (2005). *Nanoscale science and technology*. London: John Wiley&Sons Ltd. 40-58.
- Kijima T., Yoshimura T., Uota M., Ikeda T., Fujiyama D., Mouri S. and Uoyama S. (2003). Noble-metal nanotubes (Pt, Pd, Ag) from lyotropic mixed-surfactant liquid-crystal templates, *Angewandte Chemie*, **116(2)**:230-234.
- Kishida M., Hanaoka T., Hayashi H., Tashiro S. and Wakabayashi K. (1998). Novel preparation method for supported metal catalysts using microemulsion - Control of catalyst surface area. *Studies in Surface Science and Catalysis*, **118**:265-268.
- Klem M. T., Young M. and Douglas T. (2005). Biomimetic magnetic nanoparticles. *Materials Today*, 28-37. ISSN: 1369 7021 © Elsevier Ltd 2005.
- Klink T.A., Woycechowsky K.J., Taylor K.M. and Raines R.T. (2000). Contribution of disulfide bonds to the conformational stability and catalytic activity of ribonuclease A. *European Journal of Biochemistry*, **267**:566-572.
- Kokura S., Handa O., Takagi T., Ishikawa T., Naito Y. and Yoshikawa T. (2010). Silver nanoparticles as a safe preservative for use in cosmetics. *Nanomedicine: Nanotechnology, Biology and Medicine*, **6**:570-574.
- Kong J. and Yu S. (2007). Fourier transform infrared spectroscopic analysis of protein secondary structures. *Acta Biochimica et Biophysica Sinica*, **39(8)**:549-559.
- Krebs R.E. (2006). Platinum. In: Krebs R.E. *The history and use of our earth's chemical elements: a reference guide*. 2nd ed. Westport: Greenwood Publishing Group. 162-167.

-
- Kroto H.W. and Walton D.R.M. (2011). Fullerene. *Encyclopædia Britannica Online*, <http://www.britannica.com/EBchecked/topic/221916/fullerene>, accessed on 04/02/2011.
- Kyprianidou-Leodidou T., Caseri W. and Suter U.W. (1994). Size variation of PbS particles in high-refractive-index nanocomposites. *Journal of Physical Chemistry*, **98**:8992-8997.
- Leland P.A. and Raines R. T. (2001). Cancer chemotherapy-ribonucleases to the rescue. *Chemistry & Biology*, **8**:405-413.
- León Y., Brito I., Cárdenas G. and Godoy O. (2009). Synthesis and characterizations of Ag, Cu and AgCu metallic nanoparticles stabilized by divalent sulfur ligands. *Journal of Chilean Chemical Society*, **54(1)**:51-54.
- Leslie-Pelecky D.L. and Reike R.D. (1996). Magnetic properties of nanostructured materials. *Chemistry of Material*, **8**:1770-1783.
- Li W., Sun C., Hou B. and Zhou X. (2011). Room temperature synthesis and catalytic properties of surfactant-modified Ag nanoparticles. *International Journal of Spectroscopy*, **2012**:1-7.
- Liu W., Wu Y., Wang C., Li H. C., Wang T., Liao C. Y., Cui L., Zhou Q. F., Yan B. and Jiang G.B. (2010). Impact of silver nanoparticles on human cells: Effect of particle size. *Nanotoxicology*, **4(3)**:319-330.
- Liu W.T. (2006). Nanoparticles and their biological and environmental applications. *Journal of Bioscience and Bioengineering*, **102(1)**:1-7.
- Liu X., Wei W., Wang C., Yue H., Ma D., Zhu C., Ma G. and Du Y. (2011). Apoferritin-camouflaged Pt nanoparticles: surface effects on cellular uptake and cytotoxicity. *Journal of Materials Chemistry*, **21**:7105-7110.

-
- Liu Z., Ling X. Y., Su X., and Lee J. Y. (2004). Carbon-supported Pt and PtRu nanoparticles as catalysts for a direct methanol fuel cell. *Journal of Physical Chemistry B*, **108**:8234-8240.
- Liz-Marzán L.M. (2004). Nanometals: formation and color. *Materials Today*, 26-31.
- Loewenstein D. A., Acevedo A., Czaja S.J. and Duara R. (2004). Cognitive rehabilitation of mildly impaired Alzheimer disease patients on cholinesterase inhibitors. *American Journal of Geriatric Psychiatry*, **12(4)**:395-402.
- Lu C., Dönch I., Nolte M. and Fery A. (2006). Au nanoparticle-based multilayer ultrathin films with covalently linked nanostructures: Spraying layer-by-layer assembly and mechanical property characterization. *Chemistry of Materials*, **18 (26)**:6204–6210.
- Luther W. (2004). Bottom-up method for making nanotechnology products. *Future Technologies Division of VDI (Verein Deutscher Ingenieure)*. Report: Industrial Application of nanomaterials - Chances and Risks: Technology Analysis. <http://www.azonano.com/Details.asp?ArticleID=1079> , accessed 12/03/2011.
- Macara I.G., Hoy T.G. and Harrison P.M. (1972). The formation of ferritin from apoferritin: Kinetics and Mechanism of Iron uptake. *Biochemical Journal*, **126**:151-162.
- Macara I.G., Hoy T.G. and Harrison P.M. (1973). The formation of ferritin from apoferritin: Catalytic action of Apoferritin. *Biochemical Journal*, **135(2)**:343-348
- MacDonald N. C. and Waldrop, J. R. (1971). Auger electron spectroscopy in the scanning electron microscope: Auger electron images. *Applied Physics Letters*, **19(9)**:315-318.
- Marshall T. and Williams K. (1986). Phenol addition to the Bradford dye binding assay improves sensitivity and gives a characteristic response with different proteins. *Journal of Biochemical and Biophysical Methods*, **13(3)**:145-150.

-
- Martel R., Derycke V., Lavoie C., Appenzeller J., Chan K. K., Tersoff J., Avouris Ph. (2001). Ambipolar electrical transport in semiconducting Single-wall carbon nanotubes, *Physical Review Letters*, **87**:256805-256809.
- Marx K. A. (2003). Quartz crystal microbalance: A useful tool for studying thin polymer films and complex bimolecular systems at the solution interface *Biomacromolecules*, **4**(5):1099-1120.
- Matoušek J. (2001). Ribonucleases and their antitumor activity. *Comparative Biochemistry and Physiology Part C*, **129**:175-191.
- Mayes E.L. and Mann S. (2004). Mineralization in nanstructured biocompartments: Ferritin for high-density data storage. In: Niemeyer, C.M. and Mirkin, C.A. *Nanobiotechnology: Concepts, Applications and Perspectives*. Weinheim: WILEY-VCH Verlag GmbH & Co. KGaA. 278-287.
- McMillan R.A., Paavola C.D., Howard J., Chan S.L., Zaluzec N.J. and Trent J.D. (2002). Ordered nanoparticle arrays formed on engineered chaperonin protein templates, *Nature Materials*, **1**:247-252.
- McNeil S.E. (2011). Challenges for nanoparticle characterization. In: McNeil S.E. *Characterization of Nanoparticles Intended for Drug Delivery*. London: Humana Press. 9-6.
- Melkani G.C., Zardeneta G. and Mendoza J.A. (2003). The ATPase activity of GroEL is supported at high temperatures by divalent cations that stabilize its structure. *Biomaterials*, **16**:479-484.
- Mendoza J.A., Warren T. and Dulin P. (1996). The ATPase activity of chaperonin GroEL is highly stimulated at elevated temperatures. *Biochemical and Biophysical Research Communications*, **229**:271-274.
- Mintmire J.W., Dunlap B.I. and White C.T. (1992). Are fullerene tubules metallic? *Physical Review Letters*, **68** (5):631-634.
-

-
- Mironava T., Hadjiargyrou M., Simon M., Jurukovski V. and Rafailovich M.H. (2010). Gold nanoparticles cellular toxicity and recovery: Effect of size, concentration and exposure time. *Nanotoxicology*, **4**(1):120-137.
- Mishra M., Kumar H. and Tripathi. (2008). Diabetic delayed wound healing and the role of silver nanoparticles. *Journal of Nanomaterials and Biostructures*, **3**(2):49-54.
- Mitsudome T., Arita S., Mori H., Mizugaki T., Jitsukawa K. and Kaneda K. (2008). Supported silver-nanoparticles-catalyzed highly efficient aqueous oxidation of phenylsilanes to silanols. *Angewandte Chemie*, **120**:8056-8058.
- Modisakeng K.W., Jiwaji M., Pesce E-R., Robert J., Amemiya C.T., Dorrington R.A. and Blatch G.L. (2009). Isolation of *Latimera menadoensis* heat shock protein 70 (Lmhs70) that has all the features of an inducible gene and encodes a functional molecular chaperone. *Molecular Genetics & Genomics*, **282**:185-196.
- Mohanty A., Garg N. and Jin R. (2010). A universal approach to the synthesis of noble metal nanodendrites and their catalytic properties. *Angewandte Chemie International Edition*, **49**:4962-4966.
- Monti D.M., Yu W., Pizza E., Shima K., Hu M.G., DiMalta C., Piccoli R., D'Alessio G. and Hu G.F. (2009). Characterization of the angiogenic activity of zebrafish ribonucleases. *FEBS Journal*, **276**(15):4077-4090.
- Moore A. and Goettmann F. (2006). The plasmon band in noble metal nanoparticles: an introduction to theory and applications. *New Journal of Chemistry*, **30**:1121-1132.
- Morais P.C., Santos R.L., Pimenta A.C.M., Azevedo R.B. and Lima E.C.D. (2006). Preparation and characterization of ultra-stable biocompatible magnetic fluids using citrate-coated cobalt ferrite nanoparticles. *Thin Solid Films*, **515**(1):266-270.
- Moretti G. (2003). Auger spectroscopy. In: Briggs D. and Grant J.T *Surface analysis by auger and X-ray photoelectron spectroscopy*. Chichester: Surface spectra and IM Publications. 501-530.
-

-
- Mukherjee P., Ahmad A., Mandal D., Senapati S., Sainkar S.R., Khan M.I., Ramani R., Parischa R., Ajayakumar P.V., Alam M., Sastry M. and Kumar R. (2001). Bioreduction of AuCl_4^- ions by the fungus, *Verticillium* sp. and surface trapping of the gold nanoparticles formed. *Angewandte Chemie- International edition*, **40(19)**:3585-3588.
- Müller E.W., Panitz J.A. and McLane S.B. (1968). The atom-probe field ion microscope. *Review of Scientific Instruments*, **39**:83-86.
- Murray C.B., Kagan C.R. and Bawendi M. G. (2000). Synthesis and characterization of monodisperse nanocrystals and close-packed nanocrystal assemblies. *Annual Review of Materials Research*, **30 (1)**:545–610.
- Murray C.B., Norris D.J. and Bawendi M.G. (1993). Synthesis and characterization of nearly monodisperse CdE (E= sulfur, selenium, tellurium) semiconductor nanocrystallites. *Journal of the American Chemical Society*, **115(19)**:8706-8715.
- Nam J.M., Thaxton C.S. and Mirkin C.A. (2003). Nanoparticle-based bio-bar codes for the ultrasensitive detection of proteins. *Science*, **301**:1884-1886.
- Narayana K. B. and Sakthivel N. (2010). Biological synthesis of metal nanoparticles by microbes. *Advances in Colloids and Interface Science*, **156(1-2)**:1-3.
- Neuberger T., Schöpf B., Hofmann H., Hofmann M. and Von Rechenberg B. (2005). Superparamagnetic nanoparticles for biomedical applications: Possibilities and limitations of a new drug delivery system. *Journal of Magnetism and Magnetic Materials*, **293(1)**: 483-496.
- Nie S., Xing Y., Kim G.J. and Simons J.W. (2007). Nanotechnology applications in Cancer. *Annual Review of Biomedical Engineering*, **9**:257-288.
- Niederer W. (1970). Ferritin: Iron incorporation and iron release. *Cellular and Molecular Life Sciences*, **26(2)**:218-220.

-
- Nomura Y., Ikeda M., Yamaguchi N., Aoyama Y. and Akiyoshi K. (2003). Protein refolding assisted by self-assembled nanogels as novel artificial molecular chaperone. *FEBS Letters*, **553**:271-276.
- Nowack B. and Bucheli T.D. (2007). Occurrence, behavior and effects of nanoparticles in the environment. *Environmental Pollution*, **150**:5-22.
- Oberdörster G., Oberdörster E. and Oberdörster J. (2005). Nanotoxicology: An emerging discipline evolving from studies of ultrafine particles. *Environmental Health Perspectives*, **113**(7):823-839.
- Oberdörster G., Stone V. and Donaldson K. (2007). Toxicology of nanoparticles: A historical perspective. *Nanotoxicology*, **1**(1):2-25.
- Ormonde A. D., Hicks E. C. M., Castillo J. and Van Duyne R. P. (2004). Nanosphere lithography: Fabrication of large-area Ag nanoparticle arrays by convective self-assembly and their characterization by surface plasmon resonance extinction spectroscopy. *Langmuir*, **20** (16):6927–6931
- Ortac I. and Severan F. (2007). Spectroscopy of biological nanocrystals. *Spectroscopy*, **21**: 31-41.
- Pang L. S. K., Saxby J.D. and Chatfield S. P. (1993). Thermogravimetric analysis of carbon nanotubes and nanoparticles, *Journal of Physical Chemistry*, **97**(27):6941-6942.
- Panitz J.A. (1974). The crystallographic distribution of field-desorbed species, *Journal of Vacuum Science and Technology*, **11**(1):207-210.
- Panitz J.A. (1978). Imaging atom-probe mass spectroscopy. *Progress in surface Science*, **8**(6):219-263.
- Parsons J.G., Peralta-Videa J.R. and Gardea-Torresdey J.L. (2007). Use of plants in biotechnology: Synthesis of metal nanoparticles by inactivated plant tissues, plant extracts, and living plants, *Developments in Environmental Sciences*, **5**:463-485.
-

-
- Pead, S., Durrant, E., Webb, B., Larsen, C., Heaton, D., Johnson, J. and Watt, G. D. (1995). Metal ion binding to apo, holo and reconstituted horse spleen apoferritin. *Journal of Inorganic Biochemistry*, **59**:15-27.
- Peet M., Babu S.S., Miller M.K. and Bhadeshia H.K.D.H. (2004). Three dimensional atom probe analysis of carbon distribution in low-temperature bainite. *Scripta Materialia*, **50(10)**:1277-1281.
- Pfaller T., Colognato R., Nelissen I., Favilli F., Casals E., Ooms D., Leppens H., Ponti J., Stritzinger R., Puentes V., Boraschi D., Duschl A. and Oostingh G. J. (2010). The suitability of different cellular in vitro immunotoxicity and genotoxicity methods for the analysis of nanoparticle-induced events. *Nanotoxicology*, **4(1)**:52-72.
- Philip D. (2009). Biosynthesis of Au, Ag and Au–Ag nanoparticles using edible mushroom extract. *Spectrochimica Acta Part A*, **73**:374–381.
- Phillips T. (2004). Nanoparticles used in biotechnology, www.biotech.about.com/od/nanotechnology/a/typesnanopart.htm, accessed on 03/01/2011.
- Pissuwan D., Valenzuela S.M. and Cortie M.B. (2006). Therapeutic possibilities of plasmonically heated gold nanoparticles. *Trends in Biotechnology*, **24(2)**:62-67.
- Poole C.P. and Owens F.J. (2003). Methods of measuring properties. In: Poole C.P. and Owens F.J. *Introduction to nanotechnology*. New York: John Wiley & Sons, Inc. 35-71.
- Prabhu B.M., Ali S. F., Murdock R. C., Hussain S. M. and Srivatsan M. (2010). Copper nanoparticles exert size and concentration dependent toxicity on somatosensory neurons of rat. *Nanotoxicology*, **4(2)**:150-160.
- Prasad D. and Jemmis E. (2008). Stuffing improves the stability of fullerene-like boron clusters. *Physical Review Letters*, **100(16)**:165504-165508.
- Prathna T.C., Chandrasekaran N., Raichur A.M and Mukherjee A. (2011). Biomimetic synthesis of silver nanoparticles by *Citrus limon* (lemon) aqueous extract and

theoretical prediction of particle size. *Colloids and Surfaces B: Biointerfaces*, **82**:152-159.

Press D. and Alexander M. (2011). Cholinesterase inhibitors in the treatment of dementia. <http://www.uptodate.com/contents/cholinesterase-inhibitors-in-the-treatment-of-dementia>, accessed on 27/11/2011.

Protopedia life in 3D. Cholinergic synapse. <http://www.protopedia.org/wiki/index.php/Acetylcholinesterase>, accessed on 1/08/2011.

Raffi M. (2007). Nanoparticles synthesis and characterization techniques: In *Synthesis and characterization of metal nanoparticles*, PhD Thesis, 36-44. <http://eprints.hec.gov.pk/2152/1/2068.htm>, accessed on 24/04/2011.

Rahimnejad M., Mokhtarian N. and Ghasemi M. (2009). Production of protein nanoparticles for food and drug delivery system, *African Journal of Biotechnology*, **8(19)**:4738-4743.

Raines R.T. (1998). Ribonuclease A. *Chemical Reviews*, **98(3)**:1045-1066.

Riddin T.L., Gericke M. and Whiteley C.G. (2006). Analysis of the inter- and extracellular formation of platinum nanoparticles by *Fusarium oxysporum* f.sp. *Lycopersici* using surface response methodology. *Nanotechnology*, **14**:3482-3489.

Robert N. G. and Wendelin J. S. (2006). Gas phase synthesis of fcc-cobalt nanoparticles. *Journal of Materials Chemistry*, **16**:1825-1830.

Roy D. and Fendler J. (2004). Reflection and absorption techniques for optical characterization of chemically assembled nanomaterials, *Advanced Materials*, **6(6)**:479-508.

Safavi A. and Zeinali S. (2010). Synthesis of highly stable gold nanoparticles using conventional and germinal ionic liquids. *Colloids and Surfaces A: Physicochemical and Engineering Aspects*, **362**:121-126.

-
- Salata O. (2004). Applications of nanoparticles in biology and medicine. *Journal of Nanobiotechnology*, **2(1)**:3-9.
- San H.B., Kim S., Moh S. H., Lee H., Jung D-Y. and Kim K. K. (2011). Platinum nanoparticles encapsulated by Aminopeptidase: A multifunctional bioinorganic nanohybrid catalyst. *Angewandte Chemie International Edition*, **50**:1-6.
- Sarmento B., Ferreira D., Veiga F. and Ribeiro A. (2006). Characterization of insulin-loaded alginate nanoparticles produced by ionotropic pre-gelation through DSC and FTIR studies. *Carbohydrate Polymers*, **66(1)**:1-7.
- Sastry M., Ahmad A., Khan M. I. and Kumar R. (2003). Biosynthesis of metal nanoparticles using fungi and actinomycete, *Current Science*, **85**:162-170.
- Sau T.K., Rogach A.L., Jäckel F., Klar T.A. and Feldmann J. (2010). Properties and applications of colloidal nonspherical noble metal nanoparticles. *Advanced Materials*, **22**:1805-1825.
- Saxena R.K., Williams W., McGee J.K., Daniels M. J., Boykin E. and Gilmour M.I. (2007). Enhanced *in vitro* and *in vivo* toxicity of poly-dispersed acid-functionalized single-wall carbon nanotubes. *Nanotoxicology*, **1(4)**:291-300.
- Scheraga H.A. (2011). Ribonucleases as models for understanding protein folding. In: Nicholson A.W. *Ribonucleases*. New York: Springer-Verlag Berlin Heidelberg. 367-397.
- Schüth F., Lu A. and Salabas E.L. (2007). Magnetic nanoparticles: synthesis, protection, functionalization, and application. *Angewandte Chemie International Edition*, **46**:1222 – 1244.
- Scott R.P.W. (2011). Thermal analysis. *In books in the physical chemistry series*. http://physicalchemistryresources.com/Book5_sections/pc_ec_titleandcontents_101320_09.htm, accessed on 26/06/2011.
-

-
- Sennuga A.T., van Marwijk J. and Whiteley C.G. (2011). Ferroxidase activity of apoferritin is increased in the presence of platinum nanoparticles. *Journal of Nanoparticle Research*, Article in Press.
- Sergeev G. B. (2006). Mass spectroscopy. In: Sergeev G. B. *Nanochemistry*. The Netherlands: Elsevier B.V. 44.
- Shang L., Wang Y., Jiang, J., Dong S. (2007). pH-Dependent protein conformational changes in albumin: gold nanoparticle bioconjugates: A spectroscopic study. *Langmuir*, **23**:2714-2721.
- Shrivastava S., Bera T., Roy A., Singh G., Ramachandrarao P. and Dash D. (2007). Characterization of enhanced antibacterial effects of novel silver nanoparticles. *Nanotechnology*, **18**:1-189.
- Skoog D.A., Holler F. J. and Crouch S. R (2007). *Principles of instrumental analysis*. 6th ed. Belmont, C.A: Thomson Brooks/Cole. 169-173.
- Skoog, D. A., Holler F. J. and Nieman T (1998). *Principles of instrumental analysis*. 5th ed. Australia, United States: Brooks/Cole: Thomson Learning. 805-808.
- Smith D.K. (2008). Nanomedicine arrives.
<http://www.rsc.org/Education/EiC/issues/2008July/NanomedicineArrives.asp>, accessed on 21/02/2011.
- Smith D.K. and Diederich F. (2000). Supramolecular dendrimer chemistry: a journey through the branched architecture. *Topics in Current Chemistry*, **210**:183-227.
- Smith P.K., Krohn R.I., Hermanson G.T., Mallia A.K., Gartner F.H., Provenzano M.D., Fujimoto E.K., Goeke N.M., Olson, B.J. and Klenk D.C (1985). Measurement of protein using bicinchoninic acid. *Analytical Biochemistry* **150**:76-85.
- Solomon S.D., Bahadory M., Jeyarajasingam A.V., Rutkowsky S.A. and Boritz C. (2007). Synthesis and study of silver nanoparticles. *Journal of Chemical Education*, **82**:322-325.

Sunstrom IV J.E., Moser W.R. and Marshik-Guerts B. (1996). General route to nanocrystalline oxides by hydrodynamic cavitation. *Chemistry of Materials*, **8**:2061-2067.

Sureshkumar M., Siswanto D. Y. and Lee C-K. (2010). Magnetic antimicrobial nanocomposite based on bacterial cellulose and silver nanoparticles. *Journal of Materials Chemistry*, **20**:6948-6955.

Suslick K.S. (1997). Sonocatalysis. In: Ertl, G., Knözinger, H., Weitkamp, J. *Handbook of Heterogeneous Catalysis*. 3rd ed. Weinheim: WILEY-VCH . 1350-1357

Swapp, S. (2011). Scanning electron microscope.

http://serc.carleton.edu/research_education/geochemsheets/techniques/SEM.html,

Accessed 18/06/2011.

Talley C.E., Jackson J. B., Oubre C., Grady N.K., Hollars C.W., Lane S.M., Huser T.R., Nordlander P. and Halas N.J. (2005). Surface-enhanced Raman scattering from individual Au nanoparticles and nanoparticle dimer substrates. *Nano Letters*, **5**(8):1569–1574.

The University of Queensland center for microscopy and microanalysis. Scanning electron microscope,

<http://www.uq.edu.au/nanoworld/index.html?page=35668&pid=0> , accessed on

16/05/2011.

Theodore L. and Kunz R.G. (2005). Nanotechnology: Prime Materials and Manufacturing Methods. In: Theodore L. and Kunz R.G *Nanotechnology: Environmental implications and solutions*. Hoboken, New Jersey: John Wiley& Sons, Inc. 70-79.

Thesen A.E., Matijevic M., Benner G. (2005). Design features and ultimate performance of an ultra-high resolution aberration-corrected, monochromatized 200 keV FEG-TEM, *Microscopy and Microanalysis*, **11**:2144-2145.

-
- Thierry de Ville d'Avray A., Carpenter E.E., O' Connor C.J. and Cole R.B. (1998). Characterization of ferrite nanoparticles by laser desorption/ionization mass spectroscopy. *European Journal of Mass Spectrometry*, **4**:441-449.
- Thompson D.T. (2007). Using gold nanoparticles for catalyst. *Nanotoday*, **2**:40-43
- Todd R. C. and Lippard S. J. (2009). Inhibition of transcription by platinum antitumor compounds. *Metallomics*, **1**:280-291.
- Tomalia D.A. (2005). Birth of a new macromolecular architecture: dendrimers as quantized building blocks for nanoscale synthetic polymer chemistry. *Progress in Polymer Science*, **30**:294-324.
- Tsong T. (1990). *Atom-probe field ion microscopy*. New York: Cambridge University press. 1-9.
- Ueno T., Suzuki M., Goto T., Matsumoto T., Nagayama K. and Watanabe Y. (2004). Size- selective olefin hydrogenation by Pd nanocluster provided in an apoferritin cage. *Angewandte Chemie, International Edition*, **43**:2527-2530.
- Unfried K., Albrecht C., Klotz L-O., Mikecz A. V., Grether-Beck S. and Schins R. P. F. (2007). Cellular responses to nanoparticles: Target structures and mechanisms. *Nanotoxicology*, **1(1)**:52-71.
- Urban C. and Schurtenberger P. (1998). Characterization of turbid colloidal suspensions using light scattering techniques combined with cross-correlation methods. *Journal of Colloid and Interface Science*, **207(1)**:150-158.
- Vaidyanathan R., Gopalram S., Kalishwaralal K., Deepak V., Pandian S.R.K. and Gurunathan S. (2010).. Enhanced silver nanoparticles synthesis by optimization of nitrate reductase activity. *Colloids and Surfaces B: Biointerfaces*, **75**:335-341.
- van de Weert M., Haris P.I., Hennink W. E. and Crommelin D.J.A. (2001). Fourier transform infrared spectrometric analysis of protein conformation: Effect of sampling method and stress factors. *Analytical Biochemistry*, **297**:160-169.
-

Varpness Z., Peters J.W., Young M. and Douglas T. (2005). Biomimetic synthesis of H₂ catalyst using protein cage architecture. *Nano Letters*, **5(11)**:2306-2309.

Vigneshwaran, N., Ashtaputre, N.M., Varadarajan, P.V., Nachane, R.P., Paralikar, K.M. and Baalasubramanya, R.H. (2007). Biological synthesis of silver nanoparticles using the fungus *Aspergillus flavus*. *Material Letters*, **61**: 1413-1418.

Viitala T. (2007). Relevant characterization techniques for thin films and coatings at liquid and solid interfaces,
http://www.nanotech.net/presentations/2007/Thursday/characterization/Tapani_Viitala.pdf, accessed on 29/06/2011.

Vinogradov S.V., Bronich T.K. and Kabanov A.V. (2002). Nanosized cationic hydrogels for drug delivery: preparation, properties and interactions with cells. *Advanced Drug Delivery Reviews*, **54(1)**:135-147.

Visaria R. K., Griffin R. J., Williams B.W., Ebbini E. S., Paciotti G. F., Song C.W. and Bischof J. C. (2006). Enhancement of tumor thermal therapy using gold nanoparticle–assisted tumor necrosis factor- α delivery. *Molecular Cancer Therapeutics*, **5**:1014-1020.

Wang C. and Ying J. Y. (1999). Sol synthesis and hydrothermal processing of anatase and rutile titania nanocrystals. *Chemistry of Materials*, **11(11)**:3113-3120.

Wang C., van der Vliet D., Chang K-C., You H., Strmcnik D., Schlueter J.A., Markovic N. M. and Stamenkovic V.R. (2009). Monodisperse Pt₃Co nanoparticles as a catalyst for the oxygen reduction reaction: Size-dependent activity. *Journal of Physical Chemistry C*, **113(45)**:19365-19368.

Wang L., Nagesha D.K., Selvarasah S., Dokmeci M.R. and Carrier R.L. (2008). Toxicity of CdSe nanoparticles in Caco-2 cell cultures. *Journal of Nanobiotechnology*, **6**:11-15.

-
- Wang X., Li Q., Xie J., Jin Z., Wang J., Li Y., Jiang K. and Fan S. (2009). Fabrication of ultralong and electrically uniform single-walled carbon nanotubes on clean substrates. *Nano Letters*, **9** (9):3137–3141.
- Wang Z., Zhang K., Zhao J., Liu X. and Xing B. (2010). Adsorption and inhibition of butyrylcholinesterase by different engineered nanoparticles. *Chemosphere*, **79**(1):86-92.
- Wang Z., Zhao J., Li F., Gao D. and Xing B. (2009). Adsorption and inhibition of acetylcholinesterase by different nanoparticles. *Chemosphere*, **77**(1):67-73.
- Wegner K., Barborini E., Piseri P. and Milani P. (2006). Gas-phase synthesis of nanostructured particulate films. *KONA*, **24**: 54-69.
- Whiteley C.G., Govender Y., Riddin T. and Gericke M. (2009). Bioreduction of platinum salt into nanoparticles: A mechanistic perspective. *Biotechnology Letters*, **31**(1):95-100.
- Whiteley C.G., Govender Y., Riddin T. and Rai M. (2011). Enzymatic synthesis of platinum nanoparticles: Prokaryote and eukaryote systems. In: Rai M., Duran N. and Southam G. *Metal nanoparticles in microbiology*. New York: Springer-Verlag. 103-134.
- Wiesendanger R. (1994). Scanning tunneling microscopy (STM). In: Wiesendanger R. *Scanning probe microscopy and spectroscopy: methods and applications*. New York: Cambridge University Press. 11-13.
- Wikipedia (2011). Ribonuclease A. http://en.wikipedia.org/wiki/Ribonuclease_A, accessed on 26/10/2011.
- Worek F., Reiter G., Eyer P. and Szinicz L. (2002). Reactivation kinetics of Acetylcholinesterase from different species inhibited by highly toxic organophosphates, *Archives of Toxicology*, **76**:523-529.

-
- Worthington (2011). Ribonuclease. <http://www.worthington-biochem.com/rnase/default.html>; <http://www.worthington-biochem.com/rnase/images/reaction.jpg> , accessed on 24/10/2011.
- WTEC hyper-librarian (1999). Nanoparticle synthesis strategies. www.wtec.org/loyola/nano/02_04.htm, accessed on 09/02/2011.
- Xie H., Gu Y. and Ploehn H. J. (2005). Dendrimer-mediated synthesis of platinum nanoparticles: new insights from dialysis and atomic force microscopy measurements, *Nanotechnology*, **16**:S492-S501.
- Xie H., Gu Y. and Ploehn H.J. (2005). Dendrimer-mediated synthesis of platinum nanoparticles: new insights from dialysis and atomic force microscopy measurements. *Nanotechnology*, **16**: S492–S501.
- Xu W. (2005). Biotemplates for nanoparticle synthesis. *Literature seminar*, http://chemistry.illinois.edu/research/inorganic/seminar_abstracts/2005-2006/Xu.LitSeminar.pdf , accessed on 04/04/2011.
- Ying J.Y. and Sun T. (1997). Research needs assessment on nanostructured catalysts. *Journal of Electroceramics* **1**:219-238.
- Yoshimura H. (2006). Protein-assisted nanoparticle synthesis. *Colloids and Surfaces A: Physicochemical and Engineering Aspects*, **282-283**:464-470.
- Yu Y.Y., Chang S.S., Lee C.L. and Wang C.R.C. (1997). Gold nanorods: electrochemical synthesis and optical properties. *Journal of Physical Chemistry B*, **101**:6661-6664.
- Zhang B., Harb J.N., Davis R.C., Kim J.W., Chu S.H., Choi S., Miller T. And Watt G.D. (2005). Kinetic and thermodynamic characterization of the cobalt and manganese oxyhydroxide cores formed in horse spleen ferritin. *Inorganic Chemistry*, **44(10)**:3738–3745.
-

Zhang J.Z. and Noguez C. (2008). Plasmonic optical properties and applications of metal nanostructures. *Plasmonic*, **3**:127-150.

Zhang L., Laug L., Mückgesang W., Pippel E., Gösele U., Brandsch M. and Knez M. (2010). Reducing stress on cells with apoferritin-encapsulated platinum nanoparticles. *Nano Letters*, **10**:219-223.

Zhang L., Swift J., Butts C.A., Yerubandi V. and Dmochowski I.J. (2007). Structure and activity of apoferritin-stabilized gold nanoparticles. *Journal of Inorganic Biochemistry*, **101**:1719-1729.

Zhao Y. and Nalwa H.S. (2006). Nanotoxicology- Interactions of nanomaterials with biological systems, <http://www.aspbs.com/toxic.html#contents>, accessed on 6/07/2011.

Appendices

Appendix A – Method of preparation of buffers and solutions

A1: Tris buffer saline (TBS), pH 8.0 (1L)

- 50 mM Tris-HCl (50 ml of 1 M Tris-HCl, pH 8.0 stock).
- 150 mM NaCl (50 ml of 3 M stock)

The solution mixtures were made up to 1 L with deionised water (dH₂O).

A2: 1 M Tris-HCl, pH 8.0 (1 L)

Tris salt (121.14 g Sigma-Aldrich) was dissolved in 800 ml of deionised water and pH was adjusted to 8.0 with concentrated (conc.) HCl (Merck). Solution was made up to 1 L with deionised water.

A3: 3 M NaCl

NaCl (175.32 g, Merck) was dissolved in 1 L of dH₂O.

A4: 50 mM borate-cacodylate buffer, pH 5.5

The salts of cacodylic acid (5.52 g, Sigma) and sodium borate (3.81 g, Merck) were dissolved in 1 L of dH₂O. Amount of salts used was calculated using the Henderson-Hasselbalch equation with PK_a of cacodylic acid = 6.15.

A5: Phosphate buffer saline (PBS) – 500 ml

- 137 mM NaCl (4 g)
- 27 mM KCl (Merck, 0.1 g)
- 4.3 mM Na₂HPO₄ (Merck, 0.72 g)
- 1.4 mM KH₂PO₄ (Merck, 0.12 g)

All reagents were dissolved in dH₂O water, made up to 500 ml, autoclaved for 10 min and cooled in the fridge.

A6: Chloramphenicol (CAM, 35 mg/ml stock, 10 ml)

CAM (0.35 g, Sigma-Aldrich) was dissolved in 10 ml of ethanol and filtered through a sterile 0.45 µm filter.

A7: L-arabinose (40 %, 10 ml)

L-arabinose (4 g, Sigma) was dissolved in 10 ml of autoclaved dH₂O and stored at -20 °C.

Appendix B – Preparation of metal standards for ICP OES and metal standard curves

B1: Platinum

Platinum standards (Sigma) were prepared as described (Table B.1). The following factors were used; 1 M of Pt = 195 100 ppm; Stock concentration of Pt standard (Sigma-Aldrich) = 100 ppm in 0.1 M HCl; Total volume of standards solution = 25 ml; Molar concentration of 37 % trace select HCl (Fluka) = 10.1 M

Table B.1: Protocol for preparation of platinum standard curve

[Pt std.]	Pt std[†].	[HCl]	37 % trace select HCl	69 % trace select HNO₃
(ppm)	(ml)	(M)	(ml)	(ml)
0	0	0	0.248	0.082
0.5	0.125	5.00E-04	0.246	0.082
1	0.25	1.00E-03	0.245	0.082
1.5	0.375	1.50E-03	0.244	0.082
2	0.5	2.00E-03	0.243	0.082
2.5	0.625	2.50E-03	0.241	0.082

Pt std. = platinum standards; ppm = parts per million. Each standard was made up to 25 ml with deionised water.

Metal quantification of Pt was determined at three wavelengths (214.4, 224.5 and 265.9 nm) by the instrument, Table B.1.1 and Fig. B.1) and was expressed in counts per second (Ct/S).

Table B.1.1: ICP OES count values of Pt standards.

Ct/S			
λ (nm)			
[Pt]			
(ppm)	214.4	224.5	265.9
0	4.072	54.44	-23.1
0.5	969.5	646.8	905.8
1	1952	1256	1844
1.5	2932	1881	2875
2	3895	2491	3867
2.5	4831	3090	4854

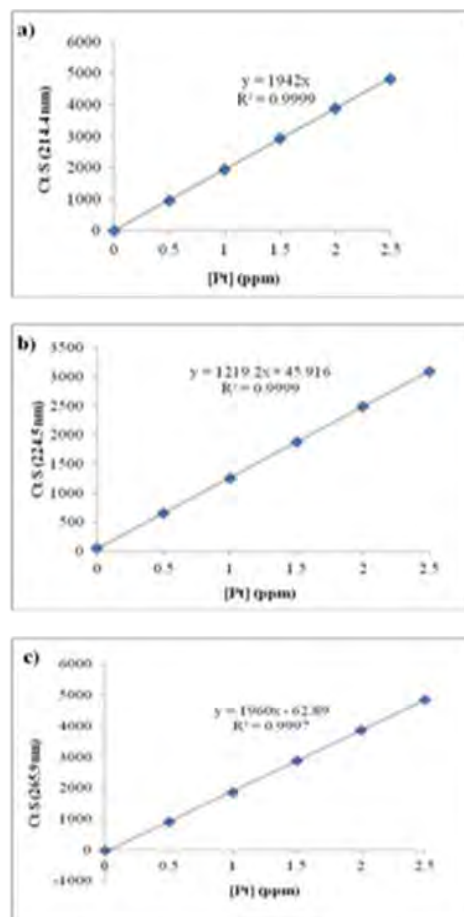


Figure B.1: Standard curves of platinum measured at different wavelengths. (a) 214.4 nm; (b) 224.5 nm and (c) 265.9 nm. Each point represents mean values with standard deviations < 10 %.

B2: Gold

Preparation of Au standard is described in Table B.2. using the following factors: 1 M of Au = 196 970 ppm; stock concentration of Au standard = 100 ppm in 0.14 M HCl; Volume of standards = 25 ml.

Table B.2: Protocol for preparation of gold standard curve

[Au std.]	Au std.	[HCl]	37 % trace select HCl	69 % trace select HNO ₃
(ppm)	(ml)	(M)	(ml)	(ml)
0	0	0	0.347	0.116
0.5	0.125	7.00E-04	0.345	0.116
1	0.25	1.40E-03	0.343	0.116
2	0.5	2.80E-03	0.340	0.116
4	1	5.60E-03	0.333	0.116
8	2	1.12E-02	0.319	0.116

Au std. = gold standards; ppm = parts per million; each standard was made up to 25 ml with deionised water

The Au content in standards and samples was read at three wavelengths (197.8, 242.7 and 267.3 nm, Table B.2.1 and Fig. B.2).

B3: Silver

1 M of Ag = 107 870 ppm; stock concentration of Ag standard = 100 ppm in 0.03 M HNO₃; Volume of standards = 25 ml. 69 % trace select HNO₃ = 10.95 M. Preparations of Ag standards are summarized in Table B.3 below.

Table B.3: Protocol for preparation of silver standard curve.

[Ag std.]	Ag std.	[HCl]	69 % trace select HNO ₃
(ppm)	(ml)	(M)	(μ l)
0	0	0	68.5
2	0.5	6.00E-04	67.0
4	1	1.20E-03	66.0
6	1.5	1.80E-03	64.0
8	2	2.40E-03	63.0
10	2.5	3.00E-02	62.0

Ag std. = silver standards; ppm = parts per million; each standard was made up to 25 ml with deionised water

The Ag content in standards and samples was read at three wavelengths (243.7, 328.2 and 338.3 nm, Table B.3.1 and Fig. B.3).

Table B.2.1: ICPOES count values of Au standards.

Ct/S			
λ (nm)			
[Au]			
(ppm)	197.8	242.7	267.5
0	1.737	65.39	56.32
0.5	6.213	1754	1140
1	9.983	3582	2109
2	17.68	7041	4120
4	33.77	14080	8268
8	55.17	28162	14020

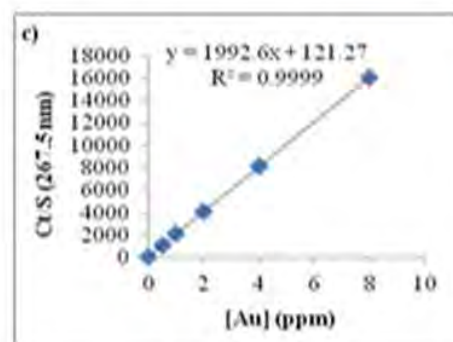
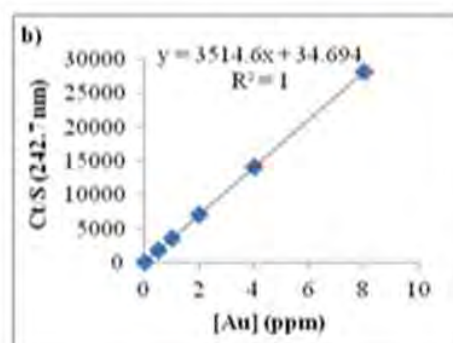
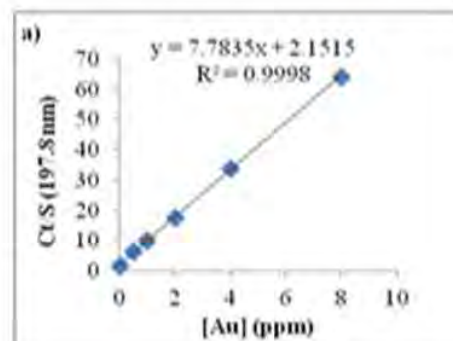


Figure B.2: Standard curves of gold measured at different wavelengths. (a) 197.8 nm; (b) 242.7 nm and (c) 267.5 nm. Each point represents mean values with standard deviations < 10 %.

Table B.3.1: ICPOES count values of Ag standards.

CVS			
λ (nm)			
[Ag]			
(ppm)	243.7	328.2	338.3
0	4.066	134.1	101.2
2	215	16860	14870
4	452	36920	28770
6	652.2	57490	45850
8	866.3	78980	59420
10	1087	100700	76640

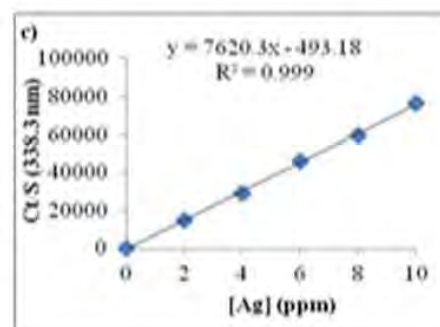
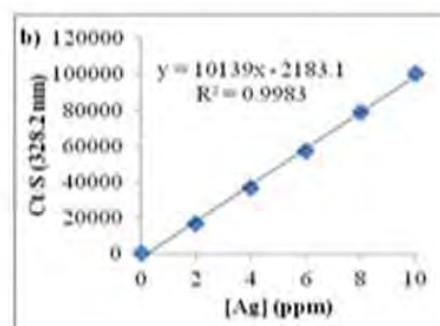
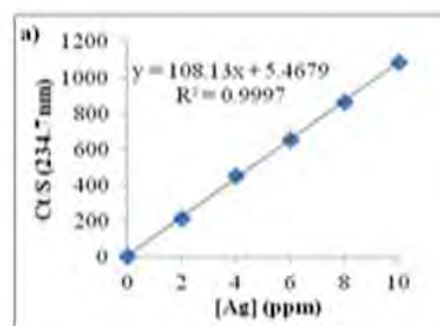


Figure B.3: Standard curves of silver measured at different wavelengths. (a) 243.7 nm; (b) 328.2 nm and (c) 338.3 nm. Each point represents mean values with standard deviations < 10 %.

Appendix C – Standard curve of ferritin

C1: Ferritin stock preparation (1 ml)

A ferritin stock solution (5 μ M) was prepared by diluting 42 μ l of ferritin (56 mg/ml, Sigma) with 958 μ l of 50 mM borate cacodylate buffer. Ferritin standards were prepared as described in Table C.1. Absorbance was taken at 420 nm.

Table C.1: Protocol of ferritin standard curve.

[Ferritin] (μ M)	5 μ M ferritin (μ l)	Borate-cacodylate buffer* (ml)	Mean** $A_{420 \text{ nm}}$
0	0	200	4.63E-18
0.5	20	180	0.173
1	40	160	0.337
1.5	60	140	0.504
2	80	120	0.674
2.5	100	100	0.852

*Total volume of reaction mixture = 200 μ l. ** Mean values are shown with standard error of means < 10 %.

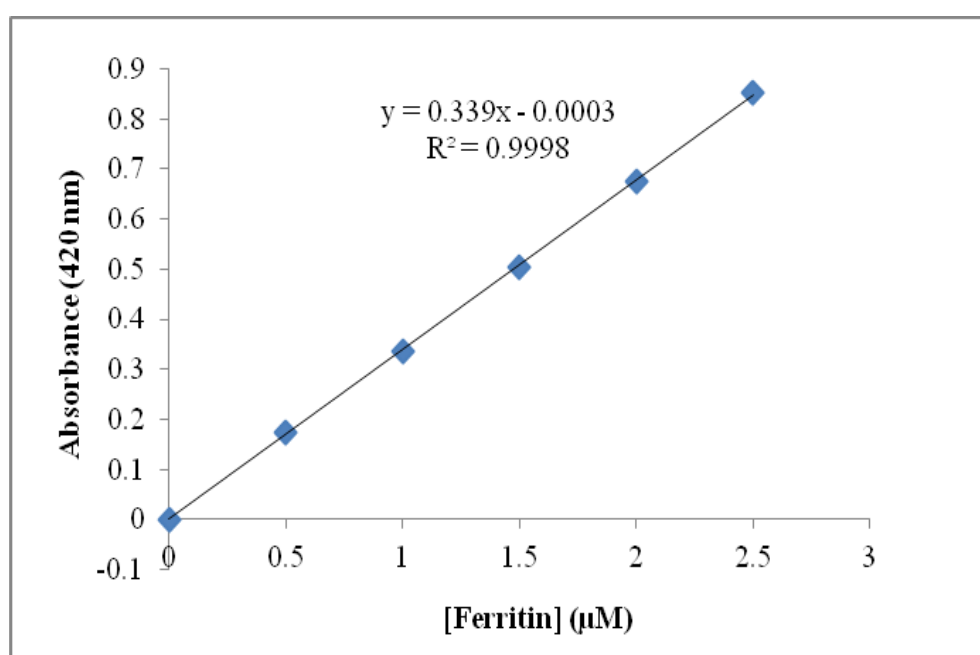


Figure C.1: Ferritin standard curve.

Appendix D- Protein standard curve for estimation of protein concentration by Bradford method

A 2mg.ml^{-1} stock solution of bovine serum albumin (BSA) was prepared in buffer/water (depending on experiment). BSA protein standard curve was constructed as illustrated in Table D.1. Bradford reagent ($245\ \mu\text{l}$, Sigma) was added to $5\ \mu\text{l}$ sample of each protein standard.

Table D.1: BSA protein standard curve protocol by Bradford method.

[BSA] (μM)	$2\ \text{mg.ml}^{-1}$ BSA (μl)	buffer/ H_2O (μl)	Mean** A_{595}
0	0	200	1.85E-17
0.1	10	180	0.027
0.2	20	160	0.049
0.4	40	140	0.103
0.8	80	120	0.212
1.2	120	80	0.315

** Values are averages of triplicate readings. Standard error of means is $< 10\%$.

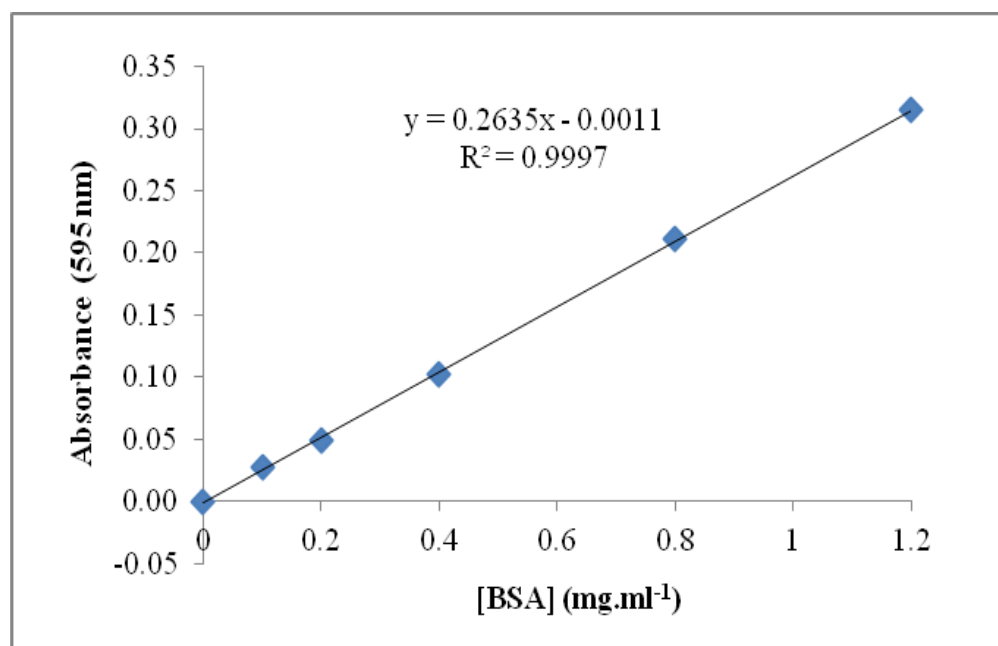


Figure D.1: Protein standard curve using BSA by Bradford method.

Appendix E- Recipe for 2x YT broth and Agar

E1: 2 x YT broth (1 L)

Bacto-tryptone = 16 g

Bacto-yeast = 10 g

NaCl = 5 g

Listed reagents were dissolved in 1 L of dH₂O and autoclaved.

E2: 2xYT Agar + CAM plates (300 ml)

- Bacto-tryptone = 4.8 g
- Bacto-yeast = 3 g
- NaCl = 1.5 g
- Bacto- agar = 4.5 g

All listed reagents were dissolved in 300 ml of deionised water and autoclaved for 10min. CAM was added to the slightly cooled solution to a final concentration of 20 µg/ml and rapidly poured into Petri dishes (10 agar plates was made from a 300 ml solution) and allowed to set .

Appendix F: Polyacrylamide gel electrophoresis (PAGE) and western analysis procedures

F1: Native PAGE protocols for Bio-Rad mini –protean II apparatus (modified method of Bollag *et al.*, 1996)

Reagent A – Acrylamide solution

30 % acrylamide + 0.8 % bis-acrylamide was purchased from Bio-Rad.

Reagent B- 4x separating gel buffer (1.5 M Tris-HCl, pH 8.8) - 100 ml

Tris (18.2 g) was dissolved in 40 ml of dH₂O; pH was adjusted to 8.8 with conc. HCl and made up to 100 ml with dH₂O.

Reagent C- 4 x stacking gel buffer (0.5 M Tris-HCl, pH 6.8) - 100 ml

Tris (6 g) was dissolved in 40 ml of water; conc. HCl was added to a pH of 6.8 and made up to 100 ml with dH₂O.

Ammonium persulfate (APS, 10 %) - 5 ml

APS (0.5 g, Merck) was dissolved in 5 ml of dH₂O and stored in 500 µl aliquots at -20 °C.

Electrophoresis buffer – 1 L

Tris (3 g) and glycine (14.4 g, Sigma-Aldrich) were dissolved and made up to 1L with dH₂O. The pH was confirmed to be 8.8 with a pH meter (Mettler, USA).

5 x sample buffer (SB) - 10 ml

- Tris- HCl (1 M, pH 6.8) - 10 ml
- Glycerol – 5 ml (i.e. 50 %)
- 1 % bromophenol blue (Merck) – 0.5 ml
- dH₂O – 1.4 ml

Protein samples for Native PAGE analysis was prepared by mixing protein samples with SB in a 5:1 ratio respectively and 10 µl of each sample was added to the well of the gels.

F2: SDS PAGE for the molecular weight determination of proteins

(modified method of Bollag *et al.*, 1996)

Reagent A – Acrylamide solution

30 % acrylamide + 0.8 % bis-acrylamide was purchased from Bio-Rad.

Reagent B- 4x separating gel buffer - 100 ml

Tris-HCl, pH 8.8 solution (2 M, 75 ml) was mixed with 10 % SDS solution (4 ml) and made up to 100ml with dH₂O.

Reagent C- 4 x stacking buffer - 100 ml

1 M Tris-HCl , pH 6.8 (50 ml) was added to 4 ml of 10 % SDS solution and made up to 100 ml with dH₂O.

Table F.1: Protocol for 5 % discontinuous native PAGE (2 x 0.75 mm gels)

Resolving gel	
Reagent	Volume (ml)
A	1.7
B	2.5
dH₂O	5.8
10 % APS	0.05
TEMED (Merck)	0.01

Stacking gel	
Reagent	Volume (ml)
A	0.67
C	1.0
dH₂O	2.3
10 % APS	0.03
TEMED	0.005

Ammonium persulfate (APS, 10 %) - 5 ml

APS (0.5 g) was dissolved in 5 ml of dH₂O and stored in 500 µl aliquots at -20 °C.

Electrophoresis buffer – 1L

Tris (3 g), glycine (14.4 g) were dissolved in dH₂O containing 10 % SDS (10 ml) and made up to 1L with dH₂O.

5 x sample buffer- 10 ml

- Tris- HCl (1 M, pH 6.8) – 0.6 ml
- Glycerol – 5 ml (i.e. 50 %)

- 10 % SDS – 2 ml
- β -mercaptoethanol (Merck) – 0.5 ml
- 1 % bromophenol blue (Merck) – 1 ml
- dH₂O – 0.9 ml

Table F.2: Recipe for 12 % SDS resolving gels (2 X 0.75 mm gels)

Seperating gel

Reagent	Volume (ml)
A	4.0
B	2.5
dH₂O	3.5
10 % APS	0.05
TEMED	0.005

Stacking gel (5 %)

Reagent	Volume (ml)
A	0.67
C	1.0
dH₂O	2.3
10 % APS	0.03
TEMED	0.005

F3: Staining and destaining solution for both native and SDS gels (Gálvez *et al.*, 2008)

Staining solution (1 L)

- 1 g of Coomassie blue (Merck)
- 400 ml of methanol
- 100 ml glacial acetic acid

- 500 ml of dH₂O

Destaining solution

- 400 ml of methanol
- 100 ml of glacial acetic acid
- 500 ml of dH₂O

The staining and destaining procedure were performed for 1 h and 3 h respectively.

F4: Protein molecular weight determination

Molecular weight of proteins using a standard curve of log of molecular weight (Mr) versus the log of relative mobility (R_f) of protein markers (10-170 kDa, Fermentas, Fig. F.1).

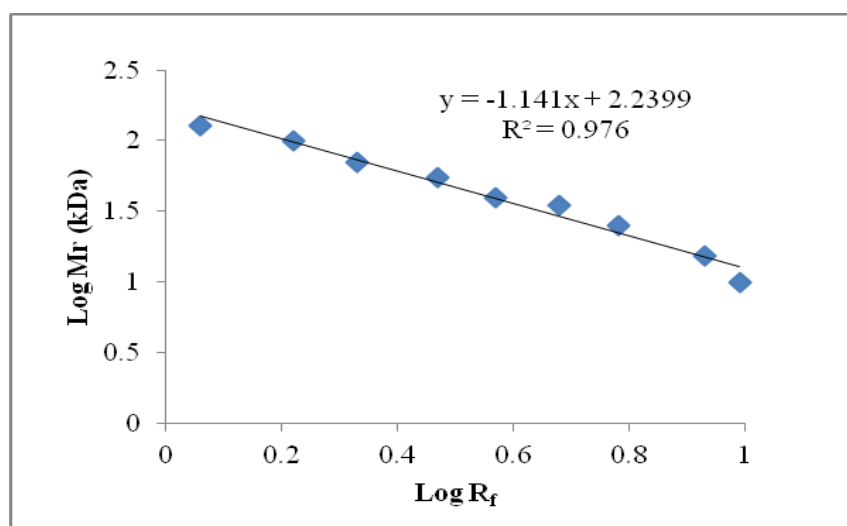


Figure F.1: Molecular weight calibration curve using protein markers ranging from 10-170 kDa (Fermentas-Inqaba Biotech, South Africa).

F5: Western blot analysis-preparation of buffers and solutions protocols

Western blot analysis was carried out as described in the manual of the Roche BM Chemiluminescence western blot kit with some modifications.

Preparation of 12 % SDS PAGE gels

SDS page gels (12 %) were made as described in F2.

Recipes for buffers and solution

Transfer buffer – 1 L

Tris (3.03 g) and glycine (14.4 g) was dissolved in 200 ml of methanol and made up to 1 L with dH₂O. Solution was made fresh and chilled in the freezer for 1 h prior to use.

Tris buffer saline (TBS), pH 7.5 – 1 L

Tris (6.05 g) and NaCl (8.76 g) was dissolved in 800 ml of dH₂O, pH was adjusted to 7.5 with conc. HCl and made up to 1 L with dH₂O.

Tris buffer saline-Tween 20 (TBST) – 500 ml

Tween 20 (0.5 ml) was made up to 500 ml of TBS.

Blocking solution (5 %) – 100 ml

Skim milk (5 g, Sigma) was dissolved in TBS to a final volume of 100 ml.

Primary (1°) antibody – 10 ml

GroEL antibody (anti-GroEL, Sigma) produced in rabbit was diluted with 5 % blocking solution in a ratio 1: 10 000 (antibody to blocking solution respectively).

Secondary (2°) antibody stock solution

Lyophilized mouse/rabbit peroxidase (POD)-labelled 2° antibody (Roche Applied Science) was reconstituted in 100 µl of double deionised water (ddH₂O).

2° antibody stock working solution – 10 ml

Stock solution of 2° antibody was diluted 5 000 fold with 5 % blocking solution.

Equipment and materials

- Trans-blot mini –Protean II western blotting equipment (Bio-Rad).
- Power supply with capacity of 200 V, 0.6 A.
- Blotting paper (Bio-Rad)
- Polyvinylidene fluoride (PVDF) membrane (Bio-Rad)
- Plastic container for gel incubation

- Rocker/rotary shaker
- A shallow tray for preparation of gel for transfer.
- Magnetic stirrer
- Gel doc equipment (Bio-Rad).

Procedure

SDS PAGE

SDS page analysis was performed on protein as described in 3.2.1.2.4 (pg. 55) without carrying out the staining/destaining procedures.

GroEL/protein transfer

PVDF membrane was made wet/ active by a short rinse in methanol and membrane appears translucent. The western unit was assembled as illustrated in Fig. F.2 below:

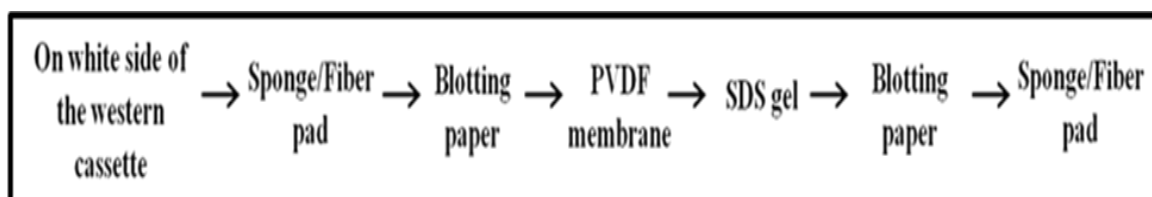


Figure F.2: A schematic illustration for the arrangement of the gel-membrane sandwich for protein transfer.

The loaded cassette was placed in the Trans-blot apparatus and protein transfer was carried in transfer buffer at 200 V for 90 min.

Preparation of transfer membrane for protein detection

The PVDF membrane after protein transfer was briefly stained with a solution of Ponceau S red (Sigma) to confirm protein transfer and afterwards rinsed off with ddH₂O. Further detection procedures are listed below:

- The transfer membrane was incubated in blocking solution at 2-8 °C for 1 h under constant shaking.

- Incubation with the solution of 1° antibody at 2-8 °C was performed for 1 h under constant shaking.
- Membrane was washed twice (10 min per wash) with TBST.
- Blocking of the transfer membrane was done with 5 % blocking solution (1 h, 2-8 °C).
- Transfer membrane was incubated with the solution of 2° antibody for 30 min at 2-8 °C under constant shaking.
- The washing of the membrane was performed twice (15 min per wash) with TBST.
- Detection of GroEL protein was performed using the mouse/rabbit BM Chemiluminescence protein detection kit as described by the product manual.

Appendix G: Phosphate standard curve for estimation of phosphate release by the ATPase activity of GroEL

G1: Ascorbate-molybdate reagent

Reagent A: 6 % ascorbic acid – 10 ml

Ascorbic acid (0.6 g, Sigma) was dissolved in a 5 % aqueous solution of glacial acetic acid (10 ml) and filtered through a 0.45 µM filter (Millipore)

Reagent B: 6 % ammonium molybdate – 10 ml

Ammonium molybdate (0.6 g, Merck) was dissolved in 5 % glacial acetic acid in ddH₂O (10 ml). Solution was filtered through 0.45 µM syringe filter (Millipore)

Ascorbate-molybdate reagent was made by mixing reagent A and B in a 1:2.5 ratio respectively at the point of use.

G2: Phosphate standard curve protocol

A 0.5 mM stock solution of dihydrogen potassium phosphate (KH₂PO₄, Merck) was prepared in phosphate-free ddH₂O. The phosphate standard curve was constructed as

illustrated in Table G.1. Ascorbate-molybdate reagent (140 μ l) was added to 10 μ l sample of each phosphate standard, incubated for 15 min and absorbance was read at 850 nm.

Table G.1: Phosphate standard curve protocol.

[KH ₂ PO ₄] (μ M)	0.5 mM KH ₂ PO ₄ (μ l)	ddH ₂ O (μ l)	Mean** A ₈₅₀
0	0	200	0
0.0625	25	175	0.010
0.125	50	150	0.020
0.250	100	100	0.040
0.375	150	50	0.060
0.500	200	-	0.079

**Values represents the mean of triplicate reading with standard error of means <10 %.

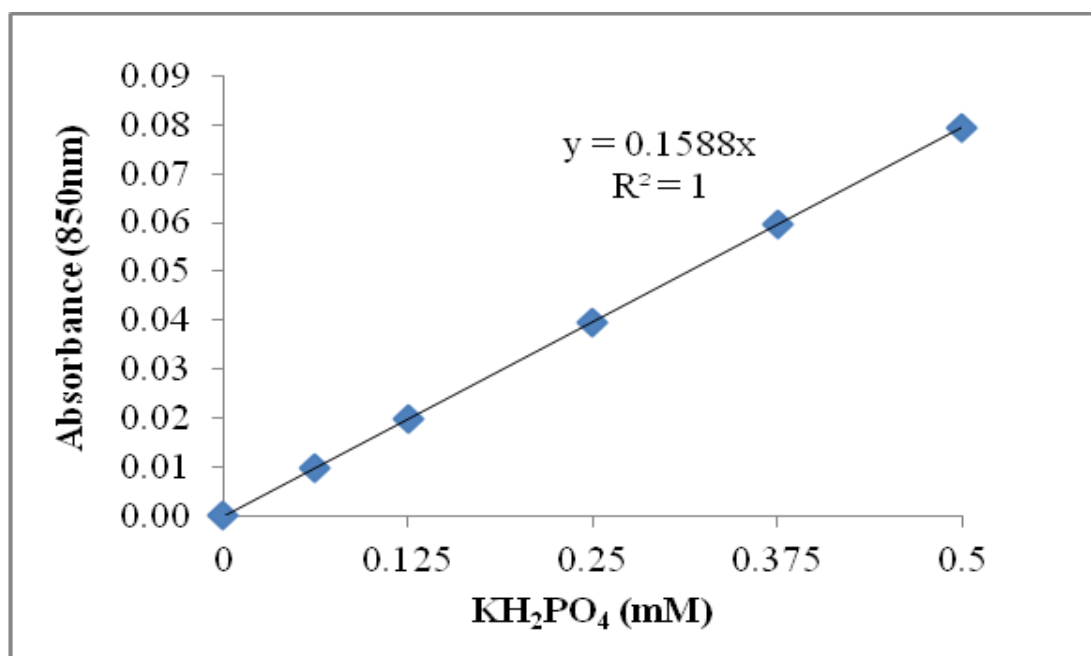


Figure G.1: Phosphate standard curve

G3: ATPase assay of GroEL

ATPase activity assay was determined as described in 3.2.1.2.5 (pg. 56). The ATPase activity was calculated using equation G.1 below and was expressed in $\mu\text{molPi}\cdot\text{ml}^{-1}\cdot\text{min}^{-1}$.

$$\text{ATPase activity } (\mu\text{molPi}\cdot\text{ml}^{-1}\cdot\text{min}^{-1}) = \frac{A_{850} \times V_T}{\epsilon \times t \times V_e} \times D.F$$

Equation G.1: GroEL ATPase activity calculation. $A_{850\text{ nm}}$ = sample absorbance at 850 nm; ϵ = extinction coefficient of phosphate ($0.1588\text{ ml}\cdot\mu\text{mol}^{-1}$) and was calculated using the phosphate standard curve (Fig. G.1); t = time (min); V_T = total volume of reaction (μl); V_e = volume of enzyme (μl) and $D.F$ = dilution factor.

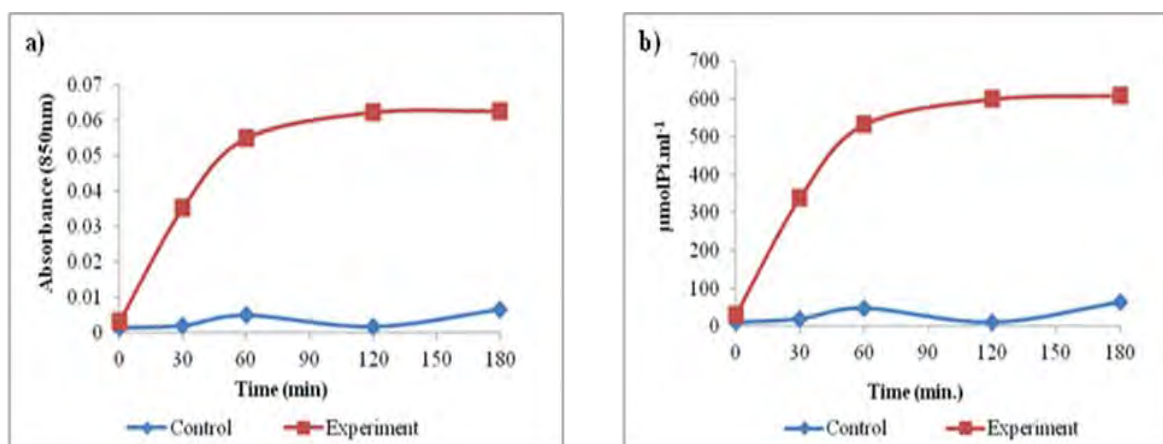


Figure G.2: A plot of ATPase of GroEL activity against time. (a) Activity absorbance at 850 nm versus time. (b) Calculated activity in $\mu\text{mol}\cdot\text{ml}^{-1}$ versus time.

Appendix H: RNase protein estimation by bicinchoninic acid(BCA) and activity determination

H1: BCA working reagent

The BCA working reagent was prepared using bicinchoninic acid protein assay kit (BCA1, Sigma-Aldrich). Reagent A (solution of bicinchoninic acid) and Reagent B [4 % (w/v) copper (II) sulphate pentahydrate) was mixed in a ratio 50:1 respectively prior to protein determination.

H2: Protein standard curve for protein estimation by BCA method (Smith, 1985)

A stock solution of bovine serum albumin (BSA, 2 mg.ml⁻¹) was prepared in ddH₂O. BSA protein standard curve was constructed as illustrated in Table H.1. BCA working reagent (200 µl Sigma-Aldrich) was added to 25 µl sample of each protein standard.

H3: Acetate-perchloric acid solution – 10 ml

Uranyl acetate (7.5 g, Sigma-Aldrich) was dissolved autoclaved ddH₂O containing 2.5 ml of perchloric acid and made up to 10 ml with ddH₂O. Solution was prepared prior to use.

Table H.1: BSA protein standard curve protocol by BCA method

[BSA] (µM)	2 mg.ml ⁻¹ BSA (µl)	H ₂ O (µl)	Mean** A ₅₆₂
0	0	200	2.313E-18
0.1	10	180	0.124
0.2	20	160	0.223
0.4	40	140	0.423
0.6	80	120	0.642
0.8	120	80	0.838

** Values are averages of triplicate readings. Standard error of means is < 10 %.

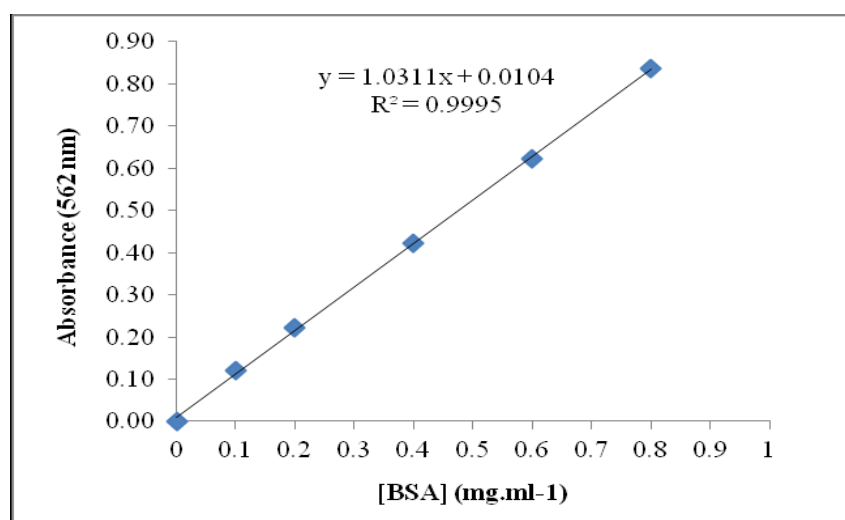


Figure H.1: BSA protein standard curve by BCA method.

H4: RNase activity preparation

The hydrolytic activity of RNase was calculated as illustrated in equation H.1. RNase activity was expressed in Units.mg⁻¹ protein.

$$\text{RNase activity (Unit.mg of protein}^{-1}\text{)} = \frac{\Delta A_{260} \times 30}{\text{mg enzyme in reaction mixture}}$$

Equation H.1: RNase activity calculation.

Appendix I: Activity calculations and percentage inhibition of AChE

I.1: Calculation of AChE activity

The activity of AChE (A) was calculated as described (Equation I.1), the activity of AChE was determined after 2 min and expressed as μmol.ml⁻¹.min⁻¹.

$$A (\mu\text{mol.ml}^{-1}.\text{min}^{-1}) = \frac{\Delta A_{412} \times V_T}{\epsilon \times t \times V_e}$$

Equation I.1: AChE activity calculation. ΔA_{412} = the absorbance change after 2 min at 412 nm; ϵ = extinction coefficient of phosphate (13.6 ml.μmol⁻¹); t = time (2 min); V_T = total volume of reaction (200 μl); V_e = volume of enzyme (20 μl).

I.2: Percentage inhibition calculation

The calculation showing the effect of nanoparticles on the activity of AChE is shown below (Equation I.2). This was expressed in % Inhibition of AChE.

$$\% \text{ Inhibition of AChE} = \frac{A_0 - A_{\text{nps}}}{A_0} \times 100$$

Equation I.2: Calculation of the % Inhibition of AChE activity by M-nps. A_0 = the AChE activity without nanoparticles; A_{nps} = the activity of AChE in the presence of nanoparticles.